広島大学学位請求論文

Nitrogen Atom Effect on Reactivity of the Localized Singlet 1,3-Diradicals

（局在化一重項1,3-ジラジカルの反応性
に及ぼす窒素原子効果）

２０１９年
広島大学大学院理学研究科
化学専攻

吉富　翔平

目　次

主論文

Table of Contents

Chapter 4. Computational study

Chapter 5. Conclusions

Acknowledgements

List of publications

Chapter 1

General Introduction

1.1 Fundamental chemical reactions; homolysis and heterolysis

  In chemistry, bond-cleavage and bond-formation of a covalent bond are most fundamental phenomena. We know that there are two types of processes—*heterolysis* and *homolysis*. Ion pairs, i.e. cation and anion, are involved in bond heterolysis. A large number of heterolysis chemistry have been reported, and established for application of the field of not only mechanistic study, but also materials chemistry, organic synthesis, and biological chemistry.[1,2]

Scheme 1. Heterolysis and homolysis.
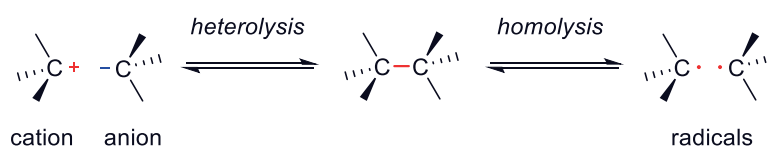
Localized singlet diradicals are key intermediates in processes involving the bond homolysis (Scheme 1).[3-8] A thorough research study of the molecular structure, electronic structure and reactivity of localized singlet diradicals is essential to understand the mechanism of homolytic bond-cleavage and bond-formation reactions. Subsequently, the fundamental knowledge makes it possible to be applied to many fields of chemistry, such as material chemistries, organic synthesis, and biological chemistry. The lifetime of localized singlet diradicals, however, is quite short due to the fast intramolecular radical–radical recombination. Thus, the chemistry of localized singlet diradicals is still developing, especially in experiments.[5,9-11] Over the last decade, the chemistry of localized singlet diradicals has significantly developed after the first findings of spectroscopically-detectable long-lived singlet diradicals.

1.2   1,3-Diradicals

"*Diradicals*" is defined as the molecular species having the two odd electrons in degenerate or nearly-degenerate molecular orbital, and produce two spin states, namely, singlet ($\uparrow\downarrow$; $S = 0$, spin multiplicity = 1) and triplet ($\uparrow\uparrow$; $S = 1$, spin multiplicity = 3). The singlet state and triplet state are in equilibrium with one another through the intersystem crossing (ISC) process.

In 1975, Buchwalter and Closs reported the EPR (Electron Paramagnetic Resonance) spectrum of cyclopentane-1,3-diyls (X = H, n=1; Scheme 2), the observation experimentally localized 1,3-diradicals for the first time.[12] In general, the lifetime of triplet diradicals is long enough to allow the diradicals to be detected using time-resolved spectroscopic analysis at ambient temperature and EPR spectroscopic analysis under low temperature matrix conditions. Thus, the chemistry of triplet diradicals has already been well investigated as reactive intermediates and extended to the field of material chemistry, e.g. organic magnets.[13]

Scheme 2. Generation of kinetic stabilized cyclopentane-1,3-diyls and cyclobutene-1,3-diyls which makes it possible to prolong lifetime.
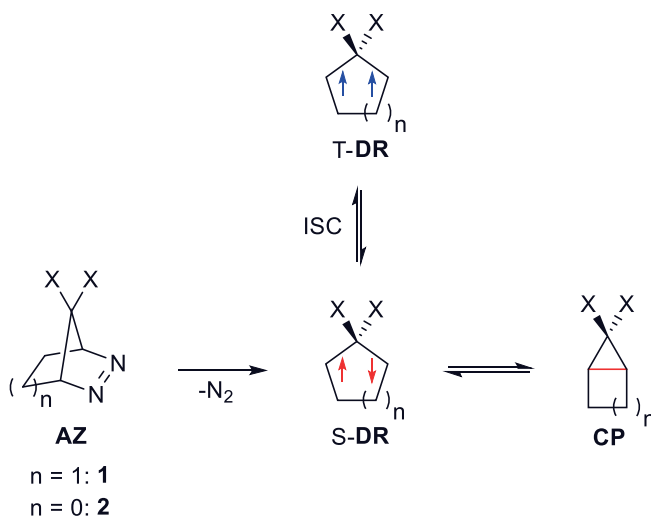
Although localized singlet diradicals is quite short-lived species, significant progress has been achieved by the application of appropriate molecular design to the generation of detectable localized singlet diradicals. Based on the findings, the direct observation of singlet diradicals has become possible, increasing the feasibility of the

experimental investigation of carbon–carbon bond homolysis processes as the original goals. Borden[14] and ourselves[15] have computationally found a notable effect of substituent (X) at the C2 position on the ground-state spin-multiplicity of cyclopentane-1,3-diyls, S-**DR1** (n = 1), and cyclobutene-1,3-diyls, S-**DR2** (n = 0), applying the molecular strains. These studies clarified that there are two types of localized singlet diradicals—type-I and type-II (Figure 1).[16–23] Through-space(TS) and
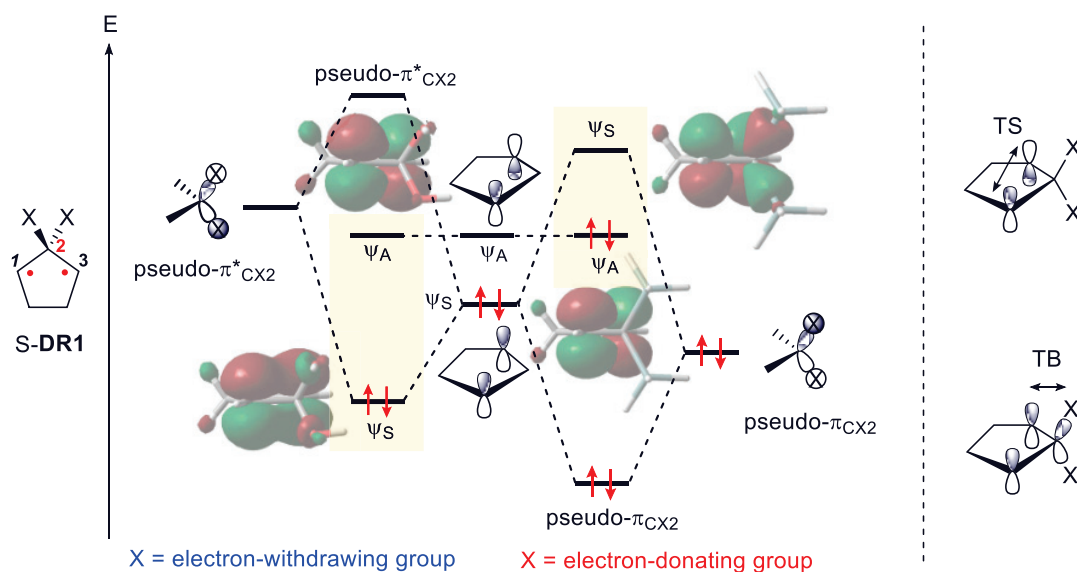
Figure 1. Through-space (TS) interaction between the two π orbitals in the 1,3-diradicals and through-bond (TB) interaction: orbital mixing diagram of the symmetric NBMO Ψ_S with pseudo π orbitals, π_{CX2} and π^*_{CX2}.

through-bond(TB) interactions play a crucial role in determining the reactivity of localized singlet diradicals. Indeed, the disrotatory ring-closing mode is energetically favored for type-I molecules having the electron-withdrawing group (X = OR, F) substituents to afford bicyclo[2.1.0]pentane derivatives. The type-II molecules having the electron-donating group (X = SiR$_3$) substituents need a high energy for the bond-formation reaction because the conrotatory ring-closing mode produces corresponding trans-fused bicyclic compounds (Scheme 3). Thus, the type-I molecules are suitable targets for investigating the bond-homolysis processes.

Scheme 3. Reactivity of type-I (left) and type-II (right) singlet 1,3-diradicals.

3
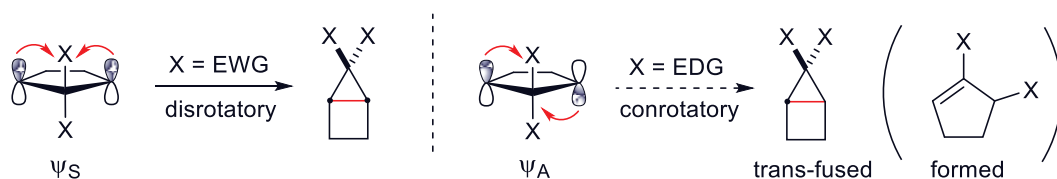
1.3   Long-lived localized singlet 1,3-diradicals

The type-I localized singlet 1,3-diradicals, S-**DR1**, which is generated by clean photochemical denitrogenation reactions of corresponding azoalkane ($\Phi_{N_2} \approx 1$), have been directly observed in the sub-microsecond time scale to elucidate these features. The electron-donating group substituted diradicals, S-**DR1b** (Ar = p-MeOC$_6$H$_4$; $\tau_{293} \approx 1050$ ns), was found to be longer-lived than that S-**DR1c** having electron-withdrawing substituents (Ar = p-CN-C$_6$H$_4$; $\tau_{293} \approx 625$ ns), even though the radical stabilization ability of the p-CN group ($\sigma_C\!\cdot = 0.47$) is much higher than that of the p-MeO group ($\sigma_C\!\cdot = 0.27$).[24,25] Thus, S-**DR1** has the characteristics of zwitterion, **ZI**, as well as radical character due to the hyperconjugation (Figure 2a). The kinetically stabilization of S-**DR1d–f** was achieved by using sterically hindered substituents and a macrocyclic system to afford extremely long-lived singlet diradicals with a lifetime up to ca. 14 µs at 293 K (Figures 2b,c).[26–29]
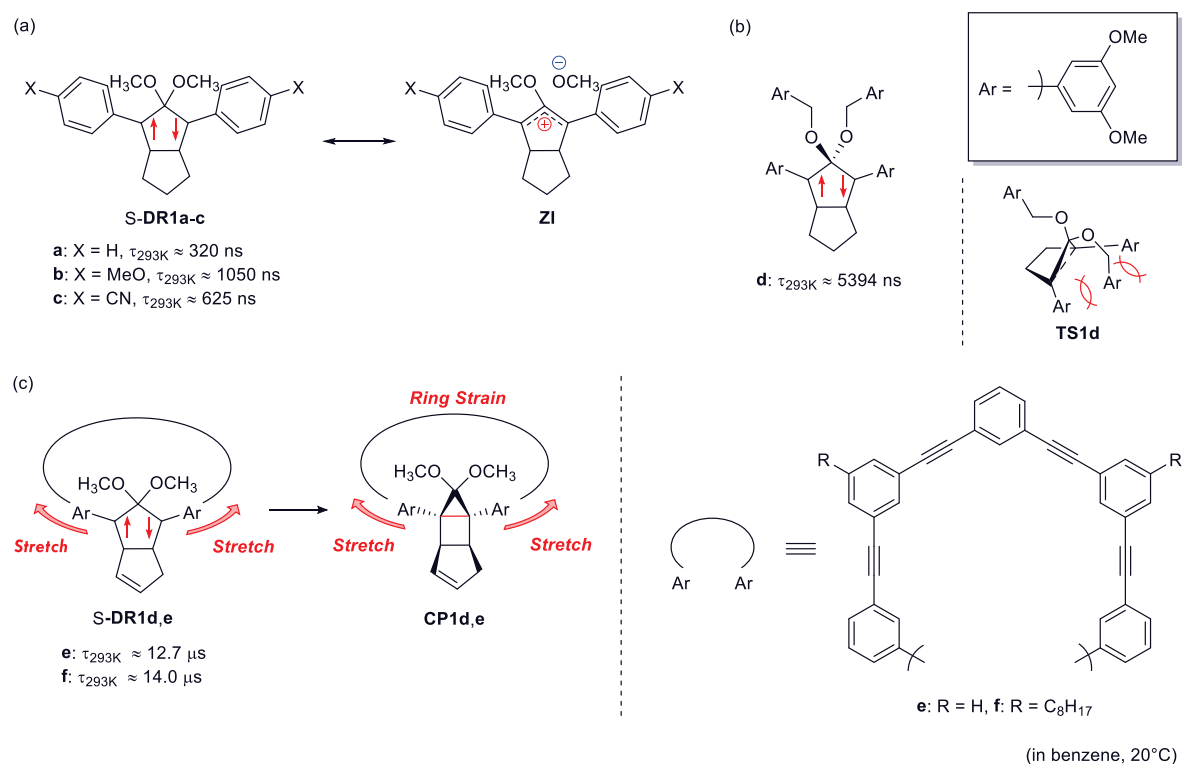
Figure 2. (a) Thermodynamic stabilization, (b) kinetic stabilization, and (c) novel kinetic stabilization (stretch effect) of localized singlet 1,3-diradicals.

1.4 Heteroatom effect on localized singlet diradicals: type-I/type-II

Since the beginning of 2000, the heteroatom effect has been experimentally and computationally found to play an important role in controlling the electronic structure and reactivity of localized singlet 1,3-diradicals.[30]

Type-I diradicals

Bertrand et al.
2002

Henke et al.
2009

Doddi et al.
2013

Type-II diradicals

Niecke et al.
1995
Ito et al.
2003

Cox et al.
2004

Demeshko et al.
2013
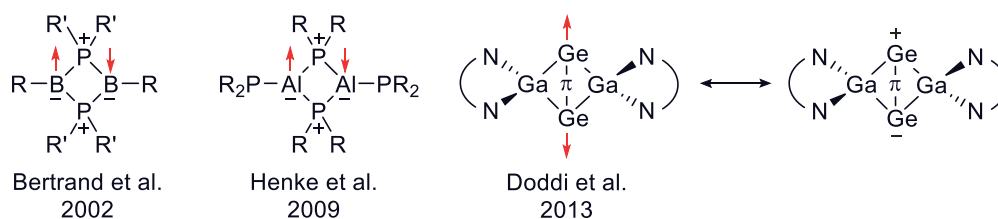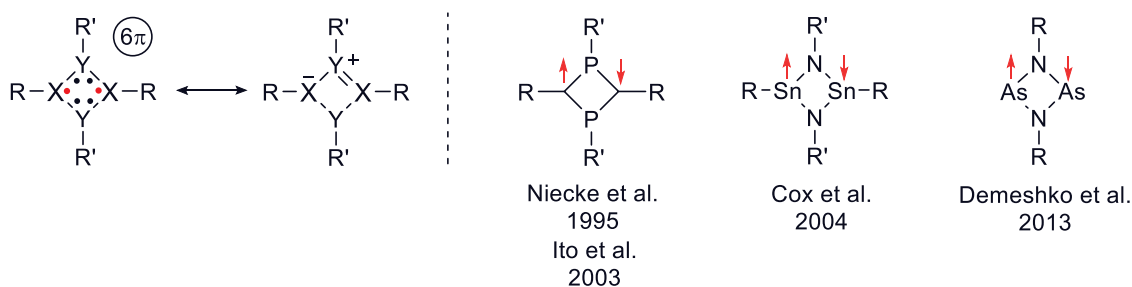
Type-I localized diradicals; B_2P_2, Al_2P_2, Ge_2Ga_2

In 2002, Bertrand and his co-workers succeeded in isolating the singlet 1,3-diradicals of B_2P_2 as extremely air-sensitive but highly thermally stable yellow crystals (Scheme 4a).[31] Two years later, his group also succeeded in detecting a B–B bond formation reaction, namely, entropy-controlled thermal equilibrium reaction between B–B σ-bond and corresponding singlet diradicals (Scheme 4b).[32] Both of

Scheme 4. (a) Indefinitely stable type-I singlet diradicals under ambient conditions, (b) Thermal equilibrium reaction between singlet diradicals and B-B σ-bond species.

(a) yellow crystals (m.p. 212 °C)

(b) $\Delta H° = +5.9$ kJ mol^{-1}
$\Delta S° = +30.1$ J K^{-1} mol^{-1}
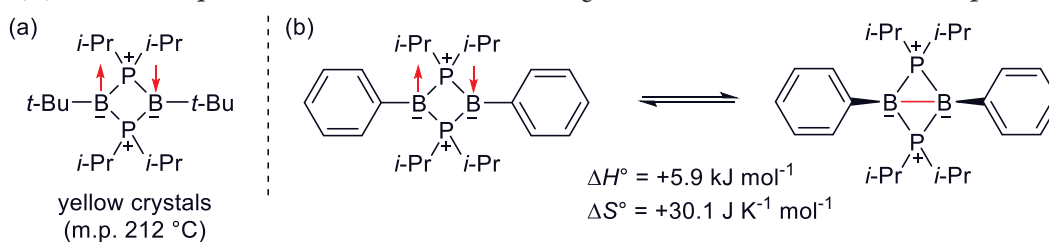
experimental and computational research study indicated that singlet 1,3-diradicals B_2P_2 are classified as type-I (HOMO = Ψ_S, LUMO = Ψ_A).

In 2009, Henke and his co-workers isolated type-I singlet diradical Al_2P_2 as a green crystal in the reaction of AlCl and LiPt-Bu.[33]

In 2013, Doddi and his co-workers reported the synthesis of an unusual molecule with a Ge−Ge π-single bond in the reduction of $GeCl_2$ with $Ga(DDP)/KC_8$. The Ge−Ge bond distance was determined to 287.14 pm, which is much longer than a typical Ge−Ge σ-bond (241 pm). The computational study of the model compound indicated the existence of a π-single-bonding system without an additional σ-bond.[34]

Type-II localized diradicals; C_2P_2, Sn_2N_2, P_2N_2, Si_2N_2

In 1995, Niecke and his co-workers first isolated the type-II singlet diradicals using the unique effect of heteroatoms on the stabilization of the singlet state of the C_2P_2 molecules (HOMO = Ψ_A; 1.6 electrons) (Scheme 5a).[35] Yoshifuji and Ito reported on the isolation of analogous C_2P_2 molecules.[36a] Because of the negligible intramolecular bond-formation reactivity of the type-II molecules, several type-II singlet diradicals were identified using X-ray crystallographic analysis (Scheme 5b). Most recently, the observation of a metastable P-heterocyclic radical by muonium, $Mu = [\mu^+e^-]$, addition to the singlet diradicals C_2P_2 unit has also been reported.[36b]

Scheme 5. Reactivity of type-II singlet diradicals C_2P_2.

(a) Niecke et al. research[35]

not formed λ_{max} = 478 nm   carbene
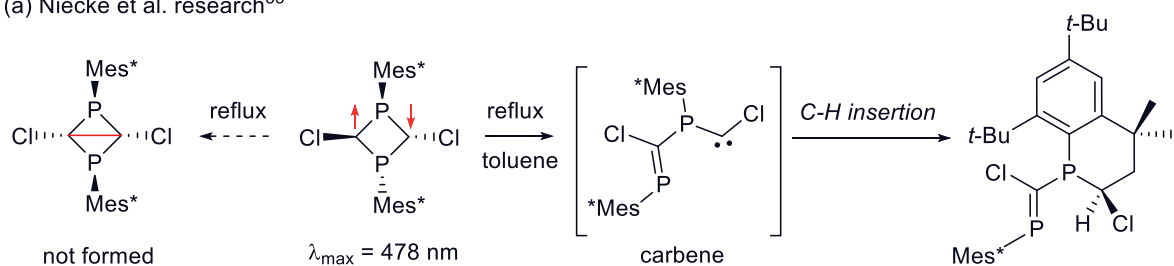
(b) Yoshifuji and Ito's research[36]

λ_{max} = 612 nm   muonium addition to C_2P_2 unit

extremly air stable   (Mes* = 2,4,6-t-Bu$_3$C$_6$H$_2$)

6
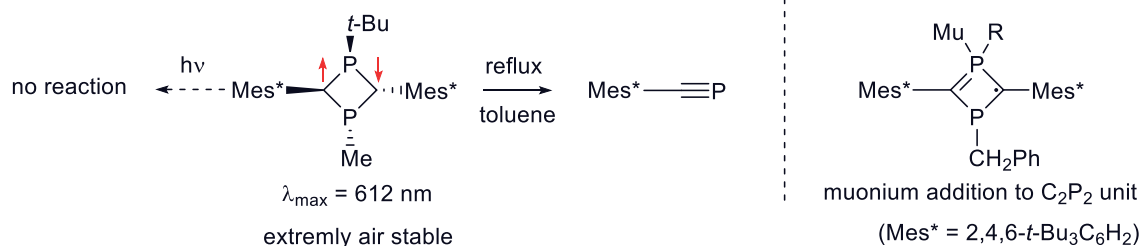
1.5 Nitrogen atom effect

The Chapter 1.4 provided the chemistry of heteroatom effect on the kinetically stabilized four-membered ring system singlet diradicals X_2Y_2. This chapter refers to another heteroatom effects, namely, *nitrogen atom effect* on the localized five-membered ring system singlet 1,3-diradicals. The electron-donating nitrogen atom makes it possible not only to increase the singlet–triplet energy gap (ΔE_{ST}), but also to thermodynamically stabilize the singlet diradicals due to hyperconjugative zwitterionic resonance structure, **ZI**. According to the computational study, Figure 3a illustrates how the lone pair electrons of the nitrogen affect the energy spacing between the two non-bonding molecular orbitals, Ψ_S and Ψ_A, whose energy spacing determines the singlet–triplet energy gap. The orbital interaction of pseudo-π combination of 2p non-bonding AOs on the nitrogen atom (n_N) with the antisymmetric combination of the 2p-π AOs (Ψ_A) destabilizes the energy of Ψ_A
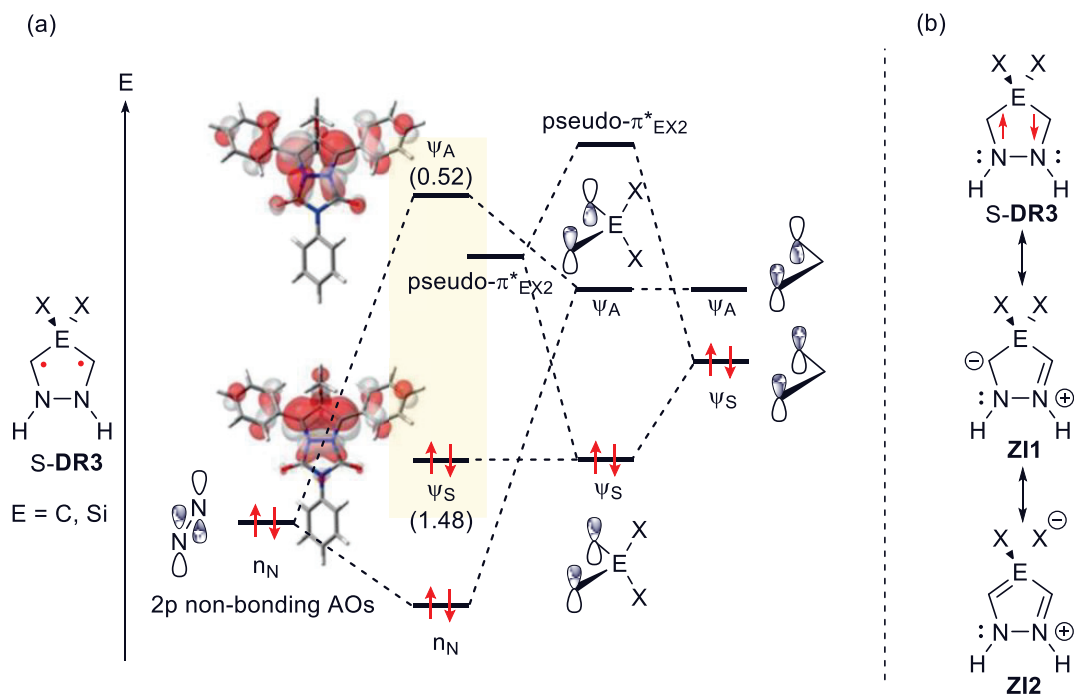

Figure 3. (a) Orbital mixing diagram of the symmetric NBMO Ψ_S with 2p non-bonding atomic orbital, n_N. The effect of nitrogen atoms on increasing the energy difference between Ψ_S and Ψ_A, (b) possible zwitterionic resonance structures of singlet diradicals, S-**DR3**.

but stabilizes the lone pair of electrons n_N. As a consequence, the orbital interaction increases the energy difference between Ψ_S and Ψ_A and pulls down energetically the singlet state below the triplet state.[37] Indeed, CASSCF calculations clarified that the occupation number in Ψ_S (HOMO) was 1.48 electrons and Ψ_A (LUMO) occupied 0.52 electrons within 2.00 electrons.[38] Experimental studies on the generation, detection and reactivity of localized singlet 1,2-diazacyclopentane-3,5-diyl derivatives has also been reported.[38,39] The singlet diradicals S-**DR1a** quantitatively react to afford the σ-bonded species **CP1a** (Scheme 6a). This intramolecular radical–radical recombination is nothing special, because σ-bonded species are generally more energetically favorable than the corresponding singlet diradicals. The localized singlet 4,4-dimethoxy-1,2-diazacyclopentane-3,5-diyls S-**DR4a**, however, does not afford the σ-bonded species **CP4a**, but alkoxy-group migrated species (Scheme 6b). The theoretical prediction regarding S-**DR4** is no doubt that the singlet diradicals S-**DR4a** is energetically more stable than the σ-bonded species **CP4a**, even though experimental findings are still insufficient. Therefore, the goal of this study was to clarify the characteristics and reactivity of localized singlet 4,4-dialkoxy-1,2-diazacyclopentane-3,5-diyls, S-**DR4**, *experimentally*.

Scheme 6. Nitrogen atoms effect on the localized singlet 1,3-diradicals.

(a) previous study (M, Abe et al. *Chem. Soc. Rev.,* **2012**, *41*, 3808–3820.; *Chem. Rev.* **2013**, *113*, 7011–7088.)
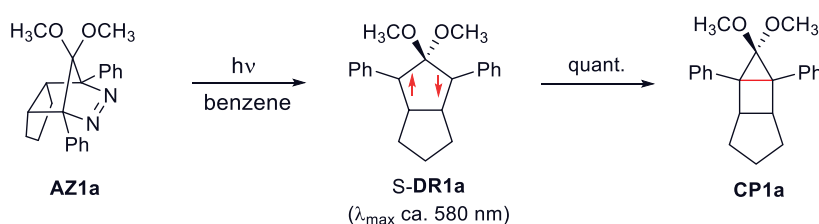
(b) nitrogen atom effect (2006–present)
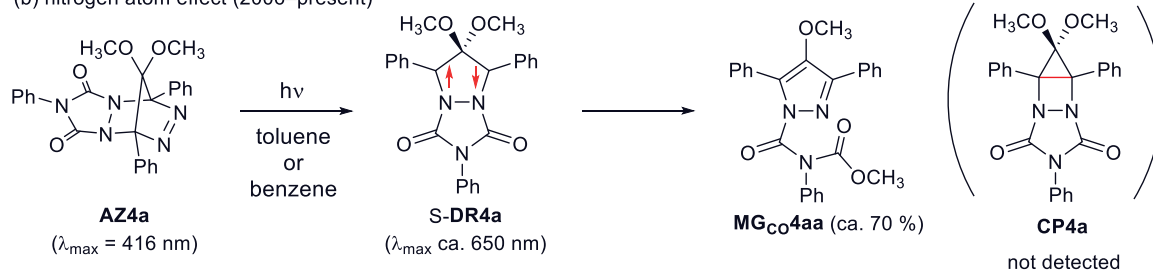
1.6   Reference

(1). (a) Amyes, T. L.; Toteva, M. M.; Richard, J. P. In *Reactive Intermediate Chemistry*; Moss, R. A., Platz, M. S., Jones Jr. M., Eds; Wiley & Sons: Hoboken, New Jersey, 2004; pp 41–68. (b) Gronert, S. In *Reactive Intermediate Chemistry*; Moss, R. A., Platz, M. S., Jones Jr. M., Eds; Wiley & Sons: Hoboken, New Jersey, 2004; pp 69–120.

(2). (a) Mayr, H.; Patz, M. Scales of Nucleophilicity and Electrophilicity : A System for Ordering Polar Organic and Organometallic Reactions. *Angew. Chem., Int. Ed. Engl.* **1994**, 33, 938–957. (b) For a comprehensive database of nucleophilicity parameters N and sN as well as electrophilicity parameters E, see: http://www.cup.lmu.de/oc/mayr/DBintro.html.

(3). Chambers, T. S.; Kistiakowsky, G. B. Kinetics of the Thermal Isomerization of Cyclopropane. *J. Am. Chem. Soc.* **1934,** *56,* 399–405.

(4). (a) Berson, J. A.; Pedersen, L. D.; Carpenter B. K. Thermal Stereomutation of Cyclopropanes, *J. Am. Chem. Soc.* **1976**, *98*, 122–143. (b) Berson, J. A. A New Class of Non-Kekule Molecules with Tunable Singlet–Triplet Energy Spacings. *Acc. Chem. Res.* **1997,** *30,* 238-244.

(5). (a) Hoffmann, R. Trimethylene and the addition of methylene to ethylene. *J. Am. Chem. Soc.* **1968,** *90,* 1475–1485. (b) Hoffmann, R. Interaction of Orbitals Through Space and Through Bonds. *Acc. Chem. Res.* **1971**, *4*, 1–9.

(6). Salem, L.; Rowland, C. The Electronic Properties of Diradicals. *Angew. Chem., Int. Ed. Engl.* **1972**, *11,* 92–111.

(7). Borden, W. T. In *Diradicals*; Borden, W. T., Eds.; Wiley-Interscience: New York, 1982; pp 1.

(8). (a) Abe, M. Diradicals. *Chem. Rev.* **2013**, *113*, 7011–7088. (b) McClelland, R. A. In *Reactive Intermediate Chemistry*; Moss, R. A., Platz, M. S., Jones Jr. M., Eds; Wiley & Sons: Hoboken, New Jersey, 2004; pp 3–40.

(9). Getty, S. J.; Hrovat, D. A.; Borden, W. T. Ab Initio Calculations on the Stereomutation of 1,1-Difluorocyclopropane. Prediction of a Substantial Preference for Coupled Disrotation of the Methylene Groups. *J. Am. Chem. Soc.* **1994,** *116,* 1521–1527.

(10). Adam, W.; Fragale, G.; Klapstein, D.; Nau, W. M.; Wirz, J. Phosphorescence and Transient Absorption of Azoalkane Triplet States. *J. Am. Chem. Soc.* **1995,** *117,* 12578–12592.

(11). Kita, F.; Adam, W.; Jordan, P.; Nau, W. M.; Wirz, J. 1,3-Cyclopentanediyl

Diradicals: Substituent and Temperature Dependence of Triplet–Singlet Intersystem Crossing. *J. Am. Chem. Soc.* **1999,** *121,* 9265–9275.

(12). Buchwalter, S. L.; Closs, G. L. An Electron Spin Resonance Study of Matrix Isolated 1,3-Cyclopentadiyl, a Localized 1,3-Carbon Biradical. *J. Am. Chem. Soc.* **1975,** *97,* 3857–3858.

(13). (a) *Magnetic Properties of Organic Materials*; Lahti, P. M., Ed.; Marcel Dekker; New York, 1999. (b) Ratera, I.; Veciana, J. Playing with organic radicals as building blocks for functional molecular materials. *Chem. Soc. Rev.* **2012,** *41,* 303–349.

(14). Lineberger, W. C.; Borden, W. T. The synergy between qualitative theory, quantitative calculations, and direct experiments in understanding, calculating, and measuring the energy differences between the lowest singlet and triplet states of organic diradicals. *Phys. Chem. Chem. Phys.* **2011,** *13,* 11792–11813.

(15). Abe, M.; Ishihara, C.; Nojima, M. DFT Prediction of Ground-State Spin Multiplicity of Cyclobutane-1,3-diyls: Notable Effects of Two Sets of Through-Bond Interactions. *J. Org. Chem.* **2003,** *68,* 1618–1621.

(16). Abe, M.; Kawanami, S.; Ishihara, C.; Nojima, M. 2-Silyl Group Effect on the Reactivity of Cyclopentane-1,3-diyls. Intramolecular Ring-Closure versus Silyl Migration. *J. Org. Chem.* **2004,** *69,* 5622–5626.

(17). Abe, M.; Je, J.; Mishima, M. The chemistry of localized singlet 1,3-diradicals (biradicals): from putative intermediates to persistent species and unusual molecules with a π-single bonded character. *Chem. Soc. Rev.* **2012,** *41,* 3808–3820.

(18). Abe, M.; Akisaka, R. Is π-Single Bonding (C–π–C) Possible? A Challenge in Organic Chemistry. *Chem. Lett.* **2017,** *46,* 1586–1592.

(19). Ishihara, C.; Abe, M. Notable Substituent Effects on the Rate Constant of Thermal Denitrogenation of Cyclic Azoalkanes: Strong Evidence for a Stepwise Denitrogenation Mechanism. *Aust. J. Chem.* **2010,** *63,* 1615–1618.

(20). Abe, M.; Adam, W.; Nau, W. M. Photochemical Generation and Methanol Trapping of Localized 1,3 and 1,4 Singlet Diradicals Derived from a Spiroepoxy-Substituted Cyclopentane-1,3-diyl. *J. Am. Chem. Soc.* **1998,** *120,* 11304–11310.

(21). Abe, M.; Adam, W.; Heidenfelder, T.; Nau, W. M.; Zhang, X. Intramolecular and Intermolecular Reactivity of Localized Singlet Diradicals: The Exceedingly Long-Lived 2,2-Diethoxy-1,3-diphenylcyclopentane-1,3-diyl. *J. Am. Chem. Soc.* **2000,** *122,* 2019–2026.

(22). Ye, J.; Hatano, S.; Abe, M.; Kishi, R.; Murata, Y.; Nakano, M.; Adam, W. A

Puckered Singlet Cyclopentane-1,3-diyl: Detection of the Third Isomer in Homolysis. *Chem. Eur. J.* **2016,** *22,* 2299–2306.

(23). Abe, M.; Tada, S.; Mizuno, T.; Yamasaki, K. Impact of Diradical Spin State (Singlet vs Triplet) and Structure (Puckered vs Planar) on the Photodenitrogenation Stereoselectivity of 2,3-Diazabicyclo[2.2.1]heptanes. *J. Phys. Chem. B,* **2016,** *120,* 7217–7226.

(24). Abe, M.; Adam, W.; Hara, M.; Hattori, M.; Majima, T.; Nojima, M.; Tachibana, K.; Tojo, S. On the Electronic Character of Localized Singlet 2,2-Dimethoxycyclopentane-1,3-diyl Diradicals: Substituent Effects on the Lifetime. *J. Am. Chem. Soc.* **2002,** *124,* 6540–6541.

(25). Abe, M.; Hattori, M.; Takegami, A.; Masuyama, A.; Hayashi, T.; Seki, S.; Tagawa, S. Experimental Probe for Hyperconjugative Resonance Contribution in Stabilizing the Singlet State of 2,2-Dialkoxy-1,3-diyls: Regioselective 1,2-Oxygen Migration. *J. Am. Chem. Soc.* **2006,** *128,* 8008–8014.

(26). Nakagaki, T.; Sakai, T.; Mizuta, T.; Fujiwara, Y.; Abe, M. Kinetic Stabilization and Reactivity of π Single-Bonded Species: Effect of the Alkoxy Group on the Lifetime of Singlet 2,2-Dialkoxy-1,3-diphenyloctahydropentalene-1,3-diyls. *Chem. Eur. J.* **2013,** *19,* 10395–10404.

(27). Ye, J.; Fujiwara, Y.; Abe, M. Substituent effect on the energy barrier for σ-bond formation from π-single-bonded species, singlet 2,2-dialkoxycyclopentane-1,3-diyls. *Beilstein. J. Org. Chem.* **2013,** *9,* 925–933.

(28). Abe, M.; Furunaga, H.; Ma, D.; Gagliardi, L.; Bodwll, G. J. Stretch Effects Induced by Molecular Strain on Weakening σ-Bonds: Molecular Design of Long-Lived Diradicals (Biradicals). *J. Org. Chem.* **2012,** *77,* 7612–7619.

(29). Harada, Y.; Wang, Z.; Kumashiro, S.; Hatano, S.; Abe, M. Extremely Long Lived Localized Singlet Diradicals in a Macrocyclic Structure: A Case Study on the Stretch Effect. *Chem. Eur. J.* **2018,** *24,* 14808–14815.

(30). (a) Schoeller, W. W.; Rozhenko, A.; Bourissou, D.; Bertrand, G. On the Electronic Structures of the 1,3-Diboracyclobutane-1,3-diyls and Their Valence Isomers with a B2E2 Skeleton (E=N, P, As). *Chem. Eur. J.* **2003,** *9,* 3611–3617. (b) Soleilhavoup, M.; Bertrand, G. Let's Play with Valence Isomers: The Influence of Different Main Group Elements on Their Relative Stability. *Bull. Chem. Soc. Jpn.* **2007,** *80,* 1241–1252. (c) Breher, F. Stretching Bonds in Main Group Element Compounds—Borderlines between Biradicals and Closed-shell Species. *Coord. Chem. Rev.* **2007,** *251,* 1007–1043. (d) Wang,

X.; Peng, P.; Olmstead, M. N.; Fettinger, J. C.; Power, P. P. An Unsymmetric Oxo/Imido-Bridged Germanium-Centered Singlet Diradicaloid. *J. Am. Chem. Soc.* **2009**, *131*, 14164–14165. (e) Cox, H.; Hitchcock, P. B.; Lappert, M. F.; Pirssens, L. J.-M. A 1,3-Diaza-2,4-distannacyclobutanediide: Synthesis, Structure, and Bonding. *Angew. Chem. Int. Ed.* **2004**, *43*, 4500–4504. (f) Demeshko, S.; Godemann, C.; Kuzora, R.; Schulz, A.; Villinger, A. An Arsenic–Nitrogen Biradicaloid: Synthesis, Properties, and Reactivity. *Angew. Chem. Int. Ed.* **2013**, *52*, 2105–2108. (g) Henke, P.; Pankewitz, T.; Klopper, W.; Breher, F.; Schncckel, H. *Angew. Chem. Int. Ed.* **2009**, *48*, 8141–8145. (h) Doddi, A.; Gemel, C.; Winter, M.; Fischer, R. A.; Goedecke, C.; Rzepa, H. S.; Frenking, G. *Angew. Chem. Int. Ed.* **2013**, *52*, 450–454. (i) Beweries, T.; Kuzora, R.; Rosenthal, E.; Schulz, A.; Villinger, A. [P(m-NTer)]2: A Biradicaloid That Is Stable at High Temperature. *Angew. Chem. Int. Ed.* **2011**, *50*, 8974–8978. (j) Takeuchi, K.; Ichinohe, M.; Sekiguchi, A. Access to a Stable Si2N2 Four-Membered Ring with Non-Kekule Singlet Biradical Character from a Disilyne. *J. Am. Chem. Soc.* **2011**, *133*, 12478–12481.

(31). Scheschkewitz, D.; Amii, H.; Gornitzka, H.; Schoeller, W. W.; Bourissou, D.; Bertrand, G. Singlet Diradicals: from Transition States to Crystalline Compounds. *Science* **2002**, *295*, 1880–1881.

(32). (a) Amii, H.; Vranicar, L.; Gornitzka, H.; Bourissou, D.; Bertrand, G. Radical-Type Reactivity of the 1,3-Dibora-2,4-Diphosphoniocyclobutane-1,3-diyl. *J. Am. Chem. Soc.* **2004**, *126*, 1344–1345. (b) Scheschkewitz, D.; Amii, H.; Gornitzizka, H.; Schoeller, W.W.; Bourissou, D.; Bertrand, G. Sigma-bond Stretching: A Static Approach for a Dynamic Process. Angew Chem., Int. Ed. **2004**, *43*, 585–587.

(33). Henke, P.; Pankewitz, T.; Klopper, W.; Breher, F.; Schncckel, H. Snapshots of the Al-Al σ-Bond Formation Starting from {AlR₂} Units: Experimental and Computational Observations. *Angew. Chem. Int. Ed.* **2009**, *48*, 8141–8145.

(34). Doddi, A.; Gemel, C.; Winter, M.; Fischer, R. A.; Goedecke, C.; Rzepa, H. S.; Frenking, G. Low-Valent Ge₂ and Ge₄ Species Trapped by N-Heterocyclic Gallylene. *Angew. Chem. Int. Ed.* **2013**, *52*, 450–454.

(35). Niecke, E.; Fuchs, A.; Baumeister, F.; Nieger, M.; Schoeller, W. W. A P₂C₂ Four-Membered Ring with Unusual Bonding—Synthesis, Structure, and Ring Opening of a 1,3-Diphosphacyclobutane-2,4-diyl. *Angew. Chem., Int. Ed.* **1995**, *34*, 555–557.

(36). Ito, S.; Ueda, Y.; Hgot, T. T. T.; Kobayashi, M.; Hashizume, D.; Nishida, J.-I.; Yamashita, Y.; Mikami, K. Direct Arylations for Study of the Air-Stable P-Heterocyclic Biradical: From Wide Electronic Tuning to Characterization of the Localized Radicalic

Electrons. *J. Am. Chem. Soc.* **2013**, *135*, 17610–17616. (b) Ito, S.; Ueta, Y.; Koshino, K.; Kojima, K. M.; Mckenzie, I.; Mikami, K. Observation of a Metastable P-Heterocyclic Radical by Muonium Addition to a 1,3-Diphosphacyclobutane-2,4-diyl. *Angew. Chem., Int. Ed.* **2018**, *57*, 8608–8613.

(37). Nakamura, T.; Gagliardi, L.; Abe, M. Computational study of the cooperative effects of nitrogen and silicon atoms on the singlet–triplet energy spacing in 1,3-diradicals and the reactivity of their singlet states. *J. Phys. Org. Chem.* **2010**, *23*, 300–307.

(38). Yoshidomi, S.; Mishima, M.; Seyama, S.; Abe, M.; Fujiwara, Y.; Ishibashi, T. Direct Detection of a Chemical Equilibrium between a Localized Singlet Diradical and Its σ-Bonded Species by Time-Resolved UV/Vis and IR Spectroscopy. *Angew. Chem., Int. Ed.* **2017**, *56*, 2984–2988.

(39). Abe, M.; Kubo, E.; Nozaki, K.; Matsuo, T.; Hayashi, T. An Extremely Long-Lived Singlet 4,4-Dimethoxy-3,5-diphenylpyrazolidine-3,5-diyl Derivative: A Notable Nitrogen-Atom Effect on Intra- and Intermolecular Reactivity. *Angew. Chem., Int. Ed.* **2006**, *45*, 7828–7831; *Corrigendum, idem, ibid*, **2012**, *51*, 11911.

Chapter 2

Thermal Equilibrium Reaction (fast process)

2.1 Direct detection of an equilibrium between a localized singlet diradicals and its σ-bonded species[1]

As already discussed in Chapter 1, for the last few decades, the long-lived localized singlet diradicals S-**DR1** (up to 14 μs at 293 K, $\lambda_{max} \approx 580$ nm; See Chapter 1.3) and S-**DR4** (up to 10 ms at 293 K, $\lambda_{max} \approx 650$ nm) were designed and generated through the photodenitrogenation of corresponding azoalkanes.[1–5] The singlet diradicals S-**DR1** quantitatively produced the σ-bonded species **CP1** despite introducing the electronic and steric effects. Thus, the formation of **CP1** is reasonable, given that σ-bonded species are energetically more stable than the corresponding singlet diradicals; $\Delta E_{DR–CP}$ = +62.76 kJ mol^{-1} at the (U)B3LYP/6-31G(d) level of theory.[6] The large energy difference between S-**DR1** and **CP1** made it impossible to investigate in more detail the C–C bond-homolytic process. On the other hand, photoly-

Scheme 7. Generation of 4,4-dimethoxy-1,2-diazacyclopentane-3,5-diyls, S-**DR4**, and its reactivity.

AZ4	p-X	p-Y
a	H	H
b	MeO	MeO
c	Me	Me
d	F	F
e	Cl	Cl
f	Br	Br
g	CN	CN
h	MeO	Br
i	MeO	H
j	CN	H
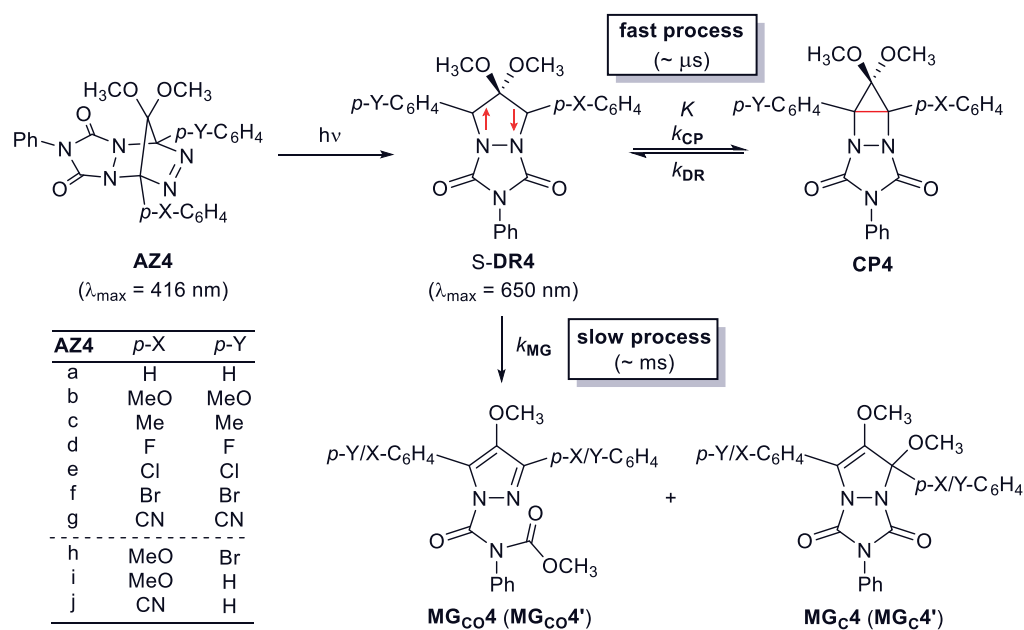
$$k_{fast} = k_{CP} + k_{DR} \quad \cdots\cdots (1)$$

$$K = k_{CP}/k_{DR} \quad \cdots\cdots (2)$$

$$k_{slow} = (k_{DR}k_{MG})/(k_{DR} + k_{CP}) \quad \cdots\cdots (3)$$

14

sates isolated from photodenitrogenation of the azoalkane **AZ4a** in non-polar toluene were two types of alkoxy-group migrated species **MG$_{CO}$4aa** (70%) and **MG$_C$4aa** (30%), even though σ-bonded species **CP4a** was the expected product (Scheme 7).[1,4] Therefore, the chemistry of the singlet diradicals S-**DR4** has a significantly potential for having a clue to elucidate the homolytic process. In Chapter 2, a thermal equilibrium reaction between S-**DR4** and **CP4** was found for the first time using nanosecond (ns) time-resolved spectroscopic analyses of the photochemical denitrogenation of **AZ4**. The simultaneous detection of S-**DR4** and **CP4** made it possible to determine the equilibrium constant K (=[**CP4**]/[S-**DR4**]) for the homolysis step, and investigate in more detail the character of the localized singlet diradicals.

To begin with, laser flash photolysis (LFP) experiments were conducted for the photodenitrogenation of **AZ4a** (X = Y = H). Interestingly, a dual decay process for S-**DR4a** at $\lambda_{max} \approx 650$ nm—one fast ($k_{fast} \approx 1.42 \times 10^6$ s^{-1}) and the other slow ($k_{slow} \approx 9.3$ s^{-1}) at 293 K, was found in toluene using a Nd: YAG-OPO laser (λ_{exc} = 430 nm, 3–4 mJ per pulse, 15 ns width; Figures 4,5). A mechanism which explains this observed phenomenon is proposed to involve the fast equilibrium reaction between S-**DR4a** and **CP4a**; *fast process*, and a slow decay process to give **MG$_{CO}$4a** and **MG$_C$4a**; *slow process*. Hence, the rate constants, k_{fast} and k_{slow}, can be expressed by the respective rate constants for the formation of **CP4a** (k_{CP}), S-**DR4a** (k_{DR}), and
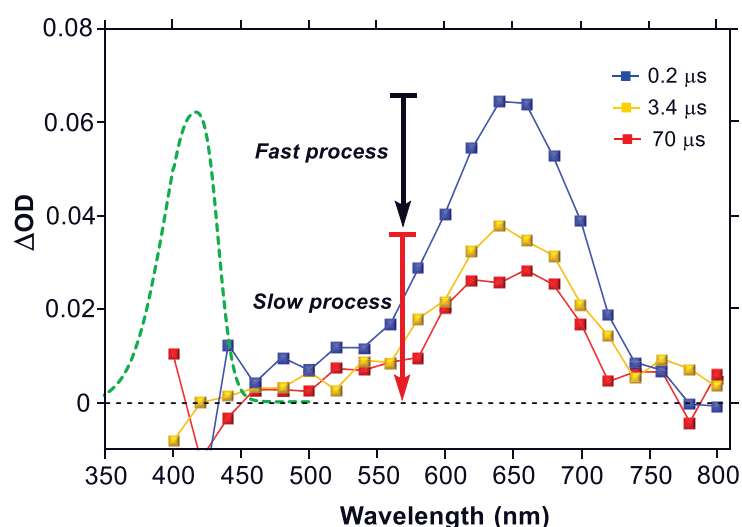

Figure 4. Transient absorption spectra for S-**DR4a** obtained after laser flash photolysis of azoalkane **AZ4a** (λ_{exc} = 430 nm, 3–4 mJ per pulse, 15 ns width; **AZ4a**: λ_{max} = 416 nm green dashed line) at 293 K in toluene.

alkoxy-group migrated products (k_{MG}). The equilibrium constant (K) can be expressed by $K = k_{CP}/k_{DR}$ (Scheme 7; Eqs. 1–3). While S-**DR4a** appeared in the visible region, it was the only detectable species by UV/Vis spectroscopic analysis. Therefore, further knowledge regarding the molecular structure during transient decay trace is essential for determine that fast process is the thermal equilibrium reaction between S-**DR4** and **CP4**; bond-homolytic process.
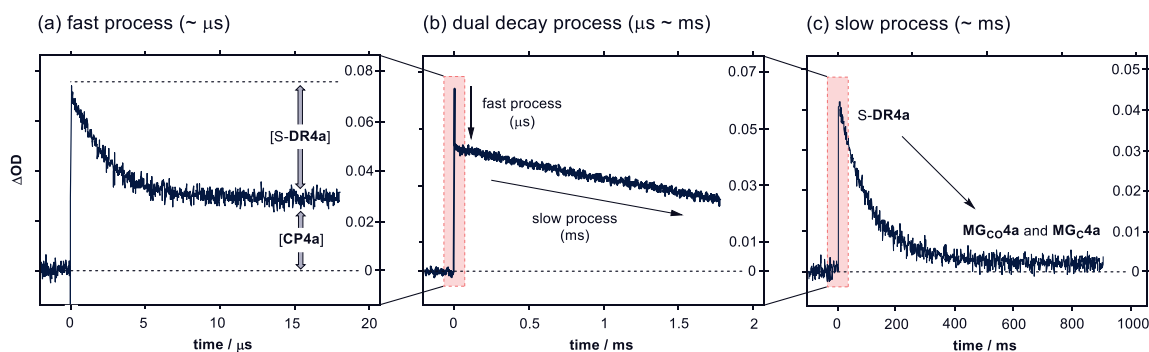

Figure 5. (a) Transient decay trace of fast process of S-**DR4a** (λ_{obs} = 650 nm); equilibrium constant K = [**CP4a**]/[S-**DR4a**], (b) transient decay trace of S-**DR4a**; observable dual process time scale, and (c) transient decay trace to give alkoxy-group migrated species **MG$_{CO}$4a** and **MG$_{C}$4a** in toluene at 293K.

To gain further information on the mechanism of the dual decay process of S-**DR4a**, time-resolved infrared (TR-IR) spectra, in the C=O stretching region, 1650–1840 cm^{-1}, were measured after 266 nm photolysis of **AZ4a** in acetonitrile (2.5 mJ cm^{-2}, 2 Hz, 10 ns pulse width) in the 0–20 μs time window, using a home-built TR-IR spectrometer (Figure 6a). This experiment was performed by professor Ishibashi and his co-workers in Tsukuba university (Ibaraki). The bleaching of the signals at 1745 cm^{-1} was observed immediately after the LFP of **AZ4a** (Figure 6c). The bleached band is assigned to the asymmetric stretching of the two C=O groups in **AZ4a**, consistent with the frequencies in the steady-state IR spectrum of **AZ4a**. The quantum yield for the photodenitrogenation of **AZ4a** was determined to be 0.97 in acetonitrile. The high quantum yield confirms that the observed negative signals in Figure 6a originate from the efficient consumption of **AZ4a**. Thus, the photodenitrogenation process was found to occur within the time response of the TR-IR spectrometer (< 35 ns). New bands appeared simultaneous with the bleaching of **AZ4a**. The higher wavenumber band at 1756 cm^{-1} decayed with a rate constant $k_{fall} \approx 2.2 \times 10^6$ s^{-1} at 294 K (Figure 6c); the band is assigned to

S-**DR4a** (Figure 6b). The decay profile and rate constant were in agreement with those determined by transient absorption spectroscopy of S-**DR4a** in acetonitrile; $k_{fast} \approx 2.5 \times 10^6$ s^{-1} at 294 K (estimated k_{fast} at 294 K from the slope and intercept of the Arrhenius plot). A band at 1736 cm^{-1} was observed to grow along with the fall of the S-**DR4a** peak at 1756 cm^{-1} (Figure 6c). The rate constant associated with this growth, $k_{growth} \approx 2.4 \times 10^6$ s^{-1}, was consistent with the rate constant for the decay of S-**DR4a** (1756 cm^{-1}). Hence, the species corresponding to the band at 1736 cm^{-1} is likely to be the primary product from S-**DR4a**. The alkoxy-group migrated species **MG$_{CO}$4aa** is one of the candidates for the signal at 1736 cm^{-1}. The C=O bond stretching mode of **MG$_{CO}$4aa**, at 1725 cm^{-1}, however, is inconsistent with this rising signal. Therefore, the band at 1736 cm^{-1} was assigned to **CP4a**, which was not observed by transient absorption spectroscopy over the wavelength range probed by our spectrometer (Figure 6). This assignment is confirmed by vibrational calculations performed using the complete active space multi-configuration self-consistent field (CASSCF) method.

The model species S-**DR**, **AZ**, and **CP** were calculated at the CASSCF(6,6)/4-31G level of theory using the Gaussian 09 suite of programs (top Figure 6). At this level of theory, the singlet state was calculated to be more stable than the triplet state; ΔE_{ST} = 24.7 kJ mol^{-1}. The calculated resonance frequencies of the asymmetric stretching modes of the C=O moieties were in the following order: $\nu_{C=O}$ for S-**DR** (1953 cm^{-1}) > $\nu_{C=O}$ for **AZ** (1950 cm^{-1}) > $\nu_{C=O}$ for endo-**CP** (1948 cm^{-1}) > $\nu_{C=O}$ for exo-**CP** (1932 cm^{-1}). The higher frequency of the singlet diradical S-**DR** is rationalized by its zwitterionic resonance structure, in which the lone pair of the electrons delocalizes to the diradicals moiety as shown in S-**DR4a**. Meanwhile, the lone pair of electrons are delocalized into the carbonyl groups as shown in **CP4a** and **AZ4a** (left Figure 6). Therefore, the resonance frequency of the C=O in S-**DR4a** should be higher than those of **AZ4a** and **CP4a**; $\nu_{C=O}$ for S-**DR4a** > $\nu_{C=O}$ for **AZ4a** ~ $\nu_{C=O}$ for **CP4a**. The predicted order was consistent with that observed from the TR-IR measurements (Figure 6). These experimental, including transient absorption spectroscopic analysis, and computational studies clarified what fast decay process for S-**DR4a** corresponds to, namely, thermal equilibrium reaction between the localized singlet diradicals and its σ-bonded species. There is no question that fast decay process for S-**DR4a** is C–C bond-homolytic process, so that the findings on the electronic structure and reactivity of S-**DR4** are described from the next chapter.
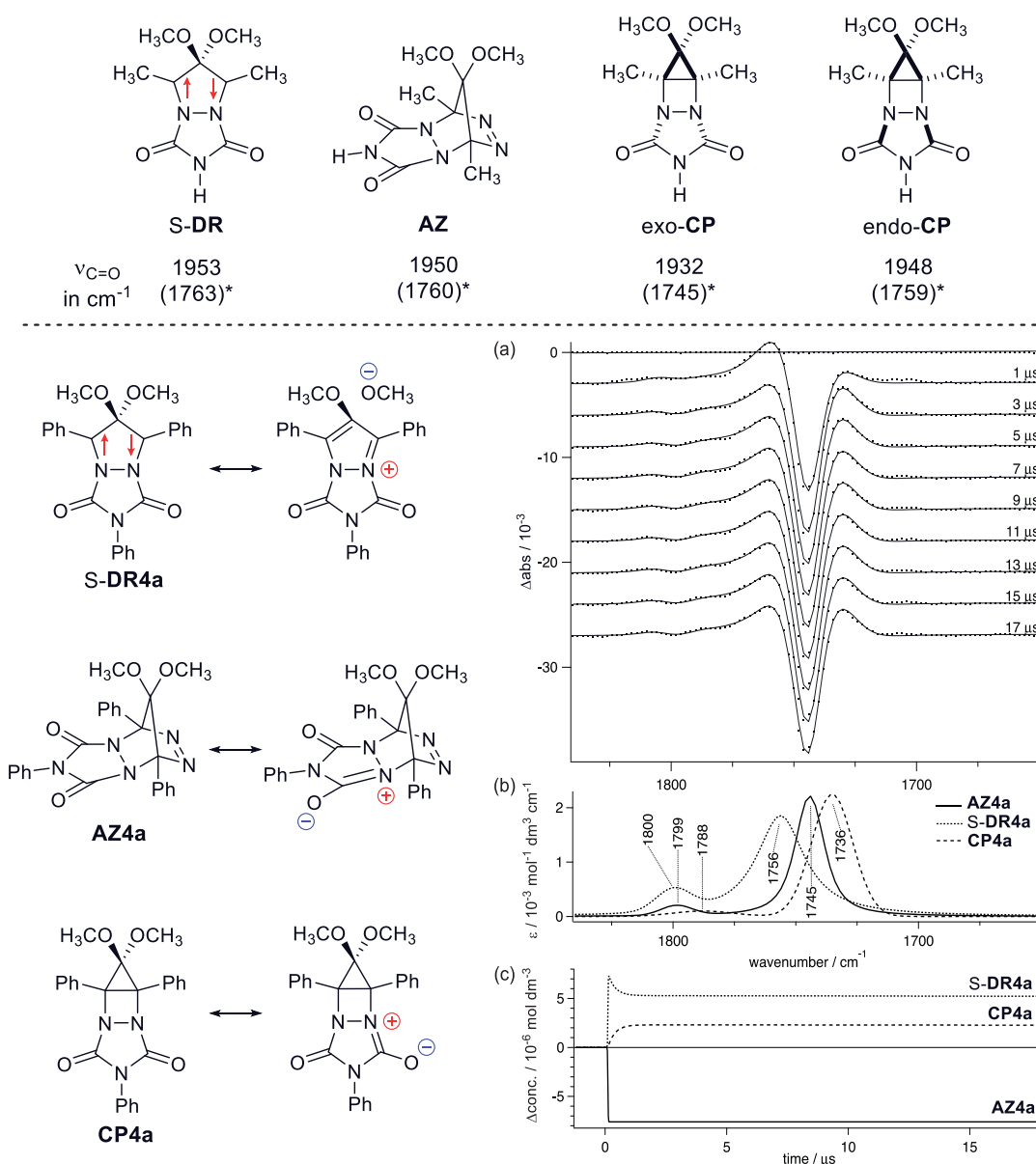
Figure 6. Resonance structures of S-**DR4a**, **AZ4a**, and **CP4a** (lower left). CASSCF(6,6)/4-31G calculated vibrational frequencies. Values in parenthesis are scaled by 0.903 (top). (a) TRIR difference spectra over 1650–1840 cm^{-1} obtained after the LFP of **AZ4a** (λ_{exc} = 266 nm, 2.5 mJ cm^{-2}, 2 Hz, 10 ns pulse width) at 294 K in acetonitrile. Dots are observed data and lines are the results of global fitting analysis. The analysis was conducted assuming that each of **AZ4a**, S-**DR4a**, and **CP4a** has two vibrational bands (symmetric and asymmetric C=O stretching) with Gaussian shapes and concentrations varies in accordance with kinetic Scheme [Scheme 7]. (b) IR spectra for **AZ4a**, S-**DR4a**, and **CP4a** estimated by fitting. (c) Temporal profiles for the concentrations of S-**DR4a**, **CP4a**, and **AZ4a** by fitting.

18

2.2 Electronic structure of singlet diradicals

2.2.1 Effect of substituent on stability of singlet diradicals

The aryl-symmetrically and asymmetrically substituted azoalkanes, **AZ4a–j** ($\lambda_{max} \approx$ 416 nm, $\varepsilon \approx 455$ L mol^{-1} cm^{-1}), which were precursors to S-**DR4a–j**, were synthesized to investigate the characteristics of S-**DR4**, as well as their reactivity (Scheme 7, See experimental section; as for syntheses). The transient absorption spectra in the photochemical denitrogenation of **AZ4a–j** were measured in toluene using a laser flash photolysis (LFP) method based on a Nd: YAG-OPO laser ($\lambda_{exc} = 430$ nm, ca. 3 mJ, 15 ns width, Figures 7,8). As shown in Figure 7, the absorption maxima of all the S-**DR4** were observed at around 650 nm which is the typical absorption wavelength for singlet diradicals.[3,7] The species was not quenched by molecular oxygen. The absorption maxima of the aryl-asymmetrically substituted singlet diradicals, S-**DR4h,j** were slightly red-shifted from 650 to 675 nm. As described in Chapter 2.1, the time profile of the decay traces of S-**DR4** demonstrated that the S-**DR4** has dual fall process—*fast* and *slow* (Scheme 7 and Figures 4,5). From the equilibrium constant K (= k_{CP}/k_{DR}) and rate constant k_{fast} (= $k_{CP} + k_{DR}$) (Figure 8), the respective rate constants of k_{CP} and k_{DR} were determined as shown in Tables 1,2 (Eqs. 1,2 in Scheme 7, Van't Hoff and Eyring plots are shown in Experimental section 2.4).
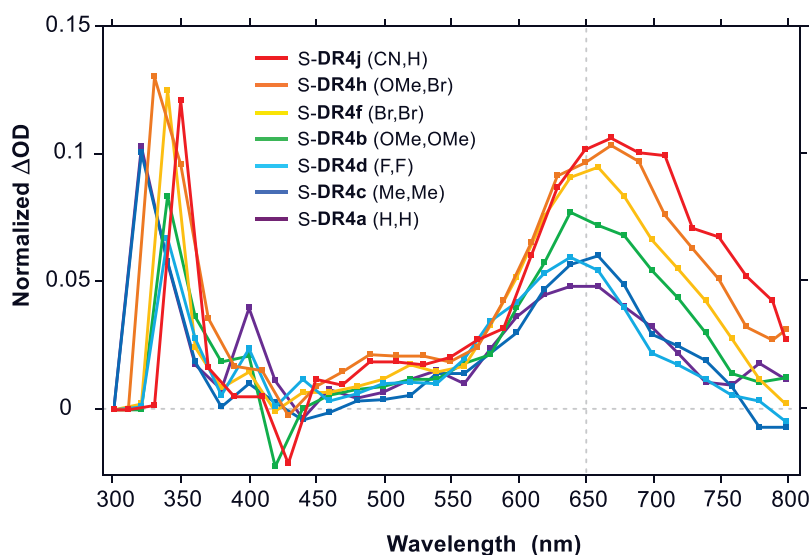
Figure 7. Transient absorption spectrum of S-**DR4a–j** (*p*-X, *p*-Y), generated from azoalkanes **AZ4a–j** (*p*-X, *p*-Y) by photolysis in toluene at 293 K.
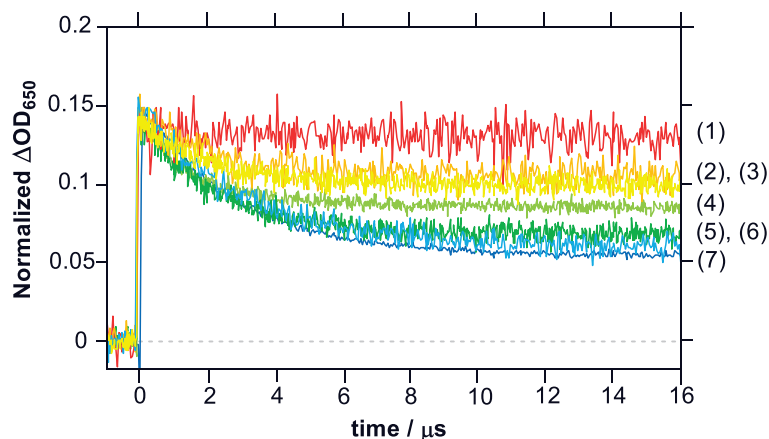
Figure 8. Transient decay traces of the aryl-symmetrically substituted singlet diradicals, S-**DR4a**–**g** (λ_{obs} = 650 nm) in toluene at 270 K; (1) p-CN-C$_6$H$_4$, (2) p-Br-C$_6$H$_4$; orange line, (3) p-Cl-C$_6$H$_4$, (4) p-MeO-C$_6$H$_4$, (5) p-Me-C$_6$H$_4$; green line, (6) p-F-C$_6$H$_4$, and (7) p-H-C$_6$H$_4$.

The bond homolysis nature and the characteristics of S-**DR4** are further discussed in the following Chapter (Chapter 2.2.2–2.2.4). The values of log$K$, logk_{CP}, and logk_{DR} were plotted against the Brown–Okamoto parameters, σ_p^+ [8], Creary's radical stability parameter, $\sigma_C.$ [9] (effect of substituent) and the empirical solvent parameter, $E_T(30)$ [10] (effect of solvent), respectively (Figures 9–14). These knowledges were very useful to understand nitrogen atom effects on the singlet 1,3-diradicals.

2.2.2 Effects of substituent and solvent on equilibrium constant K

As shown in Figure 9a, the Hammett-type plots of log$K$ both in toluene and acetonitrile exhibited reverse V-shaped lines, with the slope; Hammett reaction constant, ρ = 0.50 (R^2 = 0.99) for S-**DR4a**–**d** and ρ = –4.23 (R^2 = 0.99) for S-**DR4a**,**e**,**f**. The singlet diradicals are thermodynamically stabilized by introducing both the electron-donating group S-**DR4b**–**d** (X = Y = MeO, Me, F) and the electron-withdrawing group S-**DR4e**,**f** (X = Y = Cl, Br) at the para positions of the phenyl rings. Especially, the equilibration of S-**DR4g** (X = Y = CN) with **CP4g** was not observed (Figure 8-1), indicating that the singlet diradicals are well stabilized by the cyano group (X = Y = CN). The reverse V-shape of the Hammett-type plots is a typical example of the substituent effect on benzyl-type radicals.[11] Interestingly, the slope (ρ) for the electron-withdrawing group substituted S-**DR4e**,**f** (X = Y = Cl, Br) is negatively

larger than that for the electron-donating group substituted S-**DR4b–d** (X = Y = MeO, Me, F), suggesting that S-**DR4** are highly stabilized by the electron-withdrawing group substituents (Figure 9a). The trend in the substituent effect is very different from that for S-**DR1,** in which the singlet diradicals substituted with the electron-donating group were well stabilized than those having the electron-withdrawing groups.[3a,b] The equilibrium constant K of the polar acetonitrile was found to be smaller than that of the non-polar toluene, suggesting that the singlet diradicals has a small but certainly significant zwitterionic character which is stabilized by a polar solvent (Scheme 8).
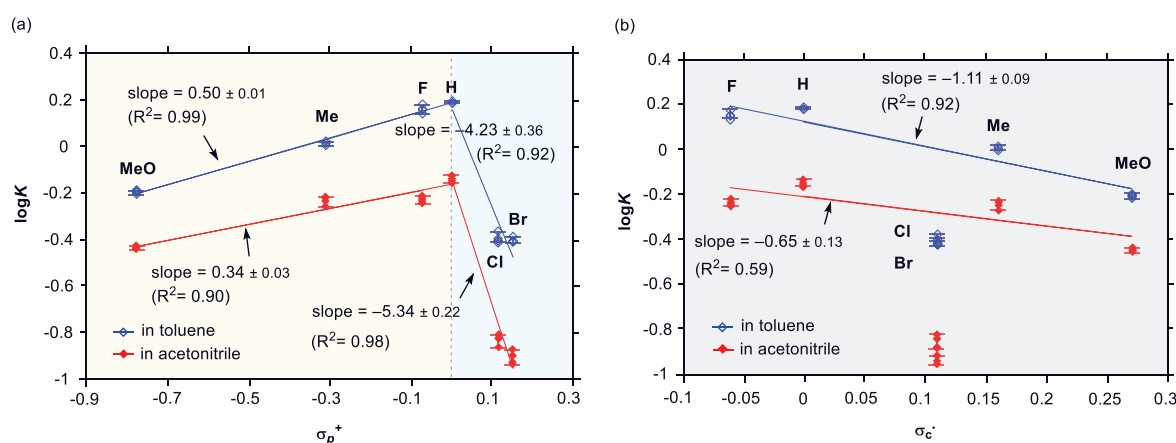
Figure 9. Hammett-type plots with a) $\sigma_p{}^+$ and b) $\sigma_C{}^{\cdot}$ for the logarithm of equilibrium constant ($\log K$); blue; toluene, red; acetonitrile, respectively.

The features of S-**DR4** were further assessed by plotting $\log K$ against the radical stability parameter $\sigma_C{}^{\cdot}$ (Figure 9b). As suggested by the Hammett-type plots, a good correlation was found for S-**DR4a–d** substituted with electron-donating groups, $\rho = -1.11$ ($R^2 = 0.92$). Whereas, the plots for S-**DR4e,f** substituted with the electron-withdrawing groups (X = Y = Cl, Br) were placed below the linear correlation observed for the case substituted by the electron-donating group. The stability of singlet diradicals substituted with electron-withdrawing groups S-**DR4e,f** is much larger than that of expected from radical characteristic, indicating that the benzylic carbon has an anionic characteristic as suggested by the reaction constant for the Hammett-type plot; $\log K$ versus $\sigma_p{}^+$. Thus, the singlet diradicals, S-**DR4,** possess the zwitterionic characteristics, such as **ZI2** (Scheme 8).[12]
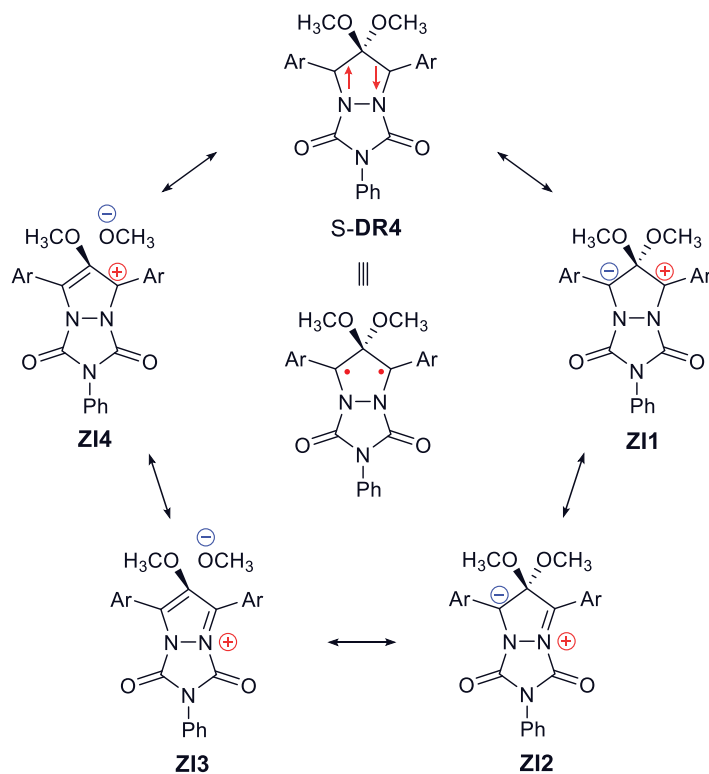
To gain further information on the characteristics of S-**DR4**, the effect of solvent on the equilibrium constant K was examined in various solvents (Tables 1,2, Figure 10). The logarithms of the equilibrium constants for S-**DR4a,b,f** (X = Y = H, MeO and Br), log$K$, were plotted against a solvent parameter $E_T(30)$. As shown in Figure 10, even though the effect of solvent is small[13], the slope is 0.020–0.036, with the solvent parameters being highly correlated with log$K$ except in the DMF case. The equilibrium constant K slightly decreases as the solvent polarity increases. Thus, the effect of solvent of the thermodynamic stability on the singlet diradicals was larger than that of the corresponding σ-bonded species, **CP4**. The effect of solvent is consistent with the correlation between the equilibrium constant K and the σ_p^+, $\sigma_C^\cdot$, demonstrating that the singlet diradicals, S-**DR4**, exhibit the zwitterionic characteristic. The effect of the solvent on the electron-withdrawing groups (X = Y = Br) was slightly larger than that on the electron-donating groups (X = Y = MeO), as indicated by the slopes of the plots in the following order;

–0.036 (Br) < –0.027 (H) < –0.020 (MeO). This result supports that the electron-withdrawing substituents increase the zwitterionic resonance structure, such as **ZI2** which possesses anionic characteristics at the benzylic position. According to the observed solvent effect, the contribution of the resonance forms of **ZI1** and **ZI4**, in which the cation charge, appears at the benzylic position appears to be low. To further elucidate the zwitterionic reso-
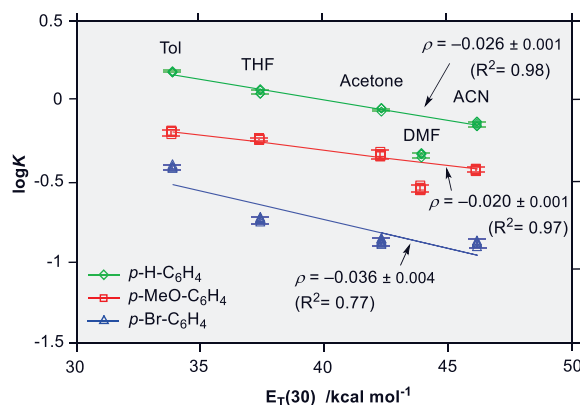
Figure 10. Correlation between the logarithm of equilibrium constant ($\log K$) and the solvent parameter $E_T(30)$ for the equilibrium reaction between S-**DR4** and **CP4**; green: p-H-C$_6$H$_4$, red: p-MeO-C$_6$H$_4$ and blue: p-Br-C$_6$H$_4$. Abbrev.; toluene = Tol, tetrahydrofuran = THF , acetone = ACE, and N,N-dimethylformamide = DMF .

nance structures in S-**DR4**, the aryl-asymmetrically substituted singlet diradicals S-**DR4h** (X = MeO, Y = Br) was generated in photodenitrogenation of azoalkane **AZ4h**, in which the electron-donating (MeO) and electron-withdrawing (Br) substituents were introduced at the para position and examined by means of laser flash photolysis method (Table 1: entries 3,4,11–14). In both toluene and acetonitrile, the equilibrium constants $K_{MeO,Br}$ were found to be 0.41 in toluene and 0.19 in acetonitrile, which were nearly the same as the values obtained for X = Y = Br, $K_{Br,Br} \approx 0.39$, 0.13 at 270 K, respectively, but differed greatly from those for X = Y = MeO, $K_{MeO,MeO} \approx 0.60$, 0.36. The notable effect of substituent evidently indicates that the contribution to the zwitterionic resonance structure, **ZI1**, is not responsible for stabilizing the singlet diradicals S-**DR4**. As suggested by the effect of solvent, the zwitterionic resonance structure, **ZI2**, is thought to contribute to the stabilization of the singlet diradicals S-**DR4**. In addition, the minor effect of the methoxy group on $K_{MeO,Br}$ suggests that the contribution

of **ZI4** is small, because the unpaired electrons of the nitrogen atoms effectively stabilize the benzylic cation to possess **ZI3**. The observed substituent effect on S-**DR4** were very different from those on the singlet diradicals S-**DR1**, which are more stabilized by the electron-donating substituents than by the electron-withdrawing groups.[3a,b]

2.2.3   Effects of substituent and solvent on ring-closing process k_{CP}

To gain a further insight into the electronic characteristics of S-**DR4** and its reactivity in the σ-bonded formation process, the effect of substituent on the ring-closing reaction rate constants (k_{CP}) was examined using Hammett-type plots (Figure 11). Surprisingly, the ring-closing reaction rate for S-**DR4b,c** substituted the electron-donating groups (X = Y = MeO, Me) were faster than that of S-**DR4a** (X = Y = H), even though S-**DR4** was more energetically stabilized by introducing electron-donating substituents compared to **CP4** (Figure 11a). Indeed, the equilibrium constant K for S-**DR4b,c** was smaller than that for S-**DR4a**. In contrast to the interesting substituent effect on k_{CP}, the electron-withdrawing group decelerated the ring-closing reaction (Table 1: entries 9–12). The negative reaction constants ρ; –0.13 in toluene and –0.45 in acetonitrile, in the Hammett-type plots, logk_{CP} versus $\sigma_p{}^+$, demonstrate that the ring-closing reaction is accelerated by the electron-donating
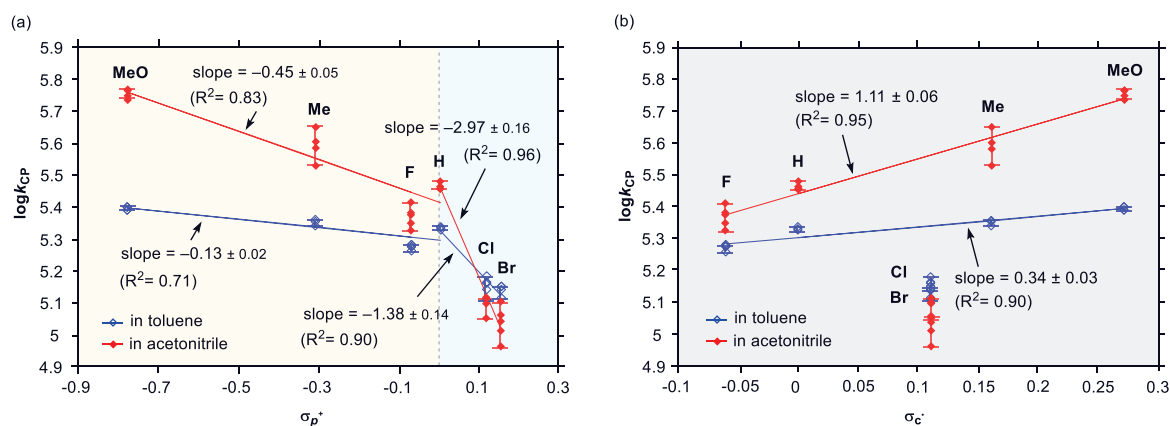
Figure 11. Hammett-type plots with (a) $\sigma_p{}^+$ and (b) $\sigma_C{}^{\cdot}$ for the logarithm of ring-closing reaction rate constant (logk_{CP}); blue; toluene, red; acetonitrile, respectively.

24

substituents (Figure 11a), indicating that the benzylic carbon is more positively charged in the transition state than S-**DR4**. Indeed, the ring-closing reaction was highly dependent on the solvent polarity for the electron-donating substituted S-**DR4b** (X = Y = MeO) (Figure 12). In contrast, the ring-closing reaction rate for S-**DR4e,f** (X = Y = Cl, Br), into which the electron-withdrawing group was substituted, were slower in polar acetonitrile than in non-polar toluene. A linear correlation for k_{CP} versus $\sigma_C{}^{\cdot}$ was observed for S-**DR4** substituted with the electron-donating group, $\rho = 1.11$ ($R^2 = 0.95$) (Figure 11b). Nevertheless, the data for the case in which the electron-withdrawing groups was substituted was found to deviate from the linear correlation observed for the case substituted by the electron-donating groups. These results evidently suggested that S-**DR4** substituted with electron-withdrawing group has a significant characteristic of zwitterion such as **ZI2**, as is the case in discussion concerning the effects of substituent and solvent on equilibrium constant K (Scheme 8 and Chapter 2.2.2). Based on the observed substituent and solvent effects on k_{CP}, the energy profile for the ring-closing process from S-**DR4** to **CP4** is shown in Scheme 9 (See Chapter summary 2.3). The curved arrows in **TS4**$_{DR\_CP}$ describe the electron movement from S-**DR4** to **CP4** via **TS4**, because the singlet diradicals S-**DR4** has the characteristic of zwitterions **ZI2** and **ZI3**. The benzylic carbon gradually becomes positive during the bond formation reaction. Therefore, the electron-donating groups accelerate the ring-closing reaction (Figures 11,12).
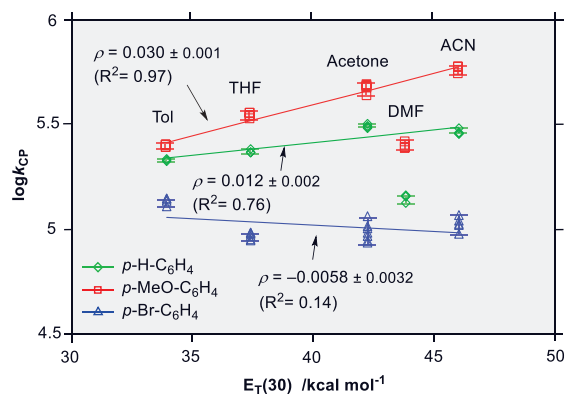
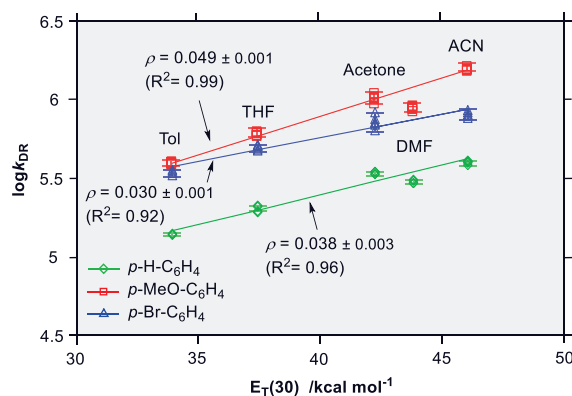**Figure 12.** Correlation between the logarithm of ring-closing reaction rate constant ($\log k_{CP}$) and the solvent parameter $E_T(30)$ for the equilibrium reaction between S-**DR4** and **CP4**; green: p-H-C$_6$H$_4$, red: p-MeO-C$_6$H$_4$ and blue: p-Br-C$_6$H$_4$.

25

The transition state being more highly charged than S-**DR4** explains the effect of the polar solvent on the acceleration of the ring-closing reaction for S-**DR4**, substituted by the electron-donating group (Scheme 9). In contrast to the rate acceleration induced by the electron-donating groups, the deceleration was observed for the singlet diradicals S-**DR4** substituted by the electron-withdrawing group, S-**DR4e,f** (entries 9–12 in Table 1, Figures 11,12). The notable substituent effects can be rationalized by the contribution of the zwitterionic resonance structure, **ZI2**, in S-**DR4**, which is well stabilized by polar solvents such as acetonitrile, increasing the energy barrier for the formation of **CP4** (Scheme 9). During the bond formation, the negative charge on the benzylic carbon decreases to decrease the stabilization of transition state, **TS4**, by the electron-withdrawing substituents. Thus, the ring-closing rate constant in a polar solvent is smaller than that in a non-polar solvent (Figures 11a,12).

2.2.4 Effects of substituent and solvent on ring-opening process k_{DR}

Next, the substituent and solvent effects on the ring-opening rate constant (k_{DR}) were also examined by the Hammett-type plots using σ_p^+ and $\sigma_C{}^{\cdot}$ parameters to understand the homolytic bond-breaking process (Tables 1,2 and Figures 13,14). First, the relation between σ_p^+ and the ring-opening rate constant $\log k_{DR}$ was investigated (Figure 13a). Both the electron-donating and
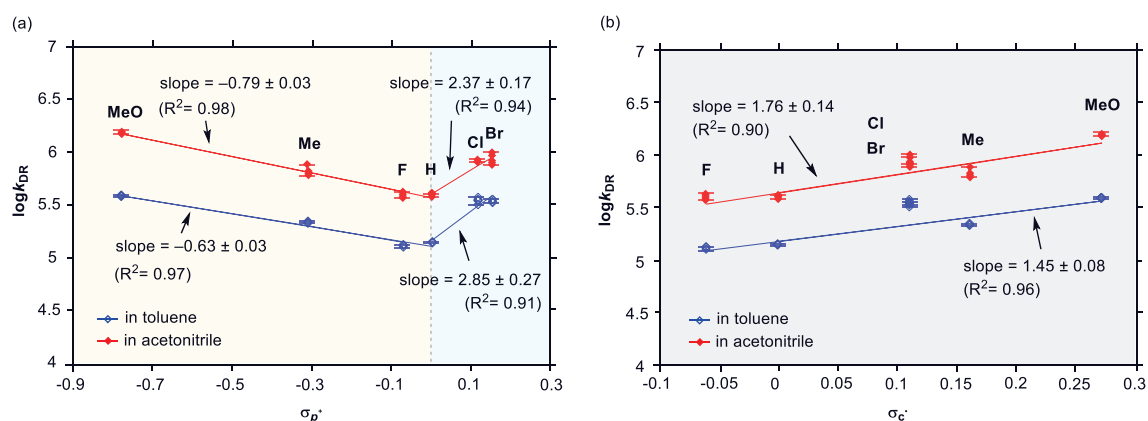
Figure 13. Hammett-type plots with a) σ_p^+ and b) $\sigma_C{}^{\cdot}$ for the logarithm of ring-opening reaction rate constant ($\log k_{DR}$); blue; toluene, red; acetonitrile, respectively.

26

electron-withdrawing groups accelerated the ring-opening reaction (V-shape plot). Thus, the reaction constant (ρ) for S-**DR4a,e,f**, substituted by the electron-withdrawing group, was found to be 2.9 ($R^2 = 0.91$) in toluene and 2.4 ($R^2 = 0.94$) in acetonitrile, respectively. The reaction constant ρ for the S-**DR4a–c**, substituted by the electron-donating group was observed to be –0.63 ($R^2 = 0.97$) in toluene and –0.79 ($R^2 = 0.98$) in acetonitrile, respectively (Figure 13a). These results clearly indicate that the transition state, **TS4**, possesses a radical character, compared to **CP4** (Scheme 9). The radical stabilization effect that accelerates the ring-opening process was also proven by the good positive linear correlation of logk_{DR} with $\sigma_C^{\cdot}$, the reaction constant; $\rho = 1.5$ ($R^2 = 0.96$) in toluene and $\rho = 1.8$ ($R^2 = 0.90$) in acetonitrile (Figure 13b). Consistent with the radical character of the transition state, the solvent effect for k_{DR} was found to be small (Figure 14). Interestingly, the plotted data for the electron-withdrawing groups (X = Y = Cl, Br) were placed slightly above the linear correlation observed for the electron-donating groups (Figure 13b). The phenomenon is also explained by the zwitterionic characteristic of **ZI2** in S-**DR4e,f**, in which the anionic characteristic exists in the benzylic carbon. To obtain further information on the ring-opening reaction, we also investigated the correlation between logk_{DR} and the solvent parameter $E_T(30)$ (Tables 1, 2 and Figure 14). Although the solvent effect was small[13], a good linear relation which gave a positive ρ value was obtained for log k_{DR} with the solvent parameters.

Figure 14. Correlation between the logarithm of ring-opening reaction rate constant (logk_{DR}) and the solvent parameter $E_T(30)$ for the equilibrium reaction between S-**DR4** and **CP4**; green: *p*-H-C$_6$H$_4$, red: *p*-MeO-C$_6$H$_4$ and blue: *p*-Br-C$_6$H$_4$.

2.3   Chapter summary

This chapter originated with the direct detection of a thermal equilibrium reaction between the localized singlet diradicals and its σ-bonded species, and focused on the electronic characteristics of the localized singlet 4,4-dialkoxy-1,2-diazacyclopentane-3,5-diyls, S-**DR4**, and its reactivity in the σ-bonded formation process. As shown in Scheme 9, S-**DR4** possess both characteristics of diradicals and zwitterion, which play an important role in determining the reactivity of the localized singlet diradicals.

Scheme 9. Homolytic ring-closing reaction of singlet diradicals S-**DR4** and homo-/heterolytic ring-opening reaction of its σ-bonded species **CP4**.
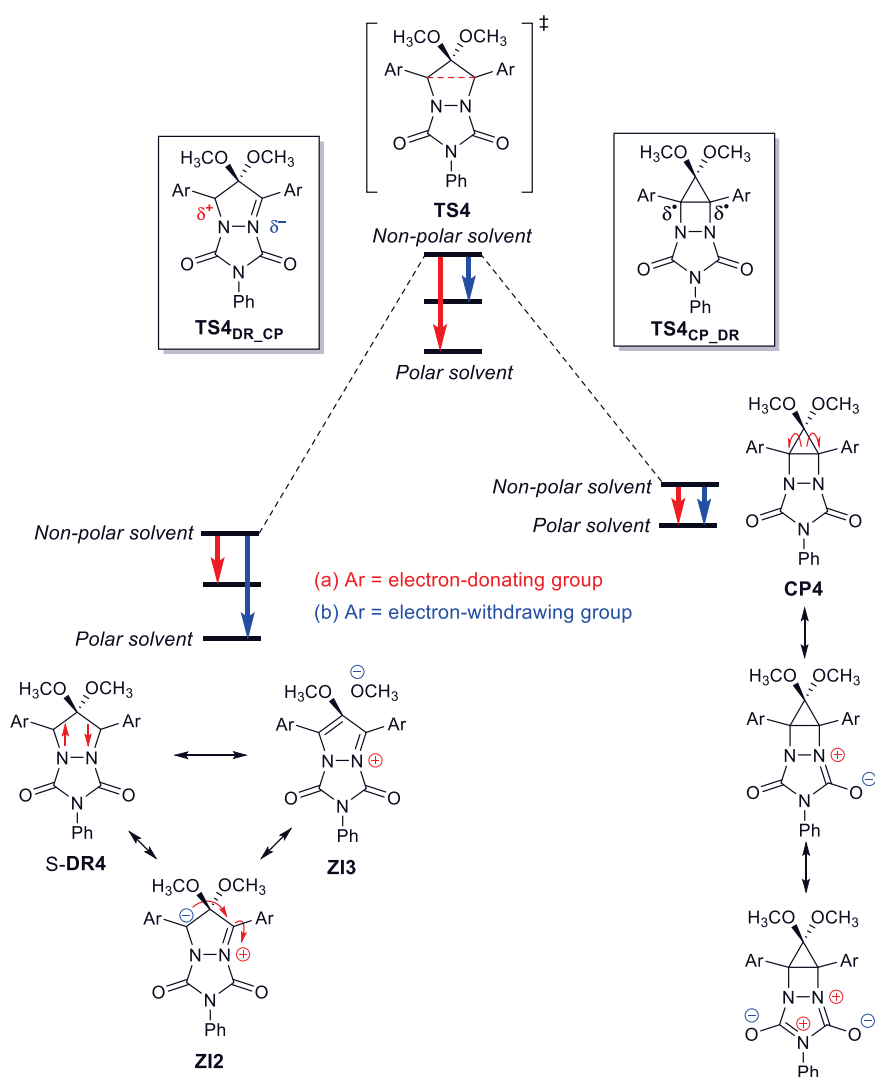
2.4   Experimental section

Laser Flash Photolysis Measurements

The concentration of samples was adjusted to an optical density of ca. 0.50 at the excited wavelength (430 nm). The excitation source for the LFP system was a tunable Nd: YAG-OPO laser that produces a 15 ns pulse of 3–4 mJ at 430 nm (LOTIS TII: LS-2145TF, LT-2214OPO). The monitoring system consisted of a 150 W xenon lamp as light source, Unisoku-MD200 monochromator and a photomultiplier. The temperature was controlled with a CoolSpek USP-203-B (Unisoku).
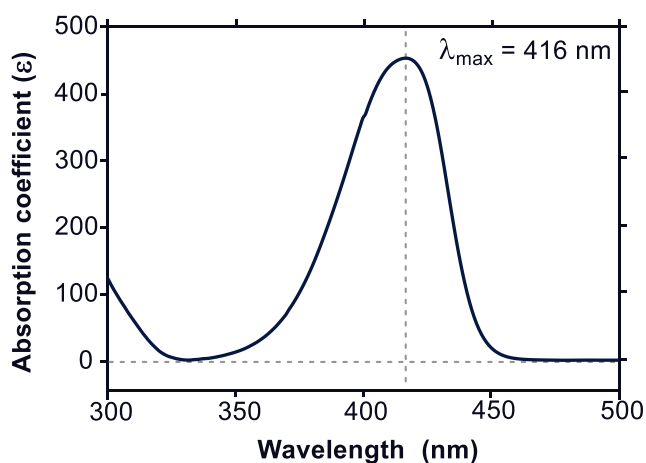
Figure 15. UV-vis absorption spectrum for the azoalkane **AZ4a** in toluene at 298 K.

Scheme 10. Nano second time-resolved transient absorption measuring system.

29
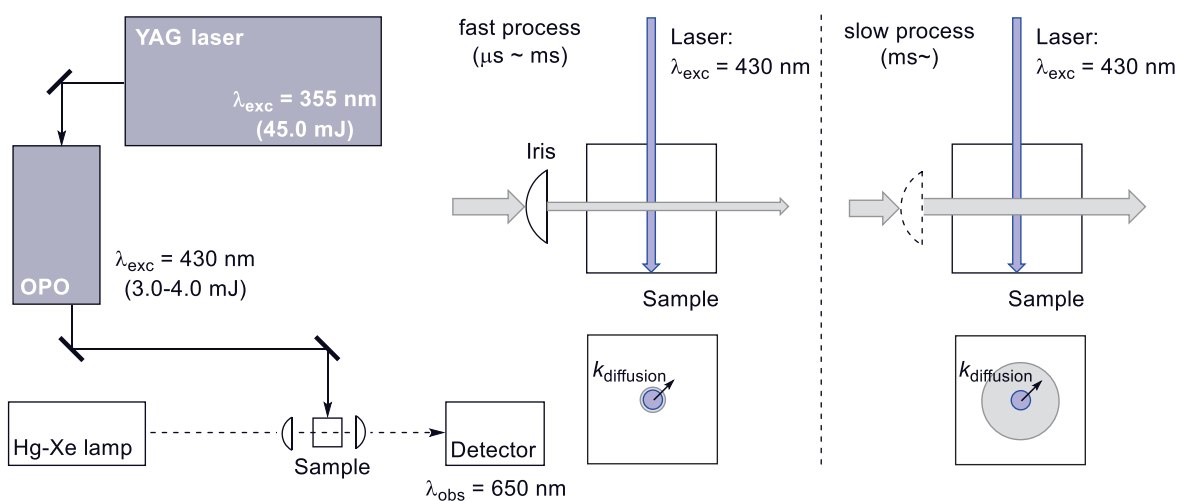
Table 1. Activation parameters $\Delta H^\ddagger$, $\Delta S^\ddagger$ and $\Delta G^\ddagger_{293}$; equilibration constant K, and rate constants k_{CP} and k_{DR} for the equilibration between S-**DR4** and **CP4** at 270 K.

Tol = toluene, ACN = acetonitrile; ΔH°, ΔG°_{293}, E_a in kJ mol^{-1}; ΔS° in J K^{-1} mol^{-1}

Entry	Substituent ($\sigma_C \cdot$)	4	Solvent ($E_T(30)$)	$K\,(=k_{CP}/k_{DR})$	k_{CP} / $\times 10^5$ s^{-1}	k_{DR} / $\times 10^5$ s^{-1}	S-DR4 $\to$ CP4 (S-DR4 $\leftarrow$ CP4)			ΔH°, ΔS°	E_a
							$\Delta G^\ddagger_{293}$ / kJ mol^{-1}	$\Delta H^\ddagger$ / kJ mol^{-1}	$\Delta S^\ddagger$ / J K mol^{-1}	ΔG°_{293}	
1	4-H (0.00)	**4a**	Tol (33.9)	1.54 ± 0.01	2.14 ± 0.03	1.39 ± 0.01	38.4 ± 0.3	37.6 ± 0.1	−2.6 ± 0.6	+1.9, +11.0	39.8
							(39.7 ± 0.8)	(35.7 ± 0.4)	(−13.6 ± 1.4)	−1.3	38.0
2			ACN (46.0)	0.72 ± 0.02	2.90 ± 0.12	4.02 ± 0.05	37.7 ± 2.0	36.4 ± 0.9	−4.6 ± 3.7	+6.3, +20.7	38.8
							(37.5 ± 0.9)	(30.1 ± 0.4)	(−25.3 ± 1.8)	+0.2	32.4
3	4-MeO (0.27)	**4b**	Tol	0.60 ± 0.02	2.12 ± 0.10	3.55 ± 0.04	38.2 ± 0.2	40.2 ± 1.1	6.8 ± 4.6	+3.6, +8.8	42.1
							(37.3 ± 0.1)	(36.8 ± 0.6)	(−2.7 ± 2.3)	+1.0	38.5
4			ACN	0.36 ± 0.01	5.71 ± 025	15.68 ± 0.42	36.6 ± 1.3	32.2 ± 0.6	−15.0 ± 2.4	+7.4, +18.9	35.3
							(34.6 ± 2.8)	(25.7 ± 1.3)	(−30.5 ± 5.1)	+1.8	27.9
5	4-Me (0.16)	**4c**	Tol	1.03 ± 0.01	2.23 ± 0.05	2.17 ± 0.02	37.8 ± 1.3	38.7 ± 0.8	1.8 ± 2.9	+2.6, +9.9	40.7
							(37.0 ± 1.5)	(36.2 ± 0.7)	(−8.1 ± 2.7)	−0.3	38.0
6			ACN	0.58 ± 0.02	3.92 ± 0.55	6.76 ± 0.59	37.3 ± 1.3	34.7 ± 0.1	−8.4 ± 4.0	+6.1, +17.3	37.1
							(36.3 ± 1.3)	(28.3 ± 0.6)	(−27.3 ± 2.4)	+1.0	30.4
7	4-F (-0.06)	**4d**	Tol	1.44 ± 0.08	1.87 ± 0.23	1.30 ± 0.22	38.9 ± 1.3	37.8 ± 0.6	−3.8 ± 2.3	+2.3, +11.8	40.2
							(39.9 ± 1.8)	(35.2 ± 0.9)	(−16.2 ± 3.0)	−1.1	37.8
8			ACN	0.59 ± 0.02	2.33 ± 0.25	3.98 ± 0.25	38.1 ± 1.5	37.6 ± 0.7	−1.9 ± 2.7	+6.6, +19.7	38.8
							(37.5 ± 2.6)	(30.6 ± 1.2)	(−23.4 ± 4.8)	+0.8	32.3
9	4-Cl (0.11)	**4e**	Tol	0.40 ± 0.01	1.40 ± 0.14	3.53 ± 0.29	39.4 ± 4.0	38.5 ± 1.8	−3.1 ± 7.5	+4.8, +10.1	40.7
							(37.5 ± 2.3)	(33.5 ± 1.0)	(−13.8 ± 4.4)	+1.9	35.5
10			ACN	0.15 ± 0.01	1.23 ± 0.12	8.41 ± 0.20	39.7 ± 1.9	39.0 ± 0.9	−2.4 ± 3.3	+11.2, +25.3	41.0
							(36.0 ± 2.1)	(27.7 ± 1.0)	(−28.2 ± 3.8)	+3.7	30.3

Continuation of **Table 1** (entry 11–14).

Entry	Substituent ($\sigma_C\cdot$)	Solvent ($E_T(30)$)	$K\,(=k_{CP}/k_{DR})$	k_{CP} / $\times 10^5$ s^{-1}	k_{DR} / $\times 10^5$ s^{-1}	S-DR4→CP4 (S-DR4←CP4)				
	4					$\Delta G^{\ddagger}_{293}$ / kJ mol^{-1}	$\Delta H^{\ddagger}$ / kJ mol^{-1}	$\Delta S^{\ddagger}$ / J K mol^{-1}	ΔH°, ΔS° ΔG°_{293}	E_a
11	**4f** 4-Br (0.11)	Tol	0.39 ± 0.01	1.36 ± 0.04	3.48 ± 0.11	41.4 ± 4.8 (37.7 ± 4.7)	38.5 ± 1.5 (33.2 ± 2.2)	-6.9 ± 2.6 (-15.2 ± 8.4)	$+5.8, +13.6$ $+1.8$	41.3 35.6
12		ACN	0.13 ± 0.01	1.06 ± 0.10	8.16 ± 0.49	40.3 ± 8.2 (35.9 ± 5.9)	38.7 ± 3.9 (30.1 ± 2.8)	-5.6 ± 14.7 (-19.9 ± 10.6)	$+9.2, +16.7$ $+4.3$	40.9 32.1
13	**4h** 4-OMe, 4'-Br	Tol	0.41 ± 0.02	1.92 ± 0.12	4.64 ± 0.36	38.6 ± 1.6 (36.9 ± 2.2)	38.3 ± 0.7 (33.7 ± 1.0)	-1.0 ± 3.0 (-10.8 ± 4.1)	$+4.6, +9.6$ $+1.7$	39.9 35.7
14		ACN	0.19 ± 0.01	2.37 ± 0.13	12.37 ± 0.23	37.9 ± 5.4 (34.6 ± 4.5)	36.7 ± 2.6 (29.5 ± 2.1)	-4.1 ± 9.6 (-17.3 ± 8.1)	$+7.9, +16.0$ $+3.2$	38.6 30.9

Table 2. Solvent effect on the fast process. THF = tetrahydrofuran, ACE = acetone, DMF = N,N-dimethylformamide

Entry	Substituent 4 ($\sigma_C \cdot$)	Solvent ($E_T(30)$)	$K\ (=k_{CP}/k_{DR})$	k_{CP} / × 10⁵ s⁻¹	k_{DR} / × 10⁵ s⁻¹	S-DR4 → CP4 (S-DR4 ← CP4)			$\Delta H°, \Delta S°$ $\Delta G°_{293}$
						$\Delta G^{\ddagger}_{293}$ / kJ mol⁻¹	$\Delta H^{\ddagger}$ / kJ mol⁻¹	$\Delta S^{\ddagger}$ / J K mol⁻¹	
1	**4a** 4-H (0.00)	THF (37.4)	1.15 ± 0.02	2.34 ± 0.03	2.03 ± 0.11	38.0 ± 3.6 (38.9 ± 1.7)	37.2 ± 1.7 (31.4 ± 0.8)	−2.9 ± 6.5 (−25.9 ± 3.1)	+5.3, +21.0 −0.8
2		ACE (42.2)	0.90 ± 0.01	3.09 ± 0.08	3.44 ± 0.05	37.4 ± 0.4 (37.9 ± 0.7)	37.2 ± 0.2 (29.3 ± 0.3)	−1.0 ± 0.7 (−29.2 ± 1.2)	+8.0, +28.5 −0.4
3		DMF (43.8)	0.45 ± 0.01	1.38 ± 0.03	3.04 ± 0.08	38.9 ± 8.1 (38.0 ± 5.5)	43.5 ± 3.8 (32.6 ± 2.6)	15.8 ± 14.6 (−18.3 ± 9.8)	+10.6, +32.7 +1.0
4	**4b** 4-MeO (0.27)	THF	0.571 ± 0.003	3.45 ± 0.08	6.05 ± 0.16	37.3 ± 1.1 (36.4 ± 0.8)	35.2 ± 0.5 (29.7 ± 0.4)	−7.3 ± 1.9 (−23.0 ± 1.5)	+5.0, +13.8 +0.9
5		ACE	0.46 ± 0.02	4.67 ± 0.19	10.22 ± 0.63	40.1 ± 4.0 (36.1 ± 3.7)	37.2 ± 1.8 (27.3 ± 1.7)	−9.9 ± 7.5 (−30.1 ± 6.7)	+9.4, +18.4 +3.9
6		DMF	0.28 ± 0.01	2.47 ± 0.12	8.87 ± 0.28	37.8 ± 2.9 (35.5 ± 3.2)	38.2 ± 1.3 (29.6 ± 1.5)	1.4 ± 5.3 (−20.2 ± 5.7)	+8.3, +20.3 +2.3
7	**4e** 4-Cl (0.11)	THF	0.20 ± 0.01	0.96 ± 0.07	4.78 ± 0.34	40.0 ± 4.7 (36.9 ± 3.7)	40.7 ± 2.2 (30.6 ± 1.7)	2.5 ± 8.6 (−21.6 ± 6.7)	+10.6, +26.1 +3.0
8		ACE	0.15 ± 0.01	1.21 ± 0.01	8.25 ± 0.18	40.1 ± 4.1 (36.1 ± 3.7)	37.2 ± 1.9 (27.3 ± 1.7)	−9.9 ± 7.5 (−30.1 ± 6.7)	+10.4, +22.5 +3.9
9		DMF	0.066 ± 0.002	0.35 ± 0.03	5.40 ± 0.25	42.0 ± 7.2 (36.4 ± 5.7)	41.0 ± 3.3 (30.4 ± 2.6)	−3.3 ± 13.4 (−20.4 ± 10.6)	+10.8, +17.5 +5.7
10	**4f** 4-Br (0.11)	THF	0.18 ± 0.01	0.93 ± 0.04	5.06 ± 0.24	40.5 ± 5.2 (37.1 ± 3.4)	38.8 ± 2.4 (29.2 ± 1.6)	−5.8 ± 9.7 (−27.1 ± 6.3)	+9.8, +21.8 +3.4
11		ACE	0.13 ± 0.01	0.97 ± 0.01	7.30 ± 0.82	40.1 ± 4.8 (36.1 ± 4.6)	39.7 ± 2.3 (31.0 ± 2.2)	−1.4 ± 8.5 (−17.5 ± 8.1)	+10.9, +23.2 +4.2
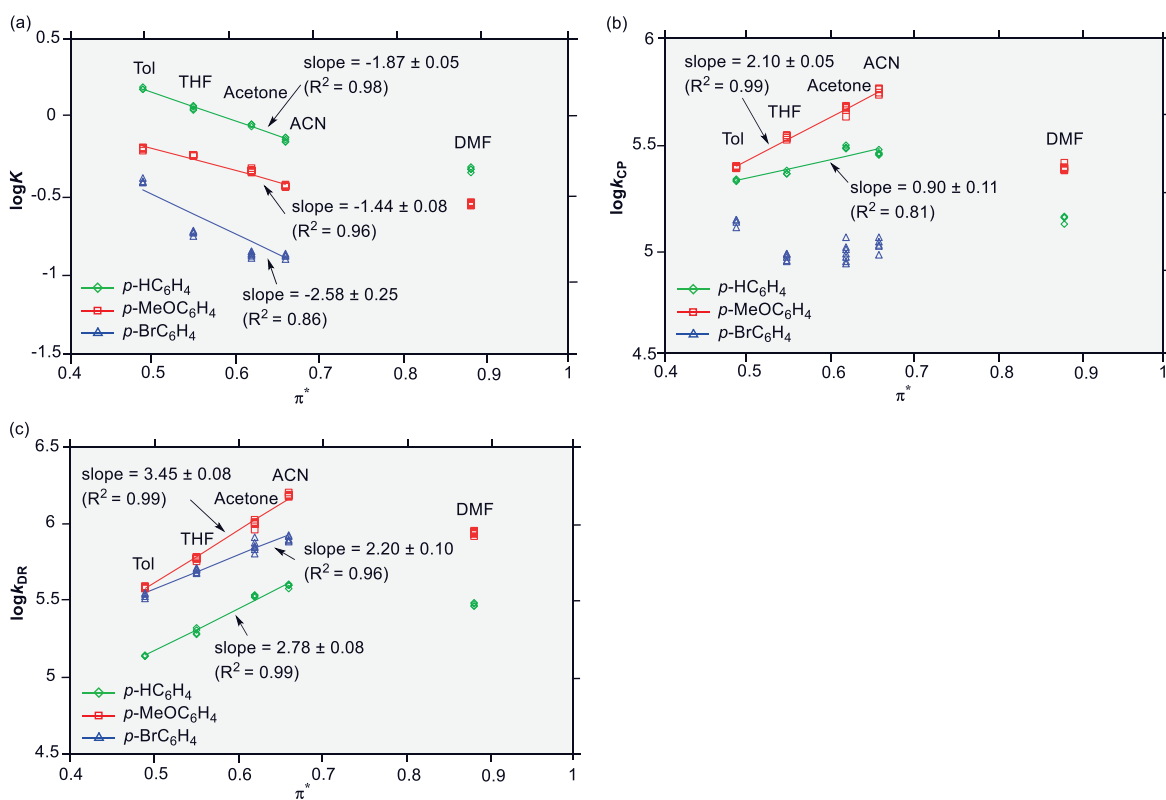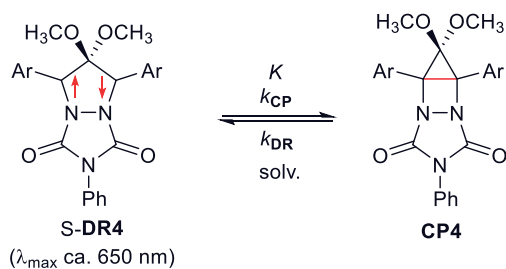
Figure 16. Correlation between (a) log$K$, (b) logk_{CP}, and (c) logk_{DR} and the other solvent parameter π^{*14} for fast process (S-**DR4** ⇌ **CP4**), respectively; green: p-H-C$_6$H$_4$, red: p-MeO-C$_6$H$_4$, blue: p-Br-C$_6$H$_4$.

33

Van't Hoff and Eyring plots: fast process

By fitting with the first-order equation $[y = a_1 + a_3 \exp(- t/a_4)]$ against transient decay trace of fast process, the equilibrium constant K which can be expressed by $K = k_{CP}/k_{DR}$, and respective rate constants of k_{CP} and k_{DR} were determined; $a_1 = [CP4]$, $a_3 = [S\text{-}DR4]$, and $a_4 = $ lifetime. The respective activation parameters were derived using the following equations (α)–(γ).

Van't Hoff equation: $\ln K = - \Delta H^{\ddagger}/(RT) + \Delta S^{\ddagger}/R$ ⋯⋯⋯⋯⋯⋯⋯⋯⋯⋯ (α)

Arrhenius equation: $\ln k = \ln A - E_a/(RT)$ ⋯⋯⋯⋯⋯⋯⋯⋯⋯⋯⋯⋯ (β)

Eyring equation[15]: $\ln(k/T) = \ln(\kappa k_B/T) - \Delta H^{\ddagger}/(RT) + \Delta S^{\ddagger}/R$ ⋯⋯⋯⋯ (γ)

- **AZ4a** $(p\text{-H-C}_6\text{H}_4)$ in toluene

- **AZ4a** in acetonitrile

34
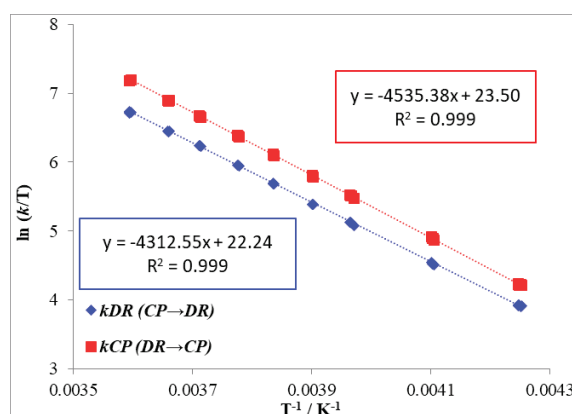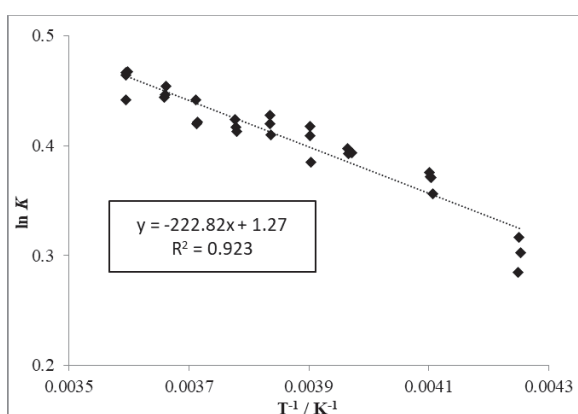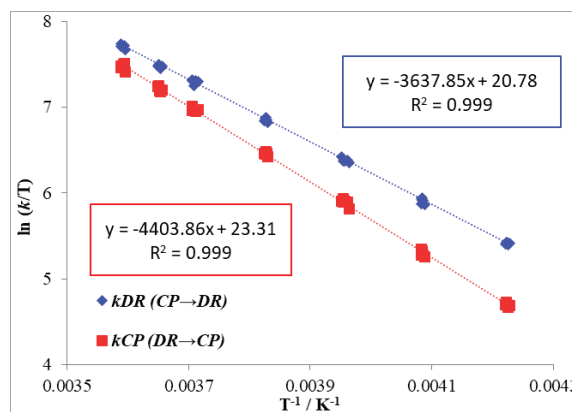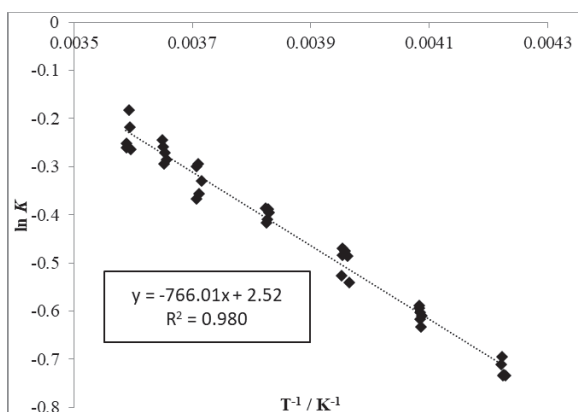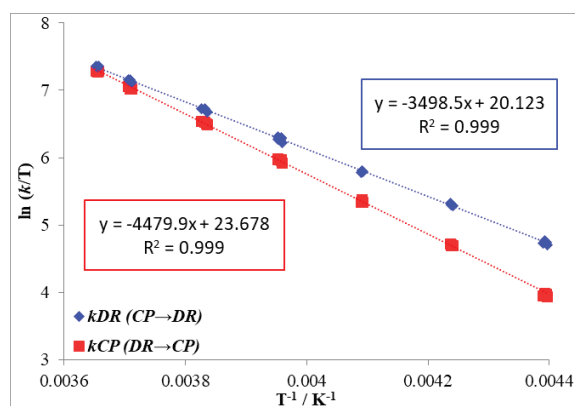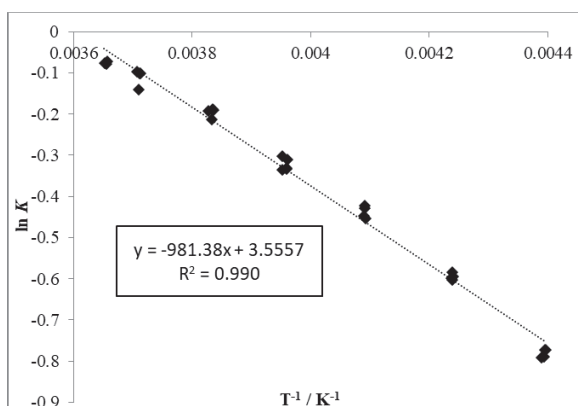
· **AZ4a** in acetone

· **AZ4a** in tetrahydrofuran (THF)
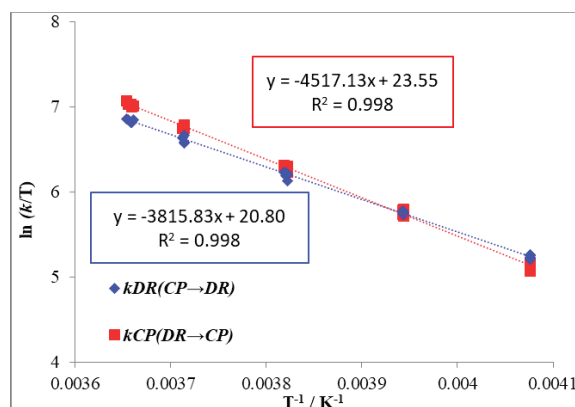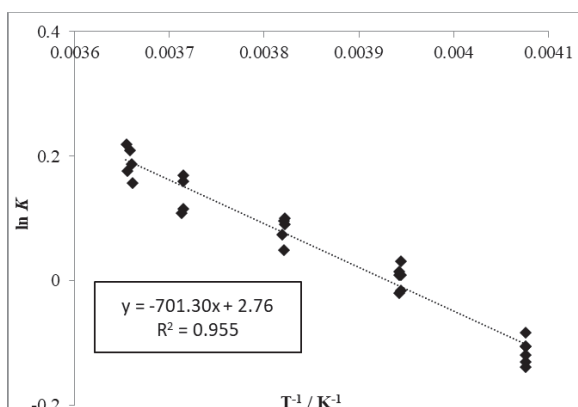

· **AZ4a** in dimethyl sulfoxide (DMSO)
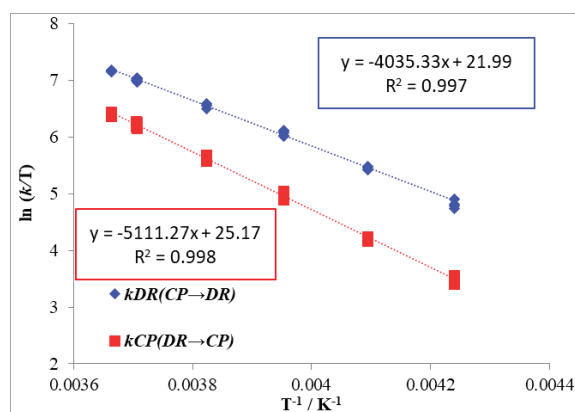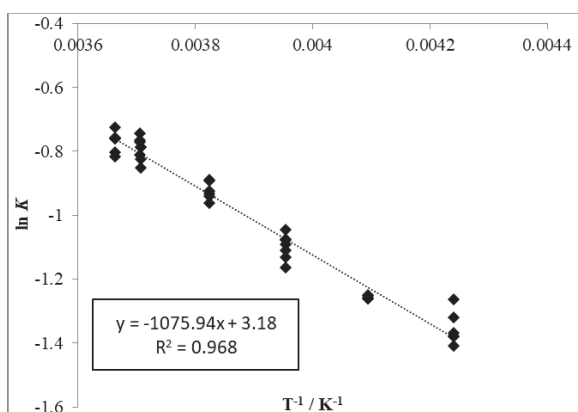
・ **AZ4b** (p-MeO-C$_6$H$_4$) in toluene

Left plot:
y = -981.38x + 3.5557
R² = 0.990

Right plot:
y = -4381.52x + 23.44
R² = 0.999

y = -4816.55x + 24.55
R² = 0.999

♦ kDR (CP→DR)
■ kCP (DR→CP)

・ **AZ4b** in acetonitrile

Left plot:
y = -886.56x + 2.27
R² = 0.986

Right plot:
y = -3101.11x + 20.15
R² = 0.995

y = -3987.67x + 22.42
R² = 0.999

♦ kDR (CP→DR)
■ kCP (DR→CP)

・ **AZ4b** in acetone

Left plot:
y = -898.62x + 2.57
R² = 0.986

Right plot:
y = -3303.96x + 20.54
R² = 0.998

y = -4202.58x + 23.12
R² = 0.997

♦ kDR (CP → DR)
■ kCP (DR → CP)

36
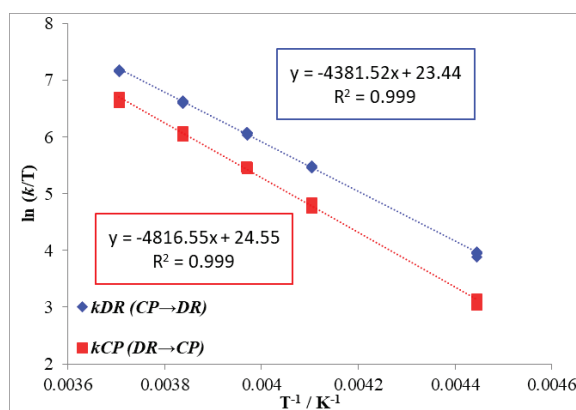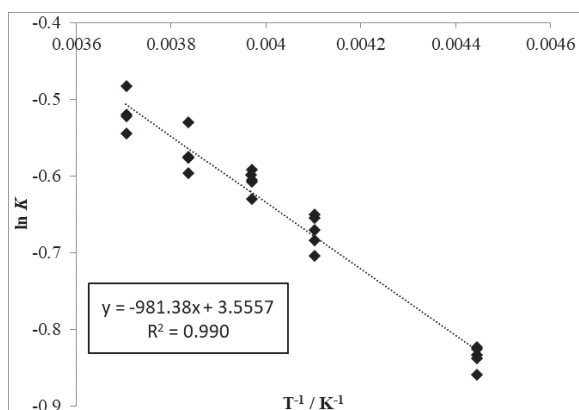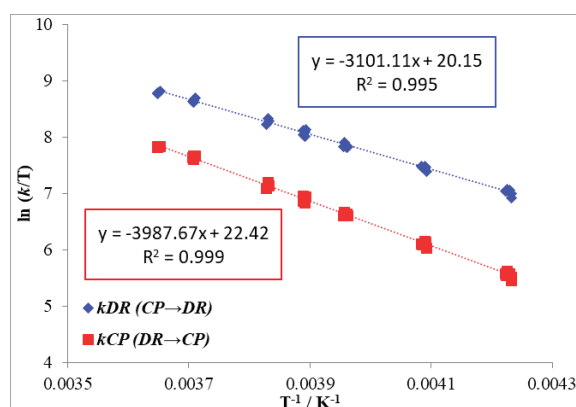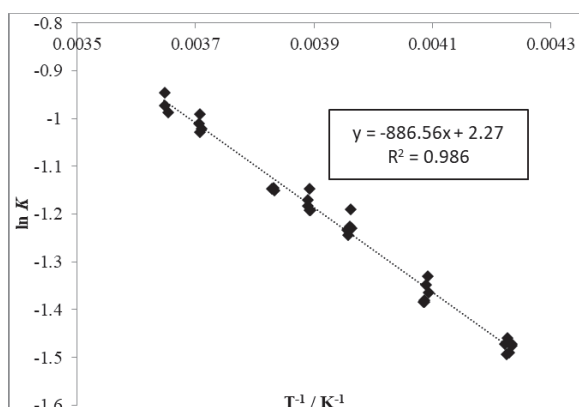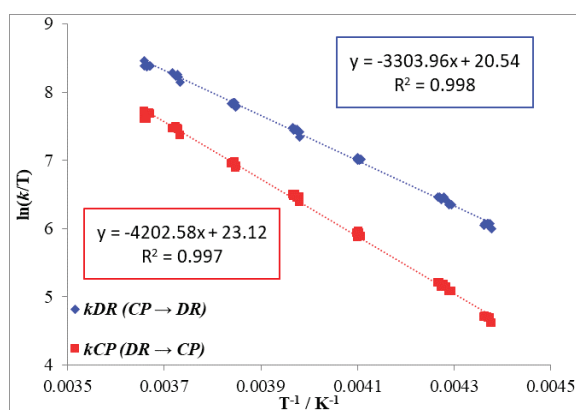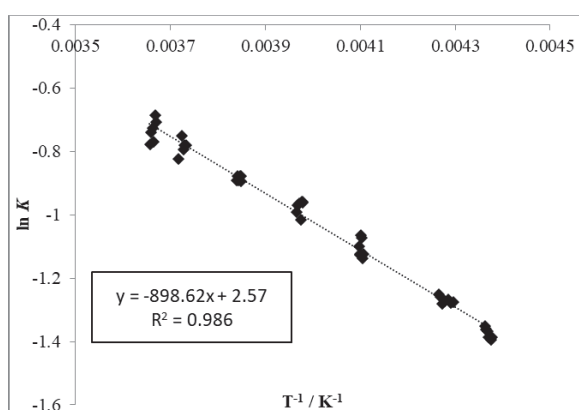
· **AZ4b** in tetrahydrofuran (THF)
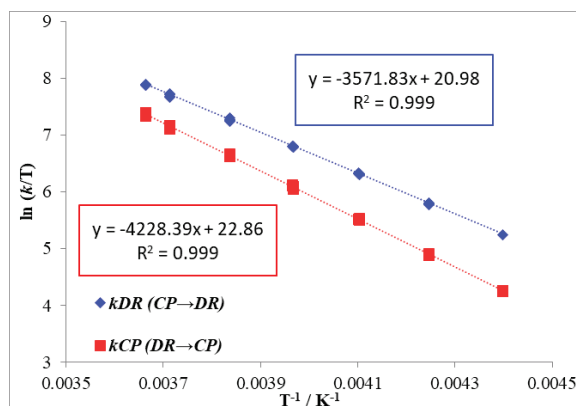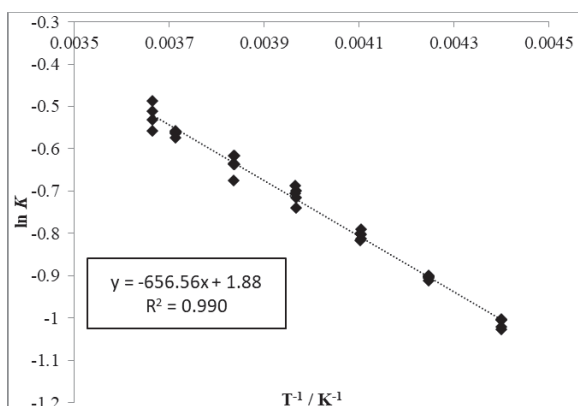
· **AZ4b** in dimethyl sulfoxide (DMSO)
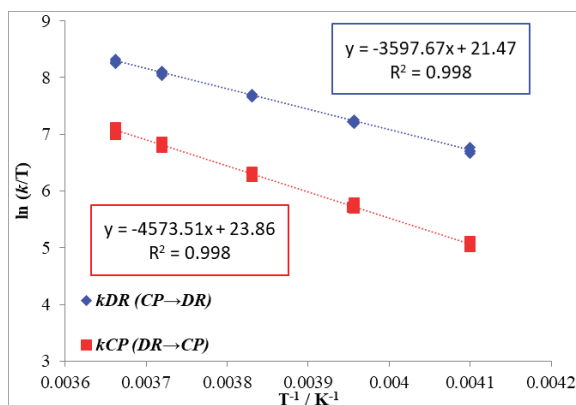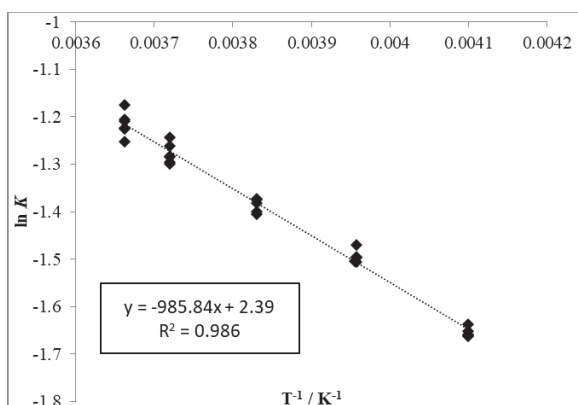
· **AZ4c** (p-Me-C$_6$H$_4$)in toluene
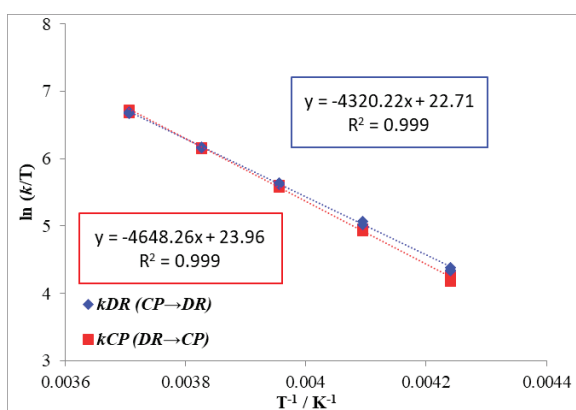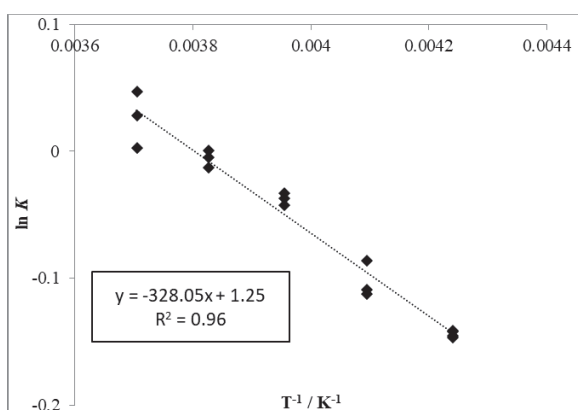
・**AZ4c** in acetonitrile
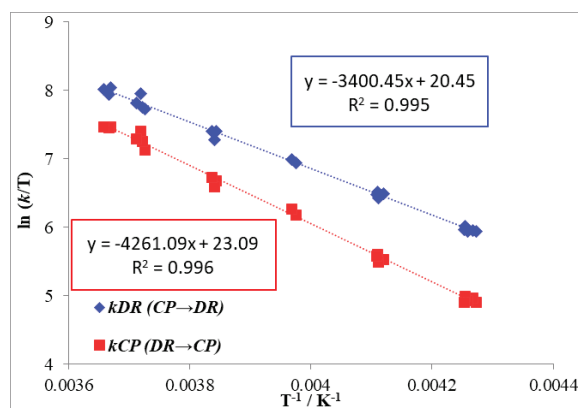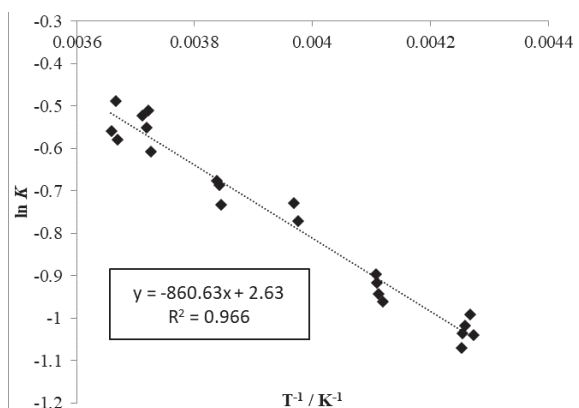
・**AZ4d** (p-F-C$_6$H$_4$)in toluene
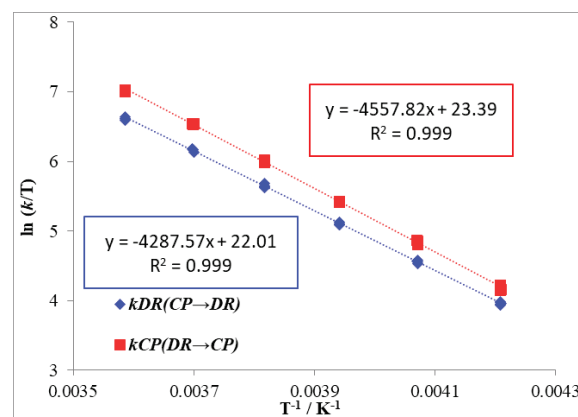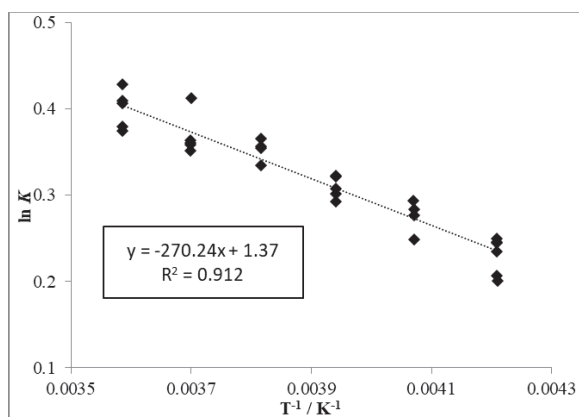
・**AZ4d** in acetonitrile

38
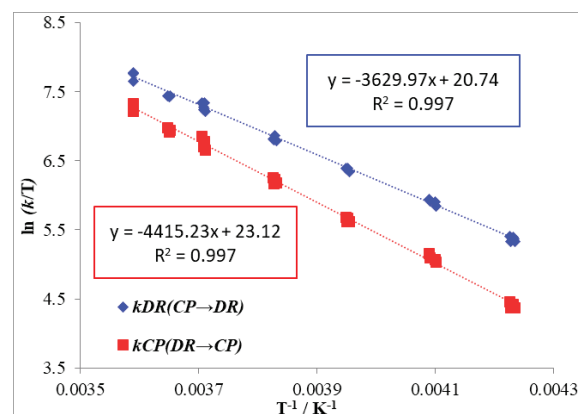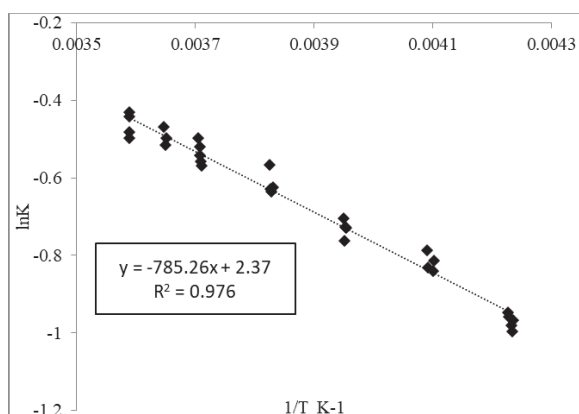
· **AZ4e** (p-Cl-C$_6$H$_4$)in toluene
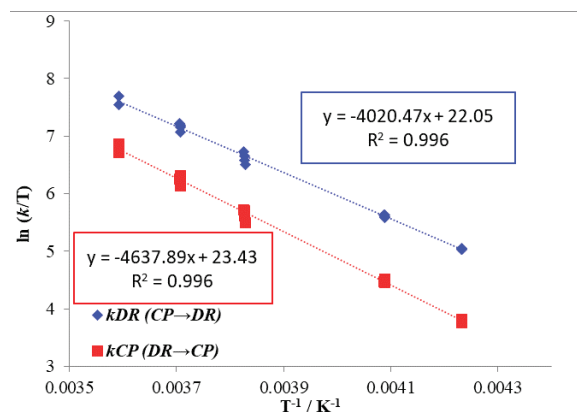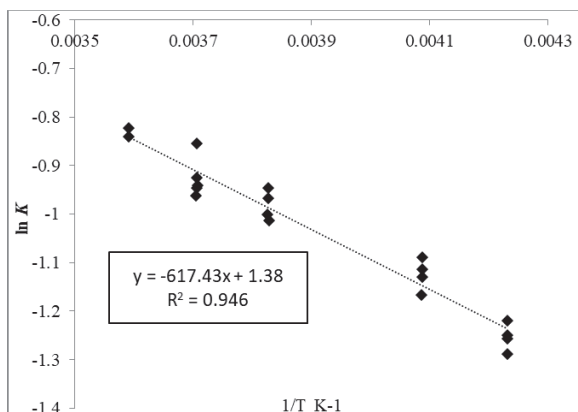
· **AZ4e** in acetonitrile
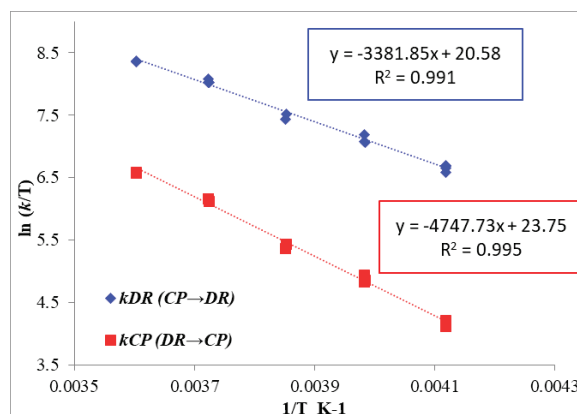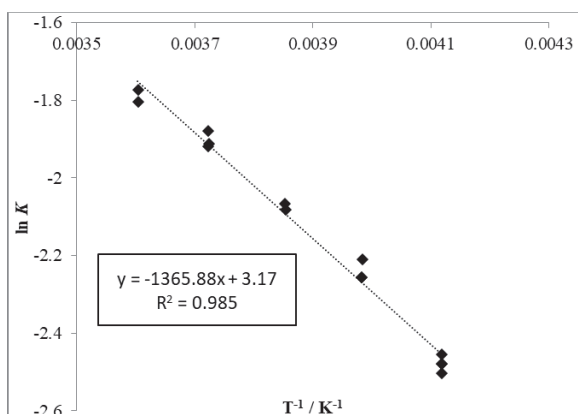
· **AZ4f** (p-Br-C$_6$H$_4$)in toluene

• **AZ4f** in acetonitrile

Left chart: y = -1062.43x + 1.87, R² = 0.973 (ln K vs T⁻¹ / K⁻¹)

Right chart: y = -3597.94x + 21.32, R² = 0.996; y = -4660.38x + 23.19, R² = 0.994; kDR (CP→DR), kCP (DR→CP) (ln (k/T) vs T⁻¹ / K⁻¹)

• **AZ4f** in acetone

Left chart: y = -1468.99x + 3.45, R² = 0.972 (ln K vs T⁻¹ / K⁻¹)

Right chart: y = -3702.75x + 21.64, R² = 0.990; y = -5171.74x + 25.09, R² = 0.992; kDR (CP→DR), kCP (DR→CP) (ln (k/T) vs T⁻¹ / K⁻¹)

• **AZ4f** in tetrahydrofuran (THF)

Left chart: y = -1196.74x + 2.74, R² = 0.975 (ln K vs T⁻¹ / K⁻¹)

Right chart: y = -3506.28x + 20.49, R² = 0.996; y = -4703.02x + 23.24, R² = 0.995; kDR (CP→DR), kCP (DR→CP) (ln (k/T) vs T⁻¹ / K⁻¹)

40
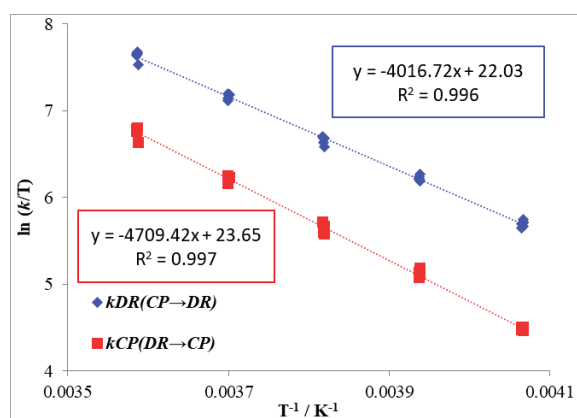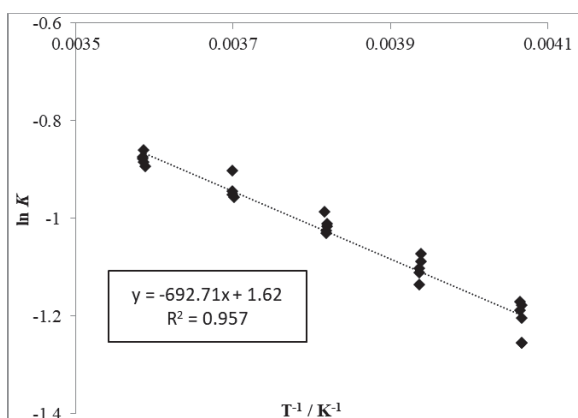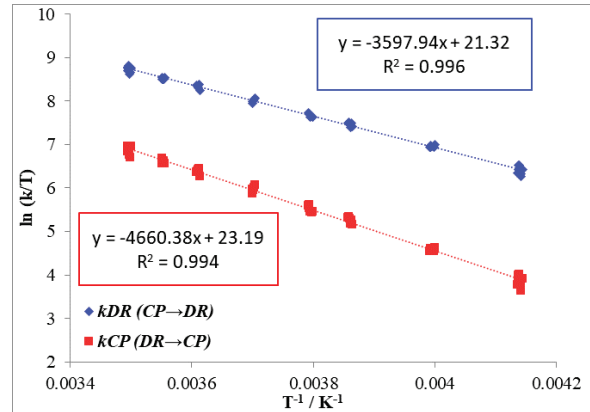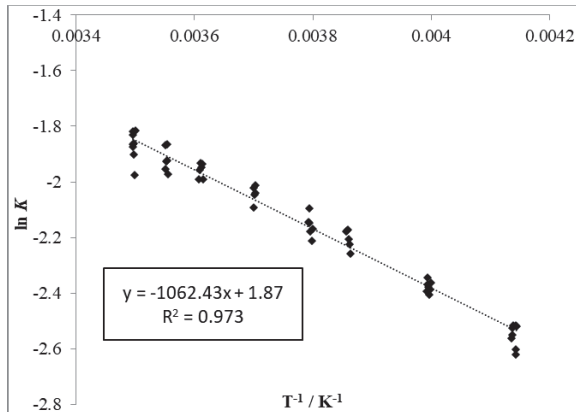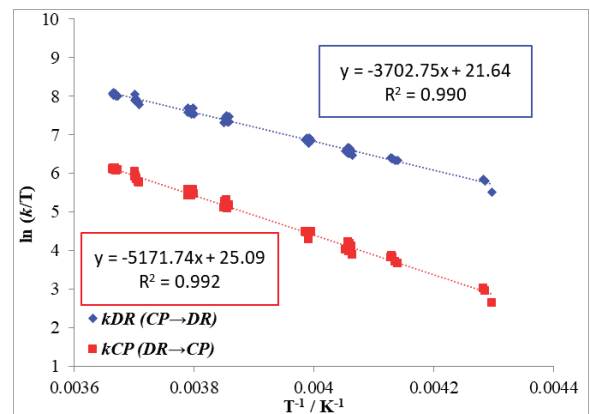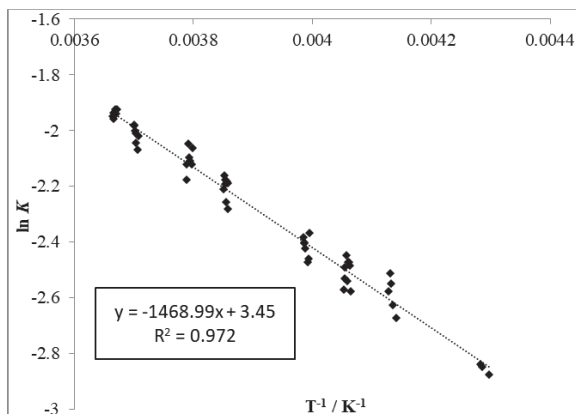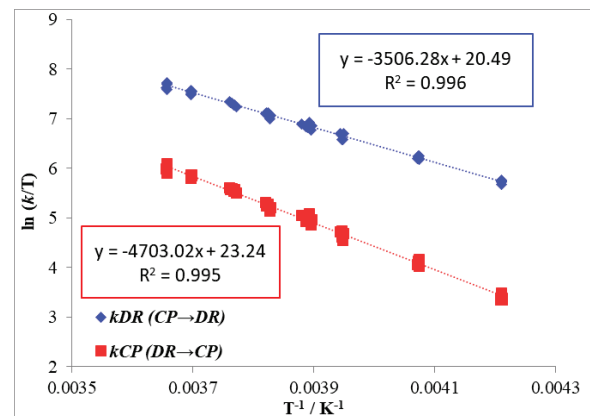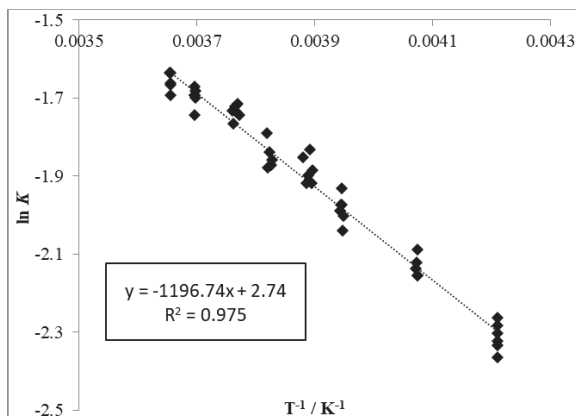
· **AZ4h** (p-OMe-C$_6$H$_4$, p-Br-C$_6$H$_4$)in toluene

y = -446.76x + 0.79
R^2 = 0.956

y = -4080.02x + 22.55
R^2 = 0.999

y = -4526.78x + 23.34
R^2 = 0.999

kDR (CP→DR)

kCP (DR→CP)

· **AZ4h** in acetonitrile

y = -927.21x + 1.80
R^2 = 0.969

y = -3461.45x + 21.28
R^2 = 0.989

y = -4388.66x + 23.08
R^2 = 0.991

kDR(CP→DR)

kCP(DR→CP)

41
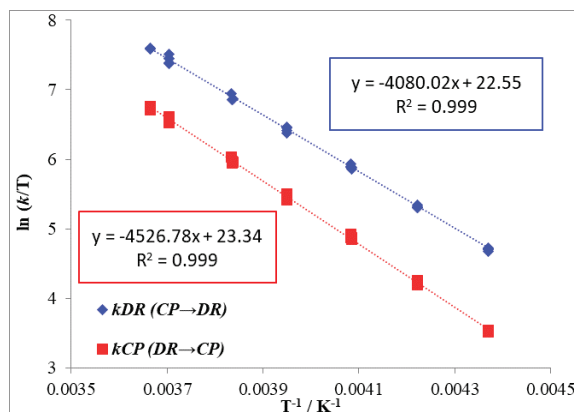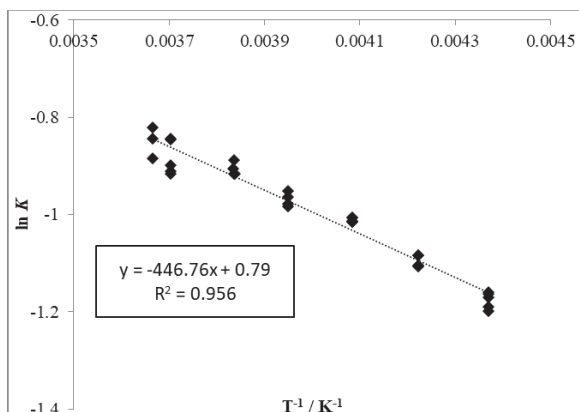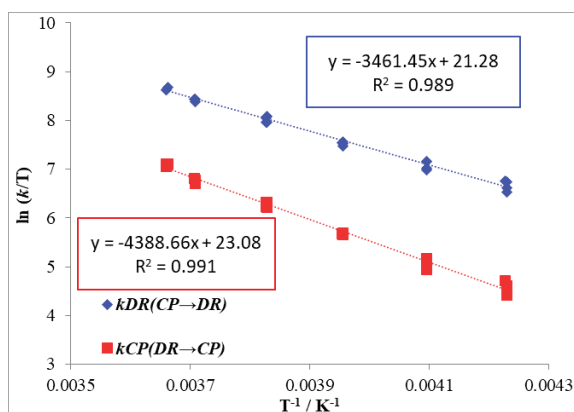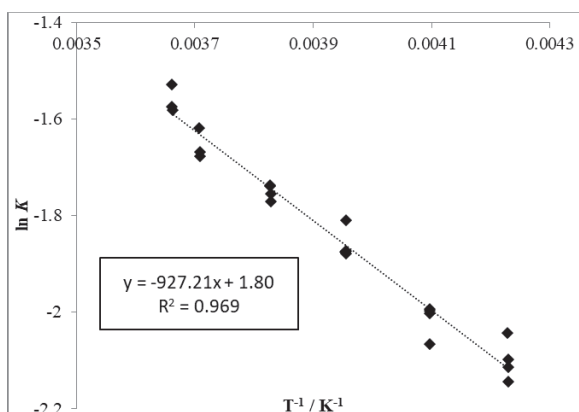
Scheme 11. Syntheses of azoalkanes **AZ4a–n**.

Method A (Aryl-group substituent)

Method B (Alkoxy-group substituent)

A Typical Procedure I
(Method A: Aa–j → PZa–j)

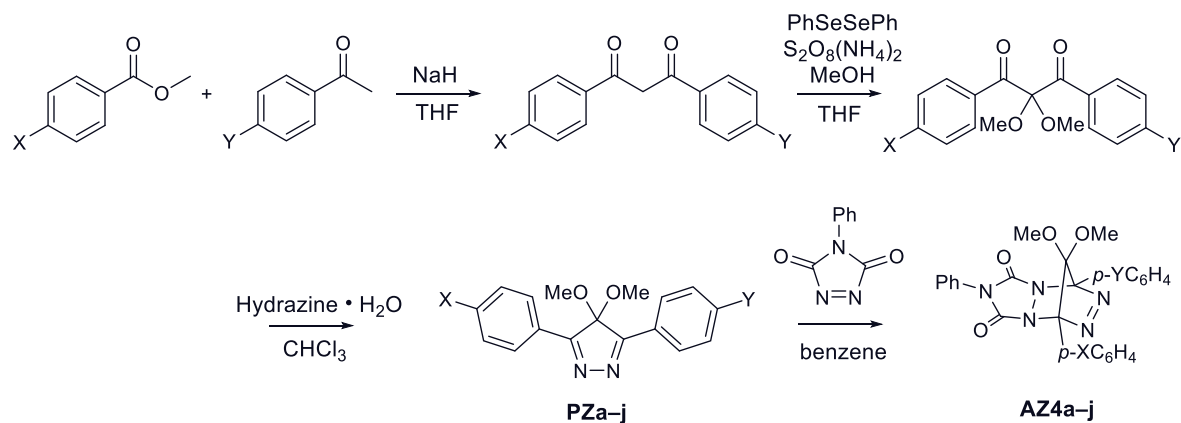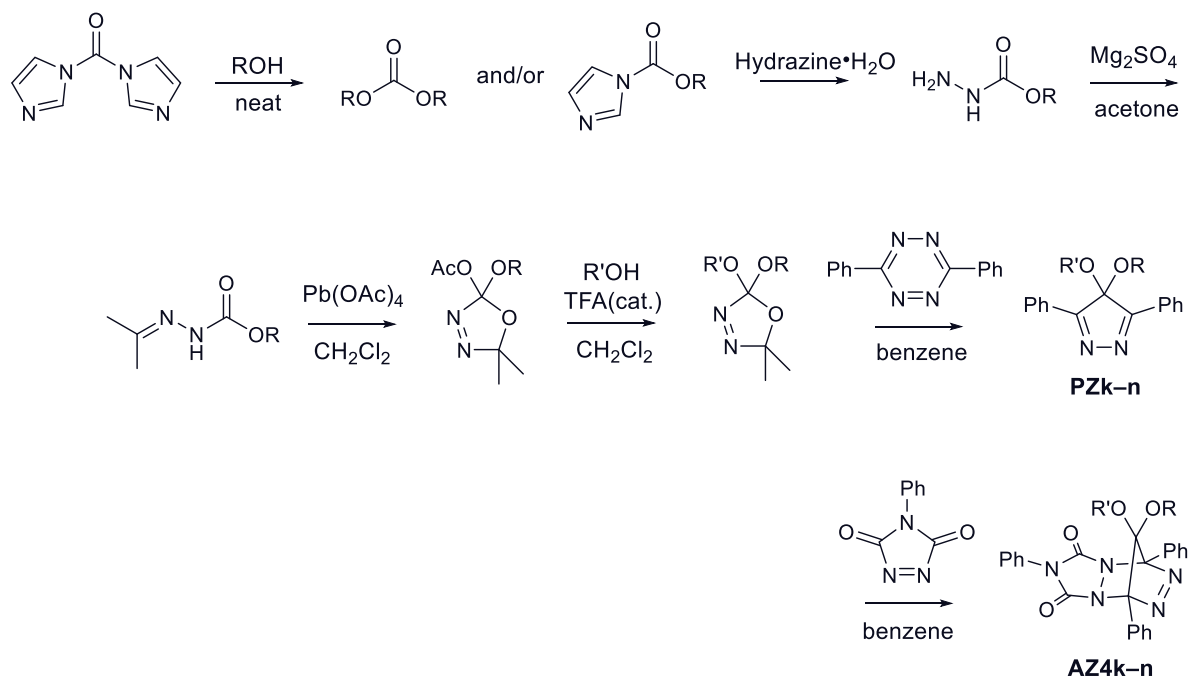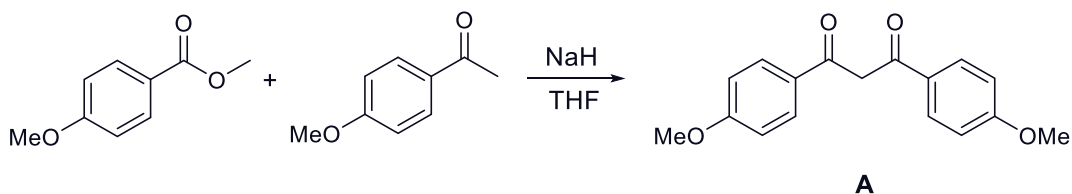A 300 mL three-necked round-bottom flask was charged with 60% suspension of sodium hydride in mineral oil (1.08 g, 45.0 mmol, 1.5 eq.), methyl 4-methoxybenzoate (4.97 g, 30.0 mmol, 1.0 eq.), and dried THF (40 mL). The solution of 4'-metoxyacetophenone (4.58 g, 30.5 mmol, 1.0 eq.) in dried THF (40 mL) was added to the flask and stirred overnight at room temperature. The reaction mixture was poured into iced 1M HCl and the precipitate was filtered, washed with iced water, and evaporated with vacuum pump to remove water. The pale yellow solid was recrystallized from THF and 2.68 g (9.4 mmol, 30 %) of **A** was afforded. ^{1}H NMR (400 MHz, CDCl$_3$) of **A**: δ 3.88 (s, 6H), 6.73 (s, 1H), 6.98 (m, 4H), 7.96 (m, 4H)
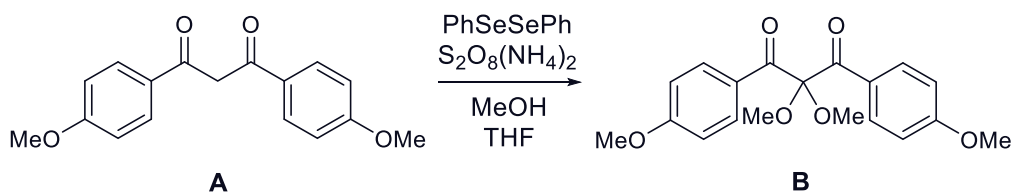
To a solution of **A** (2.68 g, 9.4 mmol, 1.0 eq.) and diphenyl diselenide (1.47 g, 4.7 mmol, 0.5 eq.) in MeOH (100 mL) and dried THF (100 mL) was added ammonium peroxydisulfate (4.3 g, 18.8 mmol, 2.0 eq.). The resulting mixture was refluxed at 75°C overnight. The reaction mixture was poured into iced water, extracted with CHCl$_3$, dried with MgSO$_4$, and filtered. After evaporation of the solvent, 4.93 g (crude) of **B** as yellow oil.
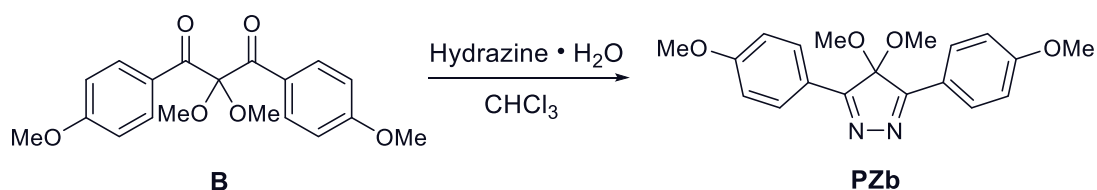
To a solution of **B** (4.93 g) in CHCl$_3$ (75 mL) was added hydrazine hydrate (0.87 g, 17.2 mmol, 1.2 eq.). The mixture was refluxed for 12h, chilled, and added 1M HCl aq. After brief stirred, filtration, extracted with NaHCO$_3$ aq. (15 mL × 3), dried with MgSO$_4$, and filtered. After evaporation of the solvent, crude material was obtained. ^{1}H NMR (400 MHz, CDCl$_3$) of **PZb**: δ 3.05 (s, 6H), 3.89 (s, 6H), 7.01 (m, 4H), 8.22 (m, 4H)

A Typical Procedure II
(**Method B:** *N,N'*-carbonyl diimidazole → **PZk–n**)
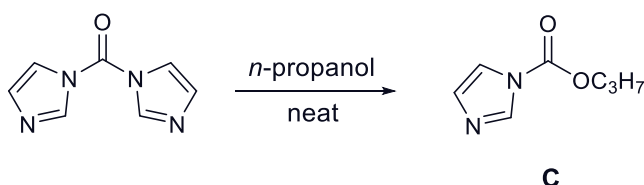
A 100 mL flask was charged with *N,N'*-carbonyl diimidazole (3.00 g, 18.5 mmol, 1.0 eq.) and *n*-propanol (4.2 mL, 56.0 mmol, 3.0 eq.). After stirring the reaction mixture for 9h at room temperature. The solution was extracted with water and chloroform, and organic layer was dried with MgSO$_4$. After filtration and evaporation, **C** (crude) was obtained.
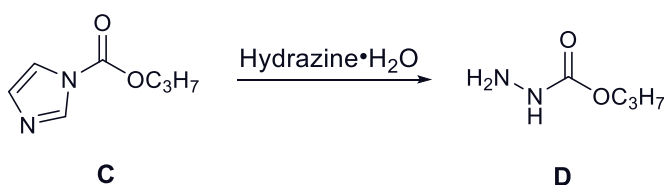
A solution of **C** and hydrazine hydrate (1.1 mL, 22.7 mmol) was refluxed at 100°C for 28h. After the reaction was completed, MgSO$_4$ was added to the reaction mixture, filtered, evaporated, and then **D** (crude) was obtained.
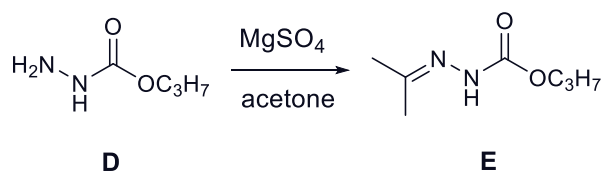
D (crude) was stirred with MgSO$_4$ (3.20 g) in acetone (80 mL) at room temperature for 22h under dry nitrogen. The crude reaction mixture was filtered and concentrated to give **E** as pale yellow oil.
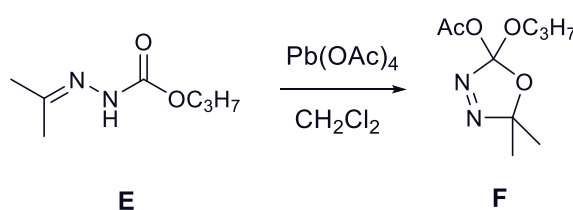
The solution of **E** (3.12 g, crude) in CH$_2$Cl$_2$ (40 mL) was added over 30min to the flask charged with lead tetraacetate (5.94 g, 13.4 mmol) in CH$_2$Cl$_2$ (48 mL) at 0°C under dry nitrogen. After the addition, the solution was kept in the ice bath for 2h and then at room temperature overnight. After filtration through celite, the solution was washed with 10% NaHCO$_3$ aq (20 mL × 4) and organic layer was dried with MgSO$_4$. After filtration and evaporation, yellow oil containing desired oxazoline **F** was obtained.

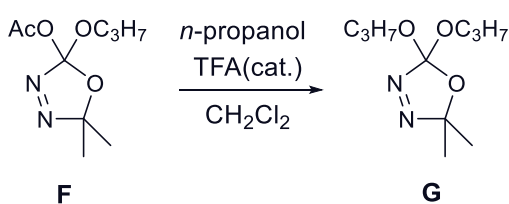A solution of **F** (2.93 g, crude) and *n*-propanol (3.00 mL) in dried CH$_2$Cl$_2$ (20 mL) was acidified with catalytic trifluoroacetic acid (0.0087 mL). After refluxing for 17h under dry nitrogen, the solution was extracted with 10% NaHCO$_3$ aq. (20 mL × 3). Separation of the organic layer, drying with MgSO$_4$, and filtration resulted in a solution of the desired oxadiazoline **G** in CH$_2$Cl$_2$. Evaporation of the solvent and purification of the residue by column

chromatography on SiO$_2$ (hexane / EtOAc = 10 / 1 (v/v)) afforded **G** (2.37 g, 5 step: 59%) as colorless oil. R_f = 0.60 (hexane / EtOAc = 10 / 1 (v/v)); ^{1}H NMR (400 MHz, CDCl$_3$): δ 0.94 (t, J = 7.3 Hz, 6H), 1.53 (s, 6H), 1.64 (sixt, J = 7.2 Hz, 4H), 3.56–3.72 (m, 4H).
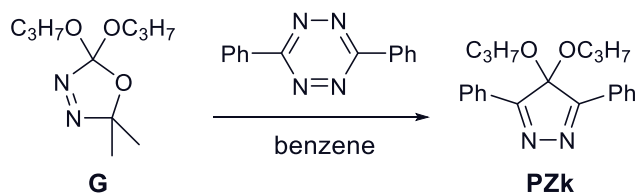
The pressure-resistant test tube was charged with 3,6-diphenyl-tetrazine (0.509 g, 2.14 mmol, 1.0 eq.) and the solution of **G** (0.462 g, 2.14 mmol, 1.0 eq.) in dried benzene (5.15 mL). The reaction mixture was stirred at 120 °C overnight under dry nitrogen and chilled. Evaporation of the solvent and purification of the residue by column chromatography on SiO$_2$ (hexane / EtOAc = 10 / 1 (v/v)) afforded **PZk** as yellow solid. R_f = 0.20 (hexane / EtOAc = 10 / 1 (v/v)); ^{1}H NMR (400 MHz, CDCl$_3$): δ 0.71 (t, J = 7.2 Hz, 6H), 1.47 (sixt, J = 6.6 Hz, 4H), 3.06 (t, J = 6.6 Hz, 4H), 7.48–7.57 (m, 6H), 8.31 (m, 4H).

PZa–n → AZ4a–n (Diels-Alder reactions)
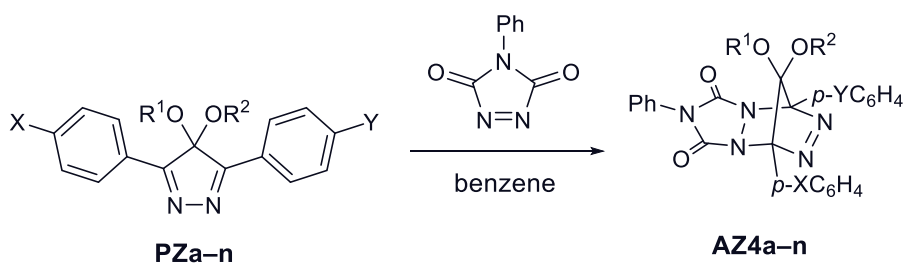
A 50 mL two-necked round-bottom flask was charged with a solution of 4-phenyl-1,2,4-triazoline-3,5-dione(PTAD) (3 eq.) and **PZa–n** (1 eq.) in benzene (25 mL) and heated at 50°C for 2 days under nitrogen atmosphere. After removing the solvent using evaporator, azoalkane **6a–n** as yellow solid was isolated by column chromatography on SiO$_2$ and recrystallization from MeOH.

4-phenyl-1,2,4-triazoline-3,5-dione (PTAD)[16]
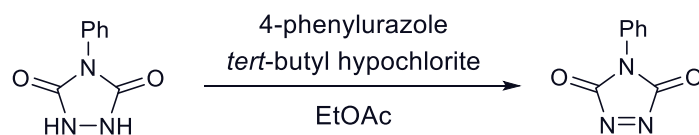
A 50 mL three-necked round-bottom flask was charged with 10 mL of ethyl acetate and 3.99 g (0.023 mol) of 4-phenylurazole. 2.3 mL (0.020 mol) of *tert*-butyl hypochlorite was added to the flask over 40 minutes under dry nitrogen, the reaction mixture was being maintained close to room temperature with a cold-water bath. After addition was completed, the resulting suspension is stirred for 1h at room temperature. The solvent was removed with evaporator and sublimated under vacuum to afford 1.34 g (38%) of the triazoline as carmine-red crystals. ^{1}H NMR (500 MHz, CDCl$_3$) δ 7.58–7.54 (m, 2H), 7.51–7.46 (m, 3H); HRMS (APCI) Calcd for [M+H]$^+$ C$_8$H$_6$O$_2$N$_3$ 176.0455, found 176.0456

Azoalkane **AZ4b.**

AZ4b
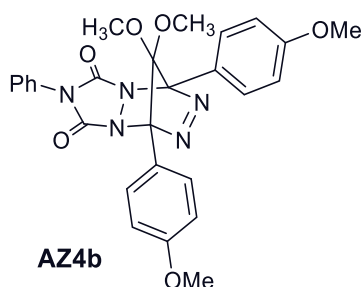
¹H NMR (400 MHz, d6-benzene): δ 2.53 (s, 3 H), 2.91 (s, 3 H), 3.25 (s, 6 H), 6.76–6.83 (m, 3 H), 6.88 (m, 4 H), 7.15 (m, 2 H), 8.29 (m, 4 H). **¹³C NMR** (100 MHz, d6-benzene): δ 161.24, 154.83, 130.40, 130.18, 128.65, 128.32, 125.85, 120.59, 113.93, 108.79, 99.51, 54.41, 51.91, 51.87.
ESI-MS found: 533.21399, calc. for $C_{27}H_{29}O_6N_6$ ($[M+NH_4]^+$): 533.21431.

Azoalkane **AZ4c** (*p*-Me-**AZ**).

AZ4c
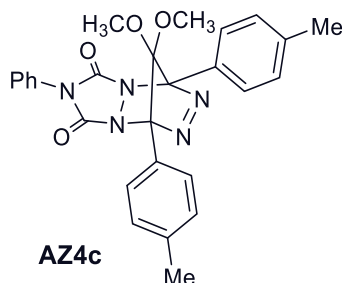
¹H NMR (400 MHz, d6-benzene): δ 2.06 (s, 6 H), 2.49 (s, 3 H), 2.87 (s, 3H), 6.78 (m, 3 H), 7.12 (m, 5 H), 8.28 (d, J = 8.4 Hz, 4 H). **¹³C NMR** (100 MHz, d6-benzene): δ 154.8, 139.9, 130.9, 129.0, 128.8, 128.6, 128.3, 128.1, 125.9, 125.8, 109.2, 99.7, 52.0, 51.9, 20.9.
ESI-MS found: 501.22421, calc. for $C_{27}H_{29}O_4N_6$ ($[M+NH_4]^+$): 501.22448.

Azoalkane **AZ4d** (*p*-F-**AZ**).

AZ4d
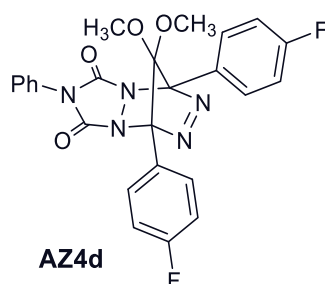
¹H NMR (400 MHz, d1-chloroform): δ 2.83 (s, 3 H), 3.17 (s, 3 H), 7.30 (m, 9 H), 8.13 (m, 4 H).

¹³C NMR (100 MHz, d1-chloroform): δ 165.4, 162.9, 130.6, 130.5, 130.4, 129.1, 128.9, 125.6, 123.8, 123.7, 115.9, 115.7, 109.1, 98.9, 52.8, 52.7.

ESI-MS found: 509.17398, calc. for C25 H23 O4 N6 F2 ([M+Na]⁺): 509.17434.

Azoalkane **AZ4e** (*p*-Cl-**AZ**).

AZ4e
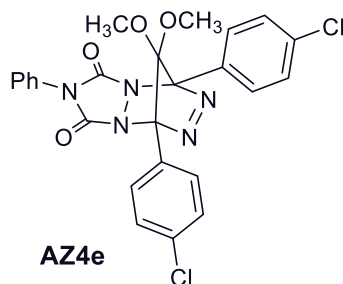
¹H NMR (400 MHz, d6-benzene): δ 2.27 (s, 3 H), 2.65 (s, 3 H), 6.79 (m, 3 H), 7.12 (d, *J* = 7.2 Hz, 2 H), 7.20 (d, *J* = 8.4 Hz, 4 H), 8.04 (d, *J* = 8.8 Hz, 4 H). **¹³C NMR** (100 MHz, d6-benzene): δ 154.58, 136.43, 130.62, 130.09, 128.77, 128.68, 128.34, 127.98, 126.98, 125.61, 109.33, 99.08, 51.95, 51.90.

ESI-MS found: 546.07019, calc. for C25 H19 O4 N5 Cl2 Na ([M+Na]⁺): 546.07063.

Azoalkane **AZ4f** (*p*-Br-**AZ**).

AZ4f
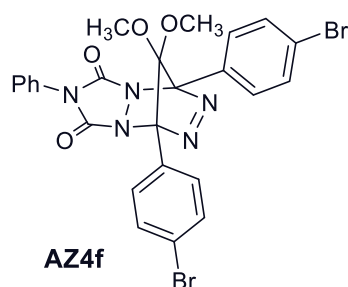
¹H NMR (400 MHz, d1-chloroform): δ 2.83 (s, 3 H), 3.17 (s, 3 H), 7.28-7.39 (m, 5 H), 7.69 (m, 4 H), 8.00 (m, 4 H). **¹³C NMR** (100 MHz, d1-chloroform): δ 154.6, 131.9, 130.3, 130.1, 129.1, 128.9, 128.3, 126.9, 125.5, 125.1, 109.4, 99.0, 52.9, 52.8.
ESI-MS found: 629.01465, calc. for C25 H23 O4 N6 Br2 ([M+NH₄]⁺): 629.01420.

Azoalkane **AZ4g** (*p*-CN-**AZ**).

AZ4g
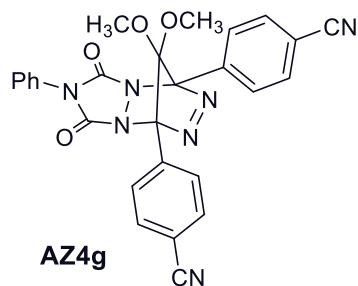
¹H NMR (400 MHz, d1-chloroform): δ 2.82 (s, 3 H), 3.17 (s, 3 H), 7.26–7.28 (m, 2 H), 7.34-7.41 (m, 3 H), 7.87 (m, 4 H), 8.26 (m, 4 H). **¹³C NMR** (100 MHz, d1-chloroform): δ 154.49, 132.70, 132.35, 130.01, 129.38, 129.27, 129.23, 125.51, 118.07, 114.65, 110.53, 98.9, 53.11, 53.08.
ESI-MS found: 528.13959, calc. for C27 H19 O4 N7 Na ([M+Na]⁺): 528.13907.

Asymmetric azoalkane **AZ4h** (*p*-MeO, *p*-Br-**AZ**).

AZ4h
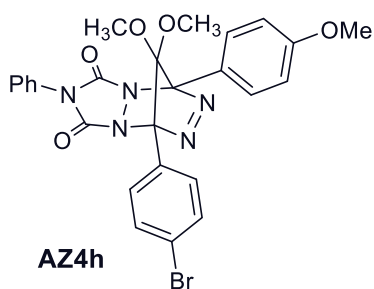
¹H NMR (400 MHz, d6-benzene): δ 2.39 (s, 3 H), 2.76 (s, 3 H), 3.23 (s, 3H), 6.78 (m, 3 H), 6.87 (d, *J* = 8.8 Hz, 2 H), 7.13 (m, 2 H), 7.35 (d, *J* = 8.8 Hz, 2 H), 8.01 (d, *J* = 8.8 Hz, 2 H), 8.26 (d, *J* = 8.8 Hz, 2 H).

ESI-MS found: 581.11493, calc. for C26 H26 O5 N6 Br ([M+NH₄]⁺): 581.11426.

2.5   Supplementary material

Azoalkane precursor: PZa–j (Method A), PZk–n (Method B) *: TMS, H_2O, CH_2Cl_2
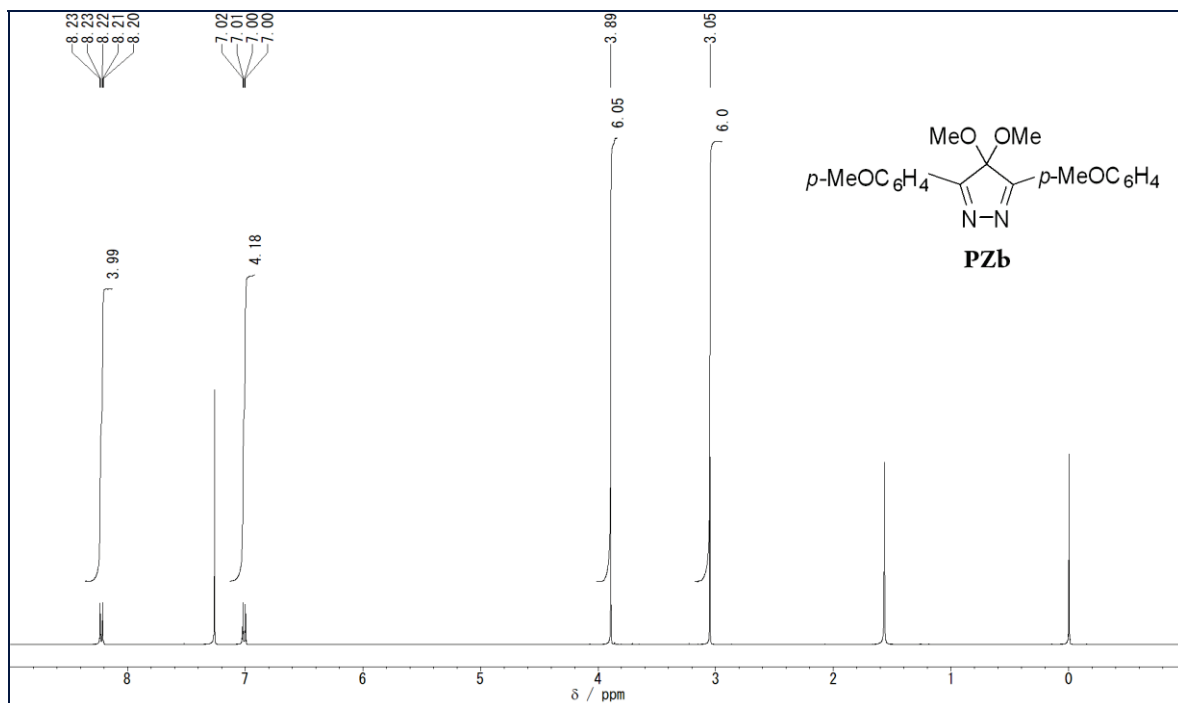
Figure 17. ^1H NMR (400 MHz, CDCl$_3$) spectra of **PZb**.
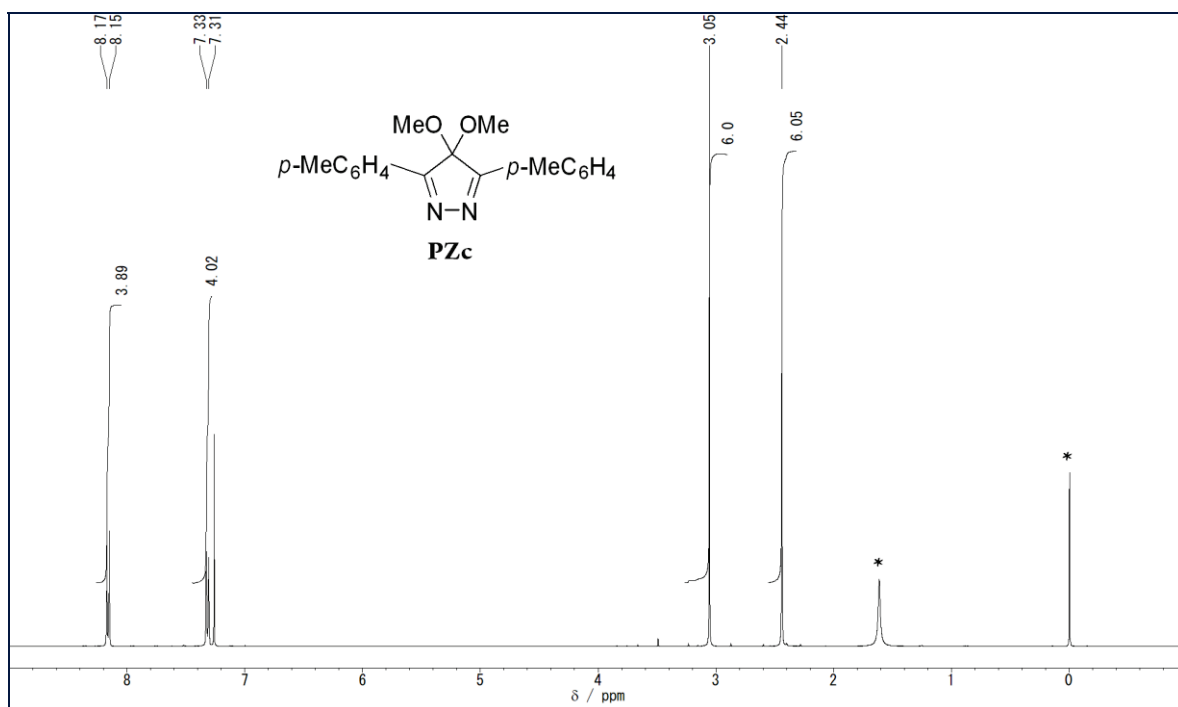
Figure 18. ^1H NMR (400 MHz, CDCl$_3$) spectra of **PZc**.
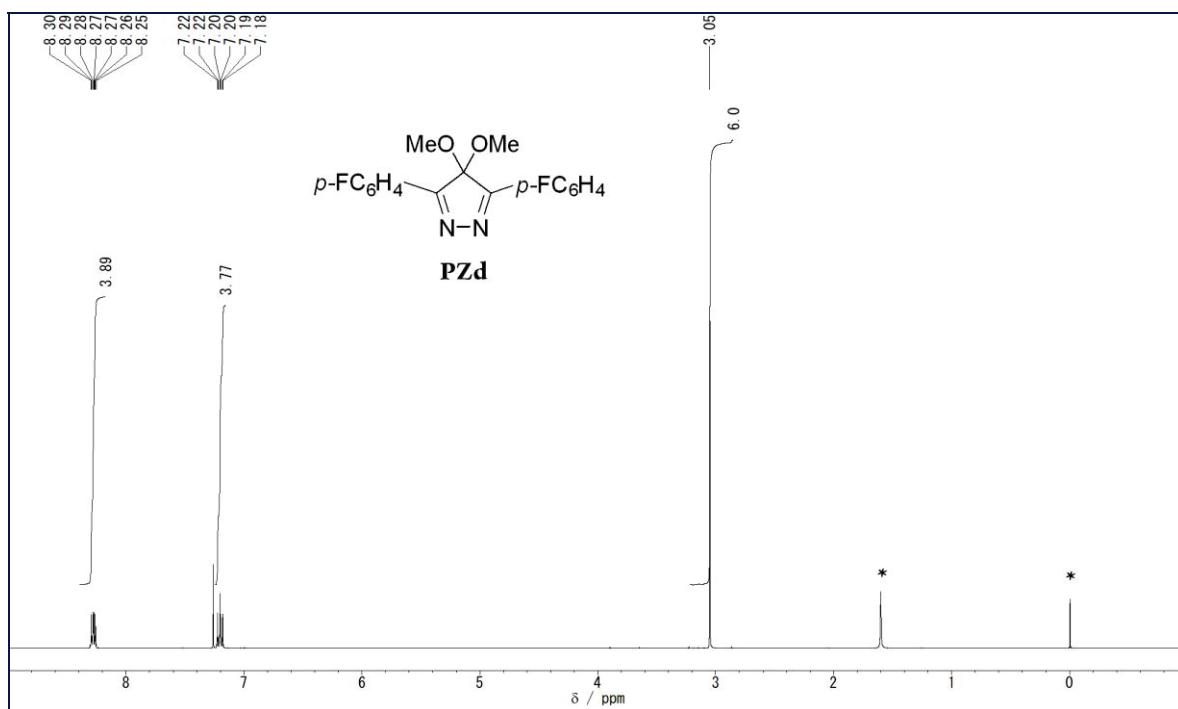
Figure 19. ^{1}H NMR (400 MHz, CDCl$_3$) spectra of **PZd**.
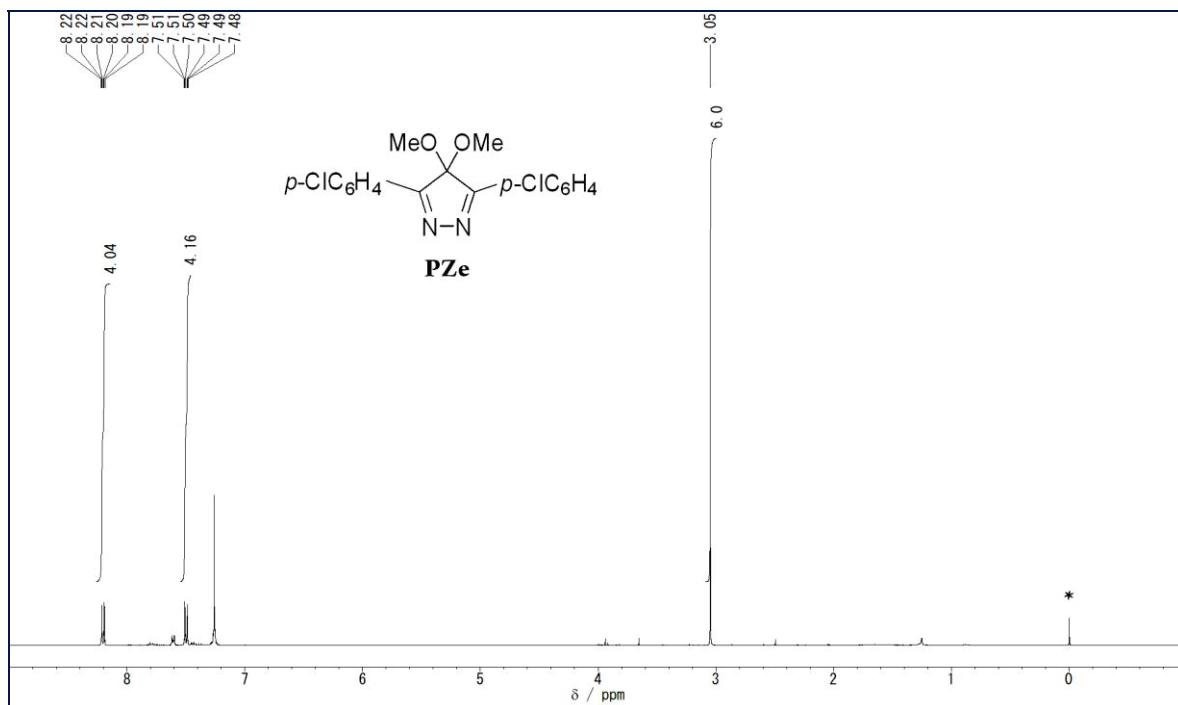
Figure 20. ^{1}H NMR (400 MHz, CDCl$_3$) spectra of **PZe** (impurity).
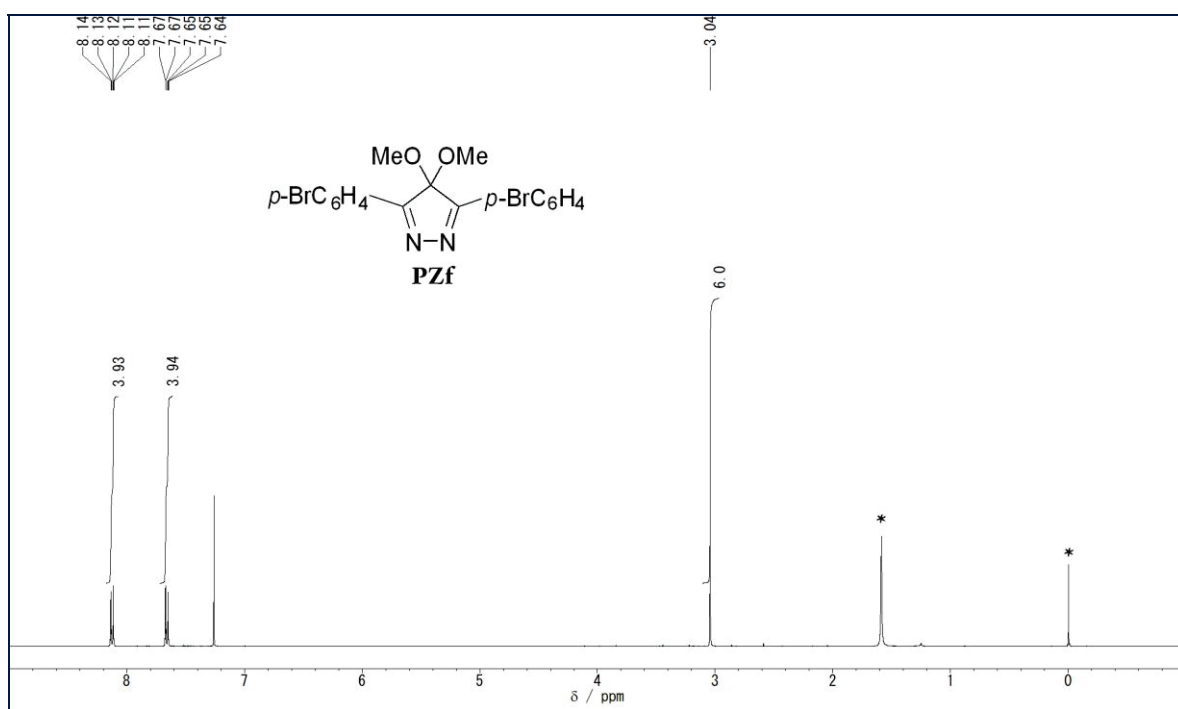
Figure 21. ^{1}H NMR (400 MHz, CDCl$_3$) spectra of **PZf**.
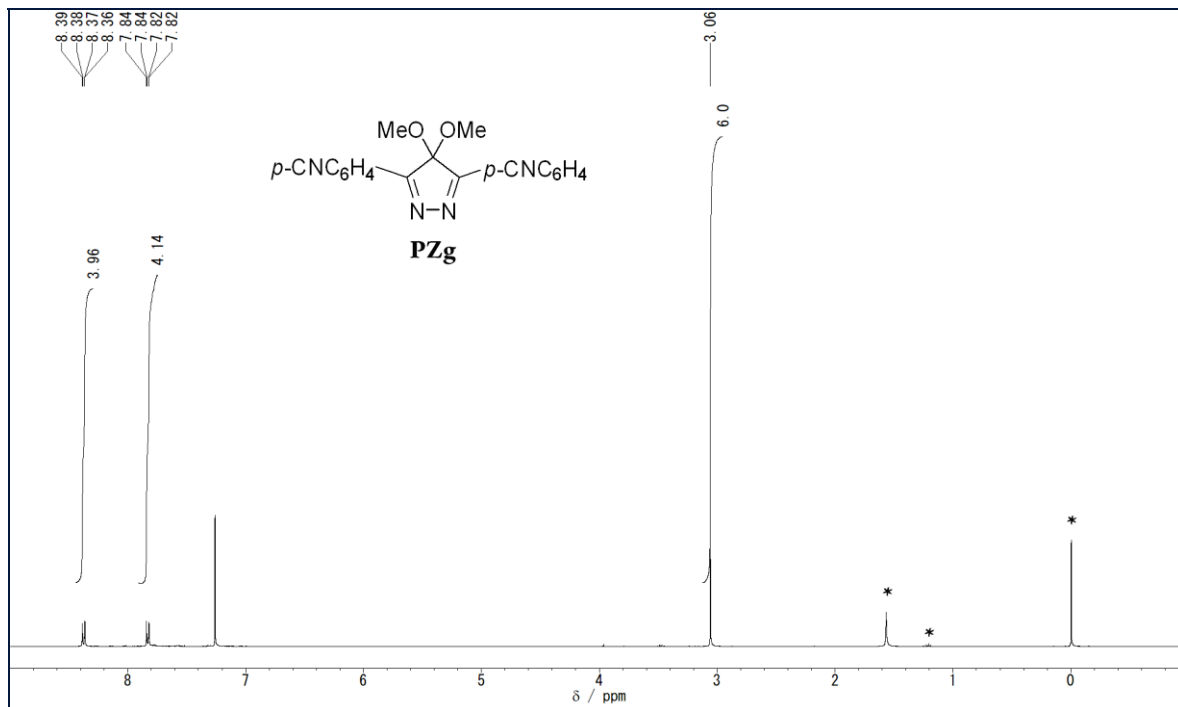
Figure 22. ^{1}H NMR (400 MHz, CDCl$_3$) spectra of **PZg**.
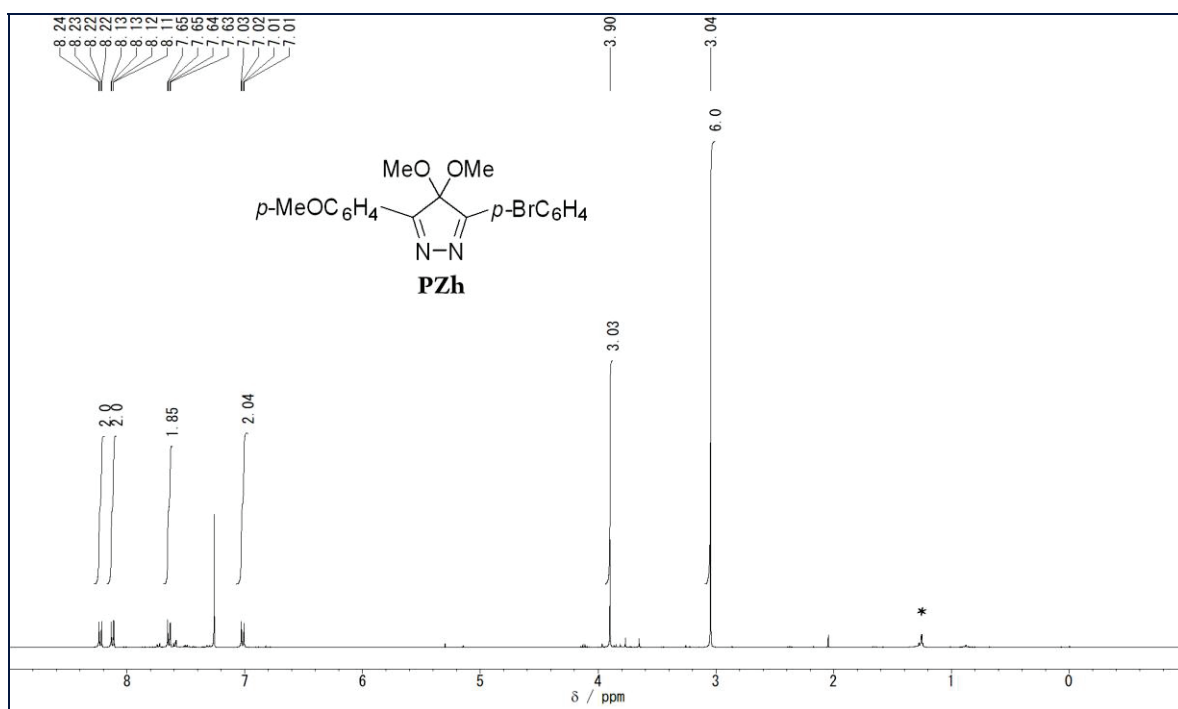
Figure 23. ^{1}H NMR (400 MHz, CDCl$_3$) spectra of **PZh**.
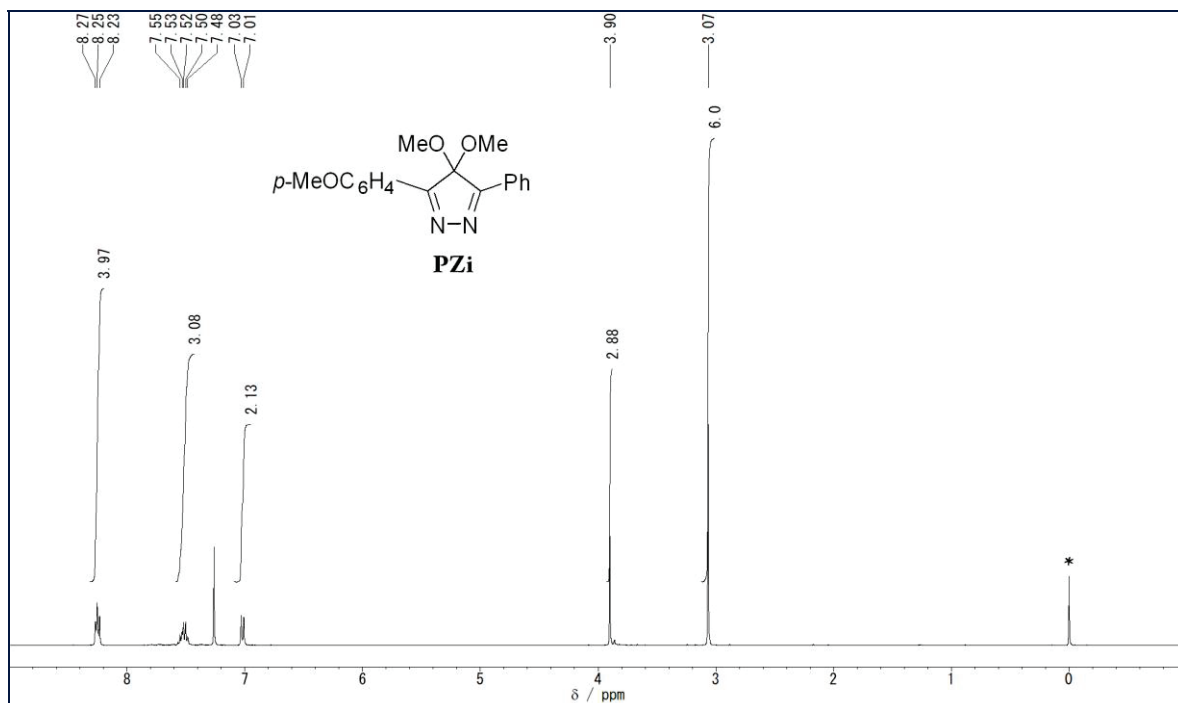
Figure 24. ^{1}H NMR (400 MHz, CDCl$_3$) spectra of **PZi**.
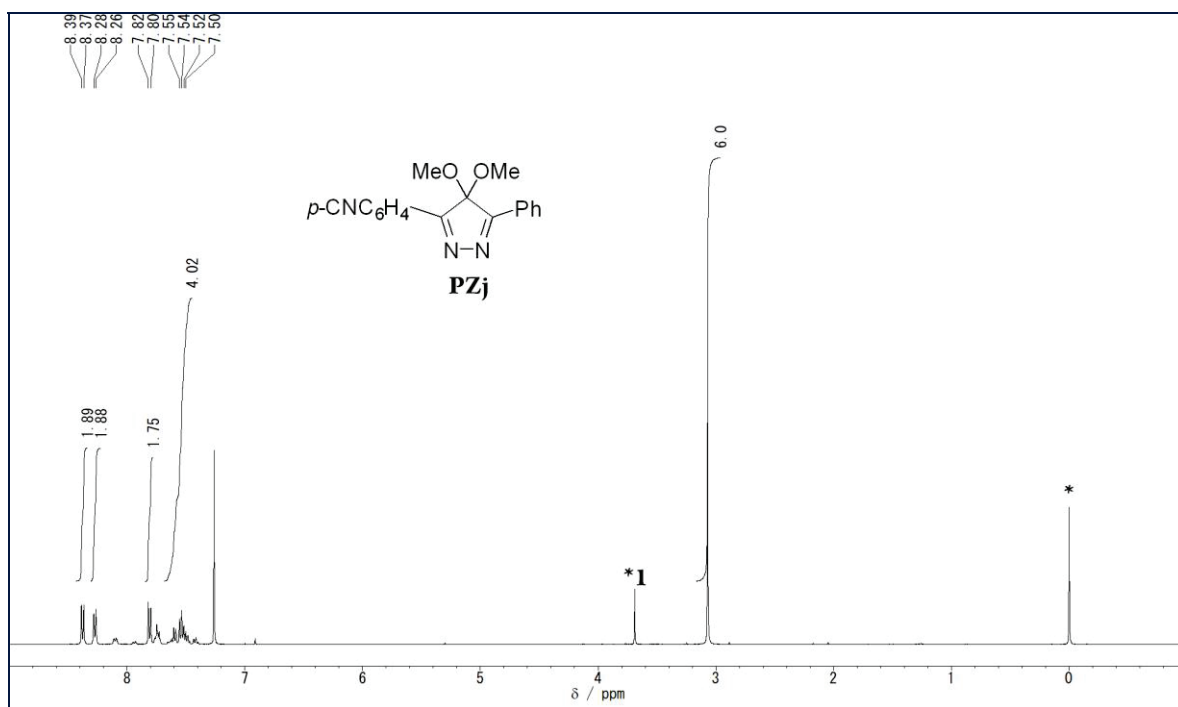
Figure 25. ^{1}H NMR (400 MHz, CDCl$_3$) spectra of **PZj** (impurity).
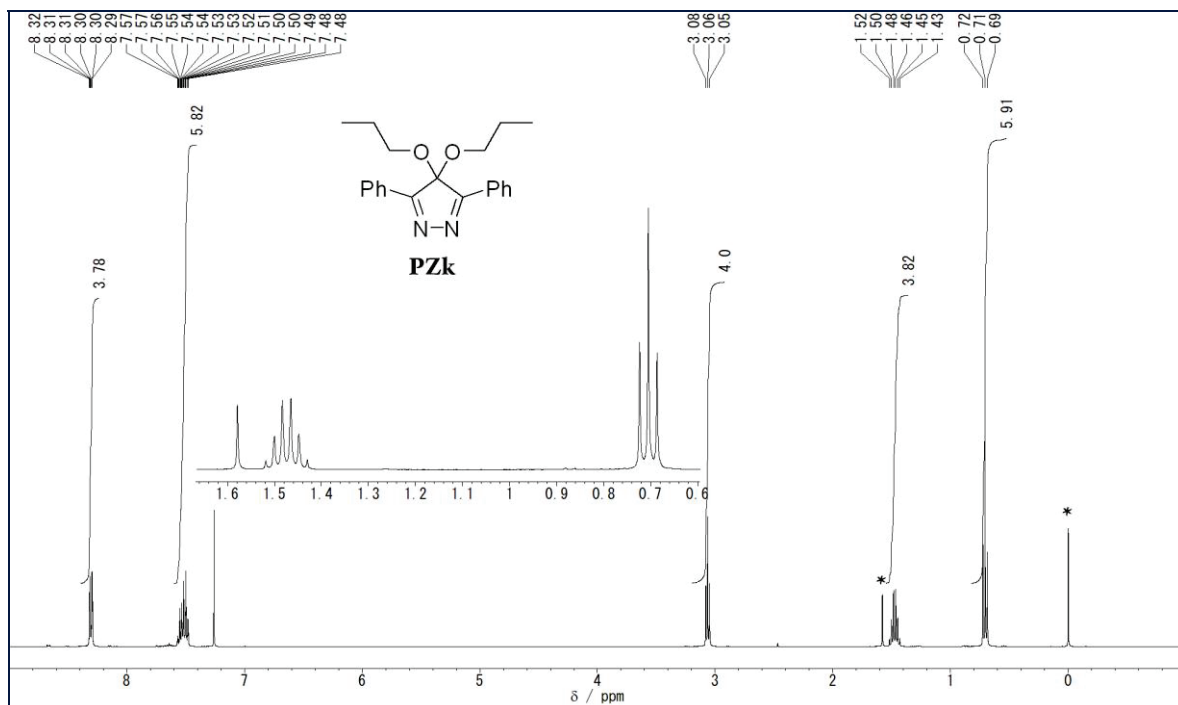
Figure 26. ^{1}H NMR (400 MHz, CDCl$_3$) spectra of **PZk**.
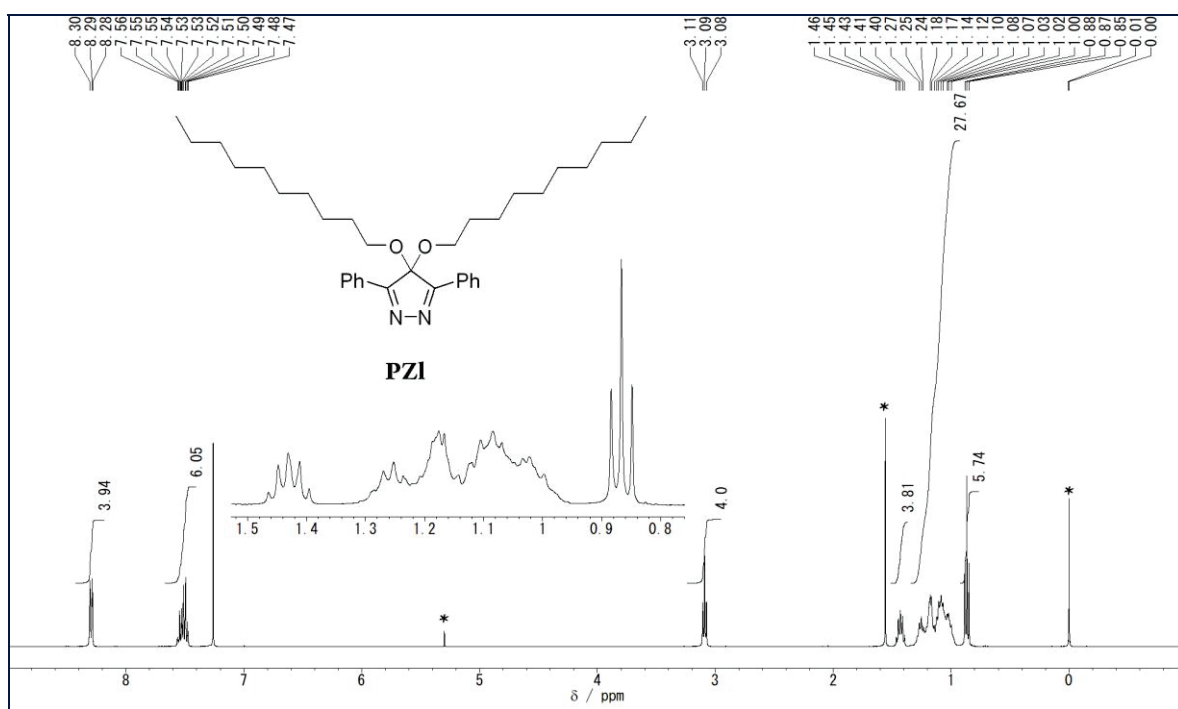
Figure 27. ^{1}H NMR (400 MHz, CDCl$_3$) spectra of **PZl**.
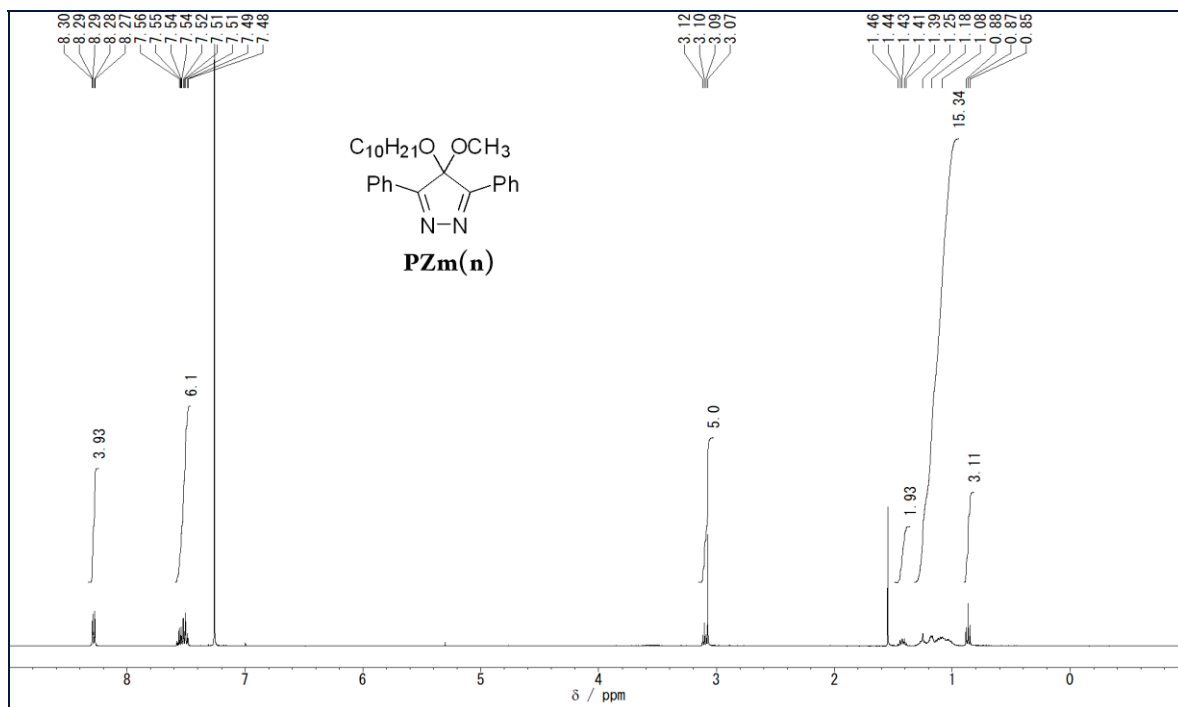
Figure 28. ^{1}H NMR (400 MHz, CDCl$_3$) spectra of **PZm(n)**.
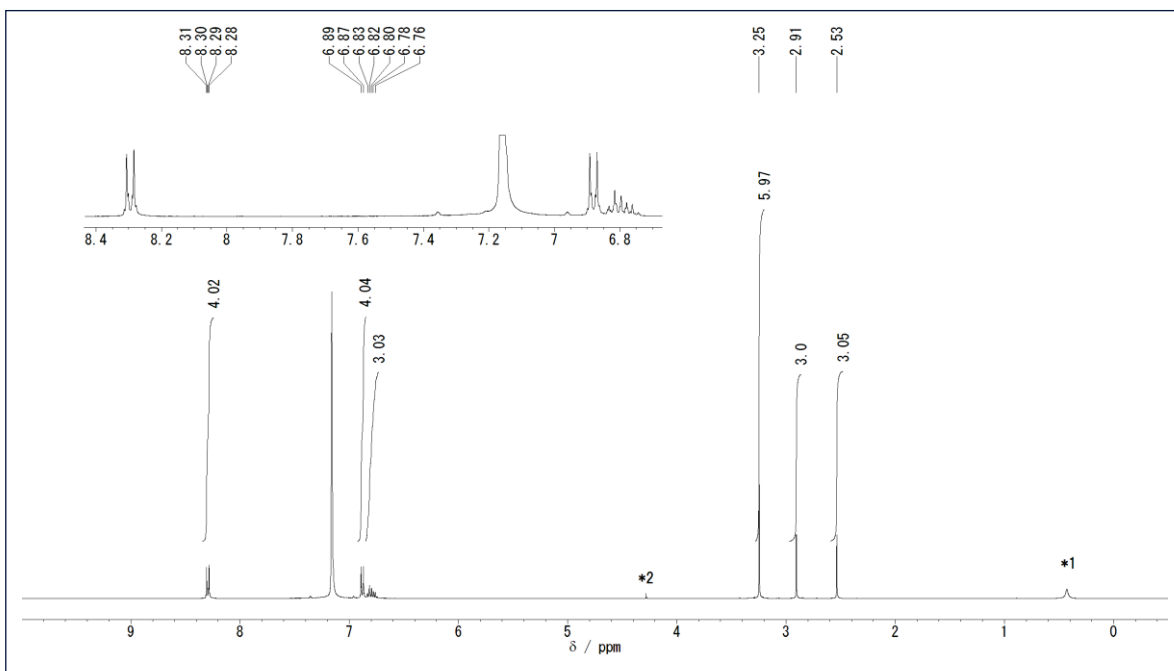
Figure 29. ^{1}H NMR (400 MHz, d6-benzene) spectrum of **AZ4b**. *1: H_2O, *2: dichloromethane.
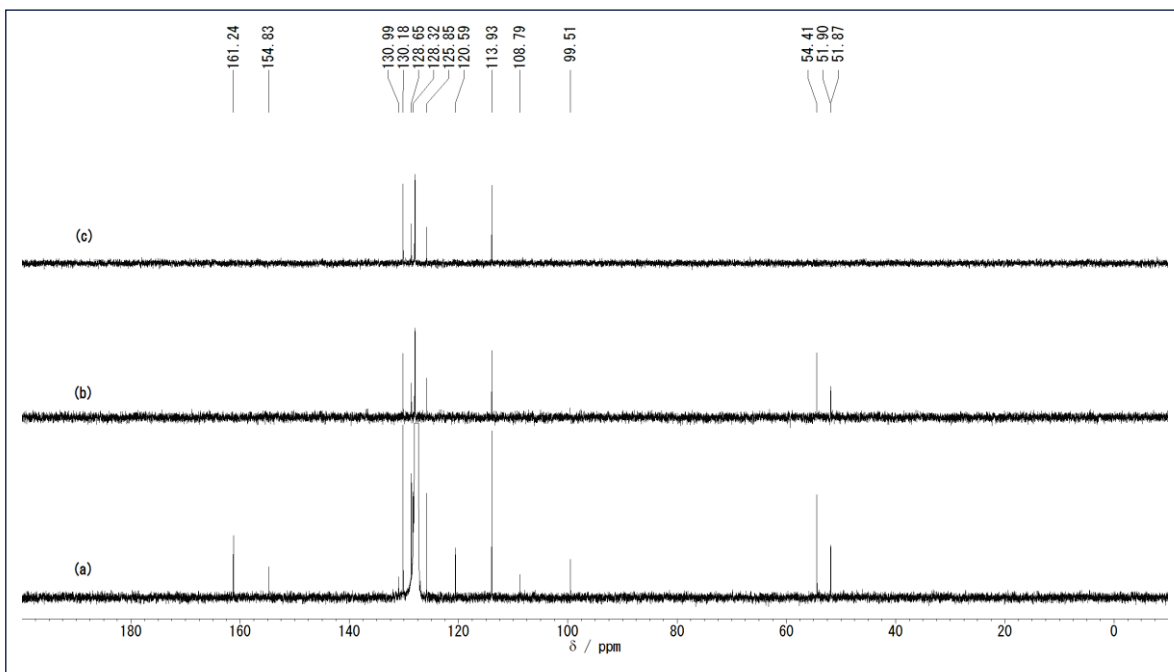
Figure 30. (a) ^{13}C NMR (100 MHz, d6-benzene) spectra of **AZ4b**, (b) DEPT135, (c) DEPT90.

58
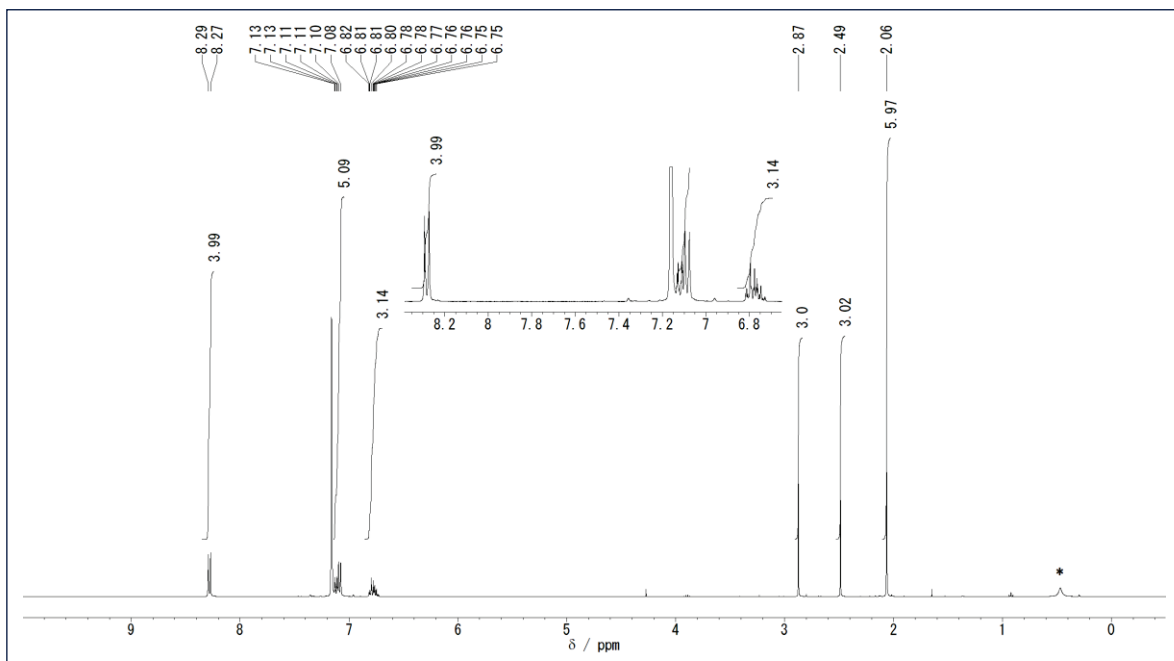
Figure 31. ^{1}H NMR (400 MHz, d6-benzene) spectrum of **AZ4c**. * H_2O
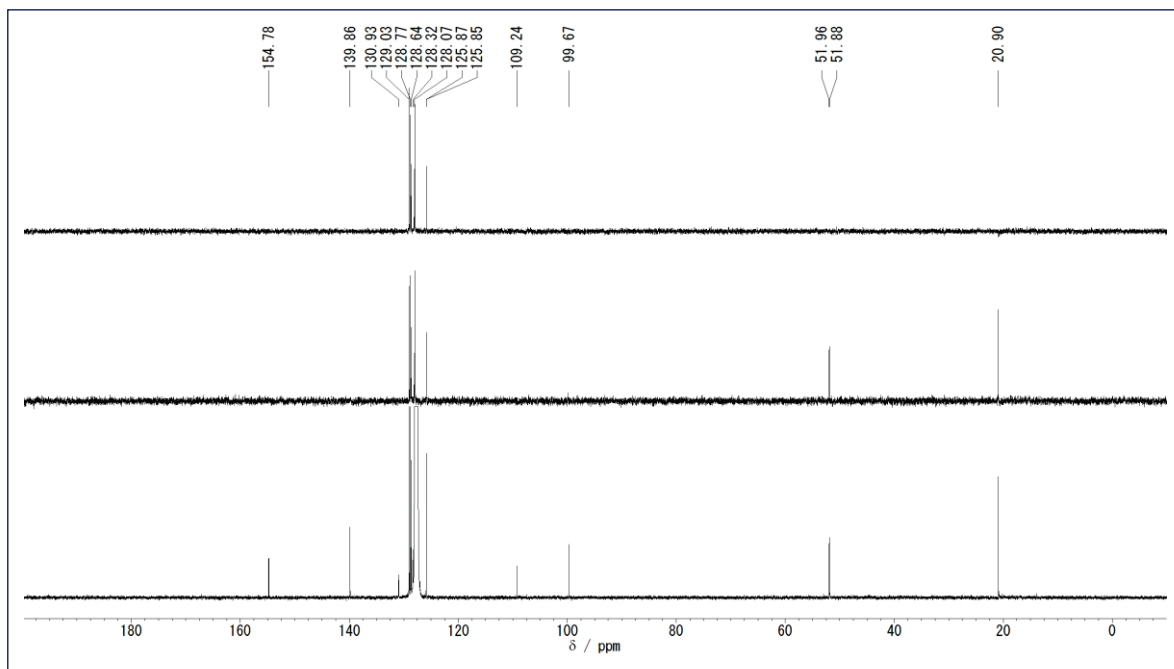
Figure 32. (a) ^{13}C NMR (100 MHz, d6-benzene) spectra of **AZ4c**, (b) DEPT135, (c) DEPT90.

59
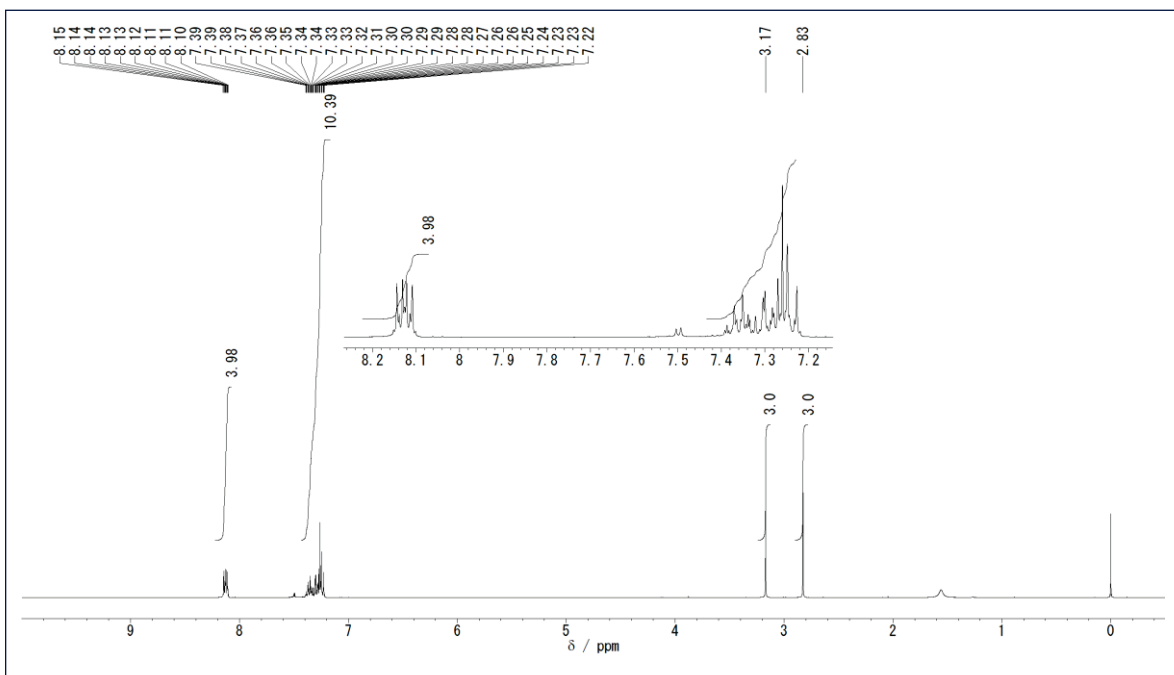
Figure 33. ^{1}H NMR (400 MHz, d1-chloroform) spectrum of **AZ4d**. *1: TMS, *2: H_2O
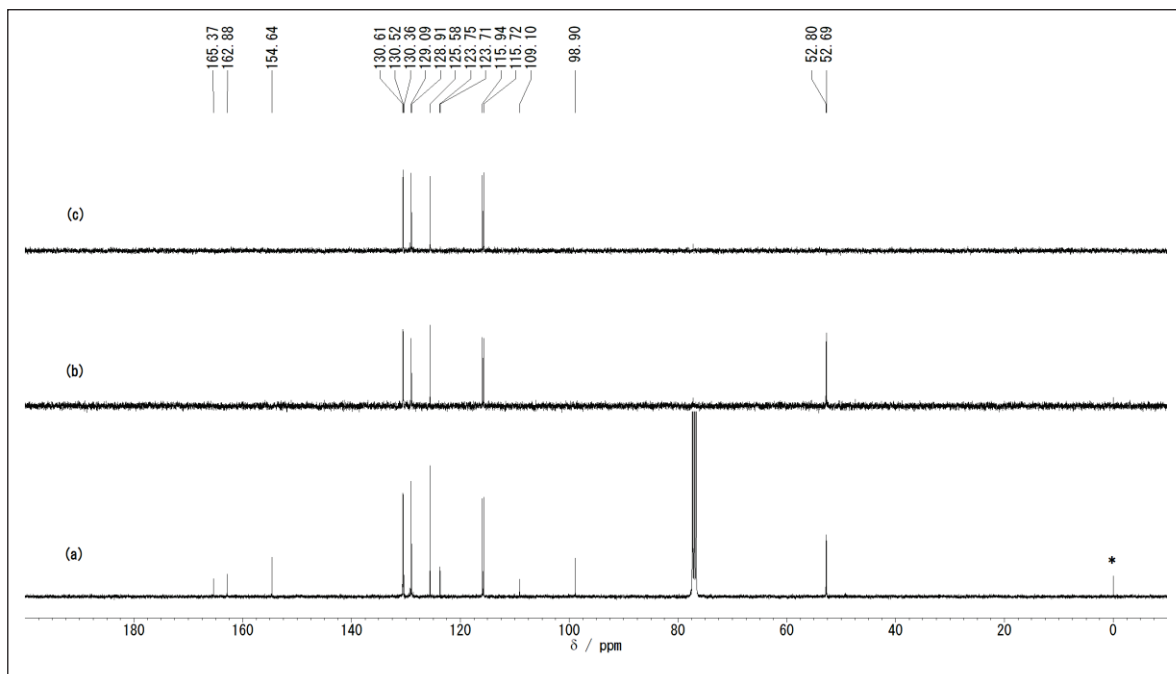
Figure 34. (a) ^{13}C NMR (100 MHz, d1-chloroform) spectra of **AZ4d**, (b) DEPT135 and (c) DEPT90. * TMS

Figure 35. ^{1}H NMR (400 MHz, d1-chloroform) spectrum of **AZ4f**. *1: TMS, *2: H_2O

Figure 36. (a) ^{13}C NMR (100 MHz, d1-chloroform) spectra of **AZ4f**, (b) DEPT135 and (c) DEPT90. * TMS
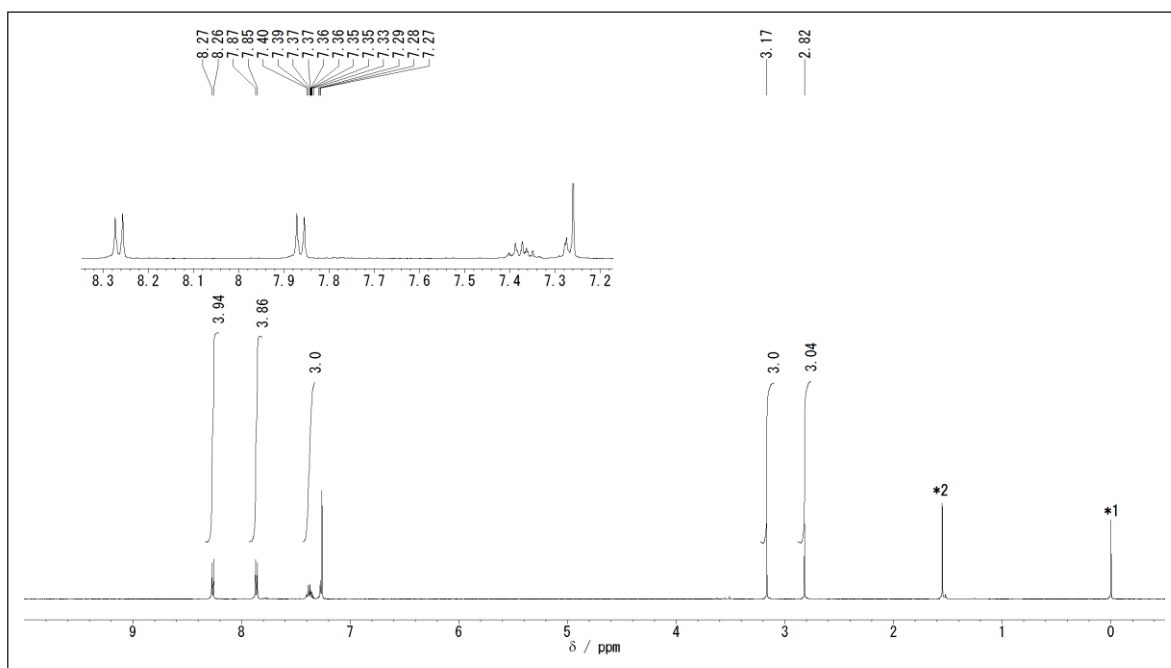
Figure 35. ¹H NMR (400 MHz, d1-chloroform) spectrum of **AZ4g**. *1: TMS, *2: H$_2$O
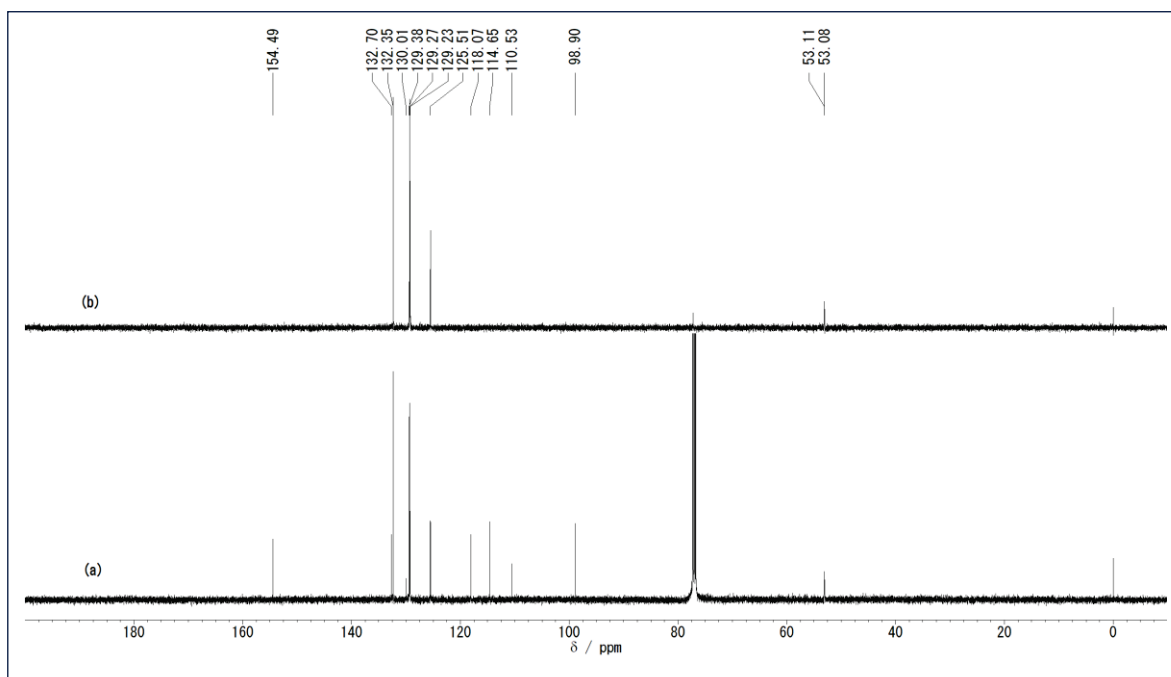
Figure 36. (a) ¹³C NMR (100 MHz, d1-chloroform) spectra of **AZ4g**, (b) DEPT135. * TMS

62
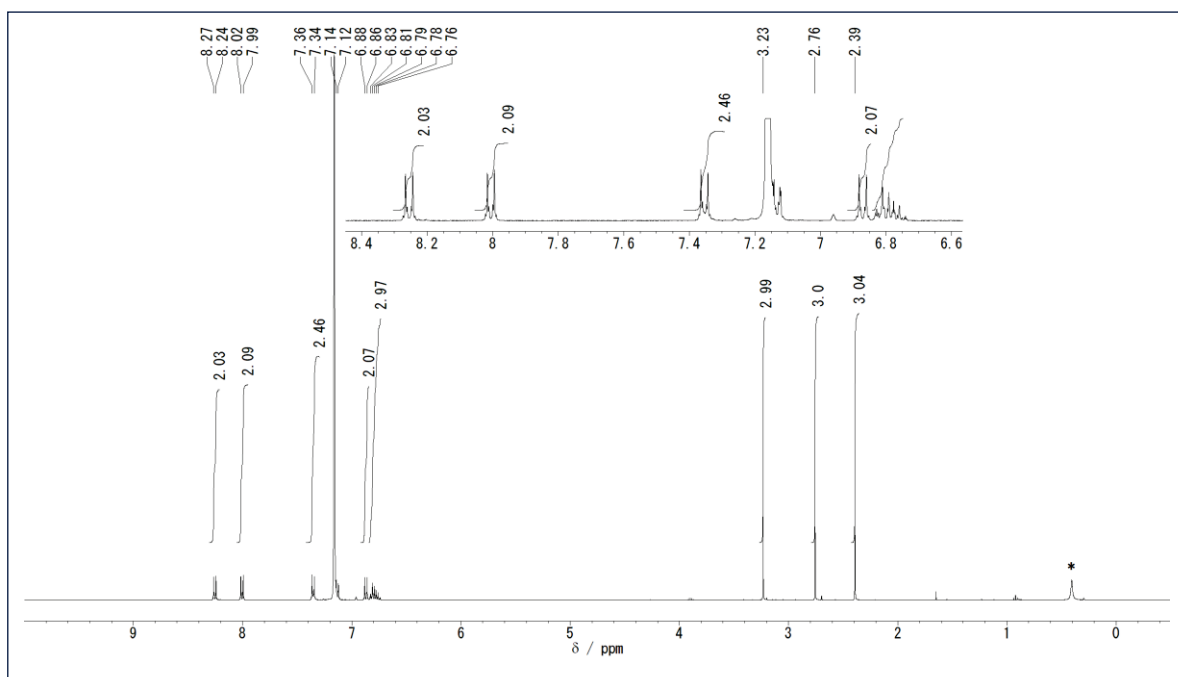
Figure 37. ^{1}H NMR (400 MHz, d6-benzene) spectrum of **AZ4h**. * H_2O

2.6　Reference

(1). Yoshidomi, S.; Mishima, M.; Seyama, S.; Abe, M.; Fujiwara, Y.; Ishibashi, T. Direct Detection of a Chemical Equilibrium between a Localized Singlet Diradical and Its σ-Bonded Species by Time-Resolved UV/Vis and IR Spectroscopy. *Angew. Chem., Int. Ed.* **2017**, *56*, 2984–2988.

(2). (a) Abe, M. Diradicals. *Chem. Rev.* **2013**, *113*, 7011–7088. (b) Abe, M.; Je, J.; Mishima, M. The chemistry of localized singlet 1,3-diradicals (biradicals): from putative intermediates to persistent species and unusual molecules with a π-single bonded character. *Chem. Soc. Rev.* **2012**, *41*, 3808–3820. (c) Abe, M.; Akisaka, R. Is π-Single Bonding (C–π–C) Possible? A Challenge in Organic Chemistry. *Chem. Lett.* **2017**, *46*, 1586–1592.

(3). (a) Abe, M.; Adam, W.; Hara, M.; Hattori, M.; Majima, T.; Nojima, M.; Tachibana, K.; Tojo, S. On the Electronic Character of Localized Singlet 2,2-Dimethoxycyclopentane-1,3-diyl Diradicals: Substituent Effects on the Lifetime. *J. Am. Chem. Soc.* **2002**, *124*, 6540–6541. (b) Abe, M.; Hattori, M.; Takegami, A.; Masuyama, A.; Hayashi, T.; Seki, S.; Tagawa, S. Experimental Probe for Hyperconjugative Resonance Contribution in Stabilizing the Singlet State of 2,2-Dialkoxy-1,3-diyls: Regioselective 1,2-Oxygen Migration. *J. Am. Chem. Soc.* **2006**, *128*, 8008–8014. (c) Nakagaki, T.; Sakai, T.; Mizuta, T.; Fujiwara, Y.; Abe, M. Kinetic Stabilization and Reactivity of π Single-Bonded Species: Effect of the Alkoxy Group on the Lifetime of Singlet 2,2-Dialkoxy-1,3-diphenyloctahydropentalene-1,3-diyls. *Chem. Eur. J.* **2013**, *19*, 10395–10404. (d) Ye, J.; Fujiwara, Y.; Abe, M. Substituent effect on the energy barrier for σ-bond formation from π-single-bonded species, singlet 2,2-dialkoxycyclopentane-1,3-diyls. *Beilstein. J. Org. Chem.* **2013**, *9*, 925–933. (e) Abe, M.; Furunaga, H.; Ma, D.; Gagliardi, L.; Bodwll, G. J. Stretch Effects Induced by Molecular Strain on Weakening σ-Bonds: Molecular Design of Long-Lived Diradicals (Biradicals). *J. Org. Chem.* **2012**, *77*, 7612–7619. (f) Harada, Y.; Wang, Z.; Kumashiro, S.; Hatano, S.; Abe, M. Extremely Long Lived Localized Singlet Diradicals in a Macrocyclic Structure: A Case Study on the Stretch Effect. *Chem. Eur. J.* **2018**, *24*, 14808–14815. (g) Abe, M.; Adam, W.; Heidenfelder, T.; Nau, W. M.; Zhang, X. Intramolecular and Intermolecular Reactivity of Localized Singlet Diradicals: The Exceedingly Long-Lived 2,2-Diethoxy-1,3-diphenylcyclopentane-1,3-diyl. *J. Am. Chem. Soc.* **2000**, *122*,

2019–2026.

(4). Abe, M.; Kubo, E.; Nozaki, K.; Matsuo, T.; Hayashi, T. An Extremely Long-Lived Singlet 4,4-Dimethoxy-3,5-diphenylpyrazolidine-3,5-diyl Derivative: A Notable Nitrogen-Atom Effect on Intra- and Intermolecular Reactivity. *Angew. Chem., Int. Ed.* **2006,** *45,* 7828–7831; *Corrigendum, idem, ibid,* **2012,** *51,* 11911.

(5). Nakamura, T.; Gagliardi, L.; Abe, M. Computational study of the cooperative effects of nitrogen and silicon atoms on the singlet–triplet energy spacing in 1,3-diradicals and the reactivity of their singlet states. *J. Phys. Org. Chem.* **2010,** *23,* 300–307.

(6). Abe, M.; Ishihara, C.; Tagegami, A. Theoretical Calculations of the Effects of 2-Heavier Group 14 Element and Substituents on the Singlet-Triplet Energy Gap in Cyclopentane-1,3-diyls and Computational Prediction of the Reactivity of Singlet 2-Silacyclopentane-1,3-diyls. *J. Org. Chem.* **2004,** *69,* 7250–7255.

(7). Abe, M.; Adam, W.; Borden, W. T.; Hattori, M.; Hrovat, D. A.; Nojima, M.; Nozaki, K.; Wirz, J. Effects of Spiroconjugation on the Calculated Singlet–Triplet Energy Gap in 2,2-Dialkoxycyclopentane-1,3-diyls and on the Experimental Electronic Absorption Spectra of Singlet 1,3-Diphenyl Derivatives. Assignment of the Lowest-Energy Electronic Transition of Singlet Cyclopentane-1,3-diyls. *J. Am. Chem. Soc.* **2004,** *126,* 574–582.

(8). (a) Brown, H. C.; Okamoto, Y. Electrophilic Substituent Constants. *J. Am. Chem. Soc.* **1958,** *80,* 4979–4987. (b) Jeffe, H. H. A Reexamination of the Hammett Equation. *Chem. Rev.* **1953,** *53,* 191–261.

(9). Creary, X. Super Radical Stabilizers. *Acc. Chem. Res.* **2006,** *39,* 761–771.

(10). Reichardt, C. Empirical Parameters of Solvent Polarity as Linear Free-Energy Relationships. *Angew. Chem., Int. Ed.* **1965,** *4,* 29–40.

(11). Tanner, D. D.; Koppula, S.; Kandanarachchi, Pramod. Mechanism of the Solution-Phase Reaction of Alkyl Sulfides with Atomic Hydrogen. Reduction via a 9-S-3 Radical Intermediate. *J. Org. Chem.* **1997,** *62,* 4210–4215.

(12). Salem, L.; Rowland, C. The Electronic Properties of Diradicals. *Angew. Chem., Int. Ed. Engl.* **1972,** *11,* 92–111.

(13). Creary, X.; Mehrsheikh-Mohammadi, M. E.; McDonald, S. A comparison of the radical-stabilizing ability of aromatic groups. $\gamma^{\bullet}$ values for aromatic groups. *J. Org. Chem.* **1989,** *54,* 2904–2910.

(14). Laurence, C.; Nicolet, P.; Dalati, M. T. The Empirical Treatment of Solvent-Solute Interactions: 15 Years of π^*. *J. Phys. Chem.* **1994,** *98,* 5807–5816.

(15). (a) Evans, M. G.; Polanyi, M. Some applications of the transition state method to the calculation of reaction velocities, especially in solution. *Trans. Faraday. Soc.* **1935,** *31,* 875–894. (b). Eyring, H. The Activated Complex in Chemical Reactions. *J. Chem. Phys.* **1935,** *107,* 107–115.

(16). Organic Syntheses. Collective Volume 6, ed. by W. E. Noland, John Wiley & Sons, New York, **1988,** 936–940.

Chapter 3

Alkoxy-group Migration Reaction (slow process)

3.1 Photodenitrogenation of azoalkane

As mentioned at the beginning of Chapter 2, two photolysates isolated in the ratio 7 to 3 (> 95% conversions) were alkoxy-group migrated species **MG$_{CO}$4aa** and **MG$_C$4aa** in the photodenitrogenation of the azoalkane **AZ4a** ($\lambda_{max} \approx 416$ nm, $\varepsilon \approx 455$ L mol^{-1} cm^{-1}) in a nonpolar solvent such as toluene or benzene.[1,2] To obtain further information about the reaction mechanism of the alkoxy-group migration reaction of singlet diradicals, S-**DR4**, the photodenitrogenation of azoalkane, **AZ4a**, was conducted using 416 nm irradiation in polar aprotic solvent such as acetonitrile. The solvent was used after thorough dehydration (for the detailed operation see the experimental section in Chapter 3.8).[3] After the disappearance of **AZ4a** the photolysate was analyzed by ^{1}H NMR to identify the products and determine the chemical yields using triphenylmethane as an internal standard (Table 3). In contrast to the photoreaction in non-polar aprotic solvent toluene, surprisingly, the major product of the photolysis was not the alkoxy-group migrated species **MG$_{CO}$4aa** (25% yield), but another alkoxy-group migrated species **MG$_C$4aa** (63% yield) (entries 2,4 in Table 3).

Table 3. Product distribution for photodenitrogenation of **AZ4a**.
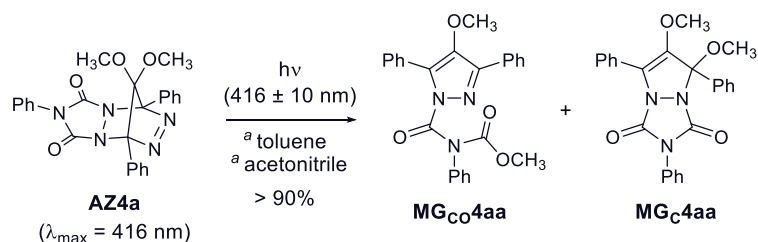
Entry	Solv.	Conc. / mM	Yield of **MG$_{CO}$4aa**	Yield of **MG$_C$4aa**	Rations of **MG$_{CO}$/MG$_C$**
1	Tol	30	75	22	77/23
2	ACN	30	25	63	28/72
3	Tol	100	70	29	71/29
4	ACN	100	29	67	30/70

^{a}The solvents were dried using 3 Å molecular sieves at 300 °C for 24 h in vacuo. ^{b}Product yields were determined by ^{1}H NMR analysis. Ph$_3$CH was used as an internal standard, ± 5% error.

Thus, the alkoxy-group migration products selectivity was found to be highly dependent on the solvent polarity, as is clear when entries 1 and 3 are compared with entries 2 and 4. No concentration effect was, however, observed for the chemical yields or product ratios, as is clear when entries 1 and 2 are compared with entries 3 and 4 (Table 3).

3.2 Crossover experiments

To gain further insights into the mechanism of the alkoxy-group migration reactions, the respective azoalkanes **AZ4k** (OR = OC_3H_7) and **AZ4l** ($OC_{10}H_{21}$) were prepared and crossover experiments in dry solvents were conducted for the photoreaction of equimolar mixtures of **AZ4a** + **AZ4k** and **AZ4a** + **AZ4l**, respectively (Scheme 12, See experimental section in Chapter 2.4; as for syntheses). In both reactions, no crossover products were observed for alkoxy-group 1,2-migrated species **MG$_C$4**, but were observed for **MG$_{CO}$4**; **MG$_{CO}$4ak** (OCH_3, OC_3H_7) and **MG$_{CO}$4ka** (OC_3H_7, OCH_3), as well as **MG$_{CO}$4al** (OCH_3, $OC_{10}H_{21}$) and **MG$_{CO}$4la** ($OC_{10}H_{21}$, OCH_3) (Tables 4,5). The results of the crossover experiments indicate that **MG$_{CO}$4** is an *intermolecular* reaction product (out-of-cage product), while **MG$_C$4** is an *intramolecular* reaction product (in-cage product). The alkoxy-migrated products, **MG$_{CO}$4aa, MG$_{CO}$4ak, MG$_{CO}$4kk,** and **MG$_{CO}$4ka,** produced by the photolysis of a 1:1 mixture of azoalkanes **AZ4a** (OR = OCH_3) and **AZ4k** were observed at the same product ratio of 21% in toluene and 5–7% in acetonitrile (Table 4, entries 1,2). Nevertheless, in-cage products **MG$_{CO}$4aa** and **MG$_{CO}$4ll** were preferably formed by the photoreaction of **AZ4a** and **AZ4l** both in toluene and acetonitrile (entries 1,2 in Table 5). The preferable formation of the in-cage products of **MG$_{CO}$4** can be rationalized by the slower diffusion rate of the large decyloxy group ($-OC_{10}H_{21}$) than the propoxy group ($-OC_3H_7$).[4] Again, these knowledges regarding crossover experiments were essential for elucidating the alkoxy-group migration reaction mechanism, and clarified that the respective alkoxy-group migrated species **MG$_{CO}$4** and **MG$_C$4** are generated via different reaction pathway—*stepwise* or *concerted*.

Scheme 12. Crossover experiments examining formation of **MG$_{co}$4** and **MG$_{C}$4** in photodeni-trogenation of **AZ4a,k,l.**
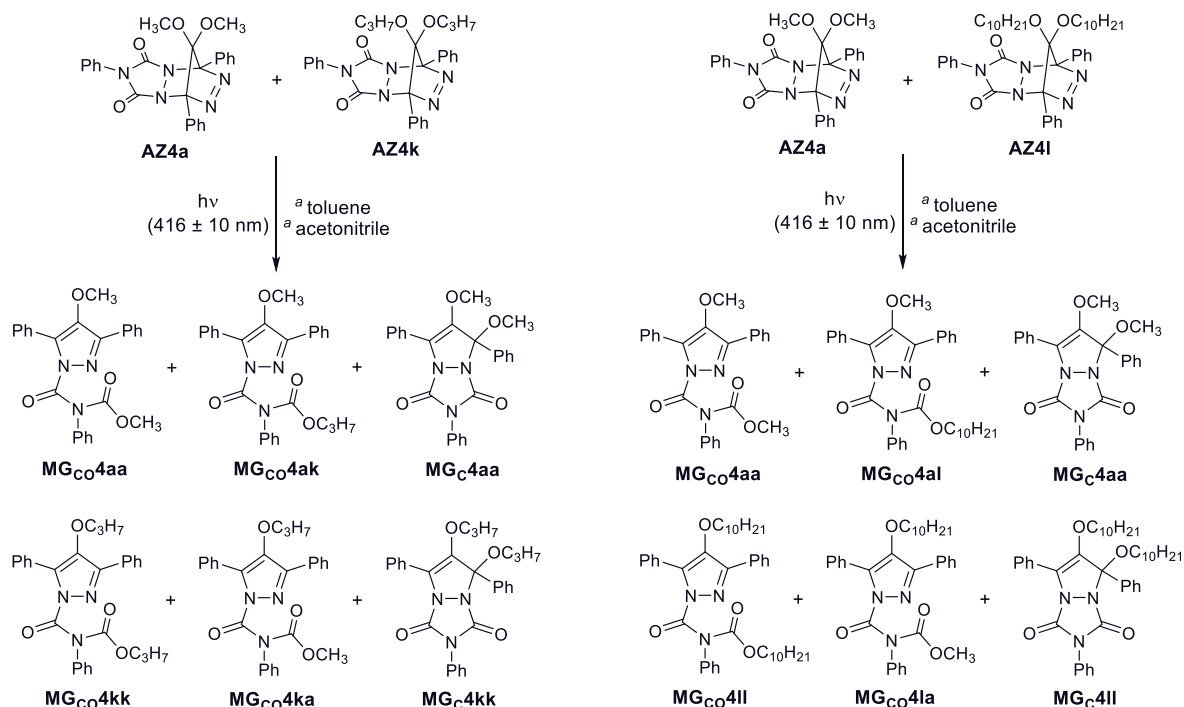
Table 4. Product distribution in photodenitrogenation of 1:1 mixture of **AZ4a** and **AZ4k.**[b,c]

Entry	Solv.	MG$_{co}$4aa	MG$_{co}$4kk	MG$_{co}$4ak	MG$_{co}$4ka	MG$_{C}$4aa	MG$_{C}$4kk	MG$_{co}$/MG$_{C}$
1	Tol	21	21	21	21	7	9	84/16
2	ACN	8	7	5	5	37	38	24/76

Table 5. Product distribution in photodenitrogenation of 1:1 mixture of **AZ4a** and **AZ4l.**[b,c]

Entry	Solv.	MG$_{co}$4aa	MG$_{co}$4ll	MG$_{co}$4al	MG$_{co}$4la	MG$_{C}$4aa	MG$_{C}$4ll	MG$_{co}$/MG$_{C}$
1	Tol	31	30	8	6	9	10	80/20
2	ACN	19	18	5	2	26	23	47/53

[a]The solvents were dried using 3 Å molecular sieves at 300 °C for 24 h in vacuo. [b]Product yields were determined by ^{1}H NMR analysis. Ph$_3$CH was used as an internal standard, ± 5% error. [c]MG$_{co}$ ≈ MG$_{co}$4aa + MG$_{co}$4kk (or 4ll) + MG$_{co}$4ak (or 4al) + MG$_{co}$4ka (or 4la), MG$_{C}$ = MG$_{C}$4aa + MG$_{C}$4kk (or 4ll).

69

Table 6 illustrates the results of another crossover experiments. The respective alkoxy-group-asymmetrically substituted azoalkanes **AZ4m** ($OR^1 = OCH_3$, $OR^2 = OC_{10}H_{21}$) and **AZ4n** ($OR^1 = OC_{10}H_{21}$, $OR^2 = OCH_3$) were prepared with reference to the experimental section (Scheme 11 in Chapter 2.4, Method B). Crossover experiments in dry solvents were carried out for the photodenitrogenation of **AZ4m** and **AZ4n**, respectively (Table 6). As described above, in any reactions, crossover products were not observed for alkoxy-group 1,2-migrated species MG_C4, but were observed for $MG_{CO}4$; $MG_{CO}4aa$ (OCH_3, OCH_3) and $MG_{CO}4ll$ ($OC_{10}H_{21}$, $OC_{10}H_{21}$). The interesting findings in these experiments are how the C-O bond of the alkoxy-group cleave. The major alkoxy-migrated product isolated with a ca. 50% yield was $MG_{CO}4la$ ($OC_{10}H_{21}$, OCH_3) in toluene (entries 1,3), and MG_C4la ($OC_{10}H_{21}$, OCH_3) in acetonitrile (entry 2) in the photo chemical denitrogenation of the respective azoalkanes **AZ4m**, **AZ4n**. These results indicate that the C-O bond of the methoxy group (C-OCH_3) is more easily cleaved than that of the decyloxy group (C-$OC_{10}H_{21}$).

Table 6. Product distribution in photodenitrogenation of asymmetric-alkoxy azoalkanes **AZ4m**(OCH_3, $OC_{10}H_{21}$) and **AZ4n**($OC_{10}H_{21}$, OCH_3).[b]
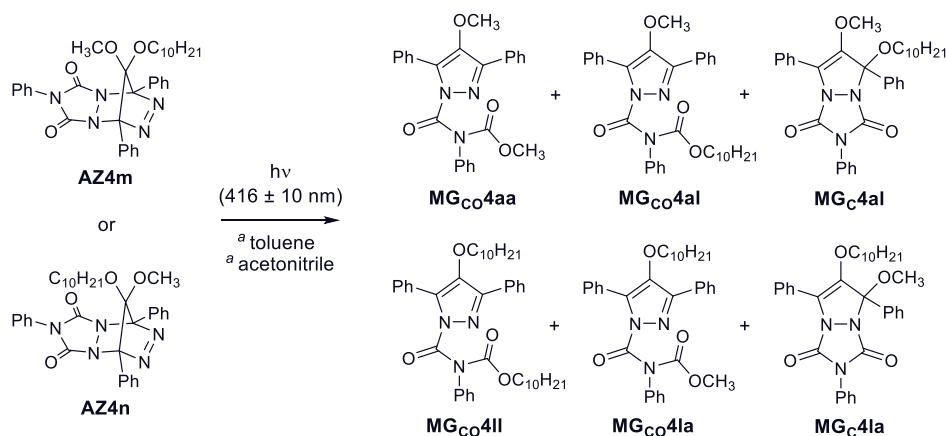
Entry	AZ	Solv.	$MG_{CO}4aa$	$MG_{CO}4ll$	$MG_{CO}4al$	$MG_{CO}4la$	MG_C4al	MG_C4la
1	**4m**	Tol	9	8	10	46	3	11
2	**4m**	ACN	6	5	3	22	10	53
3	**4n**	Tol	16	16	4	46	4	9

[a]The solvents were dried using 3 Å molecular sieves at 300 °C for 24 h in vacuo. [b]Product yields were determined by ^{1}H NMR analysis. Ph$_3$CH was used as an internal standard, ± 5% error.

Based on the results of a series of crossover experiments and the effect of solvent on the product ratio of **MG_CO4** versus **MG_C4,** the mechanism for the alkoxy-group migration reaction is proposed in Scheme 13. After the fast equilibration of S-**DR4** with **CP4**, the intramolecular 1,2-alkoxy migration occurs to produce **MG_C4** from S-**DR4**, with the process being accelerated in a polar solvent (Tables 3–6). The formation of out-of-cage product **MG_CO4** may be rationalized by the triplet pair of radical species **RP_C** and OR · , derived from the C–O bond fission in the triplet diradical T-**DR4**. After the intersystem crossing (ISC) process to the singlet state, bond-formation selectively occurs for the carbonyl carbon to produce isomer, **MG_CO4**. If the triplet pair of radicals, T-**RPs,** is formed, the respective radical species may be trapped by spin-trapping agents such as *N*-tert-butyl-α-phenylnitrone (PBN).

Scheme 13. Proposed mechanism for formation of **MG_CO4** and **MG_C4** via singlet and/or triplet diradicals.

71
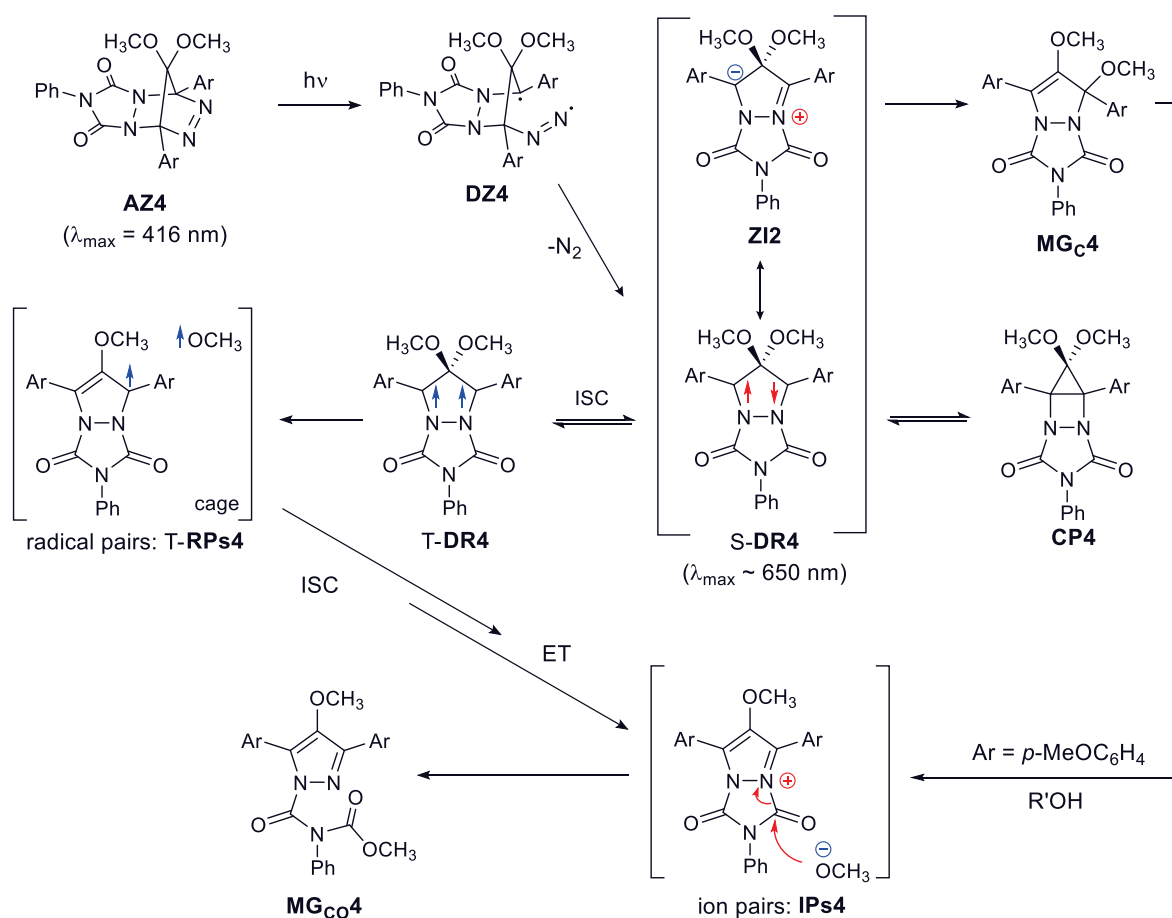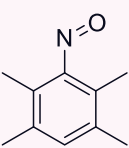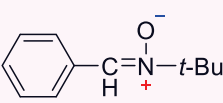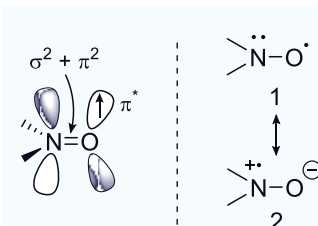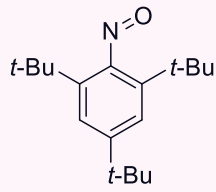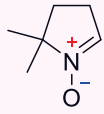
3.3 Spin-trapping experiments

3.3.1 Introduction[5a]

Lifetime of the free radicals is too short to detect with electron paramagnetic resonance (EPR) spectroscopy. Spin-trapping technique made it possible to detect the free radicals and, therefore, has been widely employed in the identification of radical intermediates, especially unstable species. To put it simply, the short-lived reactive free radicals (R·) may be transformed into more persistent paramagnetic species (the "spin adduct" abbreviation: ST-R·) by adding spin-trapped agents. As a consequence, the short-lived free radicals can be indirectly detected and identified by applying to EPR spectroscopy and mass spectrometry. The general spin trap reaction is represented by the following equation.

$$R · + ST → (ST\text{-}R ·)$$

In general, nitrones and nitroso-compounds as the spin-trapped agents, e.g. N-tert-butyl-α-phenylnitrone (PBN), 5,5-dimethyl-pyrroline-N-oxide (DMPO), nitrosodurene (ND), and tri-t-butylnitrosobenzene (TBN), are used owing to stable nitroxide radicals.

3.3.2 Evidence for the formation of triplet radical pairs

Spin-trapping experiments were conducted to examine the photodenitrogenation (high-pressure mercury lamp through the band-pass filter; 360–440 nm) of azoalkanes **AZ4a** (X = Y = H, $\sigma_C{}^{\cdot}$: 0.00), **AZ4b** (X = Y = MeO, 0.27), and **AZ4f** (X = Y = Br, 0.11) (ca. 17 mM) in the presence of *N*-tert-butyl-*α*-phenylnitrone (PBN) (ca. 102 mM) in dry benzene at room temperature (Figures 40,52). Although the in-situ EPR signals observed in the photolysis of **AZ4a** and **AZ4f** were relatively complicated (Figure 52), fortunately, the EPR signals of a nitroxide having the hyperfine coupling constants of $A_1{}^N = 14.71$ G, $A_1{}^{H\beta} = 4.79$ G were detected for the spin-trapping experiments in the photolysis of **AZ4b** (Figure 40). Atmospheric pressure chemical ionization (APCI) mass spectroscopic analysis of the in-situ EPR sample demonstrated the formation of molecular ion peaks of M+; m/z 633.27 (δ: 1.798 ppm, Theo. Mass: 633.27) that correspond to the **RP$_C$** spin adduct of PBN (Composition: C37 H37 O6 N4·; Scheme 14, Figures 50,51).

Scheme 14. Spin-trapping reactions between azoalkane **AZ4** and spin-trapped agents PBN.
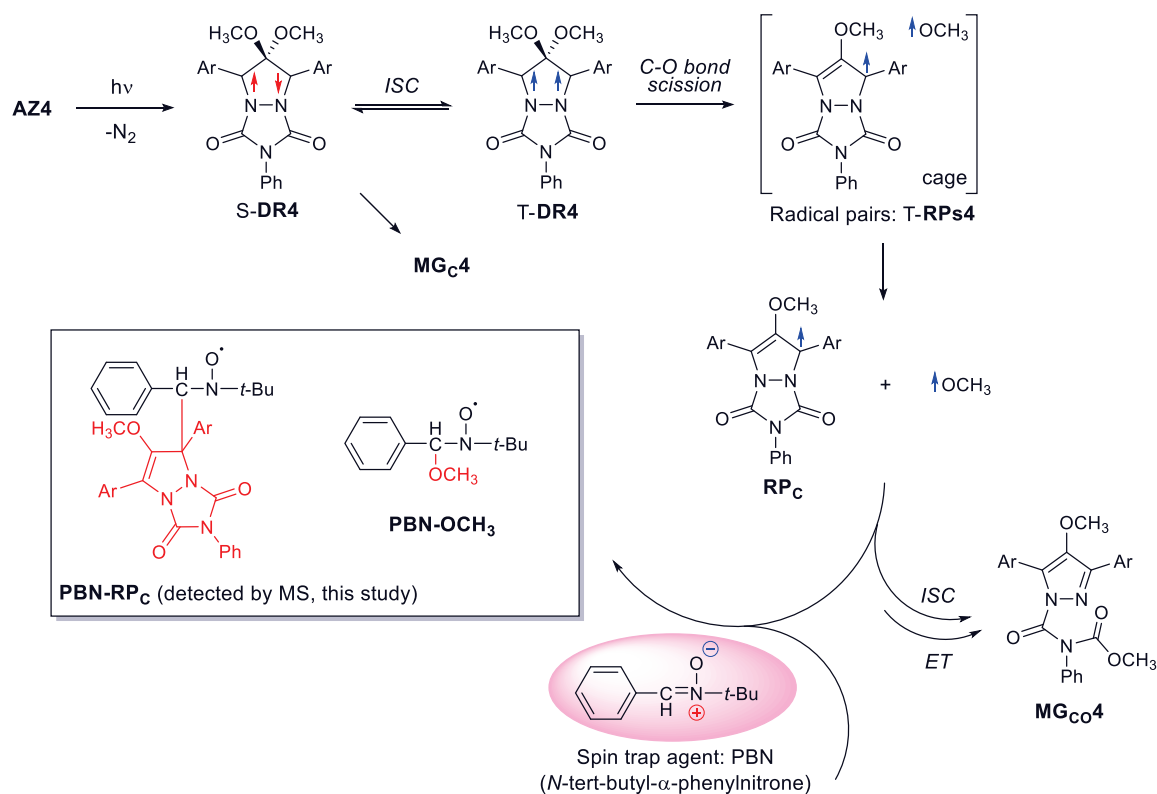
Thus, the out-of-cage product $\mathbf{MG_{CO}4}$ is proposed to be formed via the triplet radical pairs T-$\mathbf{RPs4}$ after the C-O bond homolytic cleavage from the triplet diradicals T-$\mathbf{DR4}$. As an additional information, the EPR signals did not conform to the reported MeO $\cdot$ radical trapped nitroxide $(A^N = 13.73$ G and $A^{H\beta} = 1.93$ G$)$ with PBN.[5b–d]
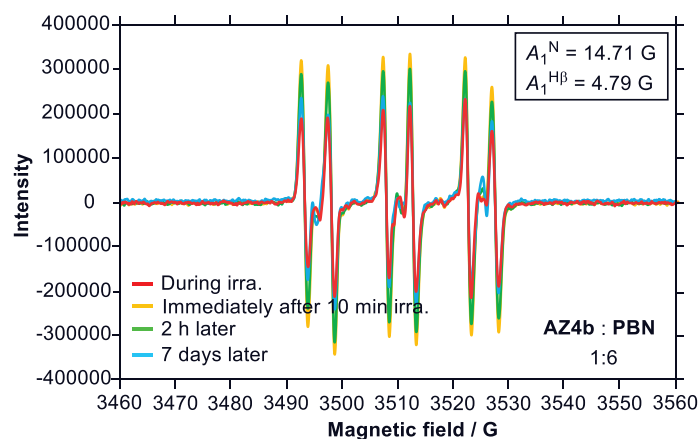
Figure 38. Spin-trapping experiments using EPR measurements. EPR spectrum obtained from photodenitrogenation of **AZ4b** in the presence of PBN in the concentration ratio of one to six. (**AZ4b**:PBN = 1:6)

Furthermore, the EPR signals of the MeO $\cdot$ radical trapped nitroxide (A_3) were observed at higher concentration of PBN (Figure 41). The short-lived alkoxy radicals $(OR \cdot)$ can be captured in the presence of excess spin-trapped agents.[5e]
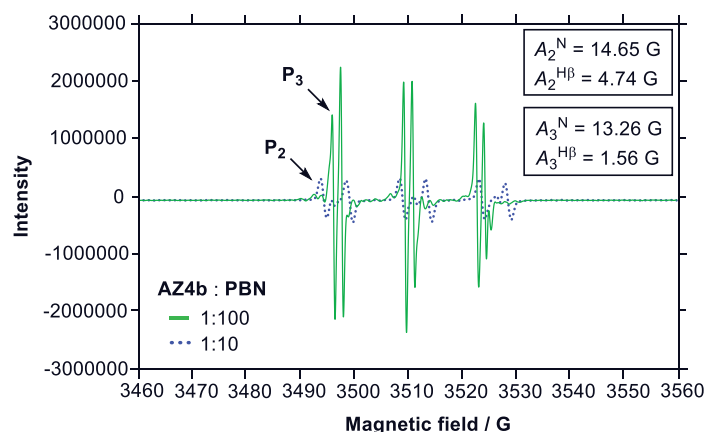
Figure 39. Concentration dependence on spin-trapping experiments. EPR spectra of $\mathbf{P_2}$ (blue dotted line): $\mathbf{RPc}$ spin adduct of PBN (in concentration ratios of 1:10 of **AZ4b**:PBN); $\mathbf{P_3}$ (green line): MeO radical trapped nitroxide (in concentration ratios of 1:100 of **AZ4b**:PBN).

3.4 Regioselectivity of alkoxy-group migration reactions

To obtain further information on the mechanism of the respective alkoxy-group migrated products **MG$_{CO}$4** and **MG$_C$4** formations, the product selectivity was investigated in the photodenitrogenation of aryl-group-asymmetrically substituted azoalkanes **AZ4i** (X = MeO, Y = H) and **AZ4j** (X = CN, Y = H) at 293 K using Xenon lamp (λ_{exc} = 416 ± 10 nm) (Table 7). The combination of these three substituents; H (σ_p^+, $\sigma_C^\cdot$ = 0.00, 0.00), MeO (−0.78, 0.27), and CN (0.99, 0.47), takes into account not only electronic effects but also radical stabilization at the benzylic position. In the photodenitrogenation for **AZ4i**, the four expected products; **MG$_{CO}$4i**, **MG$_{CO}$4i'**, **MG$_C$4i**, and **MG$_C$4i'**, were observed at products ratio of 37:38:19:6 in toluene and 9:9:55:27 in acetonitrile with > 90% total yields (entries 1,2 in Table 7), which were analyzed by [1]H NMR spectroscopy. No regioselectivity was observed for **MG$_{CO}$4**, either in toluene or acetonitrile. The selective formation of **MG$_C$4i** was, however, observed at a ratio of ca. 70:30 of **MG$_C$4i**:**MG$_C$4i'** (entries 1,2). Methoxy-group migrated reaction selectively occurred for the p-MeOC$_6$H$_4$-substituted carbon. In contrast to the effect of substituents on the regioselectivity, the selective formation of the **MG$_C$4j'**

Table 7. Product distributions for photodenitrogenation of azoalkanes **AZ4i** (entries 1,2) and **AZ4j** (entries 3,4) in dried toluene and acetonitrile at 293 K, respectively.
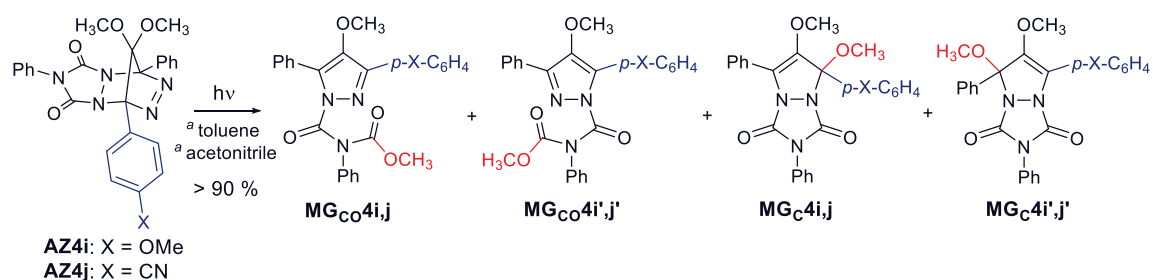
Entry	Sample (X)	Solv.^{a}	MG$_{CO}$4:MG$_{CO}$4':MG$_C$4:MG$_C$4'	MG$_C$4/ MG$_C$4'
1	**AZ4i** (MeO)	Tol	37:38:19:6	76/24
2	**AZ4i** (MeO)	ACN	9:9:55:27	67/33
3	**AZ4j** (CN)	Tol	40:40:5:15	24/76
4	**AZ4j** (CN)	ACN	0:0:28:72	28/72

^{a}The solvents were dried using 3 Å molecular sieves at 300 °C for 24 h in vacuo.

isomer, occurred at the p-HC$_6$H$_4$-substituted carbon, was observed at a ratio of ca. 30:70 of **MG$_C$4j:MG$_C$4j'** in the reaction of **AZ4j** (entries 3,4). No regioselectivity in **MG$_{CO}$4** products was also observed for the photodenitrogenation of **AZ4j,** either in toluene or acetonitrile (entries 3,4).

The selective formation of **MG$_C$4i** and **MG$_C$4j'** is rationalized by the charge distribution on the singlet diradicals S-**DR4i** and S-**DR4j** (Scheme 15a). The contribution of **ZI2**, EDG = p-MeOC$_6$H$_4$ and relatively EWG = Ph for S-**DR4i,** relatively EDG = Ph and EWG = p-CNC$_6$H$_4$ for S-**DR4j,** should be larger than **ZI2',** because the electron-withdrawing group stabilizes the anion. Thus, the methoxy group selectively migrates to the EDG group substituted carbon. Meanwhile, in the intermediate **C** that produces **MG$_{CO}$4** (Scheme 15a), an equal charge distribution would be expected because the positive charge is well stabilized by the nitrogen atoms. Thus, the methoxide equally attacks the carbonyl carbon of **C** and **C'** to give a 1:1 mixture of **MG$_{CO}$4** and **MG$_{CO}$4'**. The observed effect of substituents on these 1,2-alkoxy-group migration reactions were quite different from those on the 1,2-alkoxy-group migration reactions of aryl-group-asymmetrically substituted S-**DR1**, which quantitative migrates to the EDG group substituted carbon.[7a,b]

Scheme 15. (a) Resonance structures of donor-acceptor aryl-substituted S-**DR4**. (b) previous study: the electronic character in singlet 2,2-dimethoxycyclopentane-1,3-diyls, S-**DR1**.[7a,b]
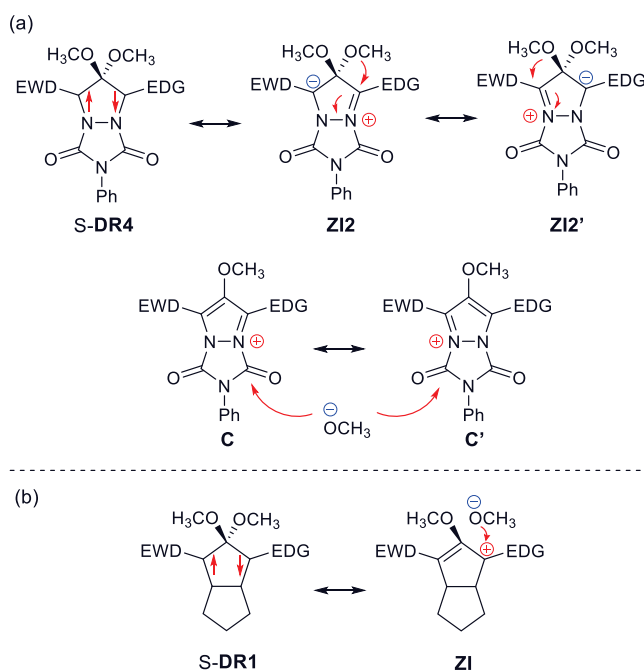
3.5 Effect of temperature on regioselectivity of alkoxy-group migration reactions

To obtain knowledges regarding the potential energy profile of the alkoxy-group migration reactions of S-**DR4**, the effect of temperature on the product selectivity, **MG$_{CO}$4** versus **MG$_C$4**, was investigated in the photochemical denitrogenation of **AZ4a** (X = Y = H), **4b** (MeO), **4e** (Cl) in dried toluene and acetonitrile over a temperatures region of 273–313 K (Figure 42, **4b**, **4e**: see Figures 54–56 in Chapter 3.8). At 273 K, **MG$_{CO}$4aa** was mainly observed in dried toluene (**MG$_{CO}$4aa/MG$_C$4aa** = 94/6) (Figures 42,43). The amount of **MG$_C$4aa** increased with the reaction temperature (**MG$_{CO}$4aa/MG$_C$4aa** = 83/17 at 293 K, 65/35 at 303 K, and 62/38 at 308 K). Unexpectedly, the yield of **MG$_C$4aa** suddenly increased at temperatures above ca. 308 K. At around this temperature, the product ratio became drastically inverted from **MG$_C$4aa/MG$_{CO}$4aa** = 62/38 (308 K) to 9/91 (311 K). Both **MG$_{CO}$4aa** and **MG$_C$4aa** were stable under the reaction conditions. Thus, the effect of temperature clearly suggests that the activation entropy plays a
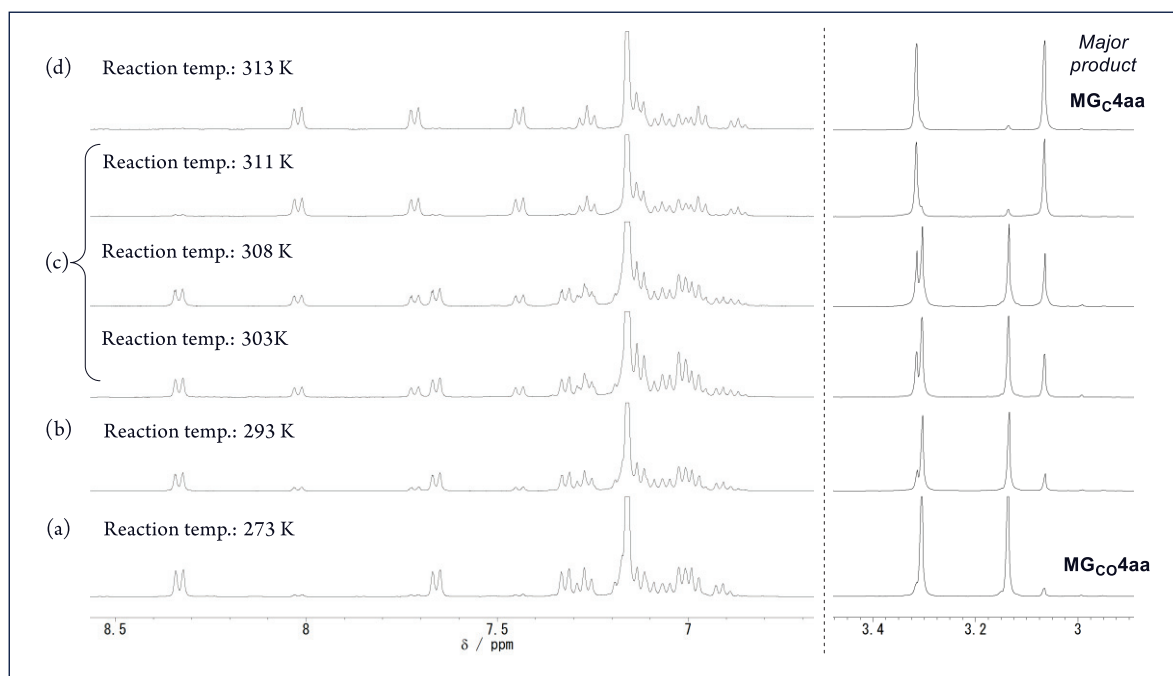

Figure 40. ^{1}H NMR spectroscopic analyses for photodenitrogenation of **AZ4a** in toluene in a variety of reaction temperature; (a) 273 K, (b) 293 K, (c) 303–311 K and (d) 313 K.

crucial role in the product selectivity. Almost $\mathbf{MG_{CO}4aa}$ was observed at a reaction temperature below 263 K (> ca. 95% yield; Figures 42a,43). At a reaction temperature above 318 K, however, only $\mathbf{MG_C4aa}$ was detected using ^{1}H NMR spectroscopic analysis (> ca. 95% yield; Figures 42d,43). The effect of temperature on the product selectivity suggests that the rate-determining step changes around 273–313 K. In contrast to the effect of temperature, in acetonitrile, the effect of temperature is essentially negligible for product ratios of $\mathbf{MG_{CO}4aa}/\mathbf{MG_C4aa}$ = 14/86 (273 K) to 9/91 (313 K). To obtain further information on effects of the temperature and solvent, as well as the reaction mechanism, on the product selectivity of $\mathbf{MG_{CO}4aa}/\mathbf{MG_C4aa}$, the effect of temperature on the decay rate (k_{slow}) for slow process of S-$\mathbf{DR4a}$ was investigated in both toluene and acetonitrile (Scheme 7, and Figure 5 in Chapter 2.1, Figure 44).
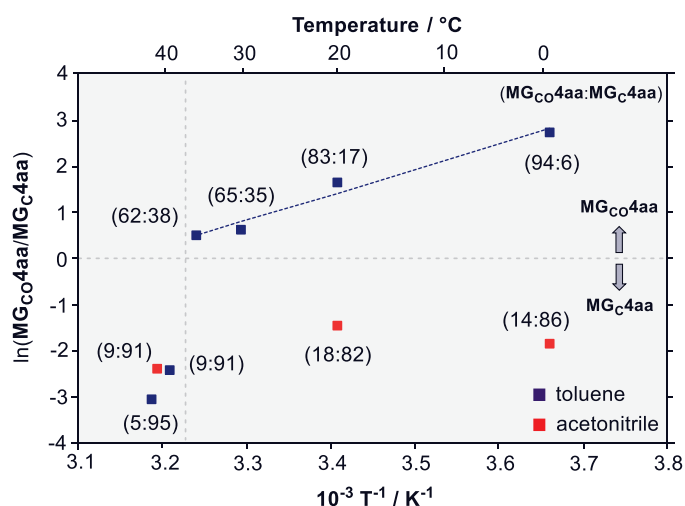
Figure 41. Temperature dependence of the alkoxy-group migrated product ratios $\mathbf{MG_{CO}4aa}$ versus $\mathbf{MG_C4aa}$. Below 273 K, $\mathbf{MG_{CO}4aa}$ was selectively isolated (> ca. 95%). Above 308 K, the alkoxy-group 1,2-migrated species $\mathbf{MG_{CO}4aa}$ was selectively isolated (> ca. 95%).

The Eyring plots, $\ln(k_{slow}/T)$ versus $1/T$, in dry toluene and acetonitrile are shown in Figure 44. The linearity of the Eyring plot was not obtained in toluene over a temperature range of 273–313 K (II). At this temperature both $\mathbf{MG_{CO}4aa}$ and $\mathbf{MG_C4aa}$ were formed (Figures 42,43). Two different linear correlations were observed in those regions with temperatures above 313 K (40 °C) (I) and below 263 K (–10 °C) (III) (Figure 44a). According to the knowledge as to the effect of temperature on the product selectivity by
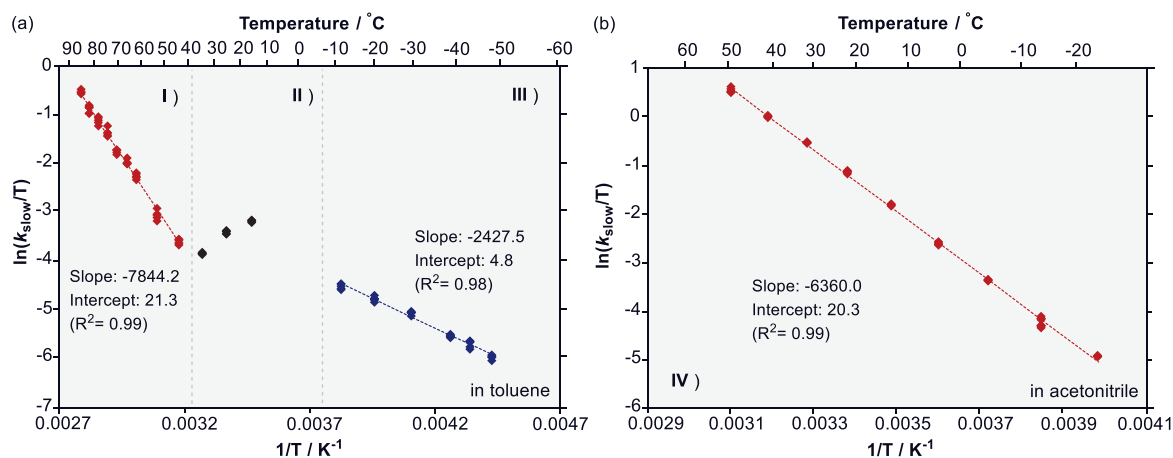
Figure 42. Eyring plots for alkoxy-group migrated reaction ($AZ4a \rightarrow MG_{Co}4aa + MG_{C}4aa$) in dry (a) toluene and (b) acetonitrile.

means of ^{1}H NMR spectroscopic analysis, **MG$_C$4aa** was exclusively formed in temperature region (I), and only **MG$_{Co}$4aa** was detected in temperature region (III) (Figures 43,44a). The obtained activation parameters in temperature regions (I) and (III) are summarized in Table 8. In temperature region (I), the enthalpy factor dominates the Gibbs activation energy, $\Delta H^{\ddagger}$ = 66.8 kJ mol^{-1}, $\Delta S^{\ddagger}$ = −7.1 J K^{-1} mol^{-1}, $\Delta G^{\ddagger}$ = 68.6 kJ mol^{-1} at 253 K, and $\Delta G^{\ddagger}$ = 69.3 kJ mol^{-1} at 353 K. On the other hand, the entropy factor greatly affects the rate constant k_{slow} in temperature region (III). In this region, the activation parameters were obtained as $\Delta H^{\ddagger}$ = 21.4 kJ mol^{-1}, $\Delta S^{\ddagger}$ = −145.3 J K^{-1} mol^{-1}, $\Delta G^{\ddagger}$ = 58.2 kJ mol^{-1} at 253 K, and $\Delta G^{\ddagger}$ = 72.7 kJ mol^{-1} at 353 K. The large entropy contribution in the low temperature region (III) is reasonable for the reason that **MG$_{Co}$4** is formed from triplet diradicals T-**DR4** via the intersystem crossing (ISC) process from singlet diradicals S-**DR4** as apparent from the spin-trapping experiments (Scheme 13, Chapter 3.3). The spin-forbidden ISC process is known to provide entropy control whereby, in general, large negative entropy and small log(A/s^{-1}) values, the Arrhenius pre-exponential factors, are observed.[8,9] Meanwhile, the log(A/s^{-1}) value of ca. 12, which is observed at a temperature above 313 K, supports the spin-allowed reaction process.[10] Indeed, in the high-temperature region (I), the activated Gibbs energy barrier for the ISC process becomes larger than the energy barrier for another reaction pathway from S-**DR4a** to **MG$_C$4aa**; $\Delta G^{\ddagger}$ (S-**DR4aa** →

$\mathbf{MG_C4aa}) = 69.3$ kJ mol^{-1} versus $\Delta G^{\ddagger}$ (S-$\mathbf{DR4aa} \to$ T-$\mathbf{DR4aa}) = 72.7$ kJ mol^{-1} at 353 K. Thus, a drastic effect of temperature was observed for the product selectivity in the photodenitrogenation of azoalkane $\mathbf{AZ4a}$. The notable effect of temperature on the product selectivity is visualized in Scheme 17 in the following Chapter 3.7. In the low temperature region (III), the ISC process dominates the fate of S-$\mathbf{DR4}$ to give the triplet state T-$\mathbf{DR4}$, from which the C–O bond scission occurs to finally afford $\mathbf{MG_{CO}4}$. In the higher temperature region (I), the energy barrier of the methoxy-migration step becomes smaller than the ISC process to produce $\mathbf{MG_C4}$ predominantly. Incidentally, in dry acetonitrile, the only one linear Eyring plot was obtained in the temperature region (IV) addressed in the present study (Figure 44b). The product ratio of $\mathbf{MG_{CO}4aa}$:$\mathbf{MG_C4aa}$ was constant at ca. 10:90 (Figure 43), that is, the obtained linear Eyring plot demonstrates the process giving $\mathbf{MG_C4aa}$. The activated Gibbs energy barrier was determined to be smaller than that in toluene. Thus, the concerted alkoxy-group 1,2-migration reaction is accelerated by the polar solvent.

Table 8. Activation parameters $\Delta H^{\ddagger}$, $\Delta S^{\ddagger}$, E_a and $\log(A/\text{s}^{-1})$ for the alkoxy-group migrated reaction under several appropriate measurement conditions.

Reaction conditions	Solv.	Reactions	Temperature range/K	$\Delta H^{\ddagger\,a}$ (E_a)	$\Delta S^{\ddagger\,b}$ $\log(A/\text{s}^{-1})$
I	Tol	S-$\mathbf{DR4a} \to \mathbf{MG_C4aa}$	314–358	66.8 (69.6)	−7.1 (12.9)
II	Tol	S-$\mathbf{DR4a} \to \mathbf{MG_{CO}4aa}$ + $\mathbf{MG_C4aa}$	273–308	—	—
III	Tol	S-$\mathbf{DR4a} \to \mathbf{MG_{CO}4aa}$	225–260	21.4 (23.4)	−145.3 (5.5)
IV	ACN	S-$\mathbf{DR4a} \to \mathbf{MG_C4aa}$	251–322	56.2 (58.6)	−12.1 (12.6)

^{a} Activation enthalpy (activation energy) in kJ mol^{-1} and ^{b} Activation entropy in J K^{-1} mol^{-1} for the alkoxy-group migrated reaction using Eqs. (1)–(3) in Scheme 7 in Chapter 2.

3.6 1,2-alkoxy-group migrated product in ethanol

To elucidate the existence of the ion pair, **IPs4**, involved in formation of **MG$_{CO}$4**, the photodenitrogenation of azoalkane **AZ4b** (X = Y = MeO) was conducted in protic solvent ethanol. In dry toluene, the absorption maxima of S-**DR4b** was only observed at around 650 nm (Figure 7 in Chapter 2.2). In ethanol, however, the decay of the absorption of S-**DR4b** was accompanied by increasing absorption at around 460 nm ($\tau_{293\,K} > 10$ ms) [According to *Ref.* 2, by laser flash photolysis of **AZ4a** (X = Y = H) in ethanol was given the absorption at ca. 380 nm; the red-shifted (from 380 nm to 460 nm) was observed due to the extended conjugation system by introducing electron-donating substituents at the *para*-positions]. The decay rate constant of the species observed at ca. 650 nm ($k_{d,650}$) was found to be $1.06 \pm 0.05 \times 10^7$ s^{-1} with single-exponential fitting, and was in good agreement with the growth rate constant of the species observed at ca. 460 nm ($k_{g,460} \approx 1.03 \pm 0.05 \times 10^7$ s^{-1}). The ethoxy-group migrated product **MG$_{CO}$4b**(-OC$_2$H$_5$) was selective formed from the thermal reaction of **MG$_C$4b** with ethanol at room temperature (Scheme 16). These results strongly suggests the existence of the ion pair, **IPs4**, through the reaction mechanism of the present study (Scheme 13).

Scheme 16. Transformation **MG$_C$4** into **MG$_{CO}$4** and generation of allylic cation ($\lambda_{max} \approx 460$ nm).
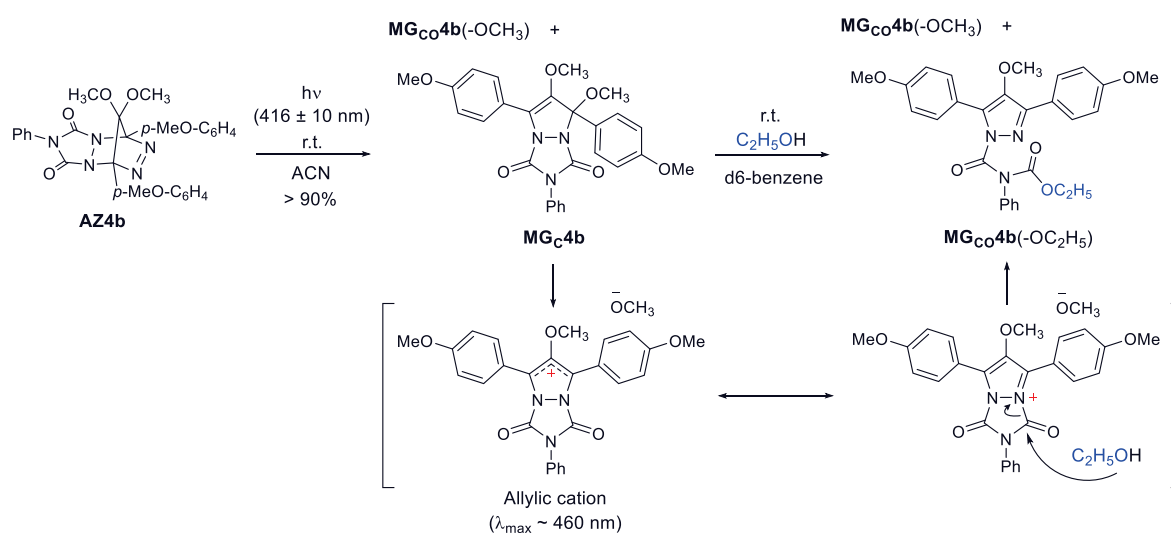
3.7   Chapter summary

In Chapter 3, the formation mechanism of alkoxy-group migrated species in the photodenitrogenation of azoalkane, **AZ4**, was described in detail; crossover, spin-trapping, regioselectivity and LFP experiments for the slow decay process. In especially, effect of temperature on regioselectivity suggested that the activation entropy ($\Delta S^{\ddagger}$) plays a key role in the product selectivity (**MG$_{CO}$4** versus **MG$_C$4**). Thus, reaction temperature makes it possible to change the respective rate-limiting step. Specifically, the intersystem crossing (ISC) process was found to be a key step in the formation of intermolecular migrated species **MG$_{CO}$4,** and the intramolecular alkoxy-group 1,2-migrated species **MG$_C$4** was found to be accelerated by a polar solvent (Scheme 17).

Scheme 17. Solvent polarity and temperature dependency of product selectivity for S-**DR4a**.
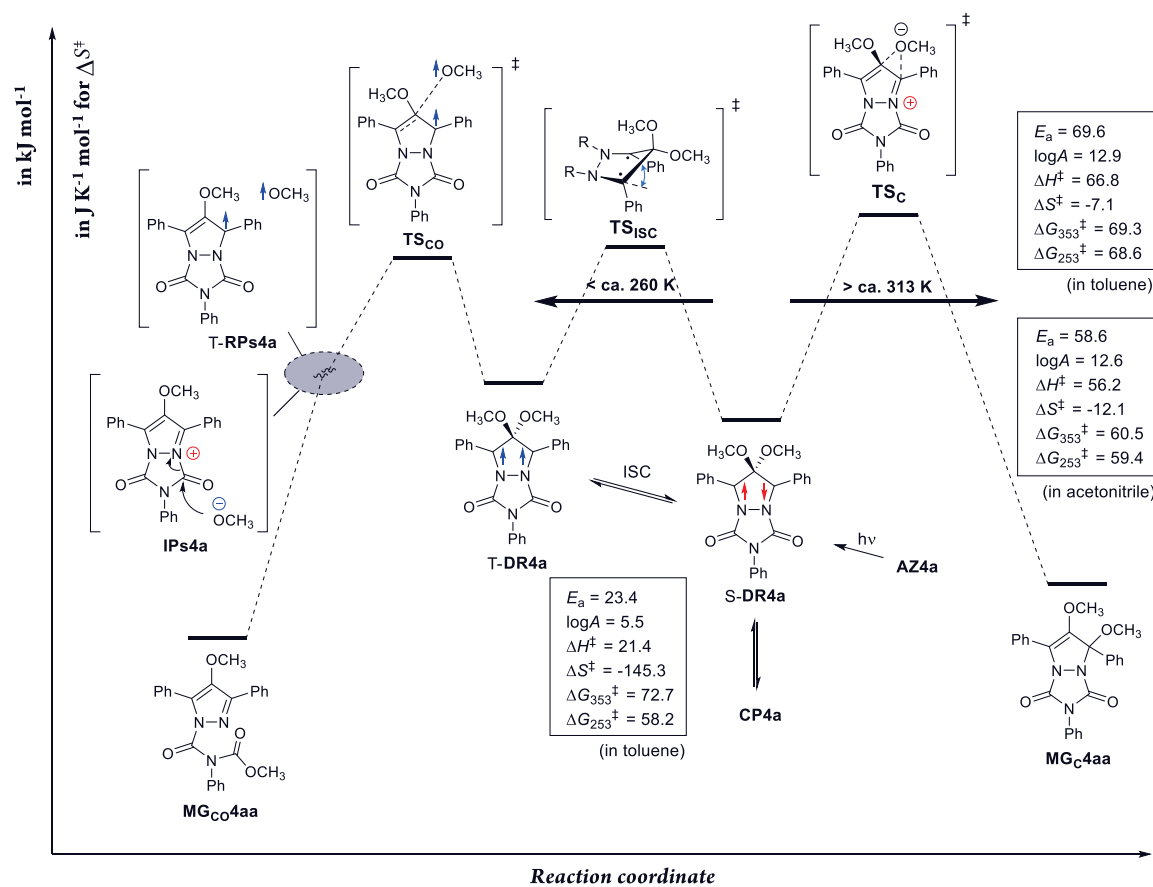
3.8   Experimental section

Dry toluene (Tol, Spectro grade), benzene (Spectro grade), acetonitrile (ACN, Spectro grade), tetrahydrofuran (THF, super dehydrated, stabilizer free), acetone (Spectro grade) and dimethylformamide (DMF, super dehydrated) were purchased from commercial suppliers and stored at least 24 h under nitrogen gas over activated 3 Å molecular sieves (3 Å MS), which were predried at 300 °C for 24 h before use.[3] Azoalkanes **AZ4a–n** were synthesized according to the literature procedure (Scheme 11 in Chapter 2.4). ^{1}H NMR spectra were obtained at 400 MHz, chemical shifts are reported in ppm, and referenced to the $CHCl_3$ and C_6H_6 singlet at 7.26 and 7.16 ppm, respectively. ^{13}C NMR spectra were obtained at 100 MHz and referenced to the center peak of the C_6D_6 triplet at 128.06 ppm. The abbreviations s, d, t, quin, sext, dt, td and m stand for the resonance multiplicities singlet, doublet, triplet, quintet, sextet, doublet of triplets, triplet of doublets and multiplet, respectively. UV-vis spectra were recorded on a SIMADZU UV-3600 Plus spectrophotometer. Mass-spectrometric data were measured with a mass spectrometric Thermo Fisher Scientific LTQ Orbitrap XL.

Scheme 18. How to prepare the sample for photodenitrogenation of azoalkane. Step 1: Preparation of dried solvent; Solvent stored at least 24h under nitrogen gas over activated 3 Å molecular sieves, which were predried at 300 °C for 24 h before use. Step 2: Transfer dried solvent to the reaction vessel on the vacuum line by means of oil diffusion.
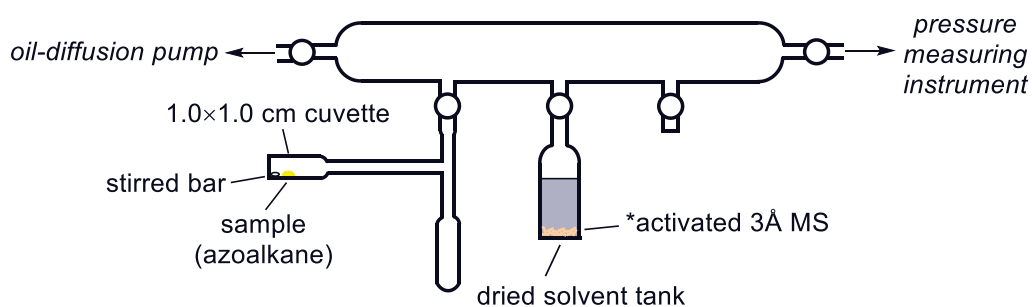
Alkoxy-migrated product after photodenitrogenation: **MG$_C$4aa**. A solution of **AZ4a** (ca. 7 mg, 5 mmol) in 3 mL dry toluene was irradiated in J. Young quartz cuvette with 416 nm light for 2 hours at 40 °C. The photoreaction was followed by ^{1}H, ^{13}C, HMBC NMR. After the solvent was removed a colorless oil was obtained.
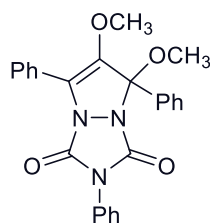
MG$_C$4aa

^{1}**H NMR** (400 MHz, d6-benzene): δ 3.06 (s, 3 H), 3.31 (s, 3 H), 6.87 (m, 1 H), 7.27 (t, *J* = 7.6 Hz, 2 H), 7.44 (d, *J* = 8.4 Hz, 2 H), 7.71 (d, *J* = 8.4 Hz, 2 H), 8.02 (d, *J* = 8.0 Hz, 2 H). ^{13}**C NMR** (100 MHz, d6-benzene): δ 150.79, 149.80, 138.53, 137.00, 131.78, 129.77, 129.08, 128.97, 128.94, 128.66, 128.62, 128.32, 128.18, 127.08, 126.76, 125.34, 122.94, 96.81, 58.13, 50.68. **ESI-MS** found: 450.14258, calc. for C25H21O4N3Na ([M+Na]$^+$): 450.14243.

Alkoxy-migrated product after photodenitrogenation: **MG$_{CO}$4aa**. A solution of **AZ4a** (ca. 7 mg, 5 mmol) in 3 mL dry toluene was irradiated in J. Young quartz cuvette with 416 nm light for 2 hours at 0 °C. The photoreaction was followed by ^{1}H, ^{13}C, HMBC NMR. After the solvent was removed a colorless oil was obtained.
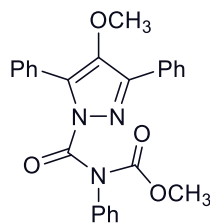
MG$_{CO}$4aa

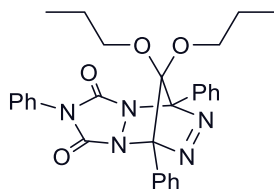^{1}**H NMR** (400 MHz, d6-benzene): δ 3.14 (s, 3 H), 3.31 (s, 3H), 6.90 (m, 1H), 6.99 (m, 2 H), 7.10 (m, 1 H), 7.27 (m, 2 H), 7.33 (m, 2 H), 7.65 (m, 2 H), 8.32 (m, 2 H). ^{13}**C NMR** (100 MHz, d6-benzene): δ 154.36, 151.15, 145.53, 143.99, 138.49, 135.16, 131.54, 129.77, 128.93, 128.73, 128.65, 128.32, 128.04, 127.98, 127.89, 127.79, 127.56, 127.11, 60.74, 53.41. **ESI-MS** found: 428.15985, calc. for

C25H22O4N3 ([M+H]⁺): 428.16048.

Azoalkane **AZ4k**.

AZ4k

¹H NMR (400 MHz, d6-benzene): δ 0.51 (t, *J* = 7.4 Hz, 3 H), 0.81 (t, *J* = 7.4 Hz, 3 H), 1.00 (sext, *J* = 7.0 Hz, 2 H), 1.39 (sext, *J* = 7.0 Hz, 2 H), 2.86 (t, *J* = 6.6 Hz, 2 H), 3.22 (t, *J* = 6.4 Hz, 2 H), 6.73–6.82 (m, 2 H), 7.09(m, 2 H), 7.18(m, 2 H), 2.78(t, *J* = 7.6, 2 H), 8.44(m, 2 H). **¹³C NMR** (100 MHz, d6-benzene): δ 150.79, 149.80, 138.53, 137.52, 137.00, 131.78, 129.77, 129.08, 128.97, 128.94, 128.66, 128.62, 128.32, 128.18, 127.08, 126.76, 125.34, 122.94, 96.81, 58.13, 50.68, 21.03. **ESI-MS** found: 529.25580, calc. for C29H33O4N6 ([M+NH₄]⁺): 529.25578.

Azoalkane **AZ4l**.
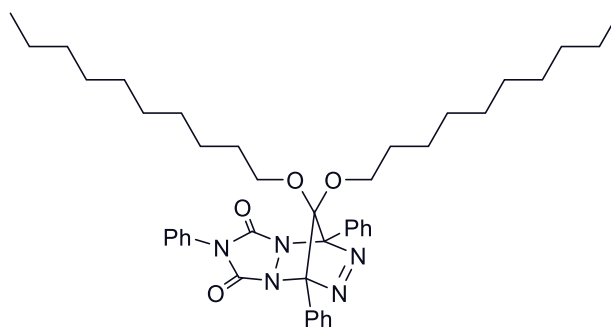
AZ4l

¹H NMR (500 MHz, d1-chloroform): δ 0.88 (t, *J* = 6.8 Hz, 6 H), 0.97–1.34 (m, 32 H), 2.92 (t, *J* = 6.4 Hz, 2 H), 3.25 (t, *J* = 6.6 Hz, 2 H), 7.30–7.35 (m, 5 H), 7.52–7.54 (m, 6 H), 8.13–8.15 (m, 4 H). **¹³C NMR** (125 MHz, d1-chloroform): δ 154.89, 130.61, 130.22, 128.96, 128.66, 128.55, 128.33, 128.28, 125.58, 119.55, 99.59, 65.26, 64.97, 31.91, 31.90, 29.75, 29.53, 29.46, 29.43, 29.33, 29.29, 29.22, 29.08, 25.82, 25.54, 22.69, 14.12.
ESI-MS found: 730.4300, calc. for C43 H57 O4 N5 Na ([M+Na]⁺): 730.4303.
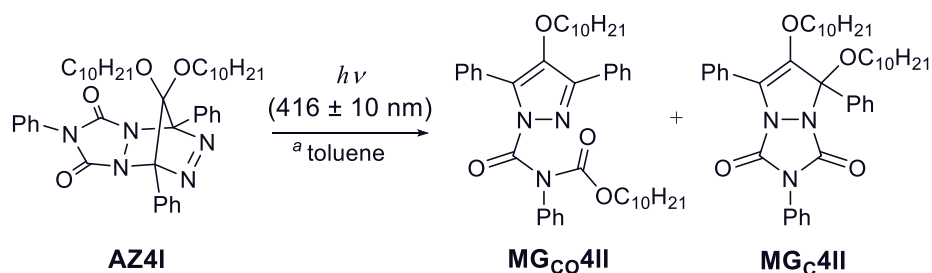
a The solvents were dried with 3 Å MS that was dried at 300 °C for 24 h in vacuo.
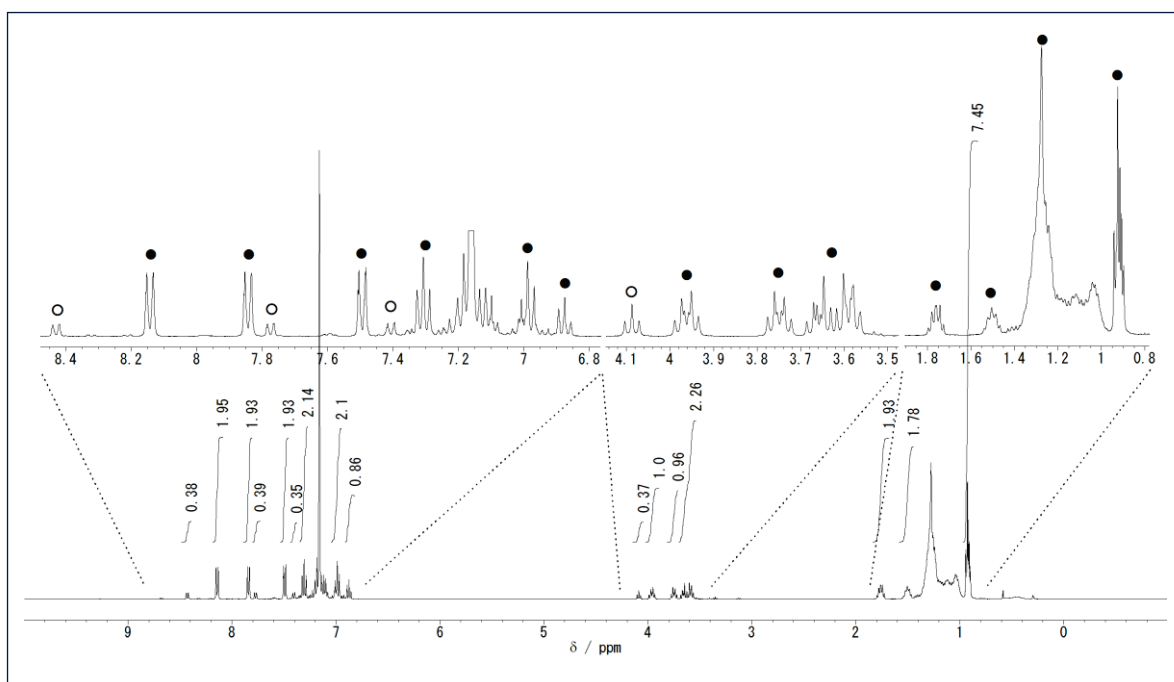
Figure 43. ^{1}H NMR (400 MHz, d6-benzene) spectrum of migrated products **MG$_{CO}$4ll**, **MG$_C$4ll** after photodenitrogenation of **AZ4l** in acetonitrile. ●: **MG$_C$4ll**, ○: **MG$_{CO}$4ll**

Alkoxy-migrated products after photodenitrogenation: **MG$_{CO}$4ll, MG$_C$4ll**. A solution of **AZ4l** (ca. 10 mg, 22 mmol) in 0.7 mL dry acetonitrile was irradiated in J. Young quartz cuvette with 416 nm light for 2 hours at 25 °C. The photoreaction was followed by ^{1}H NMR. After the solvent was removed a colorless oil was obtained.

86

MG_{CO}4ll
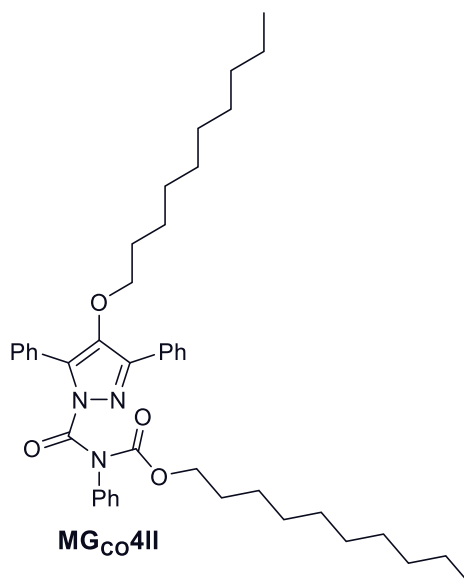
MG_{CO}4ll: **¹H NMR** (400 MHz, d6-benzene): δ 0.93 (t, *J*= 4.0 Hz, 6 H), 0.95–1.42 (m, 32 H), 3.58 (t, *J*= 6.0 Hz, 2 H), 4.09 (t, *J*= 6.0 Hz, 2 H), 7.42 (d, *J*= 6.0 Hz, 2 H), 7.77 (d, *J*= 4.0 Hz, 2 H), 8.43 (d, *J*= 4.0 Hz, 2 H). **¹³C NMR** (100 MHz, d6-benzene): δ 154.08, 151.48, 145.95, 143.23, 138.69, 131.76, 129.80, 128.92, 128.85, 128.69, 127.97, 127.74, 127.61, 127.49, 127.23, 127.07, 74.35, 67.39, 64.93, 31.99, 29.51, 29.44, 22.80, 14.06. **ESI-MS** found: 680.4423, calc. for $C_{43}H_{58}O_4N_3$ ($[M+H]^+$): 680.4422.

MG_C4ll
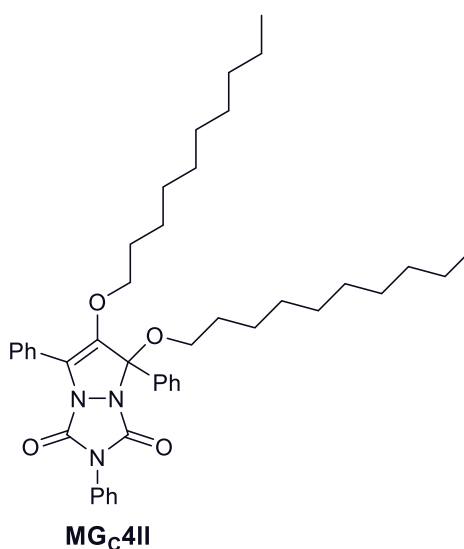
MG_C4ll: **¹H NMR** (400 MHz, d6-benzene): δ 0.93 (m, 6 H), 0.95–1.42 (m, 28 H), 1.50 (quin, 2H), 1.76 (quin, 2 H), 3.63 (m, 2 H), 3.75 (dt, 1 H), 3.96

(dt, 1 H), 6.87 (t, *J* = 7.6 Hz, 1 H), 7.00 (t, *J* = 7.8 Hz, 2 H), 7.10–7.20 (m, 4 H), 7.31 (t, *J* = 7.8 Hz, 2 H), 7.49 (m, 2H), 7.84 (m, 2H), 8.14 (m, 2H).

Asymmetric-alkoxy Azoalkane **AZ4m**.

AZ4m
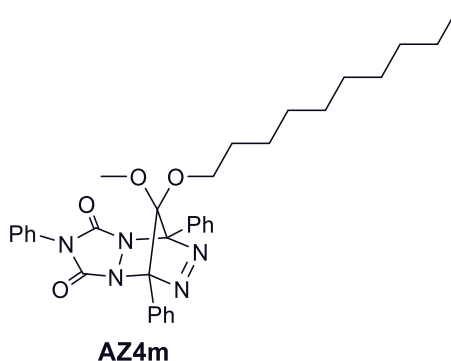
¹H NMR (400 MHz, d6-benzene): δ 0.92 (t, *J*= 7.0 Hz, 3 H), 0.96–1.32 (m, 16 H), 2.88 (t, *J* = 6.4 Hz, 2 H), 2.91 (s, 3 H), 6.75–6.82 (m, 3), 7.12 (m, 2 H), 7.19 (m, 2 H), 7.28 (m, 4 H), 8.41 (m, 4 H). **¹³C NMR** (100 MHz, d6-benzene): δ 154.73, 130.89, 129.95, 128.95, 128.89, 128.63, 128.32, 128.17, 128.08, 127.98, 125.74, 109.45, 99.73, 64.70, 52.18, 31.92, 29.51, 29.44, 29.34, 29.09, 25.53, 22.73, 13.99. **ESI-MS** found: 599.33423, calc. for C34 H43 O4 N6 ([M+NH₄]⁺): 599.33403.

Asymmetric-alkoxy Azoalkane **AZ4n**.

AZ4n
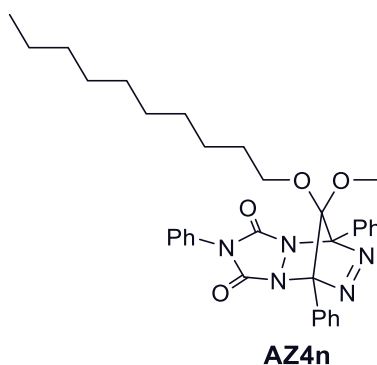
¹H NMR (400 MHz, d6-benzene): δ 0.92 (t, *J*= 7.0 Hz, 3 H), 1.12–1.39 (m, 14 H), 1.45 (quin, *J* = 6.8 Hz, 2 H), 2.51 (s, 3 H), 3.24 (t, *J* = 6.6 Hz, 2 H), 6.72–6.81 (m, 3 H), 7.07 (m, 2 H), 7.19 (m, 2 H), 7.28 (m, 4 H), 8.43 (m, 4 H). **¹³C NMR** (100 MHz, d6-benzene): δ 154.84, 130.86, 129.94, 128.99, 128.86, 128.61, 128.32, 128.19, 128.11, 127.98, 125.79, 109.38, 99.85, 64.77,

52.14, 31.92, 29.67, 29.57, 29.55, 29.36, 29.30, 25.87, 22.73, 13.96. **ESI-MS** found: 599.33417, calc. for C34 H43 O4 N6 ([M+NH$_4$]$^+$): 599.33403.
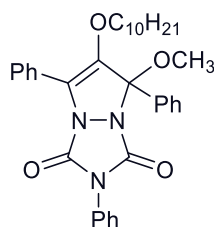
MG$_C$4la

MG$_C$4la: ^{1}**H NMR** (400 MHz, d6-benzene): δ 0.92 (t, *J*= 7.0 Hz, 3 H), 0.95-1.39 (m, 16 H), 3.40 (s, 3 H), 3.56 (td, *J* = 6.4, 2.0 Hz, 2 H), 6.88 (t, *J* = 7.4 Hz, 1 H), 6.98 (t, 8.0 Hz, 2 H), 7.10 (m, 4 H), 7.30 (t, *J* = 8.0, 2 H), 7.47 (m, 2 H), 7.77 (m, 2 H), 8.09 (m, 2 H). ^{13}**C NMR** (100 MHz, d6-benzene): δ 150.75, 149.86, 138.47, 137.19, 131.80, 128.98, 126.82, 125.37, 123.01, 96.88, 71.39, 50.83, 31.93, 29.61, 29.52, 29.48, 29.36, 29.03, 25.50, 22.74, 14.00.
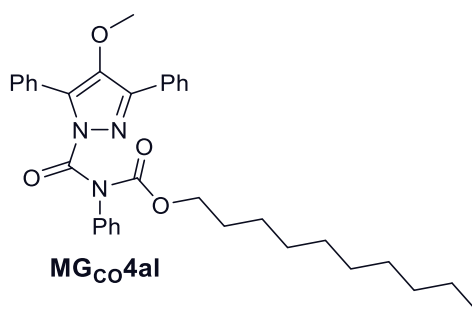
MG$_{CO}$4al

MG$_{CO}$4al: ^{1}**H NMR** (400 MHz, d6-benzene): δ 0.92 (t, *J*= 7.0 Hz, 3 H), 0.95–1.40 (m, 16 H), 3.34 (s, 3 H), 3.52 (t, *J* = 6.4 Hz, 2 H), 6.92 (t, *J* = 7.4 Hz, 1 H), 7.00 (t, 7.8 Hz, 2 H), 7.11 (m, 1 H), 7.21 (m, 3 H), 7.31 (m, 4 H), 7.73 (m, 2 H), 8.39 (m, 2 H).

Crossover experiments
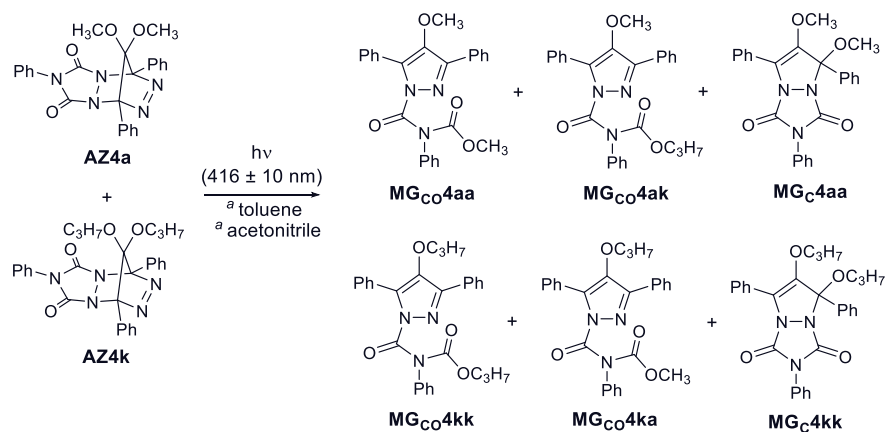
a The solvents were dried with 3 Å MS that was dried at 300 °C for 24 h in vacuo.
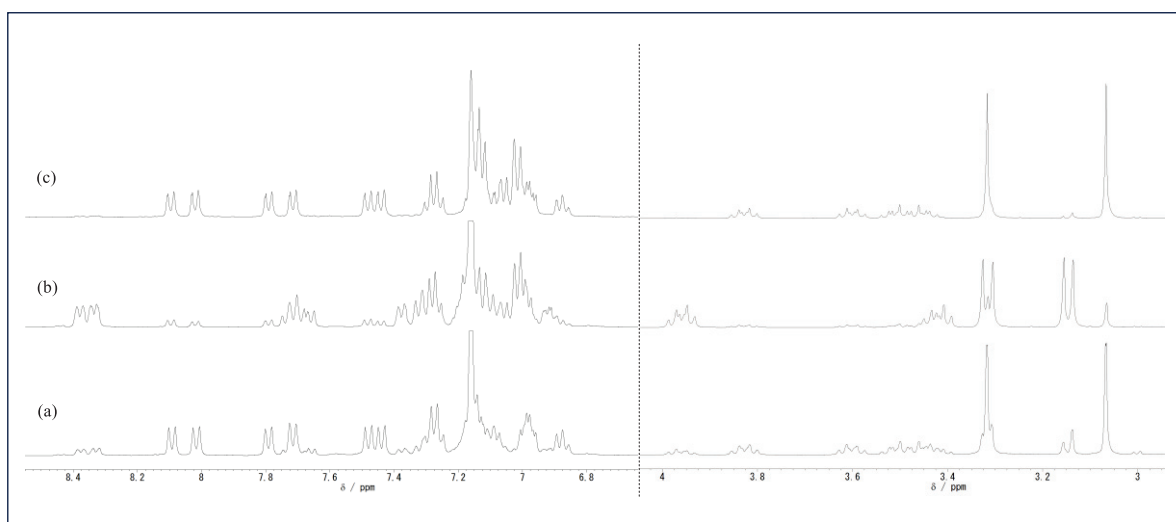
Figure 44. ^{1}H NMR (400 MHz, d6-benzene) spectra after photodenitrogenation of 1:1 mixture **AZ4a** and **AZ4k**.

(a) in acetonitrile at 293 K, (b) in toluene at 293 K, (c) in toluene at 323 K *toluene
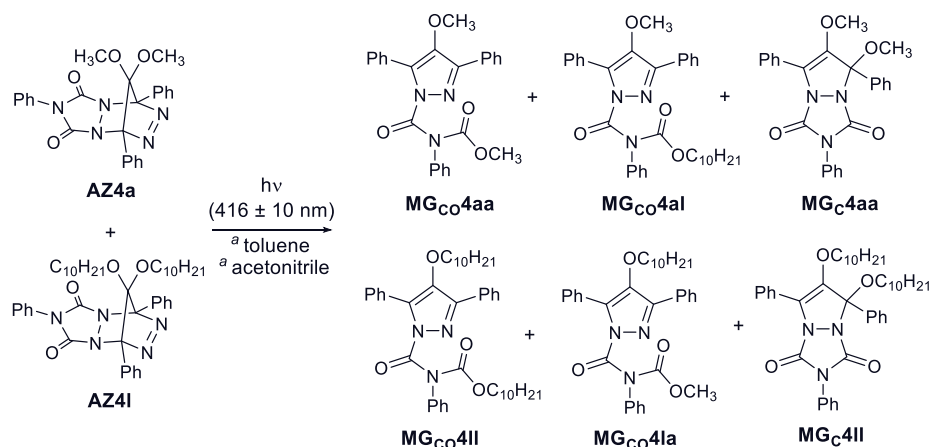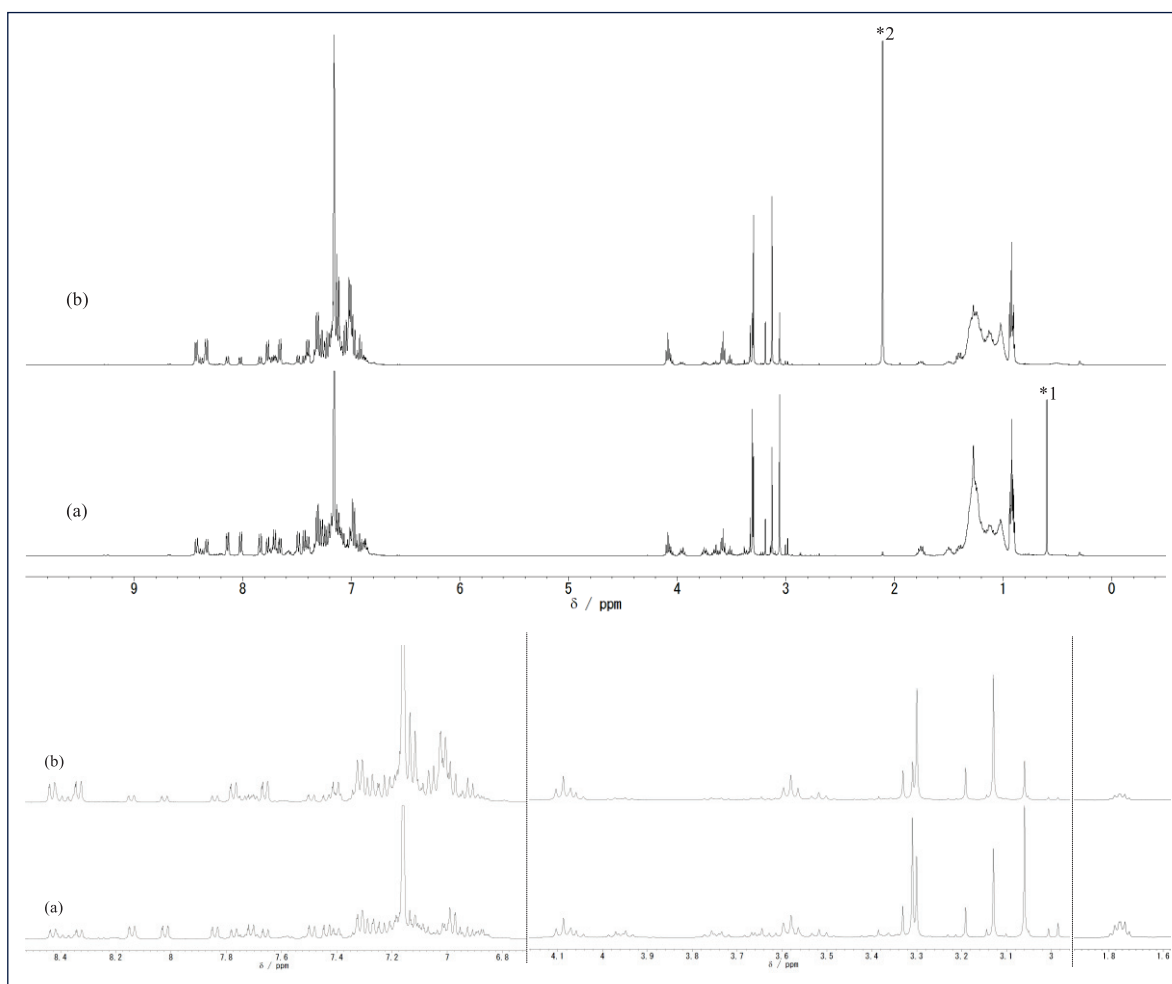
Figure 45. ^{1}H NMR (400 MHz, d6-benzene) spectra after photodenitrogenation of 1:1 mixture **AZ4a** and **AZ4l** (a) in acetonitrile at 293 K, (b) in toluene at 293 K. *1: H_2O, *2: toluene
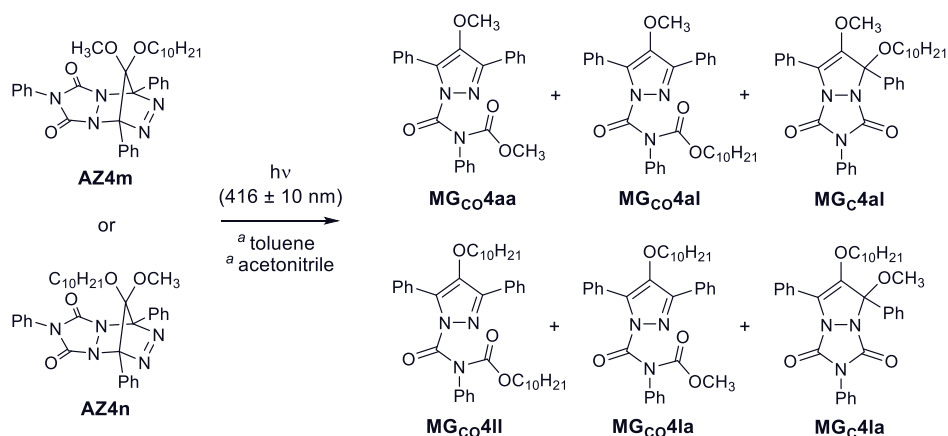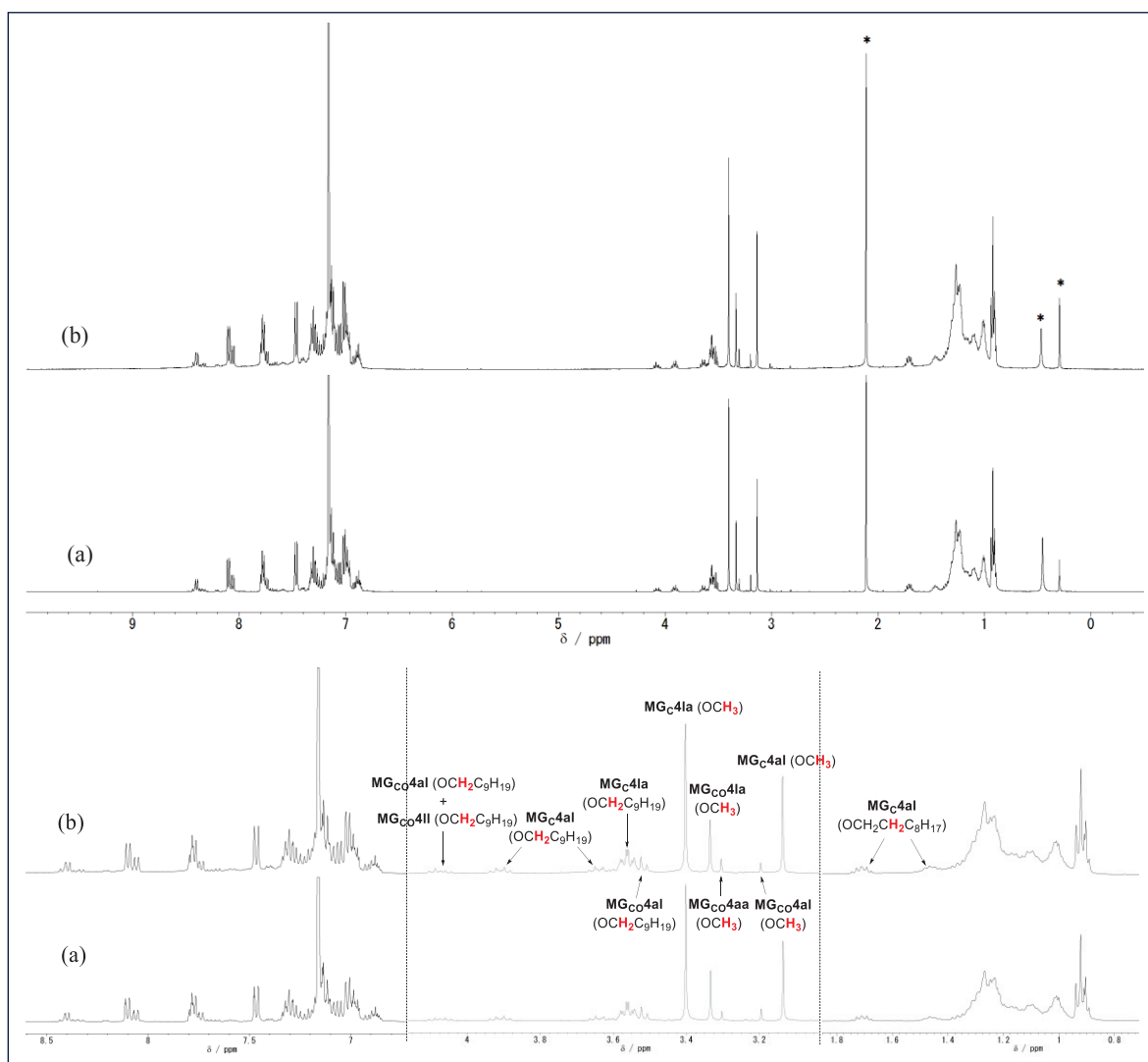
Figure 46. ^{1}H NMR (400 MHz, d6-benzene) spectra after photodenitrogenation of (a) **AZ4m** and (b) **AZ4n** in toluene at 323 K, respectively. * H$_2$O, toluene

Spin-trapping experiments

[PBN-R(OMe)]⁺

C37 H37 O6 N4

(m/z: 633.27190 δ: 1.798)

[**MG4b** + H]⁺

C27 H26 O6 N3

(m/z: 488.18178 δ: 0.344)
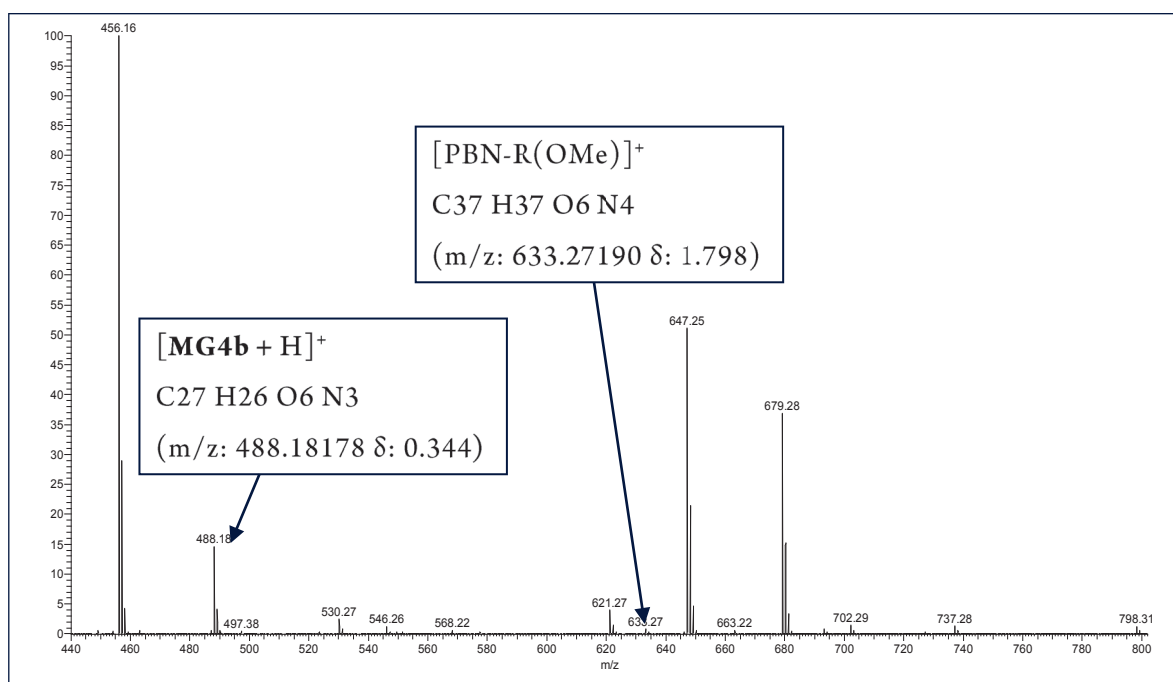
Figure 47. The mass spectrum using Atmospheric Pressure Chemical Ionization (APCI method) obtained from the photoreaction **AZ4b** in the presence of PBN in benzene.
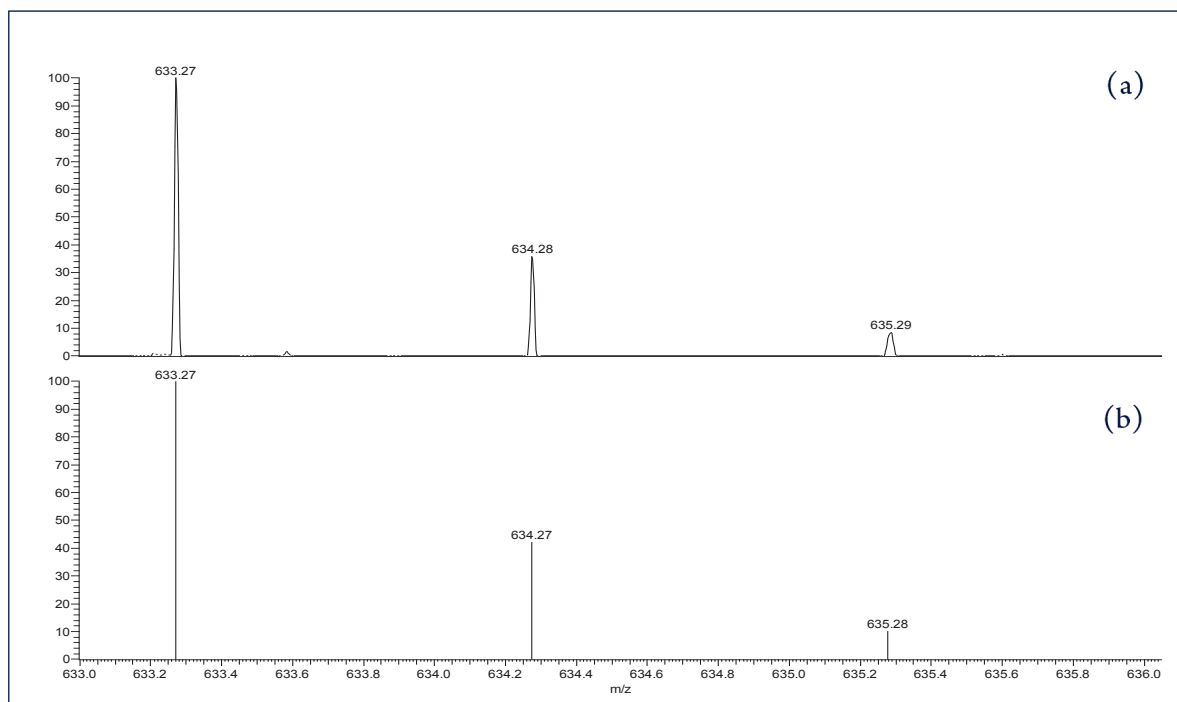
Figure 48. a) spin adduct PBN-R(MeO) (m/z 633.27), b) computer simulation of (a).

Chart 1. Expected molecular structures observable by means of mass spectroscopic analysis for this spin-trapping experiments.
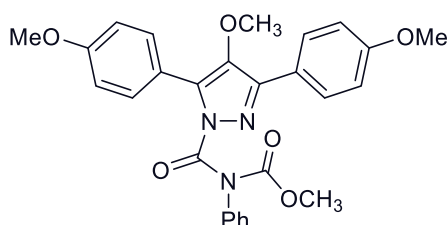
MG$_{CO}$4b
Chemical Formula: $C_{27}H_{25}N_3O_6$
Exact Mass: 487.17
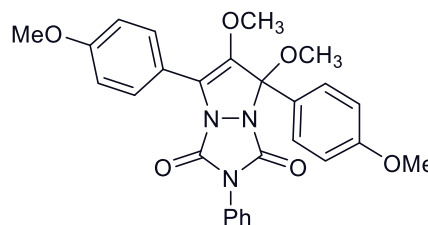
MG$_C$4b
Chemical Formula: $C_{27}H_{25}N_3O_6$
Exact Mass: 487.17
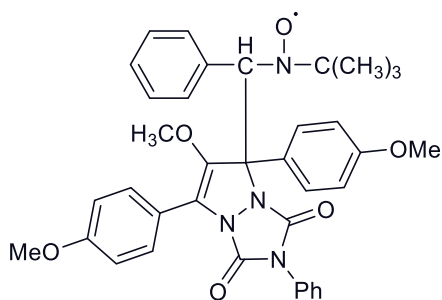
Spin adducts: **PBN-R(OMe)**
Chemical Formula: $C_{37}H_{37}N_4O_6{}^{\bullet}$
Exact Mass: 633.27
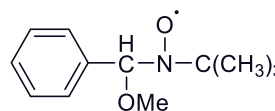
Spin adducts: **PBN-OMe**
Chemical Formula: $C_{12}H_{18}NO_2{}^{\bullet}$
Exact Mass: 208.13

(a)

$A_1{}^N = 13.53$ G
$A_1{}^{H\beta} = 1.97$ G

P_1

$A^N = 15.42$ G

During irra.
Immediately after 10 min irra.
21 days later

AZ4a : PBN
1:6

(b)

$A_2{}^N = 13.22$ G
$A_2{}^{H\beta} = 1.53$ G
$A_3{}^N = 14.17$ G
$A_3{}^{H\beta} = 4.57$ G

P_2

P_3

During irra.
Immediately after 10 min irra.
2.5 hours later
16 hours later

AZ4f : PBN
1:6
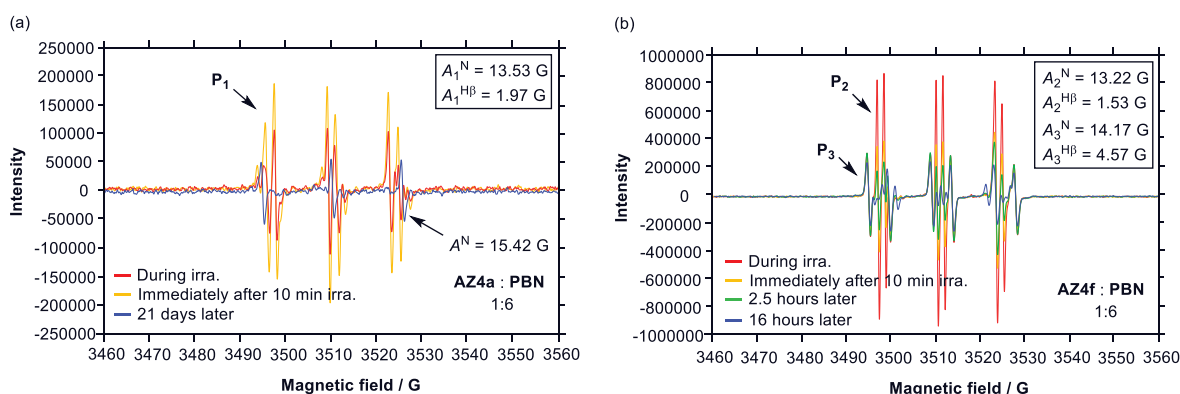
Figure 49. Spin-trapping experiments using EPR measurement. EPR spectrum obtained from the photoreaction of (a) **AZ4a** (X = Y = H) and PBN in benzene at room temperature. (b) **AZ4f** (X = Y = Br) and PBN.

Regioselectivity of alkoxy-group migration reactions

Asymmetric substituted azoalkane **AZ4i** ((*p*-OMe, *p*-H)-**AZ**).

AZ4i
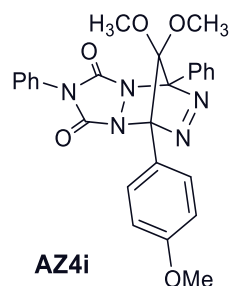
^{1}**H NMR** (400 MHz, d6-benzene): δ 2.46 (s, 3 H), 2.84 (s, 3 H), 3.23 (s, 3H), 6.77 (m, 3 H), 6.87 (d, *J* = 8.8 Hz, 2 H), 7.12 (m, 3 H), 7.25 (t, *J* = 7.6 Hz, 2 H), 8.28 (d, *J* = 8.8 Hz, 2 H), 8.35 (m, 2 H). **ESI-MS** found: 508.15875, calc. for $C_{26} H_{23} O_5 N_5 Na$ ([M+Na]$^+$): 508.15914.

Asymmetric substituted azoalkane **AZ4j** ((*p*-CN, *p*-H)-**AZ**).

AZ4j
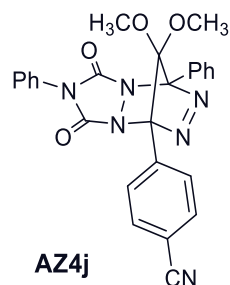
^{1}**H NMR** (400 MHz, d6-benzene): δ 2.25 (s, 3 H), 2.64 (s, 3 H), 6.79 (m, 3 H), 7.09 (m, 5 H), 7.98 (m, 2 H), 8.28 (m, 2 H). **ESI-MS** found: 503.14322, calc. for $C_{26} H_{20} O_4 N_6 Na$ ([M+Na]$^+$): 503.14382.
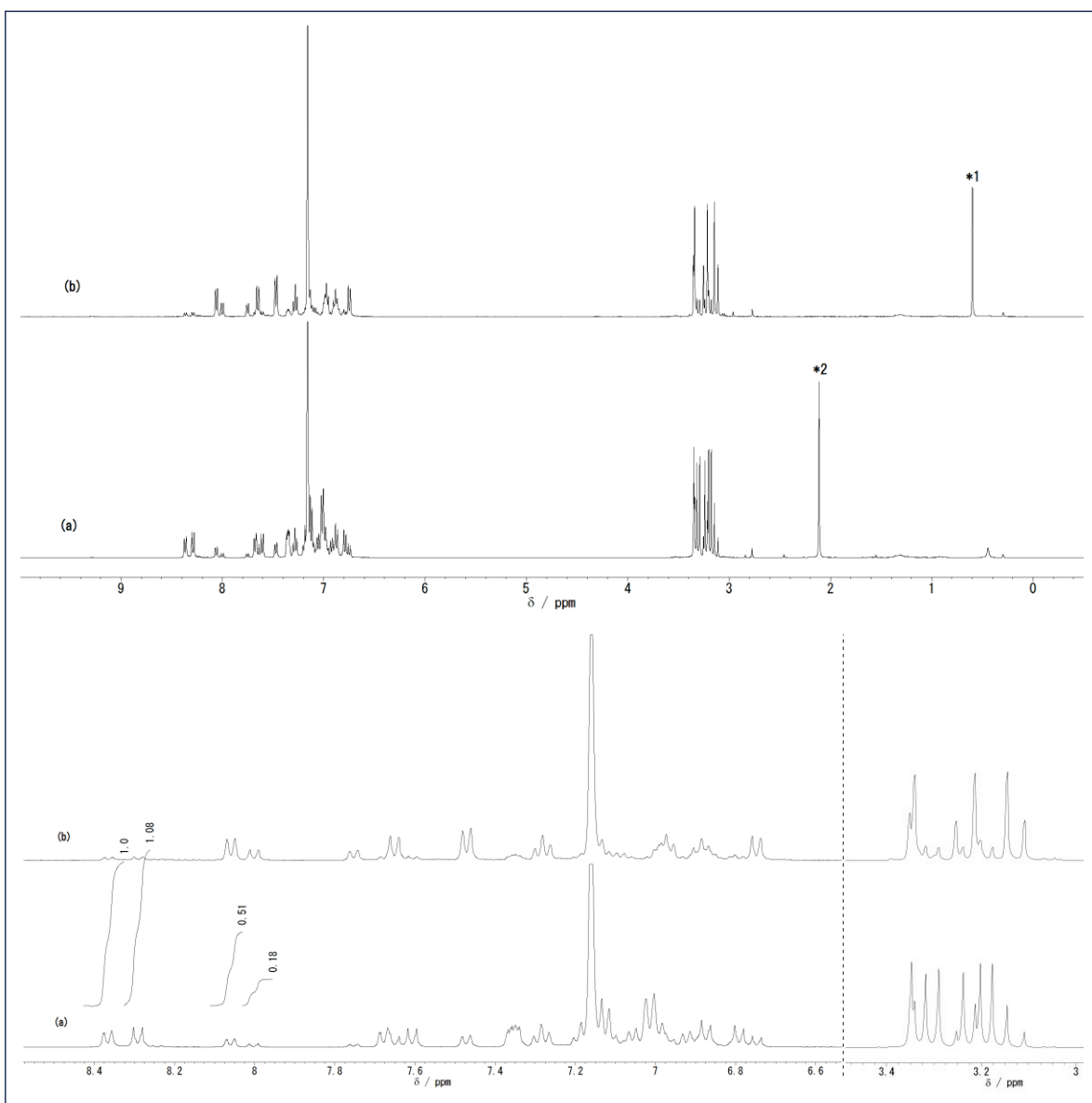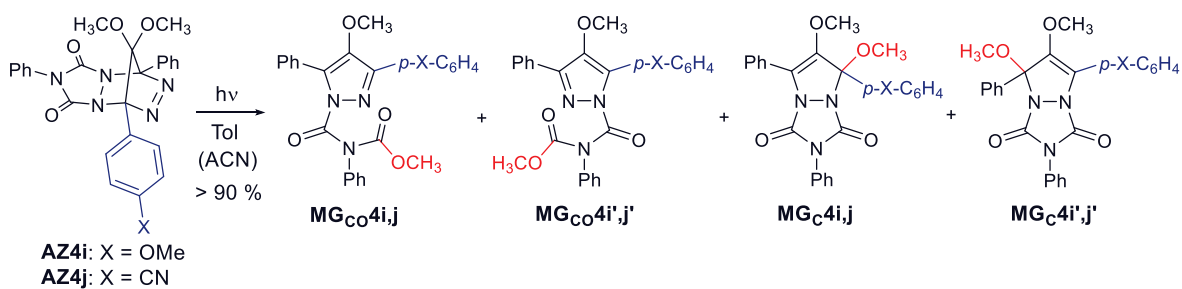
Figure 50. ^{1}H NMR (400 MHz, d6-benzene) spectra after photodenitrogenation of **AZ4i** in (a) toluene at 298 K and (b) acetonitrile at 298 K, respectively. *1: H$_2$O, *2: toluene
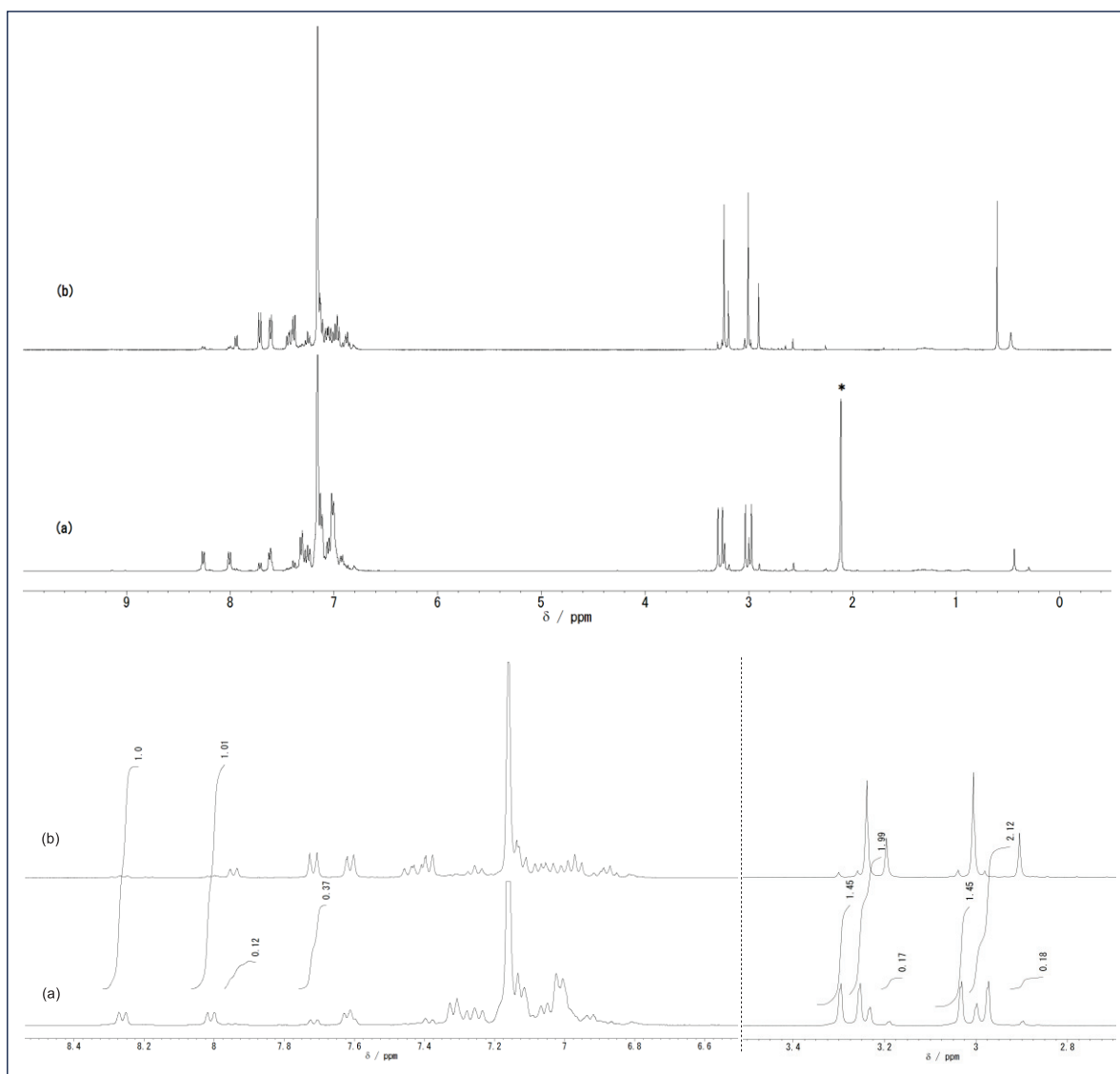
Figure 51. ^{1}H NMR spectrum after photodenitrogenation of **AZ4j** in (a) toluene, (b) acetonitrile. * H_2O, toluene

Effect of temperature on regioselectivity of alkoxy-group migration reactions
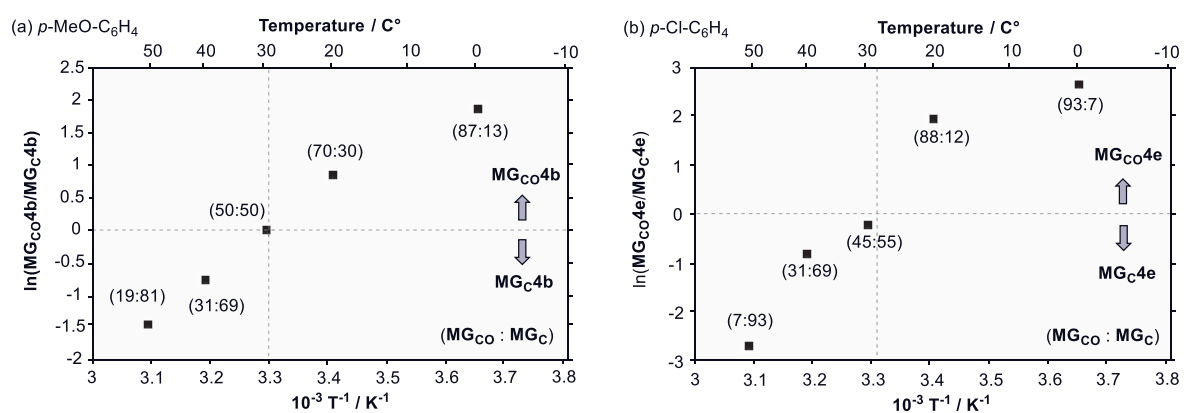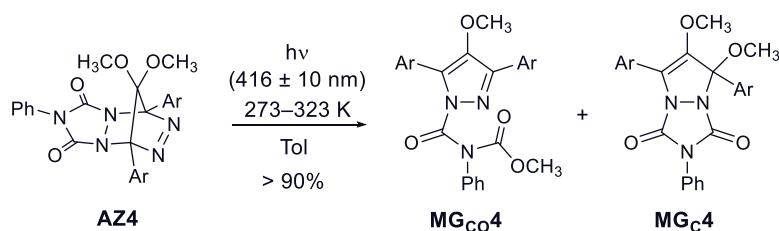
Figure 52. Temperature dependence on the alkoxy-migrated products rate (**MG$_{CO}$4** vs. **MG$_C$4**). aryl-substituted: (a) p-MeO-C$_6$H$_4$, (b) p-Cl-C$_6$H$_4$
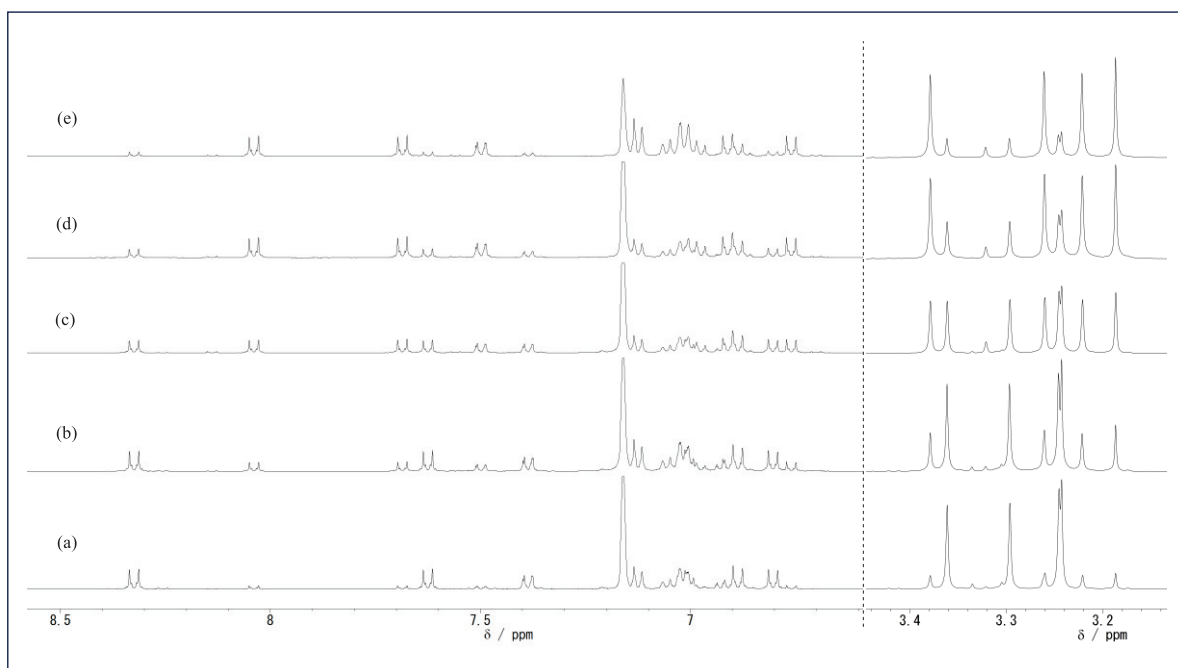
Figure 53. ^{1}H NMR spectroscopic analyses for photodenitrogenation of **AZ4b** in toluene in a variety of reaction temperature; (a) 273 K, (b) 293 K, (c) 303 K, (d) 313 K and (e) 323 K.
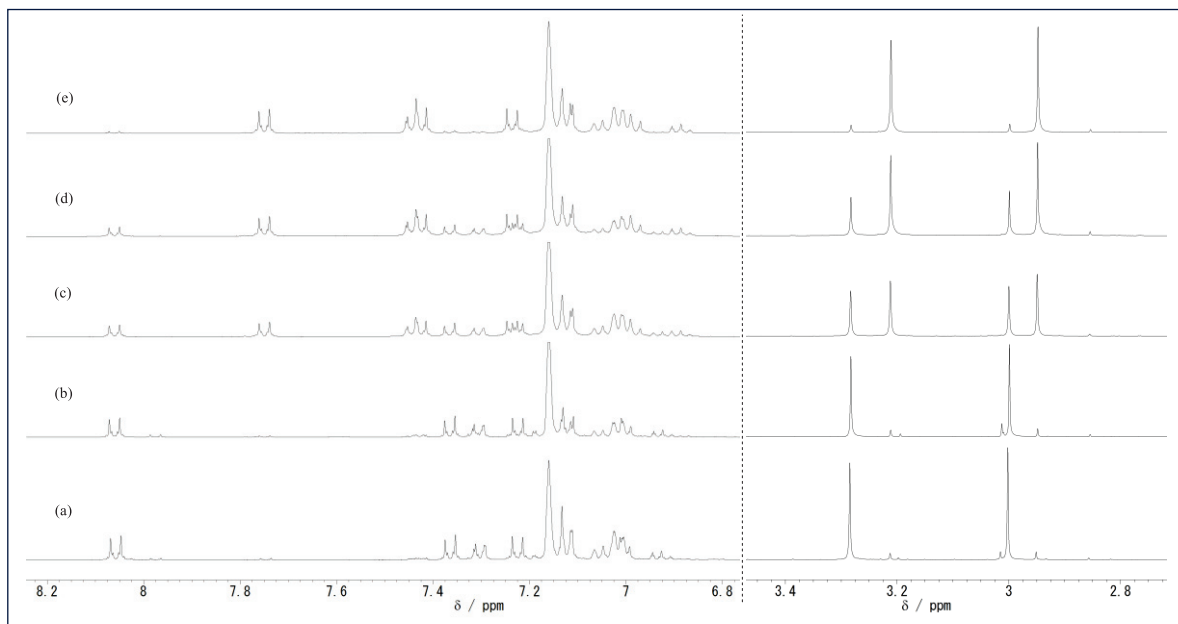
Figure 54. ^{1}H NMR spectroscopic analyses for photodenitrogenation of **AZ4e** in toluene in a variety of reaction temperature; (a) 273 K, (b) 293 K, (c) 303 K, (d) 313 K and (e) 323 K.

Alkoxy-migrated product **MG_{CO}4b**.
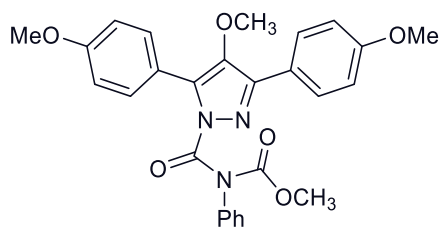
MG_{CO}4b

¹H NMR (400 MHz, d6-benzene): δ 3.24 (s, 6 H), 3.29 (s, 3H), 3.36 (s, 3H), 6.80 (d, *J* = 8.8 Hz, 2 H), 6.90 (m, 3 H), 7.01 (t, *J* = 7.8 Hz, 2 H), 7.39 (d, *J* = 7.2 Hz, 2 H),7.63 (d, *J* = 8.8 Hz, 2 H), 8.33 (d, *J* = 9.2 Hz, 2 H). **¹³C NMR** (100 MHz, d6-benzene): δ 160.57, 160.23, 154.51, 151.31, 145.52, 143.62, 138.69, 136.57, 136.15, 131.62, 131.20, 128.92, 128.88, 128.59, 128.32, 127.98, 127.88, 127.68, 124.13, 123.79, 120.90, 119.29, 114.22, 113.70, 113.31, 60.57, 54.44, 54.38, 53.38. **ESI-MS** found: 510.16330, calc. for C27 H25 O6 N3 Na ([M+Na]⁺): 510.16356.

Alkoxy-migrated product **MG_{CO}4e**.
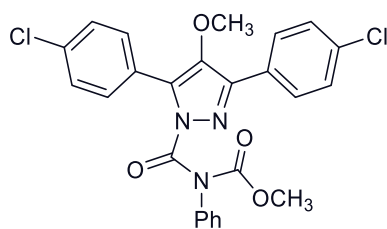
MG_{CO}4e

¹H NMR (400 MHz, d6-benzene): δ 3.00 (s, 3 H), 3.28 (s, 3H), 6.91 (m, 1 H), 7.00–7.06 (m, 4 H), 7.22 (m, 2 H), 7.30 (m, 2 H),7.36 (m, 2 H), 8.06 (m, 2 H). **¹³C NMR** (100 MHz, d6-benzene): δ 154.63, 151.38, 144.72, 144.25, 138.64, 135.46, 134.20, 131.48, 130.08, 128.84, 128.65, 128.54, 128.18, 127.95, 127.24, 61.06, 53.86.

3.9 Supplementary material
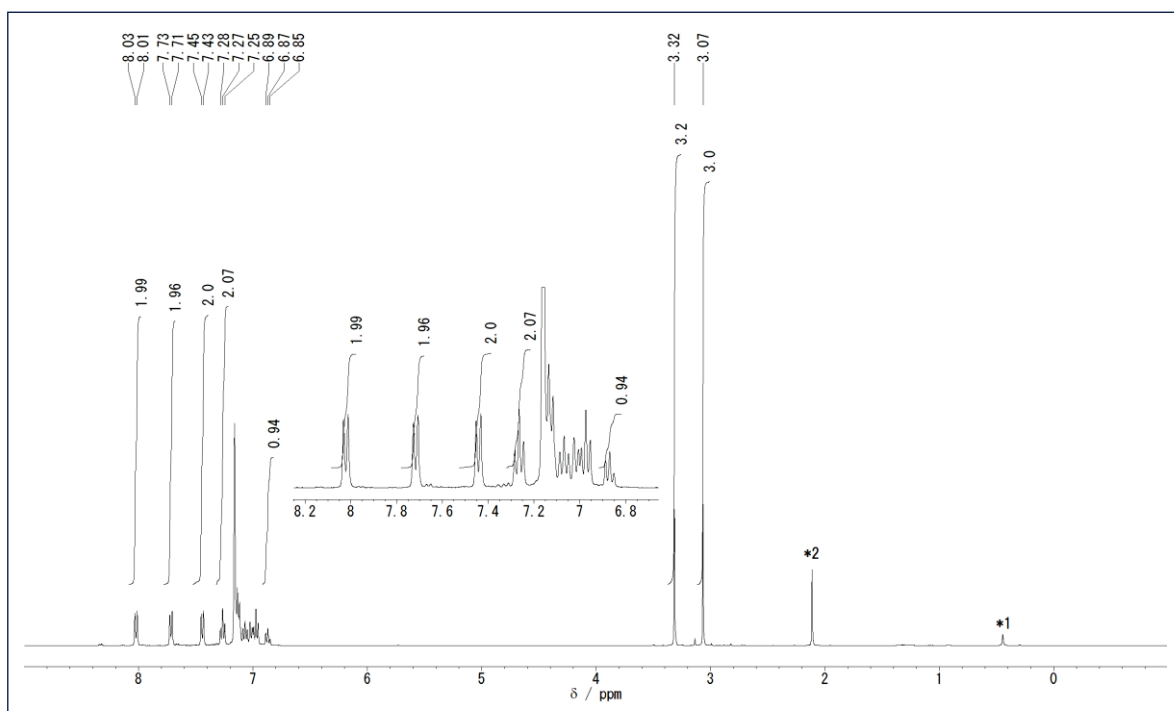
Figure 55. ^{1}H NMR (400 MHz, d6-benzene) spectrum of **MG$_C$4aa**. *1: H$_2$O, *2: toluene
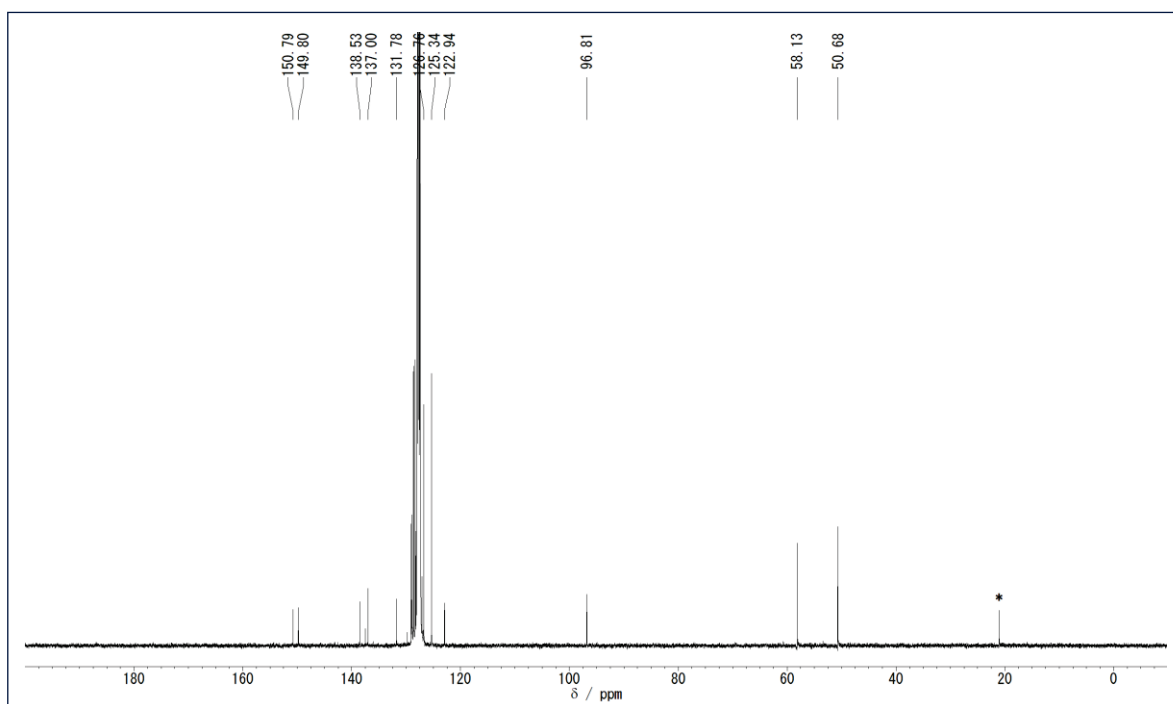
Figure 56. ^{13}C NMR (100 MHz, d6-benzene) spectrum of **MG$_C$4aa**. * toluene
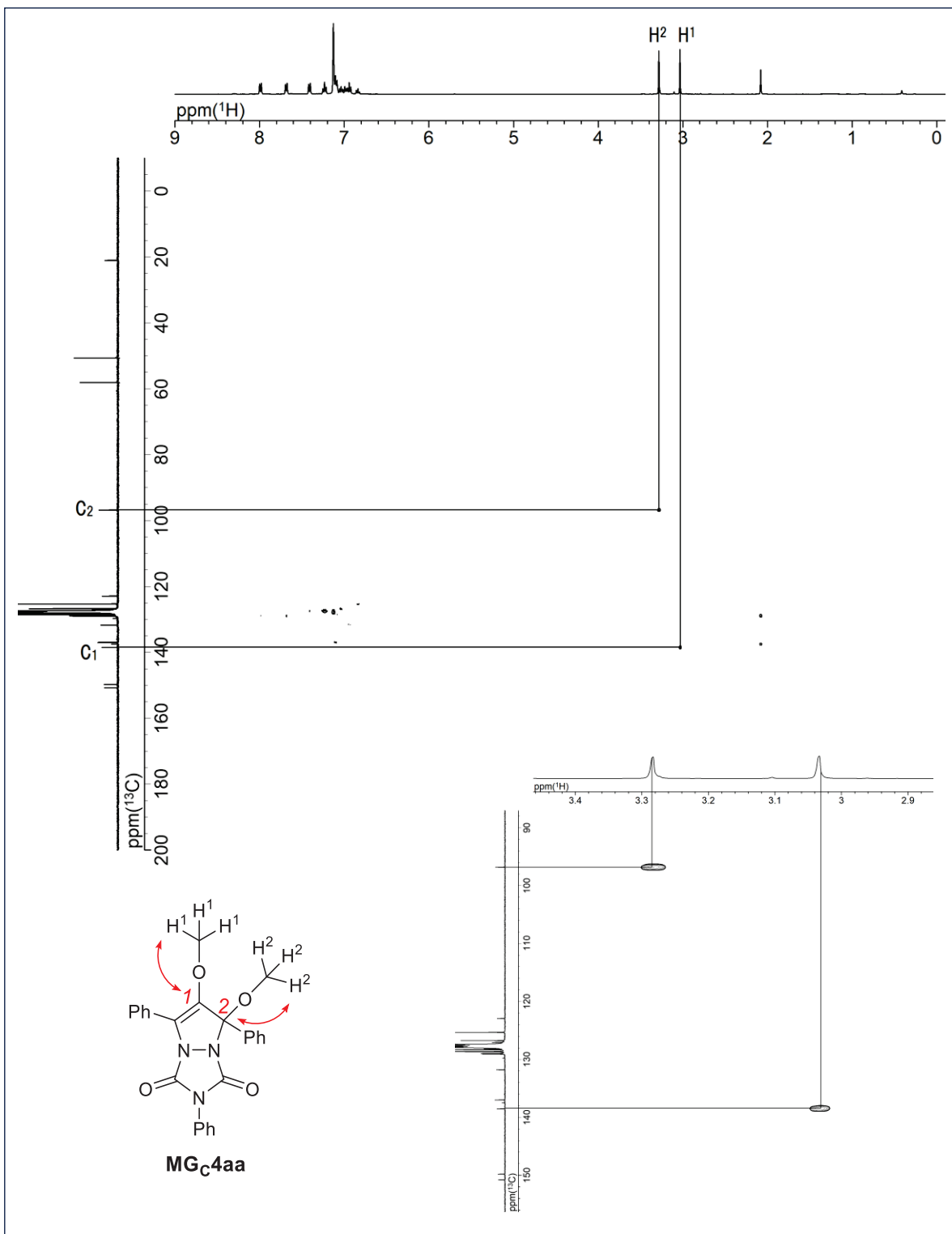
Figure 57. ^{1}H, ^{13}C-HMBC (d6-benzene) spectrum of **MG$_C$4aa**.
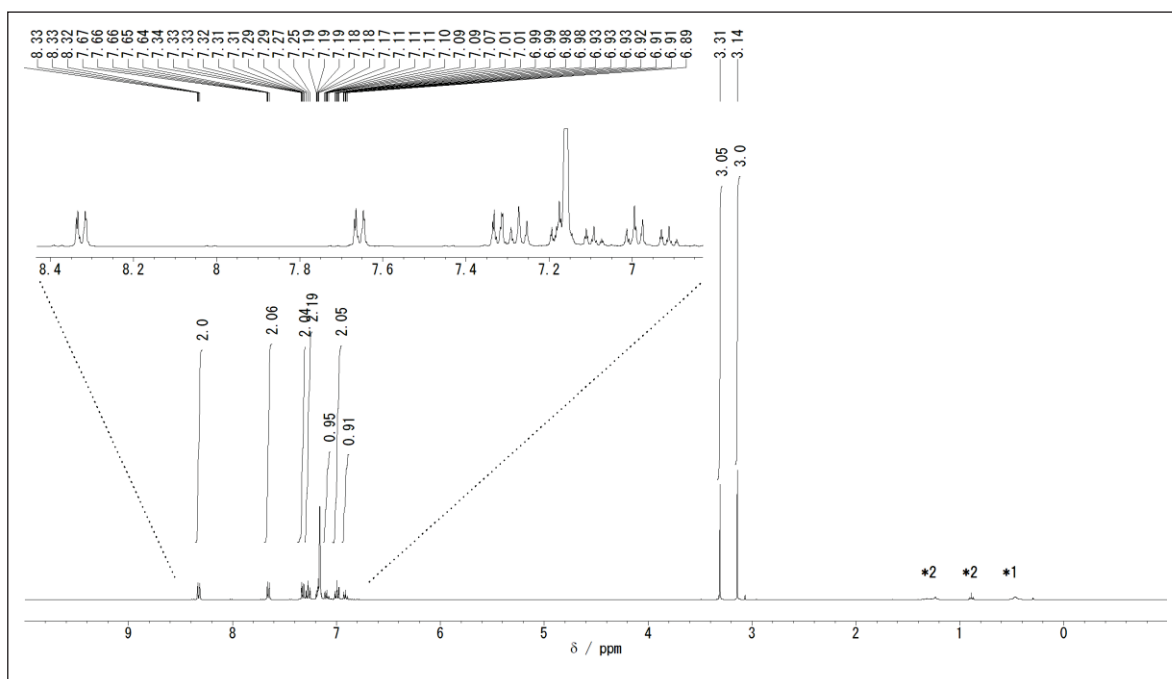
Figure 58. ^{1}H NMR (400 MHz, d6-benzene) spectrum of **MG$_{Co}$4aa**. *1: H_2O, *2: hexane
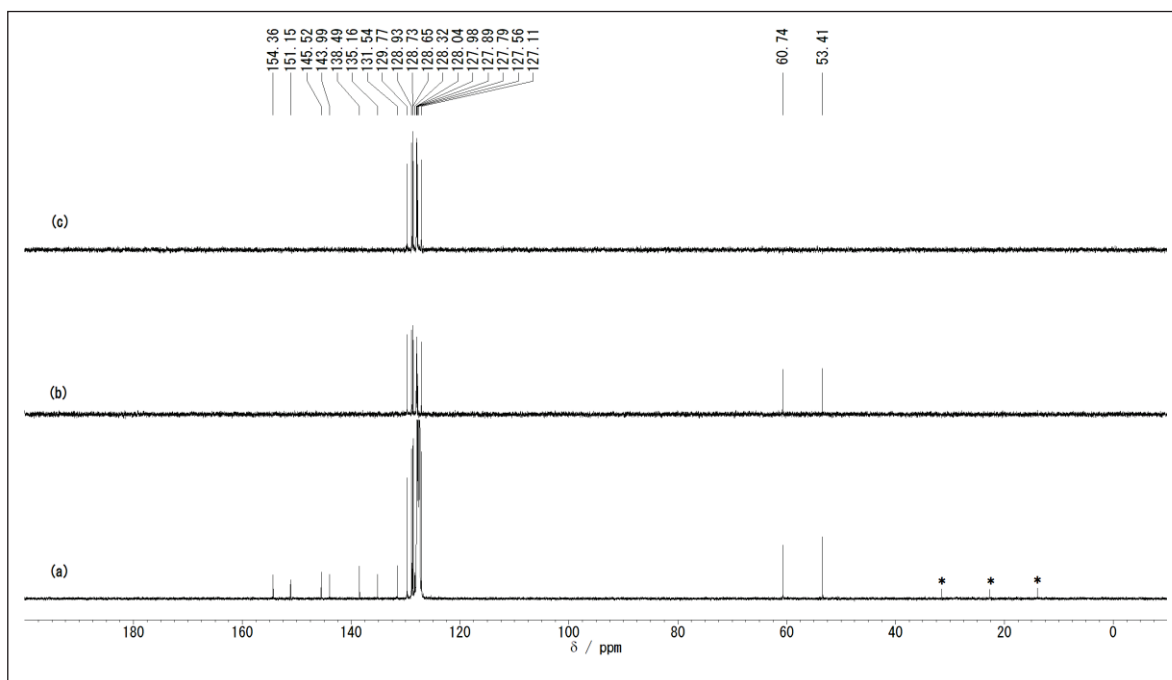
Figure 59. (a) ^{13}C NMR (100 MHz, d6-benzene) spectra of **MG$_{Co}$4aa**. (b) DEPT135, (c) DEPT90. * hexane

103
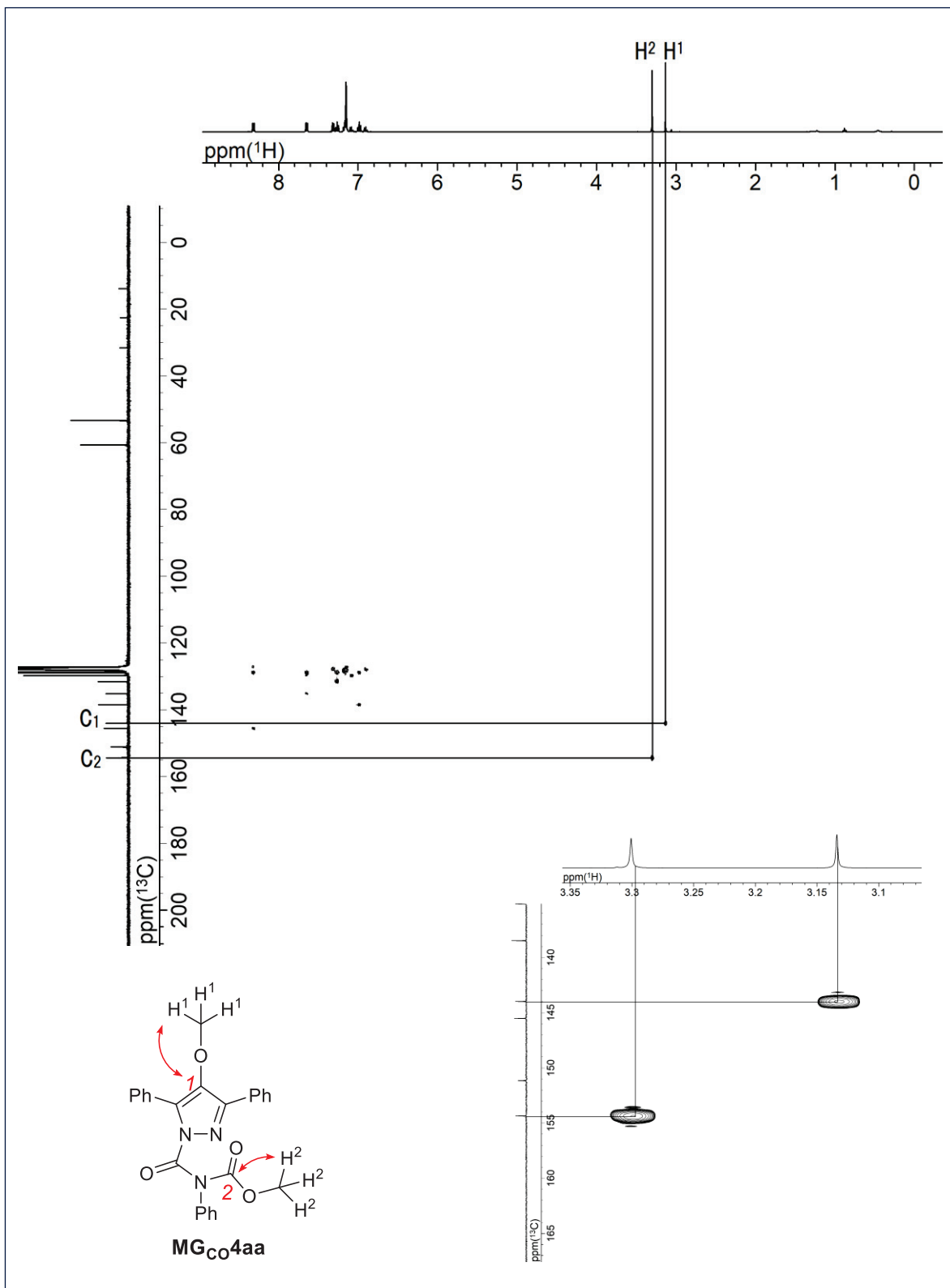
Figure 60. ^{1}H, ^{13}C-HMBC (d6-benzene) spectrum of **MG$_{CO}$4aa**.

104
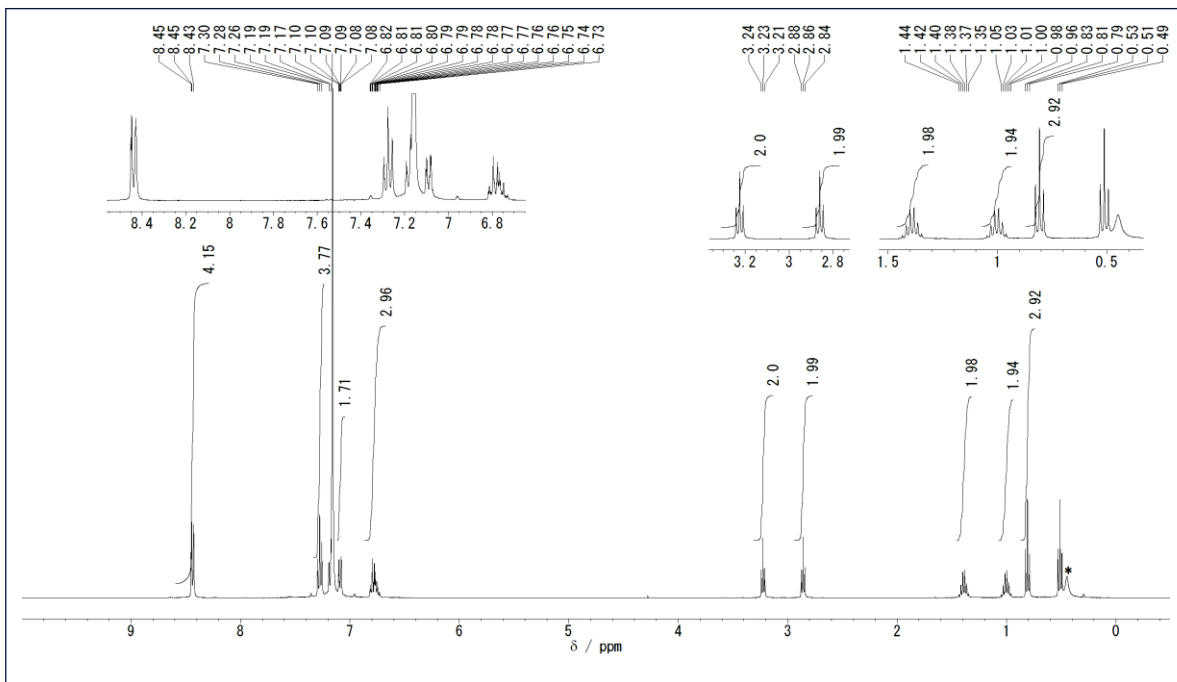
Figure 61. ^{1}H NMR (400 MHz, d6-benzene) spectrum of **AZ4k**. * H_2O
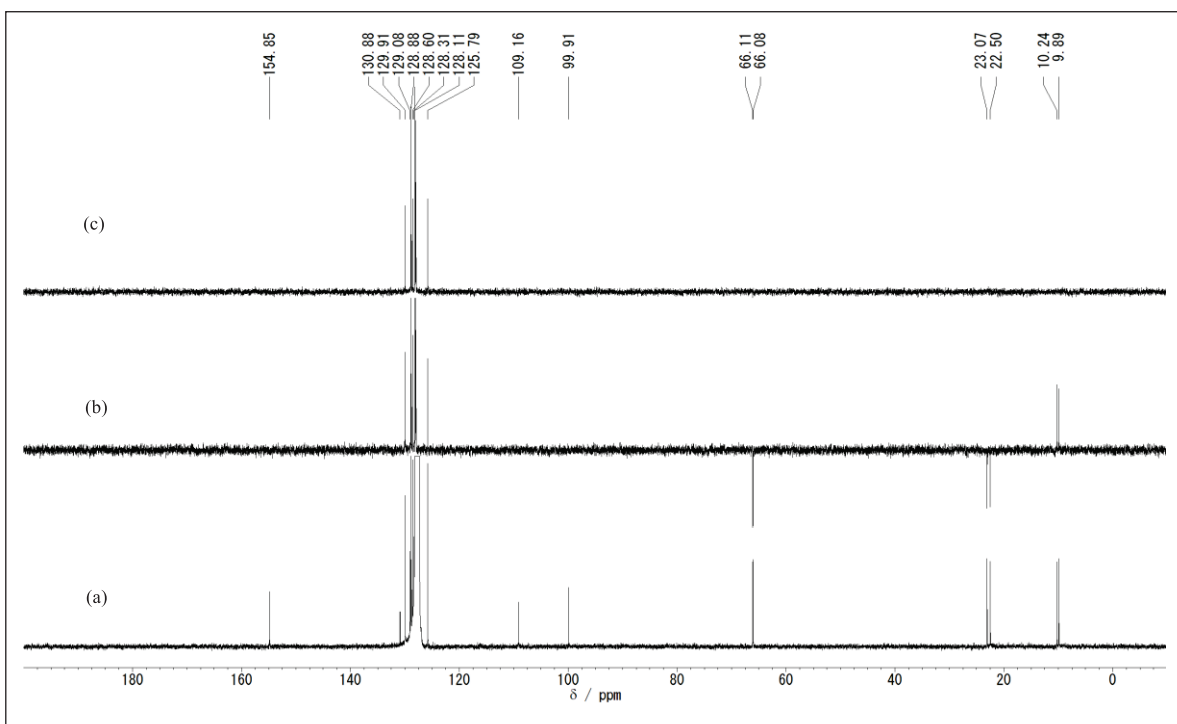
Figure 62. (a) ^{13}C NMR (100 MHz, d6-benzene) spectra of **AZ4k**. (b) DEPT135, (c) DEPT90.
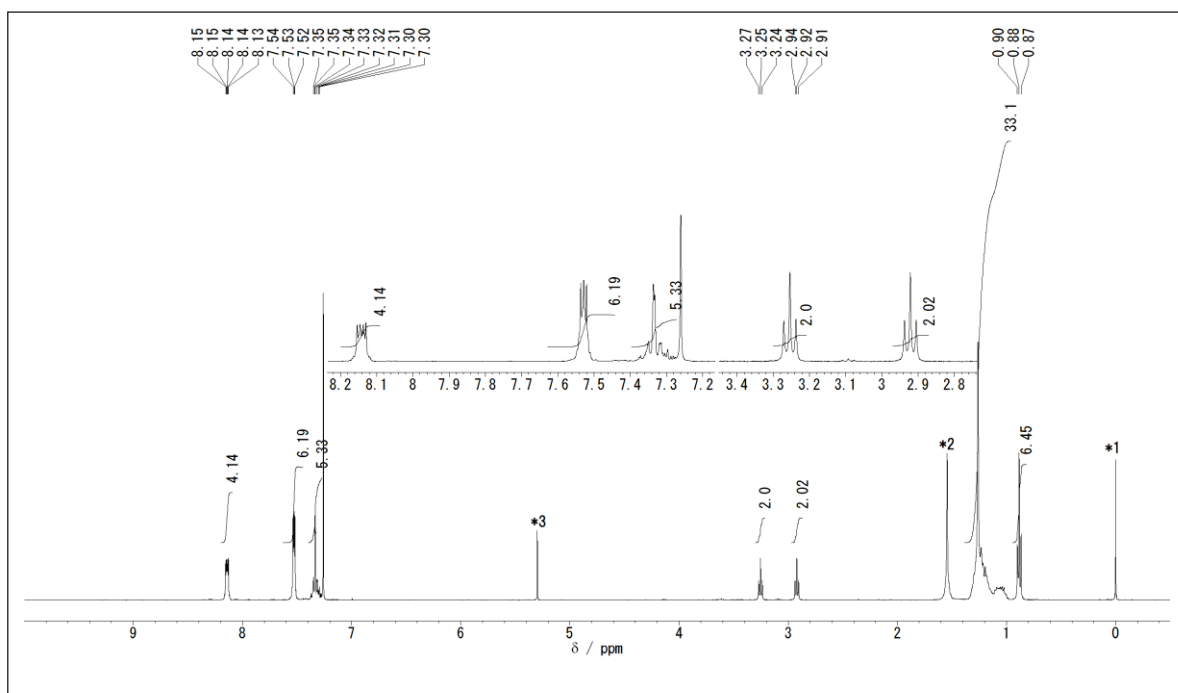
Figure 63. ^{1}H NMR (500 MHz, d1-chloroform) spectrum of **AZ4l**. *1: TMS, *2: H$_2$O, *3: CH$_2$Cl$_2$
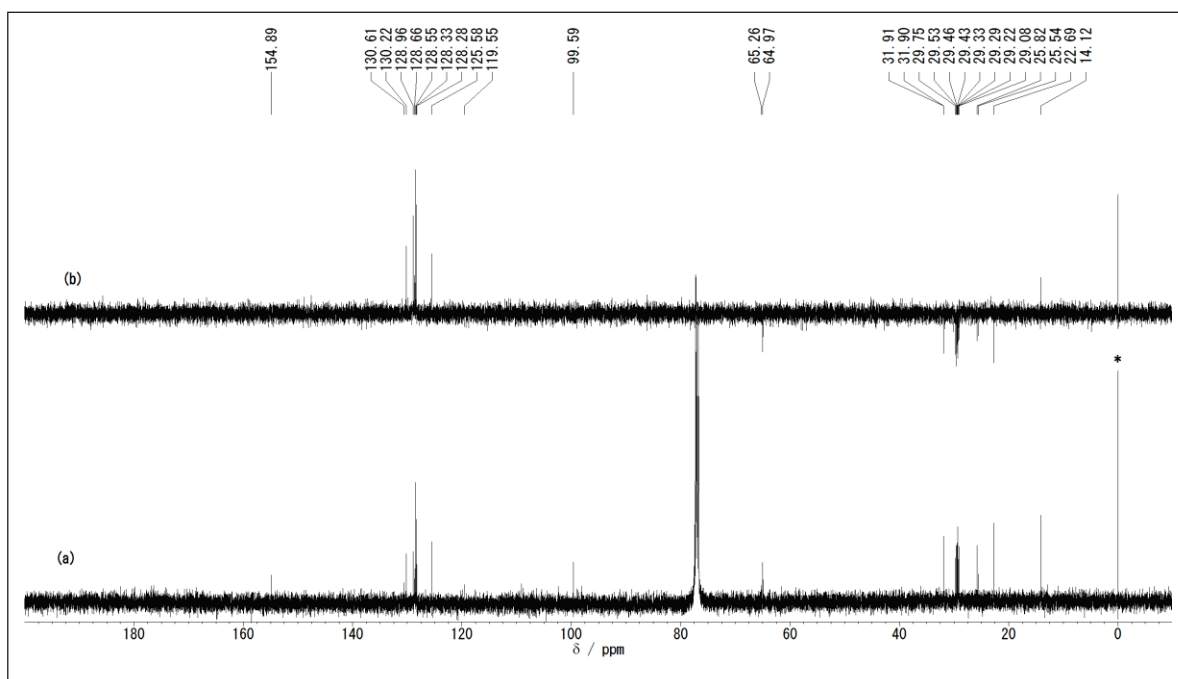
Figure 64. (a) ^{13}C NMR (125 MHz, d1-chloroform) spectra of **AZ4l**. (b) DEPT135. * TMS
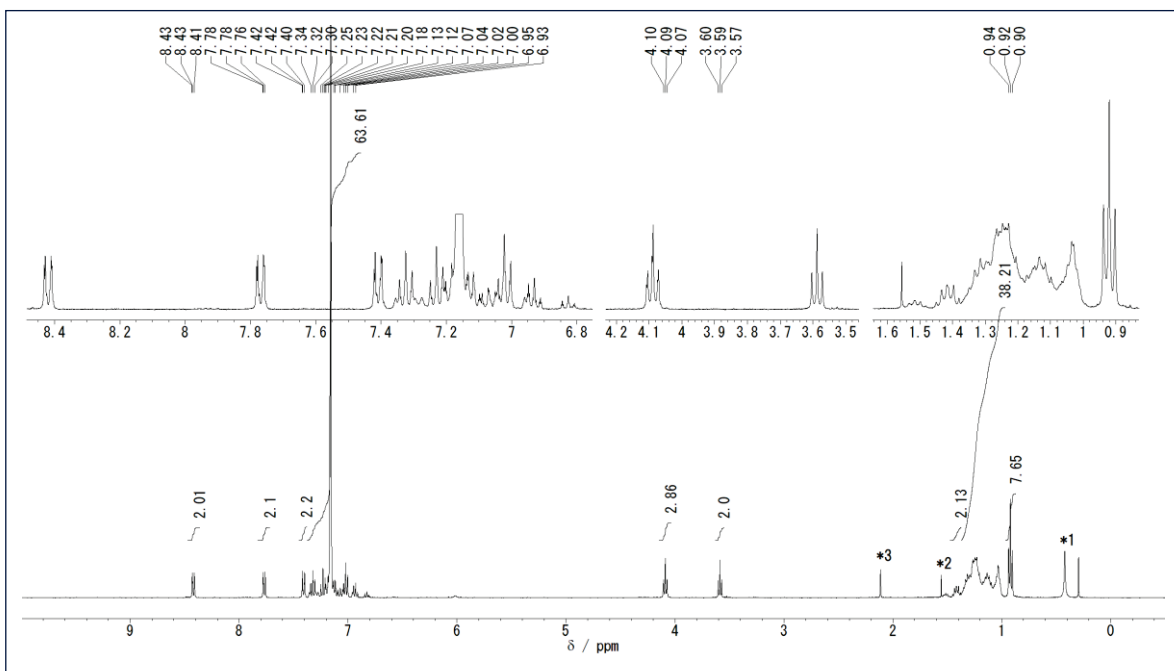
Figure 65. ¹H NMR (400 MHz, d6-benzene) spectrum of **MG$_{co}$4ll**. *1: H$_2$O, *2: acetone, *3: toluene
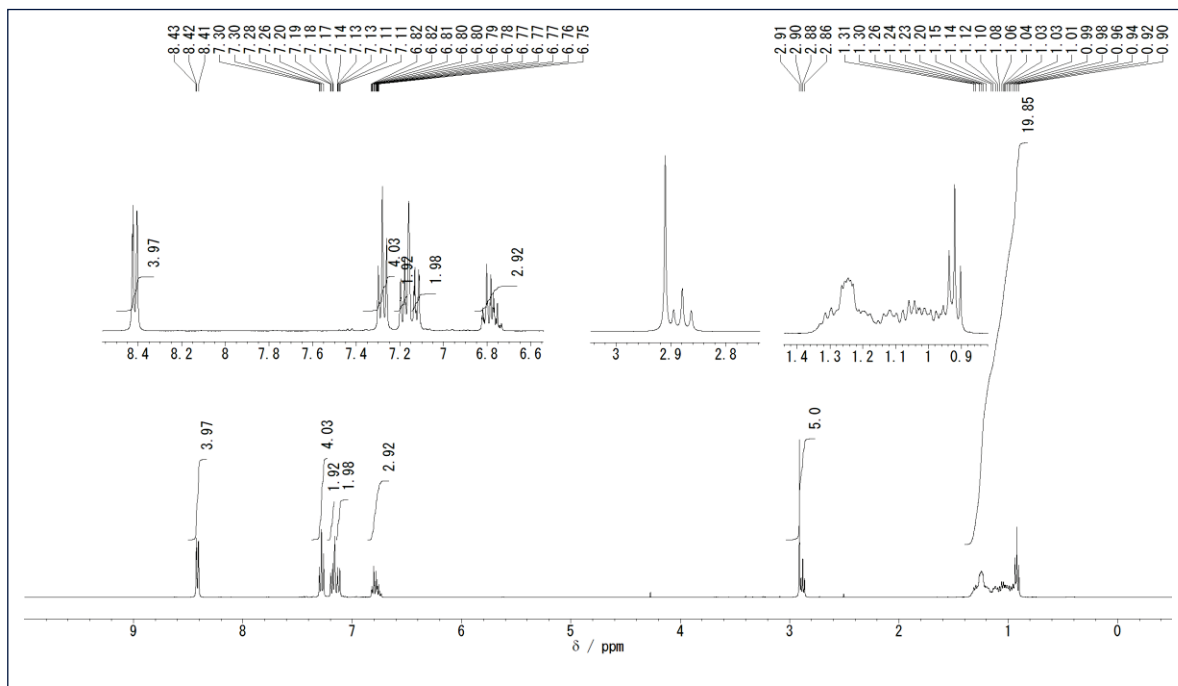
Figure 66. ¹H NMR (400 MHz, d6-benzene) spectrum of **AZ4m**.
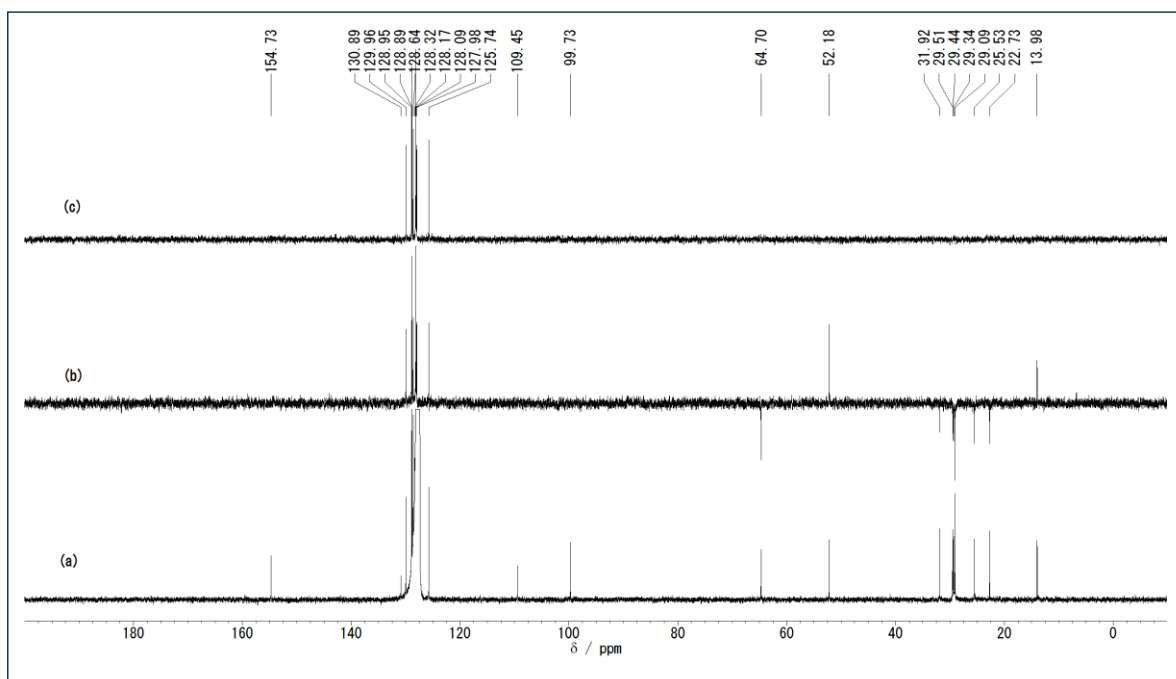
Figure 67. (a) ^{13}C NMR (100 MHz, d6-benzene) spectra of **AZ4m**. (b) DEPT135, (c) DEPT90.
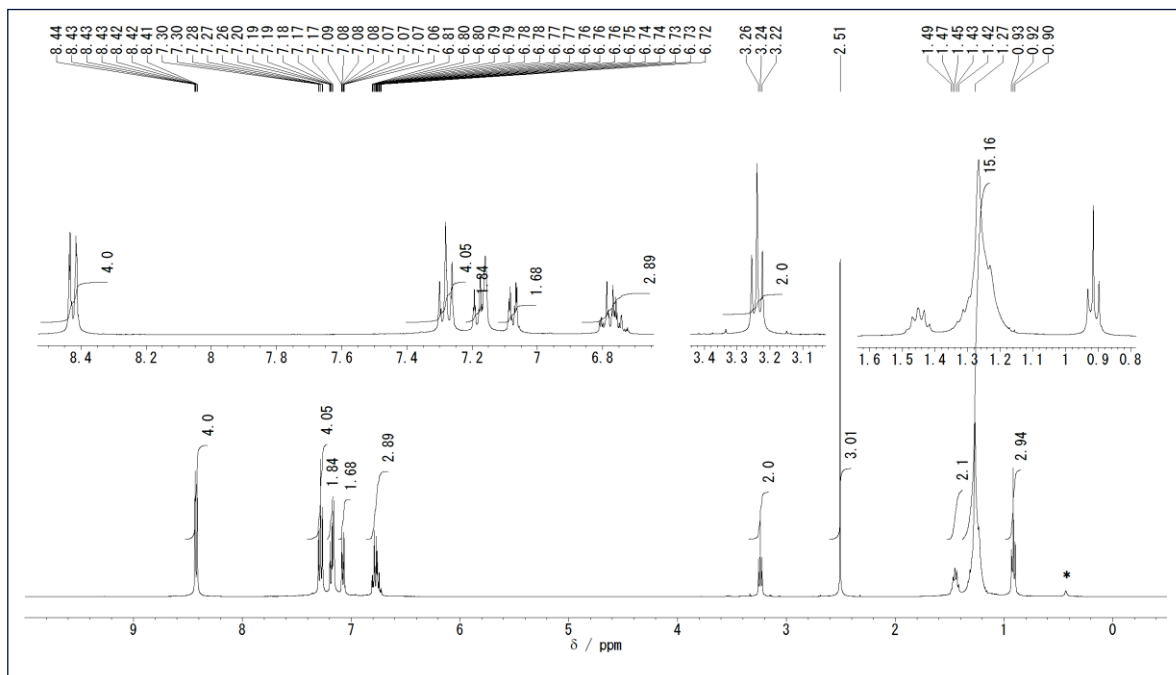
Figure 68. ^{1}H NMR (400 MHz, d6-benzene) spectrum of **AZ4n**. * H$_2$O
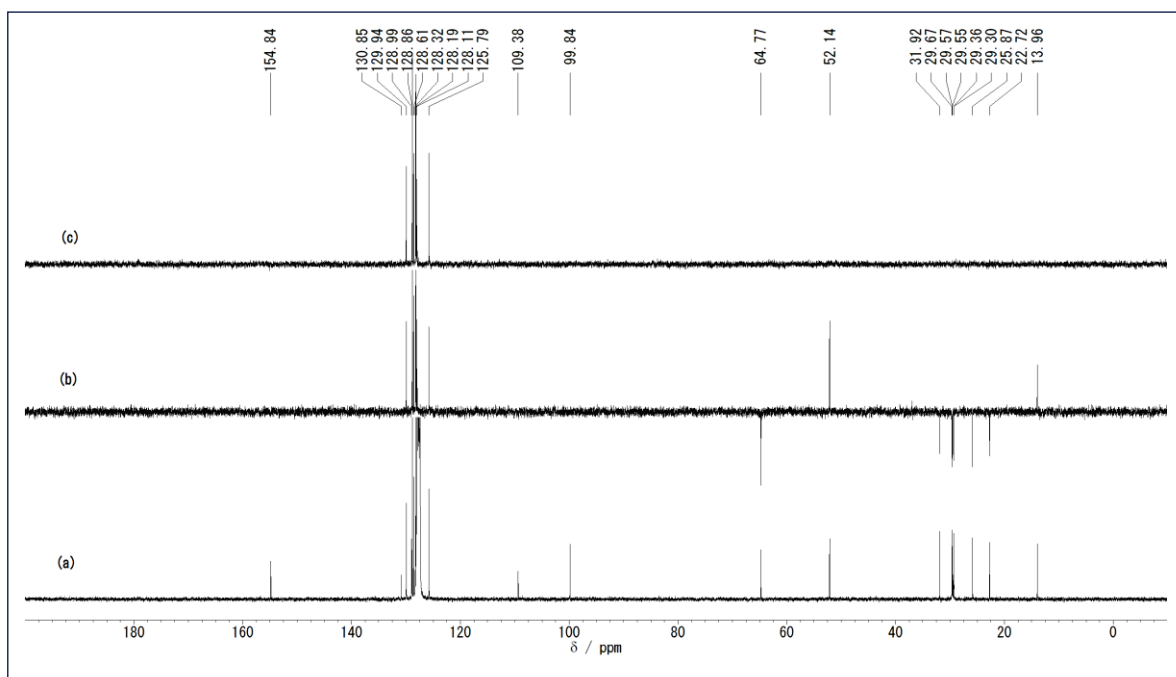
Figure 69. (a) ^{13}C NMR (100 MHz, d6-benzene) spectra of **AZ4n**. (b) DEPT135, (c) DEPT90.
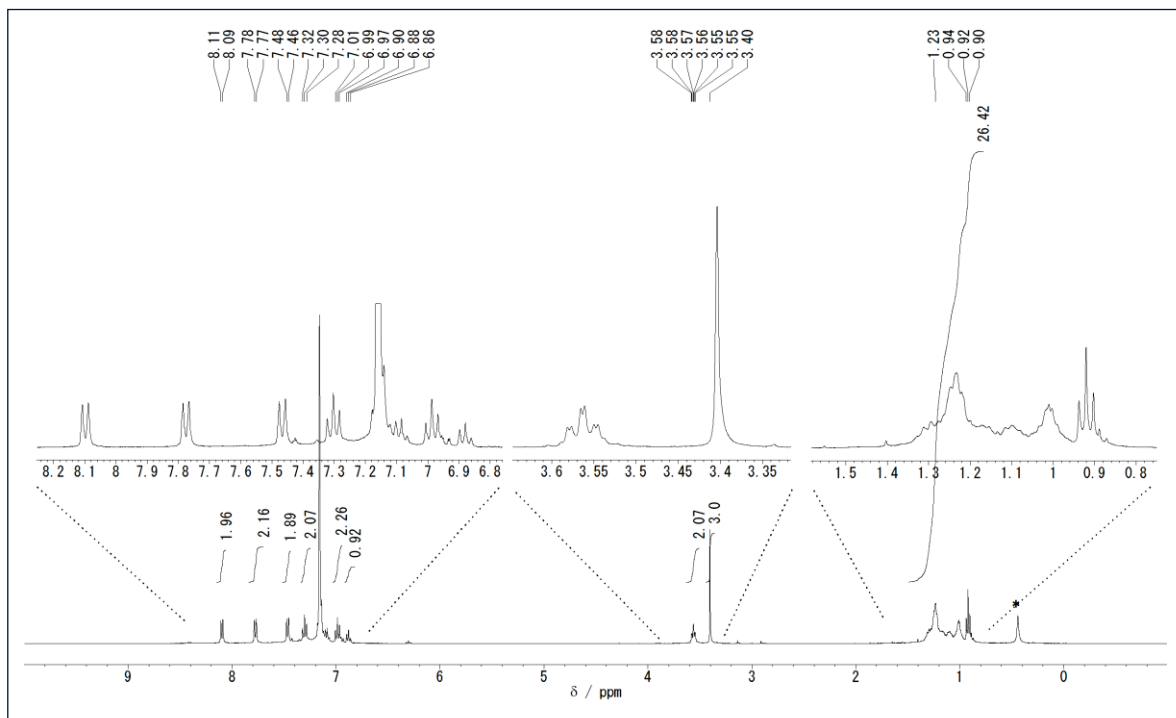
Figure 70. ^{1}H NMR (400 MHz, d6-benzene) spectrum of **MG$_C$4la**. * H$_2$O
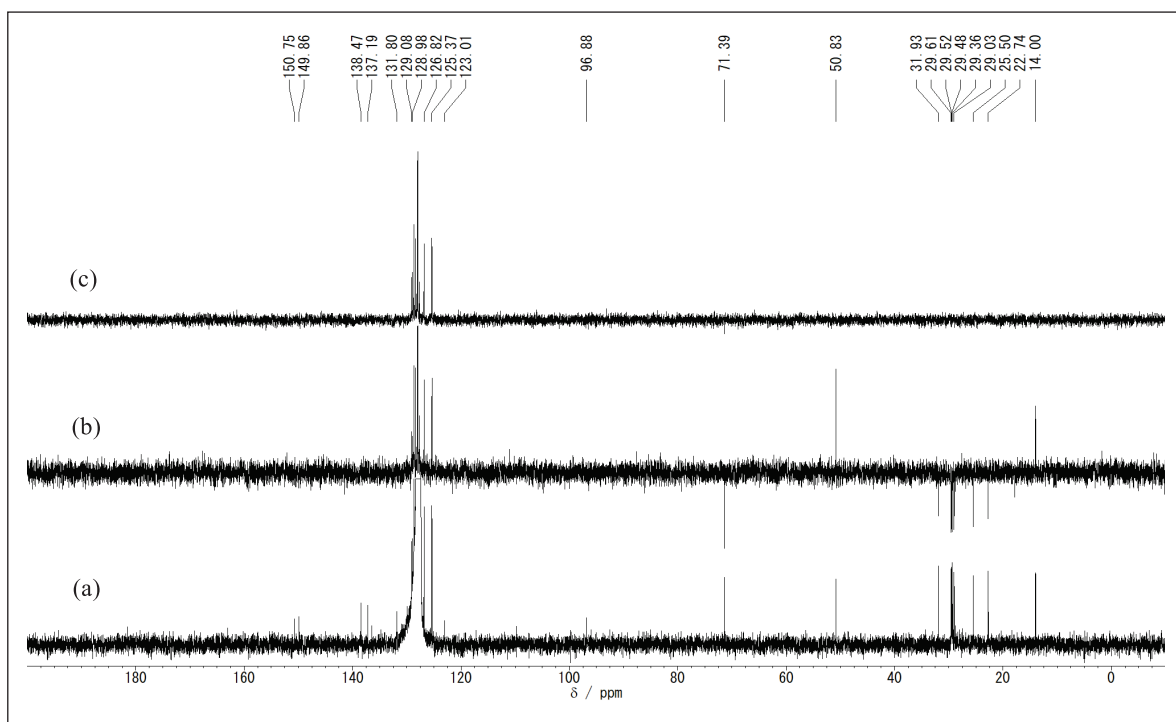
Figure 71. (a) ^{13}C NMR (100 MHz, d6-benzene) spectra of **MG$_C$4la.** (b) DEPT135, (c) DEPT90.
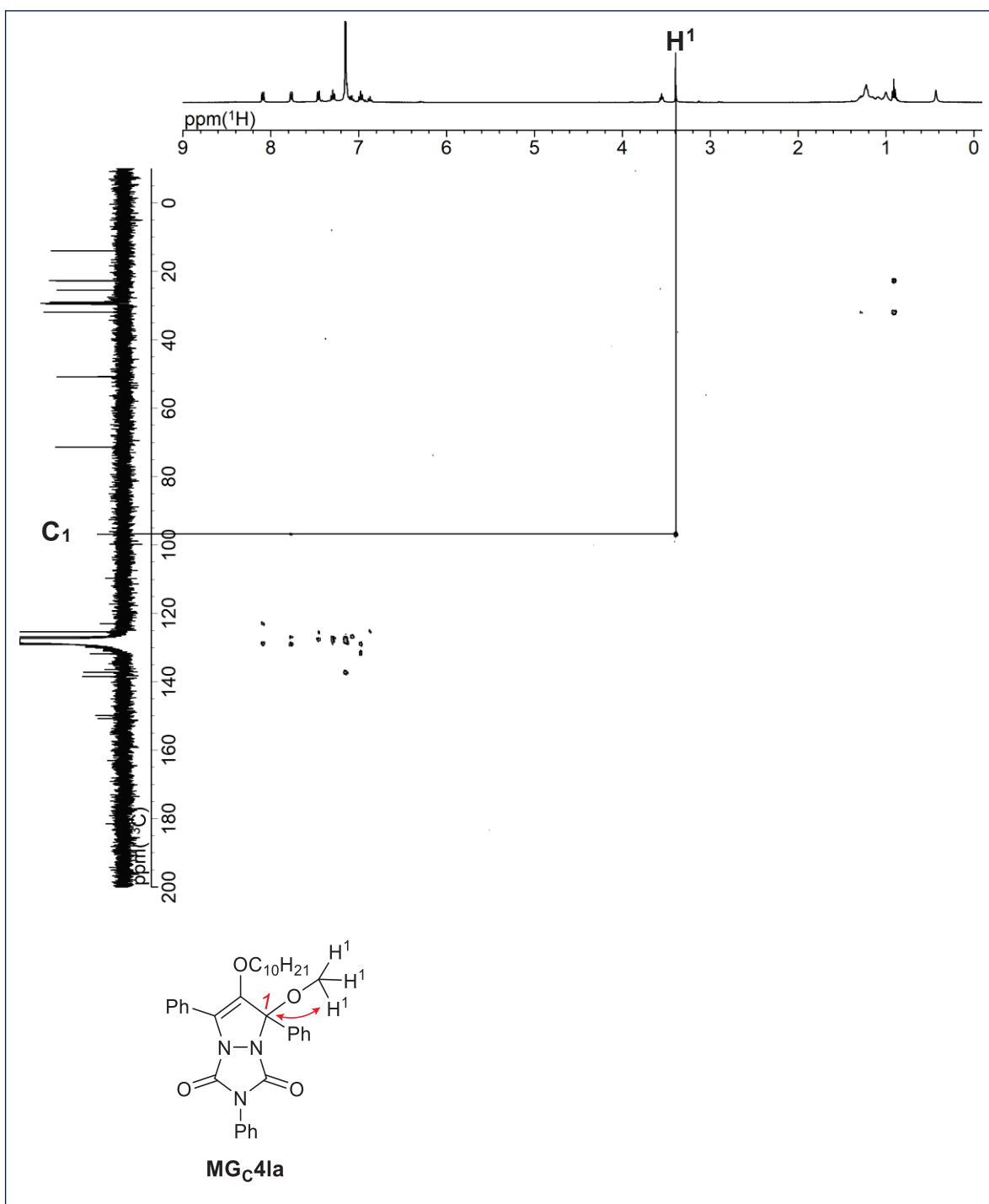
Figure 72. ^{1}H, ^{13}C-HMBC (d6-benzene) spectrum of **MG$_C$4la**.
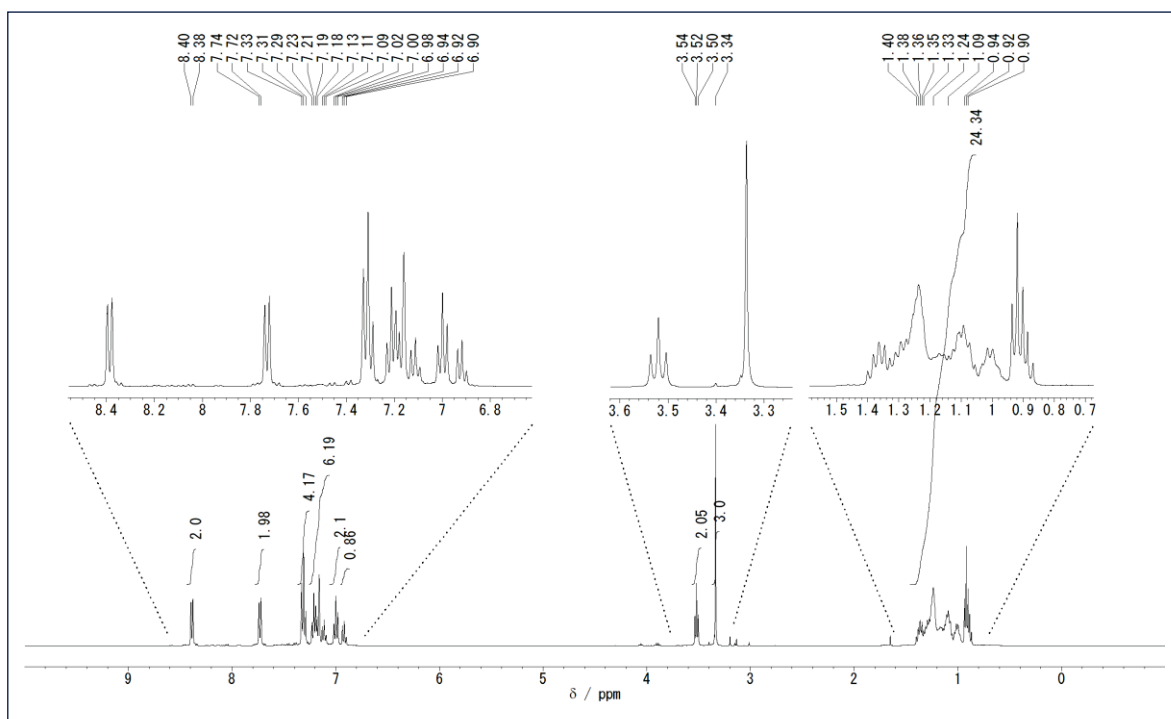
Figure 73. ¹H NMR (400 MHz, d6-benzene) spectrum of **MG_C4al**.
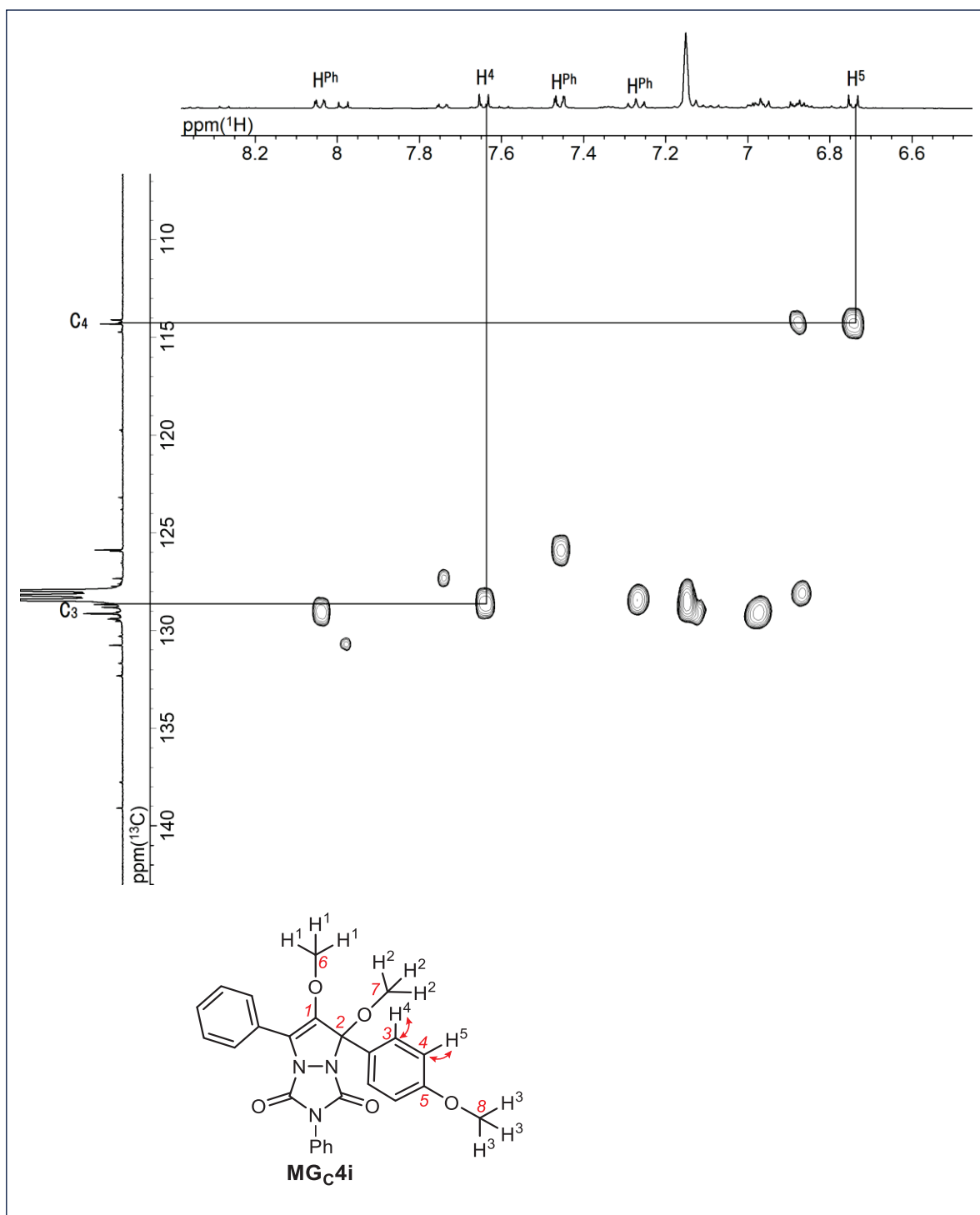
Figure 74. ^1H, ^1H-HSQC (d6-benzene) spectrum of **MG$_C$4i**.
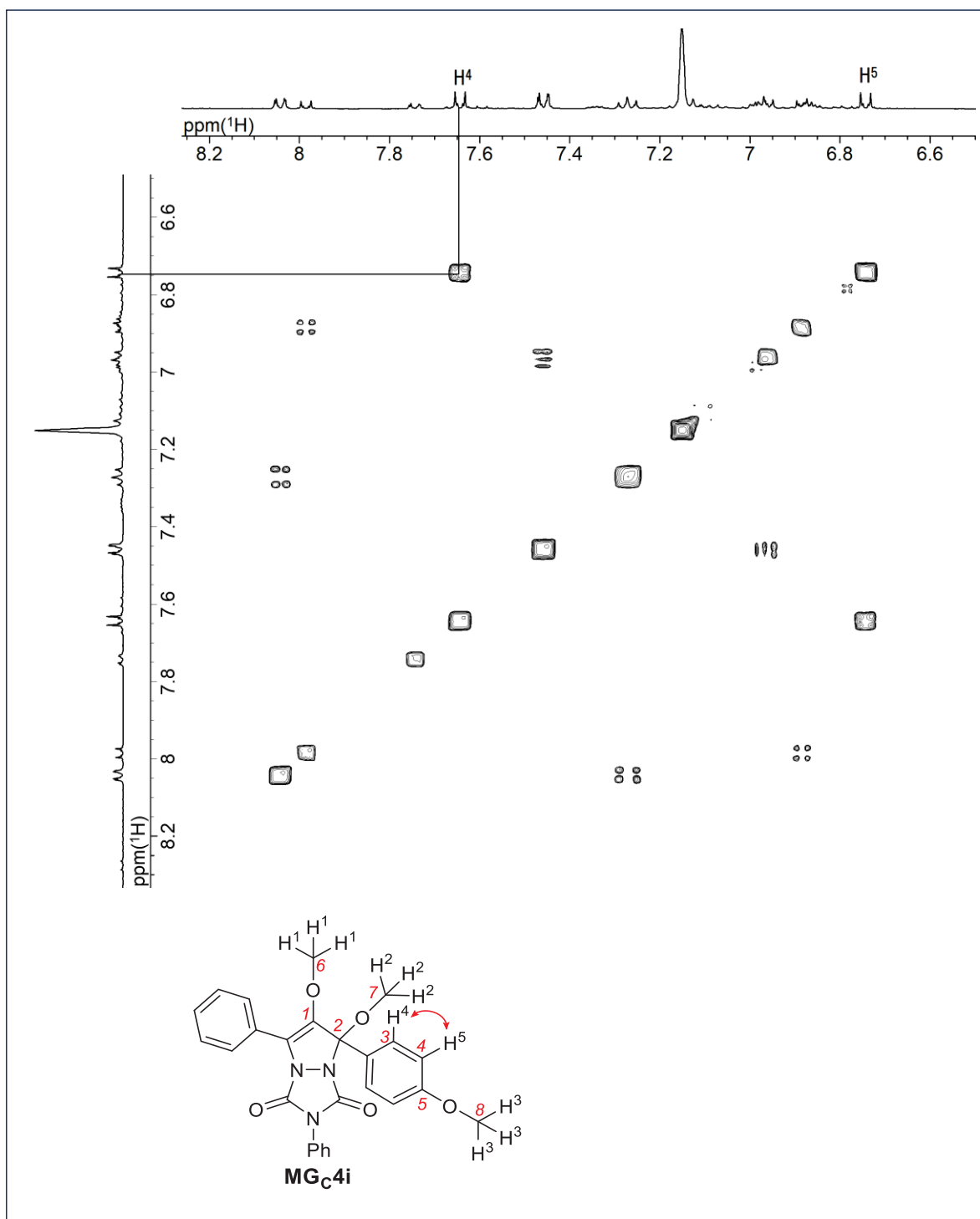
Figure 75. ^{1}H, ^{1}H-COSY (d6-benzene) spectrum of **MG$_C$4i**.

114
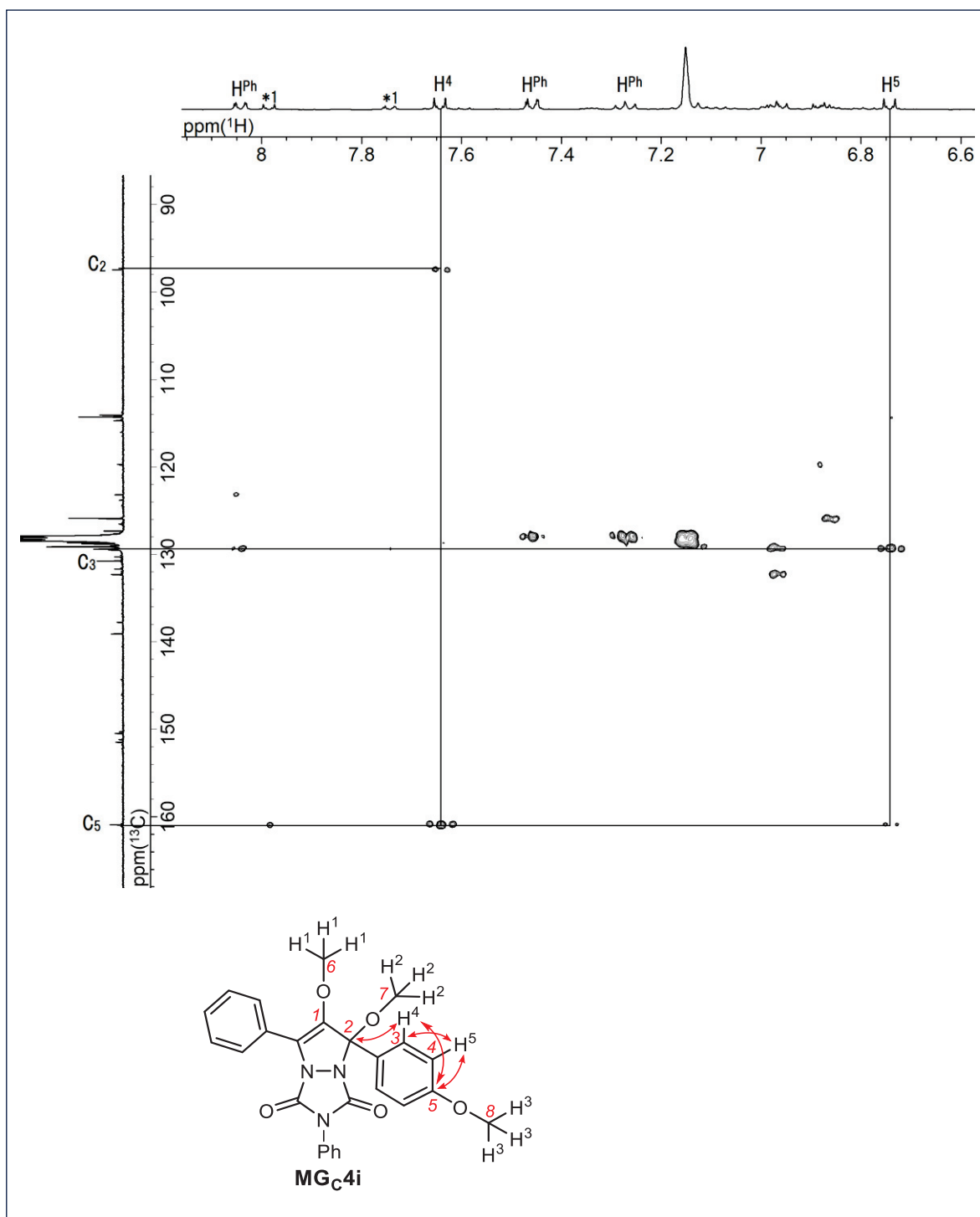
Figure 76. ^{1}H, ^{13}C-HMBC (d6-benzene) spectrum of **MG$_C$4i**. *1: minor migrated product **MG$_C$4i'**
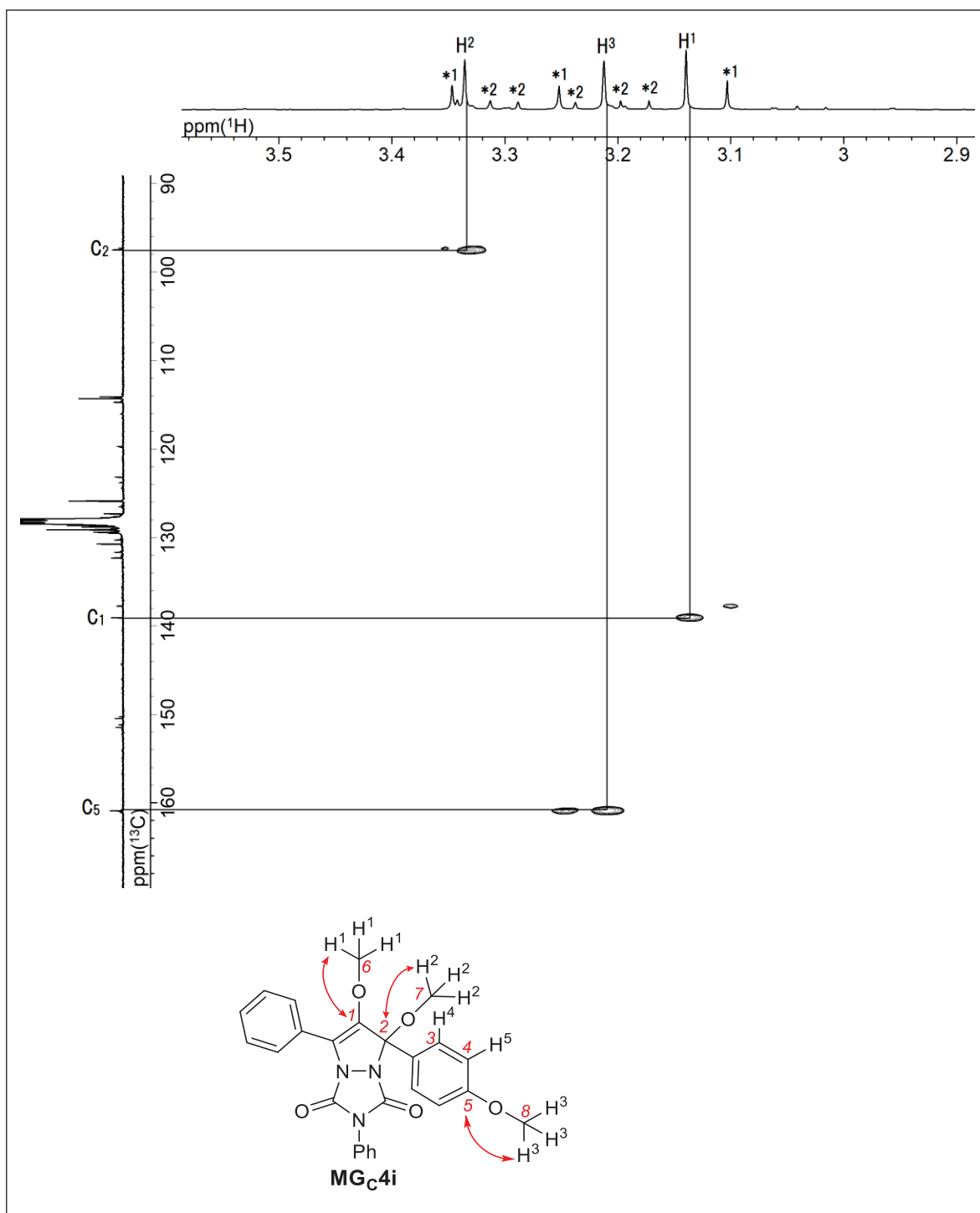
Figure 77. ^{1}H, ^{13}C-HMBC (d6-benzene) spectrum of **MG_C4i**.

*1: minor migrated product **MG_C4i'**, *2: minor migrated products **MG_Co4i** and **MG_Co4i'**.
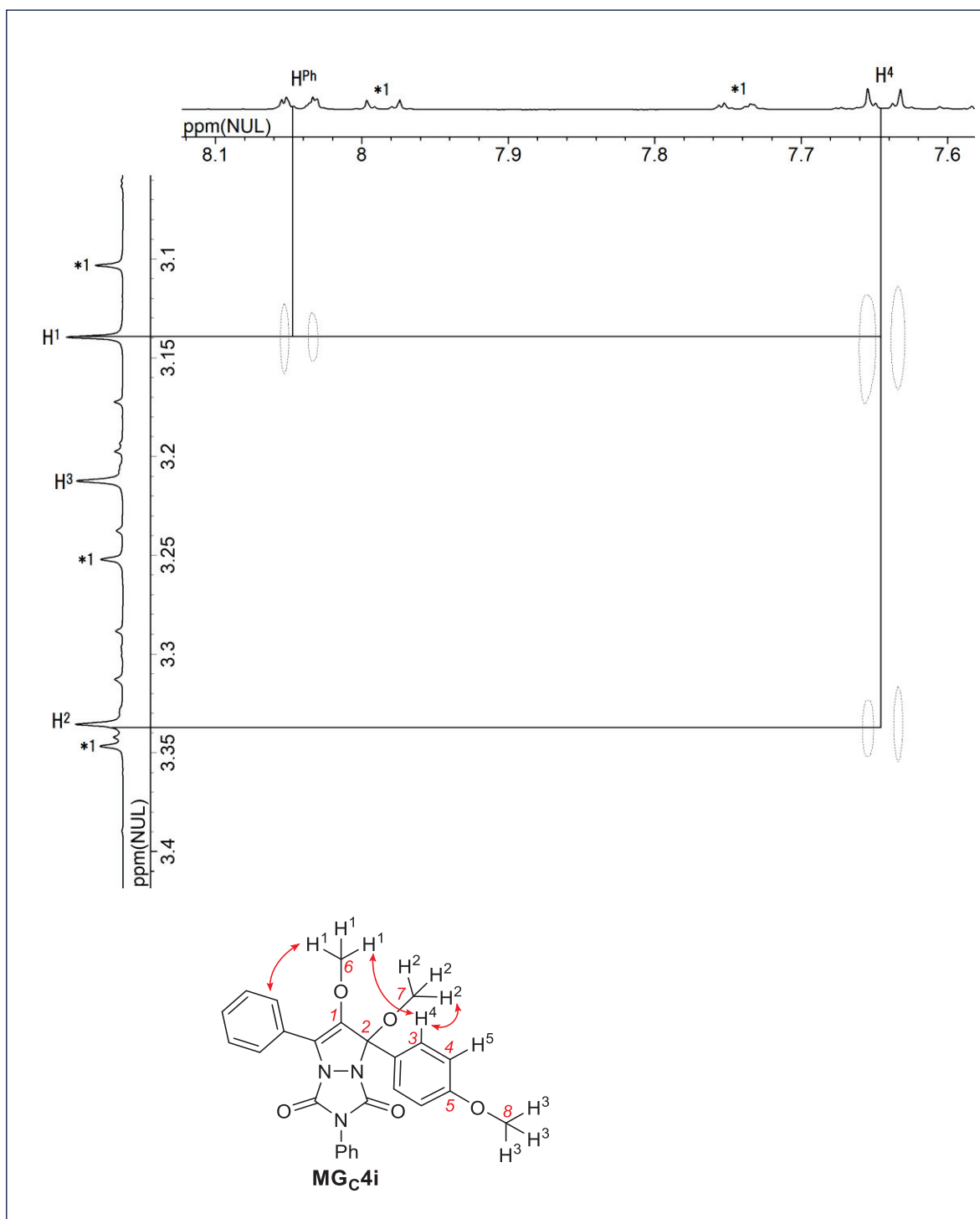
Figure 78. ^{1}H, ^{1}H-NOESY (d6-benzene) spectrum of **MG$_C$4i**. *1: minor migrated product

MG$_C$4i'
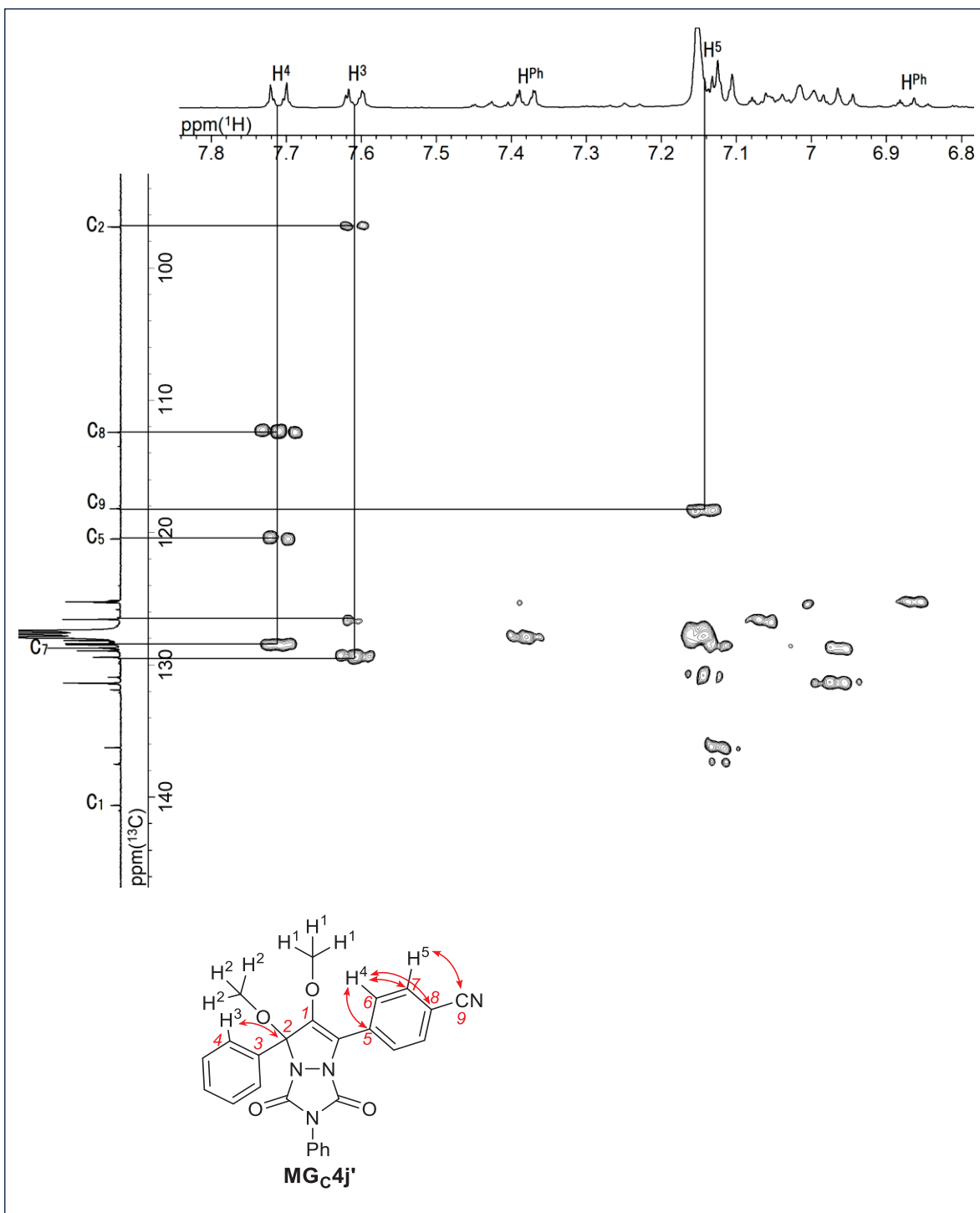
Figure 79. ^{1}H, ^{13}C-HMBC (d6-benzene) spectrum of **MG$_C$4j'**.
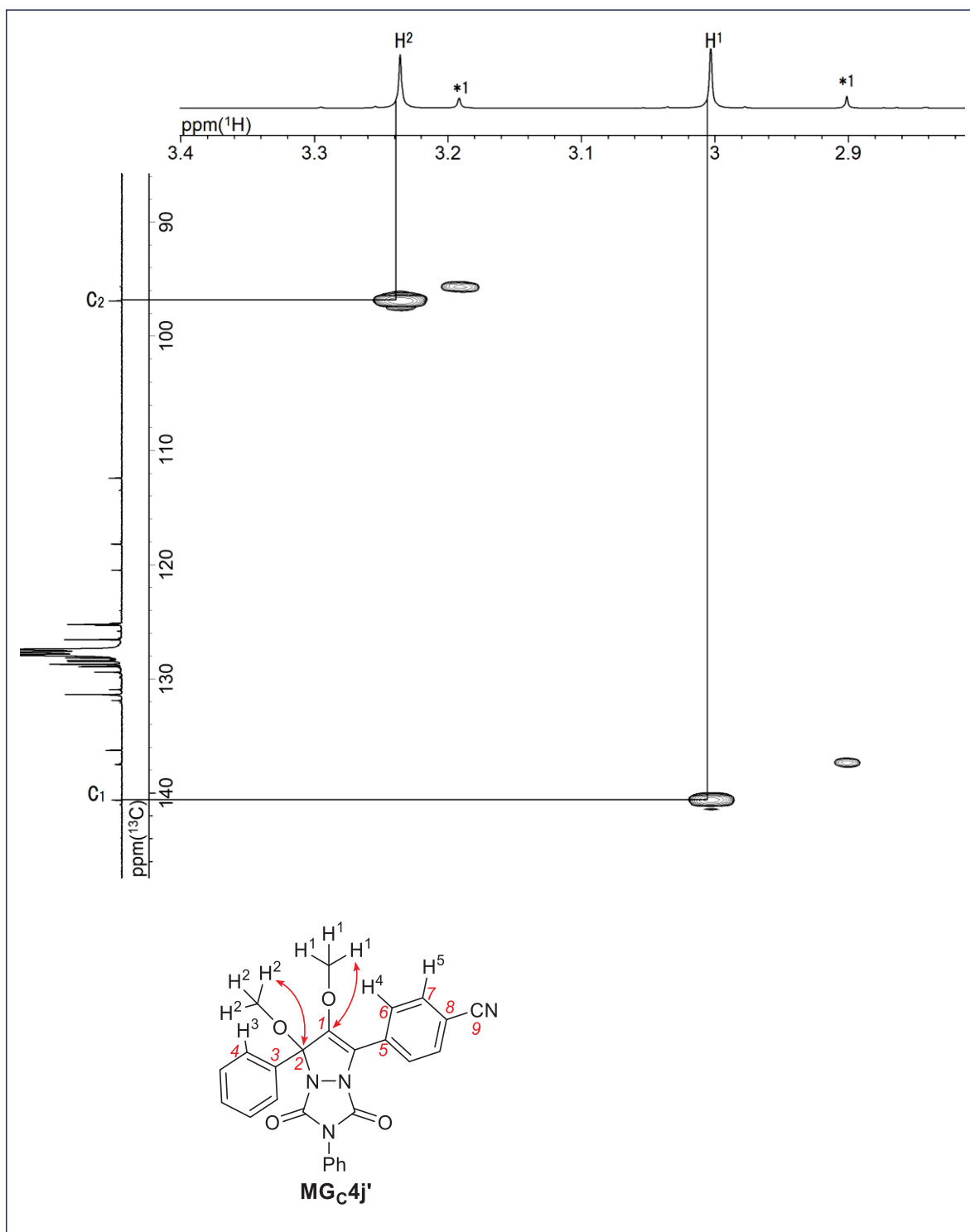
Figure 80. ^1H, ^{13}C-HMBC (d6-benzene) spectrum of **MG$_C$4j'**. *1: minor migrated product **MG$_C$4j**.
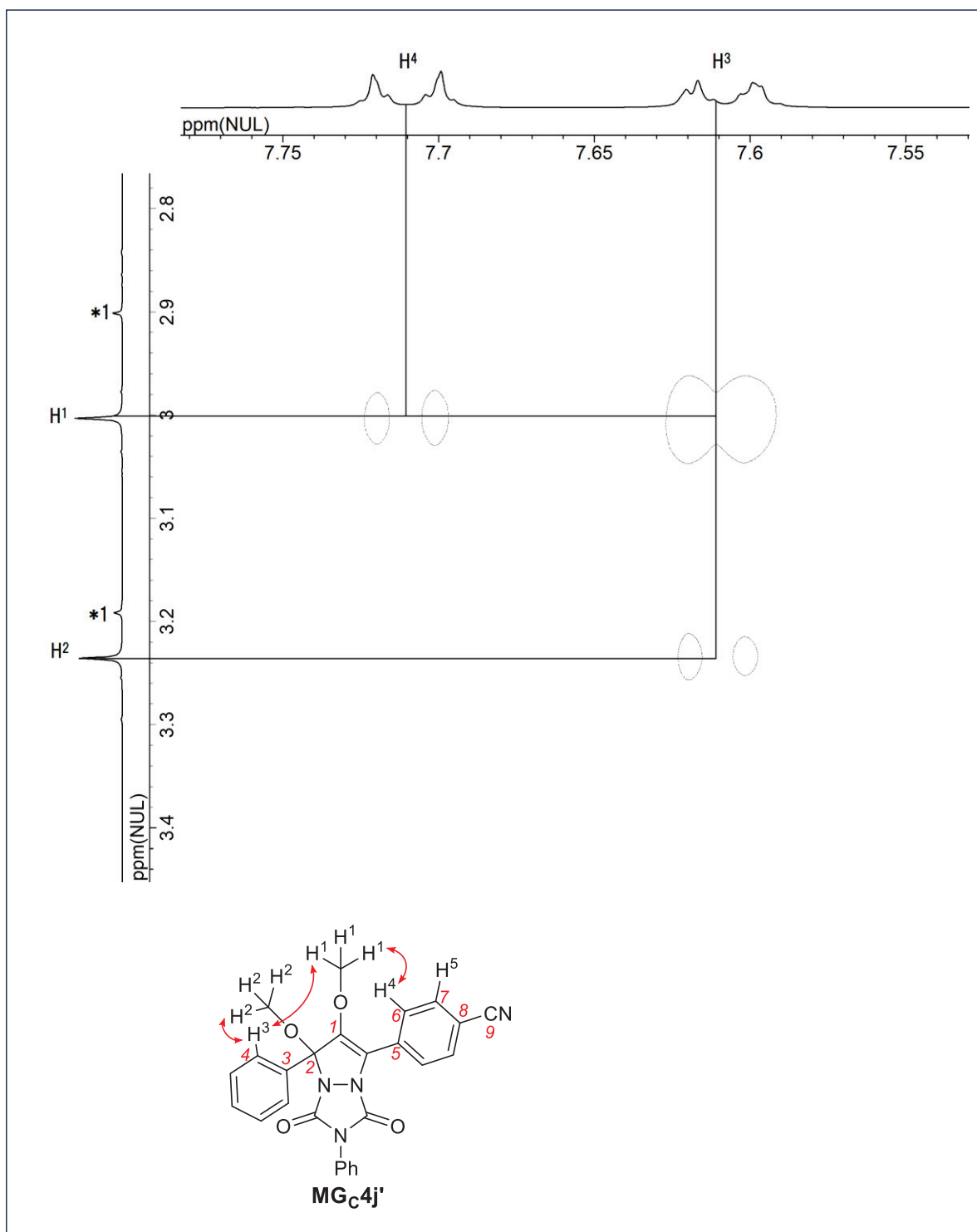
Figure 81. ^{1}H, ^{1}H-NOESY (d6-benzene) spectrum of **MG$_C$4j'**. *1: minor migrated product **MG$_C$4j**.
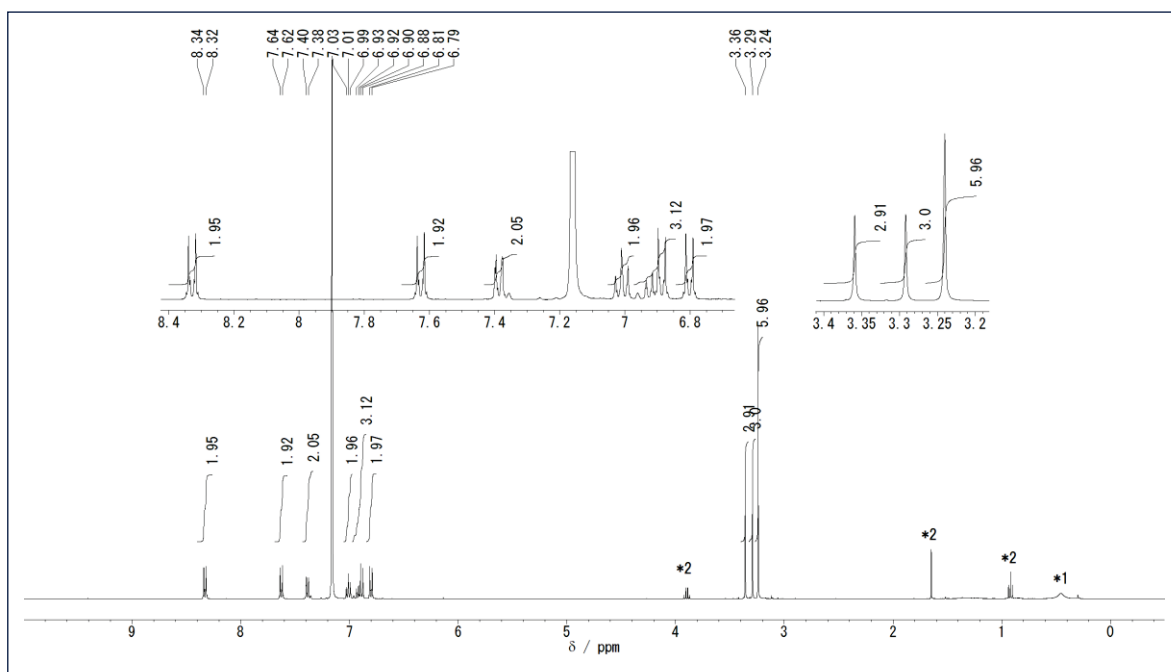
Figure 82. ^{1}H NMR (400 MHz, d6-benzene) spectrum of **MG$_{co}$4b**. *1: H$_2$O, *2: ethyl acetate.
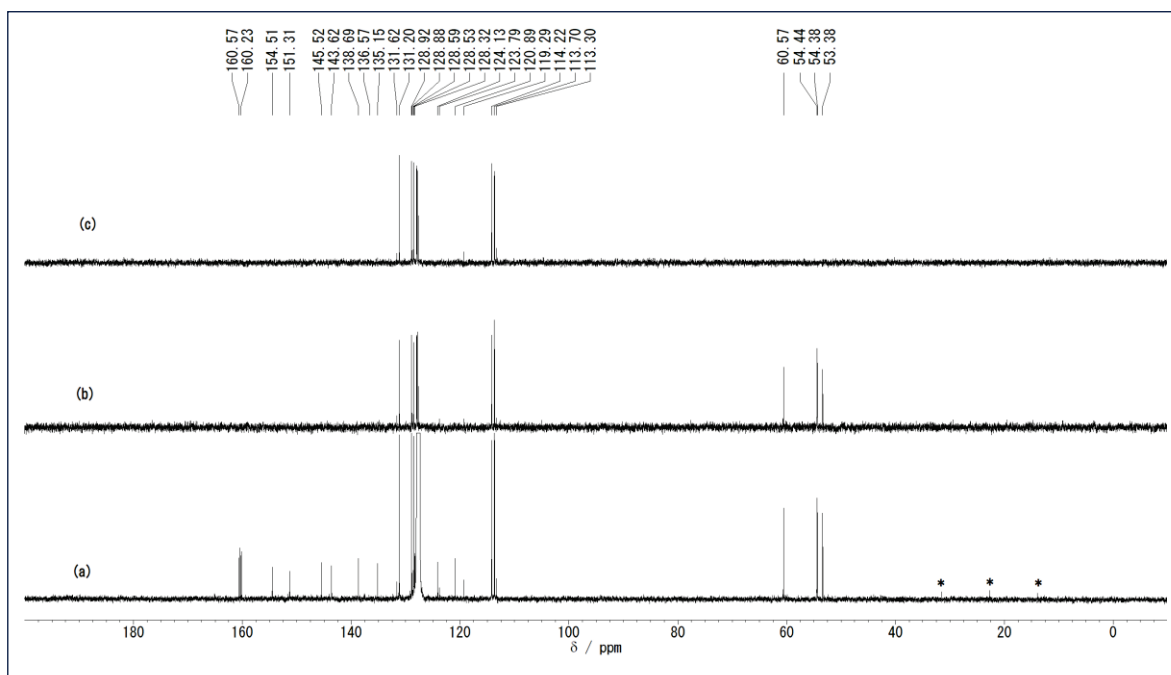
Figure 83. (a) ^{13}C NMR (100 MHz, d6-benzene) spectra of **MG$_{co}$4b,** (b) DEPT135, (c) DEPT90. * hexane
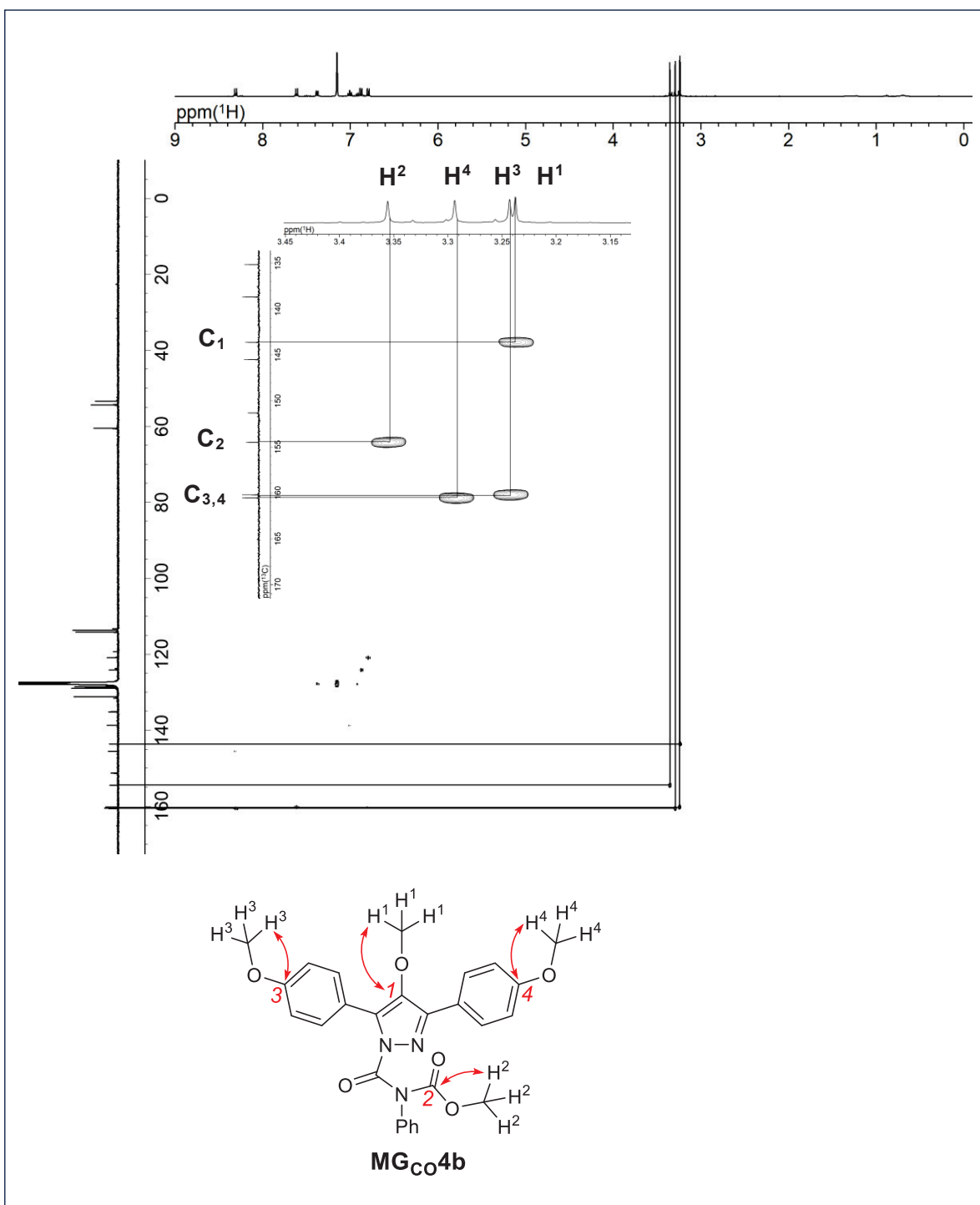
Figure 84. ^{1}H, ^{13}C-HMBC (d6-benzene) spectrum of **MG$_{CO}$4b**.
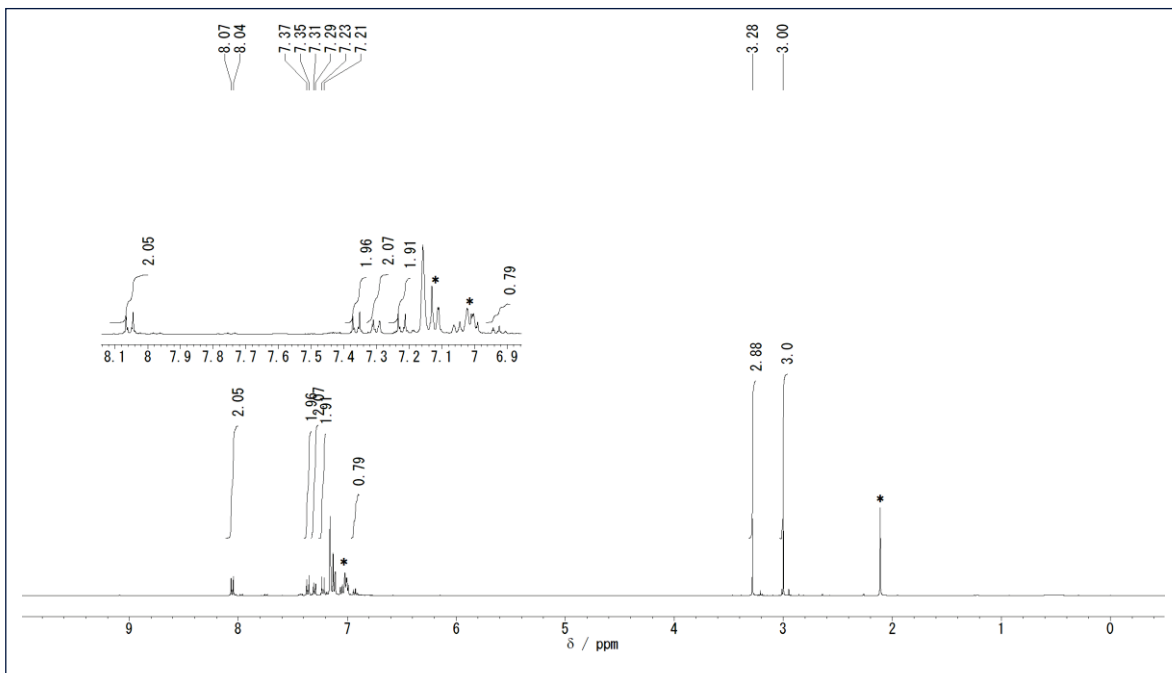
Figure 85. ¹H NMR (400 MHz, d6-benzene) spectrum of **MG_CO4e**. * toluene
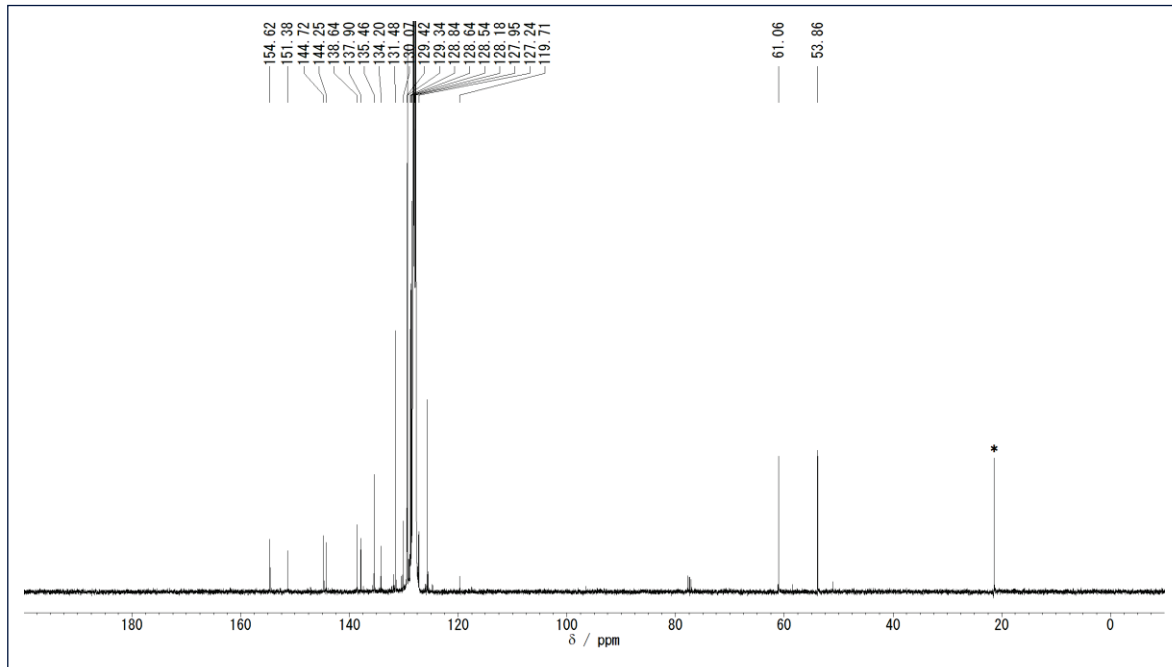
Figure 86. ¹³C NMR (100 MHz, d6-benzene) spectra of **MG_CO4e**. * toluene
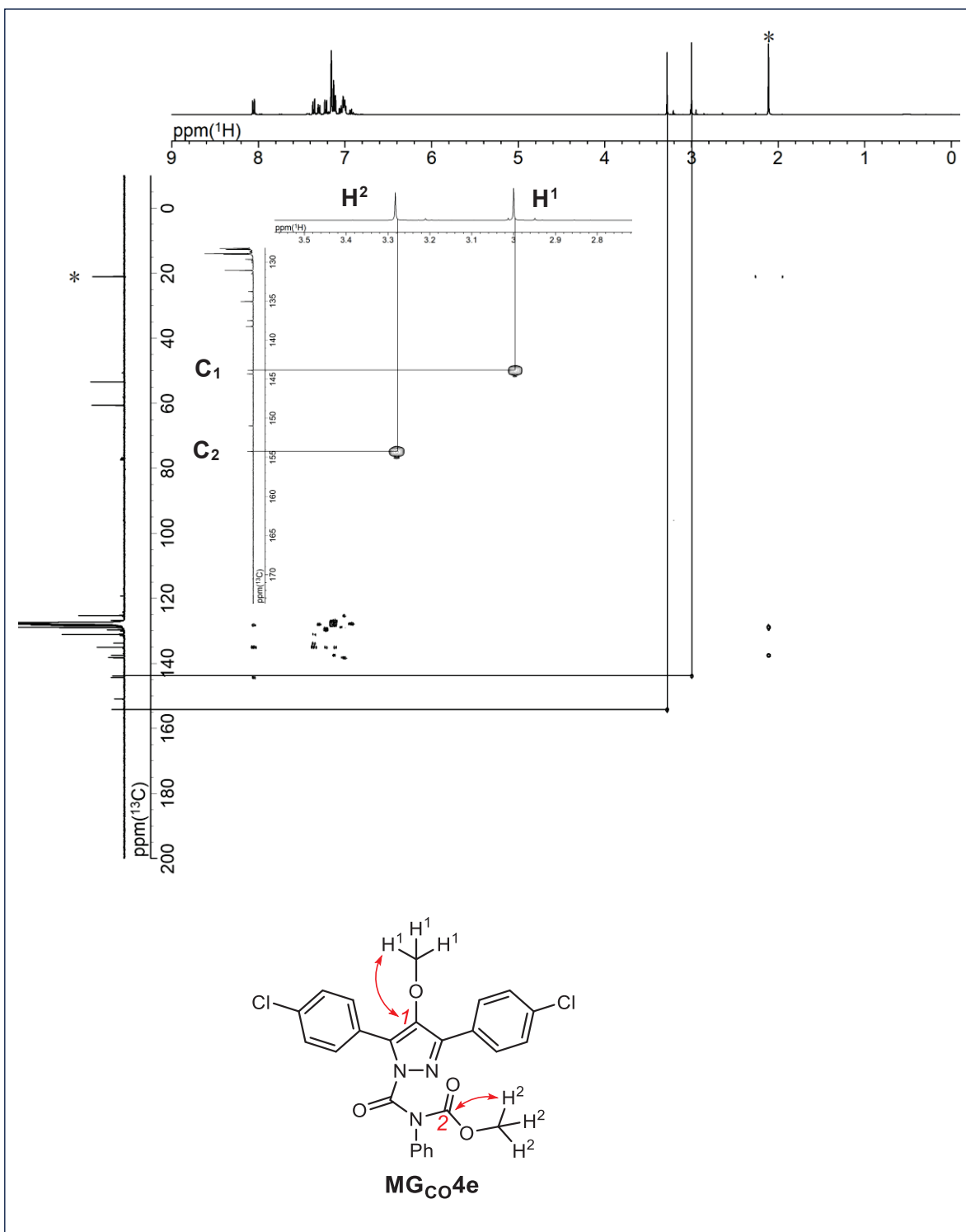
Figure 87. ^{1}H, ^{13}C-HMBC (d6-benzene) spectrum of **MG$_{CO}$4e**. * toluene

3.10 Reference

(1). Yoshidomi, S.; Mishima, M.; Seyama, S.; Abe, M.; Fujiwara, Y.; Ishibashi, T. Direct Detection of a Chemical Equilibrium between a Localized Singlet Diradical and Its σ-Bonded Species by Time-Resolved UV/Vis and IR Spectroscopy. *Angew. Chem., Int. Ed.* **2017,** *56,* 2984–2988.

(2). Abe, M.; Kubo, E.; Nozaki, K.; Matsuo, T.; Hayashi, T. An Extremely Long-Lived Singlet 4,4-Dimethoxy-3,5-diphenylpyrazolidine-3,5-diyl Derivative: A Notable Nitrogen-Atom Effect on Intra- and Intermolecular Reactivity. *Angew. Chem., Int. Ed.* **2006,** *45,* 7828–7831; *Corrigendum, idem, ibid,* **2012,** *51,* 11911.

(3). Bradley, D.; Williams, G.; Lawton, M. Drying of Organic Solvents: Quantitative Evaluation of the Efficiency of Several Desiccants. *J. Org. Chem.* **2010,** *75,* 8351–8354.

(4). Einstein, A. Über die von der molekularkinetischen Theorie der Wärme geforderte Bewegung von in ruhenden Flüssigkeiten suspendierten Teilchen. *Annalen. der. Physik,* **1905,** *17,* 549–560.

(5). (a) Perkins, M. J.; Spin Trapping. In *Advances in Physical Organic Chemistry;* Gold, V.; Bethell, D., Eds.; Academic Press: New York, **1980**; Vol. 17, pp 1–64. (b) Mao, S. W.; Kevan, L. Electron paramagnetic resonance studies of spin trapping of the primary neutral radicals formed in γ-irradiated methanol. *Chem. Phys. Lett.* **1974,** *24,* 505–507. (c) Schlick, S.; Kevan, L. Spin trapping of radicals formed in gamma-irradiated methanol: Effect of the irradiation temperature from 77 K to 300 K. *Chem. Phys. Lett.* **1976,** 38, 505–509. (d) Halpern, A. Spin trapping of radicals in tritiated methanol. *Chem. Phys. Lett.* **1984,** *103,* 523–525. (d) Acken, B. J.; Warshaw, J. A.; Gallis, D. E.; Crist, D. R. Acyclic α-Alkoxynitrones. A New Class of Spin-Trapping Agents. *J. Org. Chem.* **1989.** *54,* 1743–1745. (e) Ledwith, A.; Russell, P. J.; Sutcliffe. L. H. Alkoxy radical intermediates in the thermal and photochemical oxidation of alcohols. *Proc. R. Soc. Lond. A.* **1973,** *332,* 151–166.

(6). Forrester, A. R.; Thomson, R. H. *Nature.* **1964,** *203,* 74–75.

(7). (a) Abe, M.; Adam, W.; Hara, M.; Hattori, M.; Majima, T.; Nojima, M.; Tachibana, K.; Tojo, S. On the Electronic Character of Localized Singlet 2,2-Dimethoxycyclopentane-1,3-diyl Diradicals: Substituent Effects on the Lifetime. *J. Am. Chem. Soc.* **2002,** *124,* 6540–6541. (b) Abe, M.; Hattori, M.; Takegami, A.; Masuyama, A.; Hayashi, T.; Seki, S.; Tagawa, S. Experimental Probe for Hyperconjugative

Resonance Contribution in Stabilizing the Singlet State of 2,2-Dialkoxy-1,3-diyls: Regioselective 1,2-Oxygen Migration. *J. Am. Chem. Soc.* **2006,** *128,* 8008–8014.

(8). Kita, F.; Adam, W.; Jordan, P.; Nau, W. M.; Wirz, J. 1,3-Cyclopentanediyl Diradicals: Substituent and Temperature Dependence of Triplet–Singlet Intersystem Crossing. *J. Am. Chem. Soc.* **1999,** *121,* 9265–9275.

(9). Mizuno, T.; Abe, M.; Ikeda, N. Simultaneous Observation of Triplet and Singlet Cyclopentane-1,3-diyl Diradicals in the Intersystem Crossing Process. *Aust. J. Chem.* **2015,** *68,* 1700–1706.

(10). (a) Abe, M.; Tada, S.; Mizuno, T.; Yamasaki, K. Impact of Diradical Spin State (Singlet vs Triplet) and Structure (Puckered vs Planar) on the Photodenitrogenation Stereoselectivity of 2,3-Diazabicyclo[2.2.1]heptanes. *J. Phys. Chem. B,* **2016,** *120,* 7217–7226. (b) Ye, J.; Fujiwara, Y.; Abe, M. Substituent effect on the energy barrier for σ-bond formation from π-single-bonded species, singlet 2,2-dialkoxycyclopentane-1,3-diyls. *Beilstein. J. Org. Chem.* **2013,** *9,* 925–933.

Chapter 4

Computational Study

4.1   Nitrogen atom effect on the singlet 1,3-diradicals

The experimental results described in Chapter 2 demonstrate that I) the immediate fate of singlet diradicals, S-**DR4**, is undoubtedly the bond formation reaction to afford the σ-bonded species, **CP4**; II) S-**DR4** is ca. 2–11 kJ mol^{-1} more stable in enthalpy than **CP4**; III) the equilibrium constant K between S-**DR4** and **CP4** in polar solvent is smaller than that in non-polar solvent; 1.54 in toluene > 0.72 in acetonitrile (Ar = p-H-C$_6$H$_4$).

In Chapter 4.1, to understand the nitrogen atom effect on the small energy difference between S-**DR4** and **CP4**, the isodesmic reactions shown in following Equations (1), (2) were calculated using the broken-symmetry (BS)[1]-(R,U)CAM-B3LYP[2]/6-31G(d) level of theory (Scheme 19), because the experimentally obtained $\Delta G°_{293}$ between S-**DR4a** and **CP4a** was well reproduced at this level of theory; $\Delta G°_{293,\text{toluene}} = -1.3$ and $\Delta G°_{\text{calc.}} = -1.4$ kJ mol^{-1}. Equation (1) was calculated to be endothermic, $\Delta H_r = +15.5$ kJ mol^{-1}, while Equation (2) was found to be exothermic, $\Delta H_r = -5.9$ kJ mol^{-1}. These results suggested that the notable effect of the nitrogen atoms on the equilibrium constant K is mainly due to the enthalpic stabilization of S-**DR4**, not the ring-strain destabilization by introducing nitrogen atom. Thus, the zwitterionic resonance structures, **ZI**, which are shown in Scheme 8 (in Chapter 2) rationalize the nitrogen atoms effect on the stabilization of S-**DR4**.

Scheme 19. Isodesmic reaction.
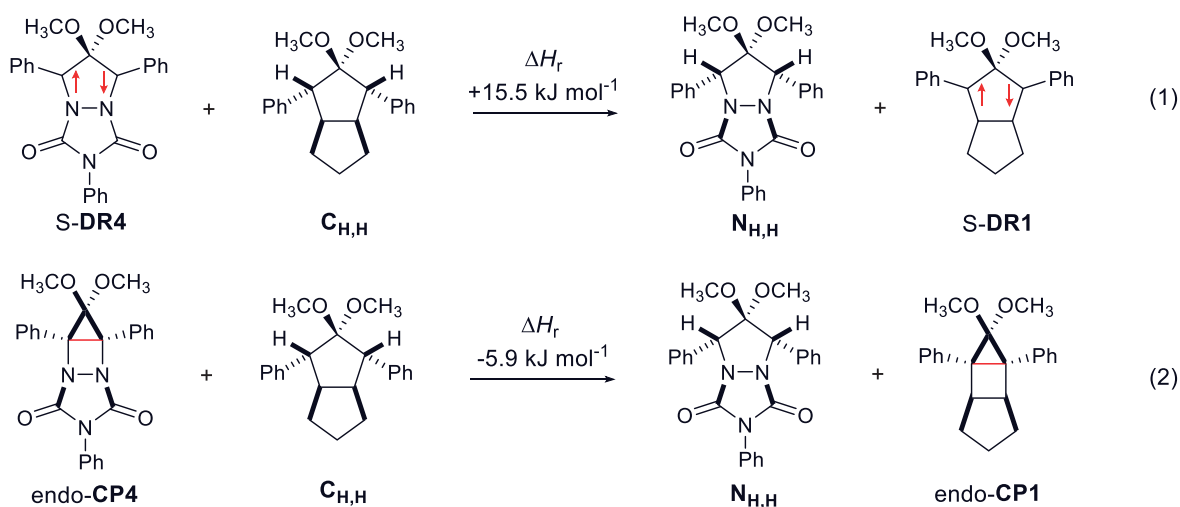
4.2   Conformers of open-shell singlet diradicals and σ-bonded species

The four conformers of the open-shell singlet diradicals S-**DR4a**, i.e. S-**DR4a-ii** , S-**DR4a-ig**, S-**DR4a-gg**, and S-**DR4a-gi** (i: in, g: gauche), were found as equilibrium structures using the broken-symmetry (BS) method at the (U)B3LYP/6-31G(d) and (U)CAM-B3LYP/6-31G(d) level of theory (Scheme 20). The value of $<S^2>$ was found to be ca. 0.75 (0.95)* for all the four conformers, suggesting the singlet ground state of S-**DR4a**,[3] *values in parenthesis are calculated at the (BS)-(U)CAM-B3LYP/6-31G(d) level of theory. The in-in conformation of the acetal moiety, i.e. S-**DR4a-ii**, was lower in energy than S-**DR4a-ig**, S-**DR4a-gi**, and S-**DR4a-gg** by 9.2 (8.3), 14.6 (16.0), and 32.5 (32.3) kJ mol^{-1}, respectively. Figure 90 illustrates further insight into the four conformation; the potential energy surfaces around the dihedral angle (φ) of the acetal moiety were calculated for the respective singlet diradicals at the (BS)-(U)CAM-B3LYP/6-31G(d) level of theory.

The singlet state was calculated to be more stable than the triplet state by 25.9 (22.0) kJ mol^{-1}, which were computed after correction for spin contamination in singlet state by using Yamaguchi's formula; $\Delta E^{SC}_{ST} = (<S^2_T>/(<S^2_T> - <S^2_S>)) \times \Delta E_{ST}$.[1] The singlet–triplet energy gap was well consistent with the value of 24.7 kJ mol^{-1} determined at the CASSCF(6/6) level of theory.[4]

Scheme 20. Four conformers of open-shell singlet diradicals S-**DR4**.

	S-DR4a-ii	S-DR4a-ig	S-DR4a-gg	S-DR4a-gi
ΔE_{zpe} in kJ mol^{-1}	0.0 (0.0)	+9.2 (+8.3)	+32.5 (+32.3)	+14.6 (+16.0)
$<S^2>$	0.76 (0.95)	0.77 (0.96)	0.73 (0.95)	0.78 (0.94)
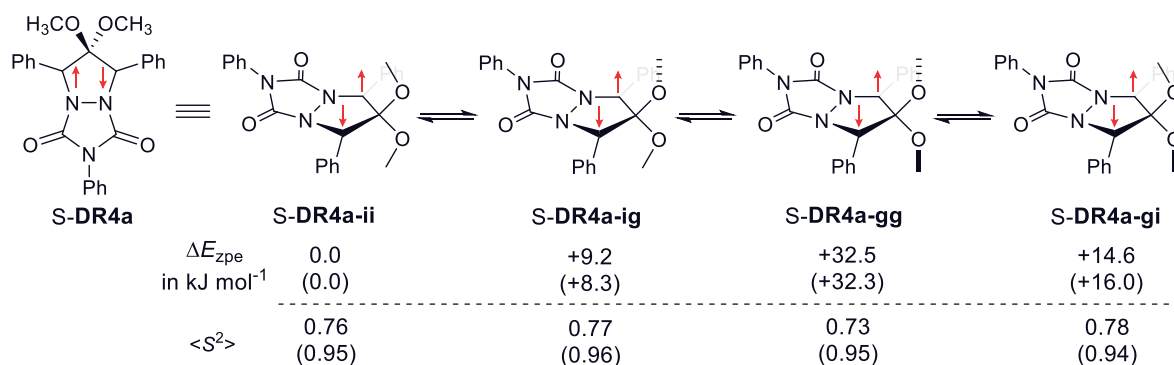
At the (BS)-(U)B3LYP/6-31G(d) level of theory.

Values in parenthesis are calculated at the (BS)-(U)CAM-B3LYP/6-31G(d) level of theory.

128
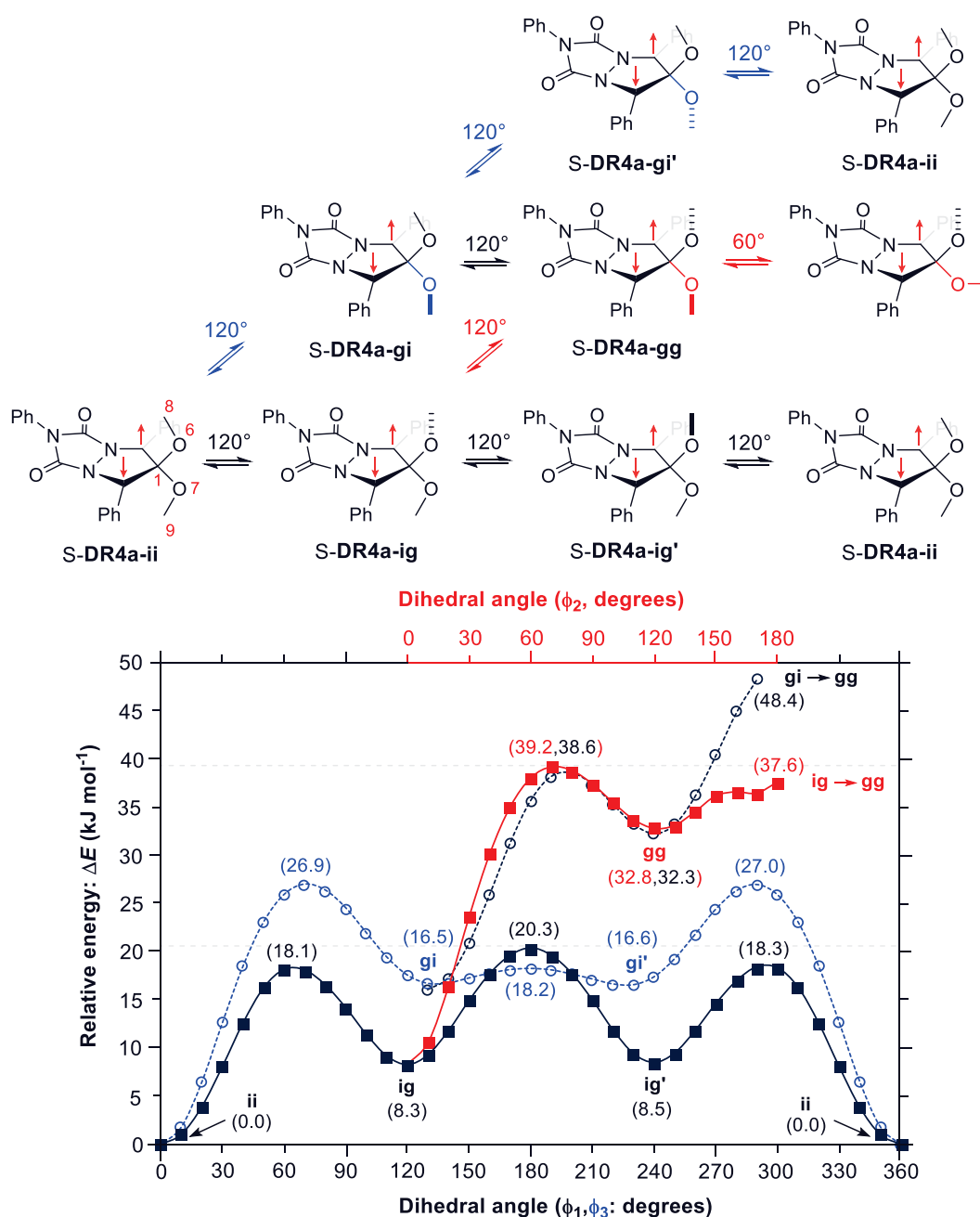
Figure 88. Relaxed potential energy scan of singlet diradicals S-**DR4a** calculated by scanning the dihedral angle φC8-O6-C1-O7 and φC9-O7-C1-O6 in gas phase at (BS)-(U)CAM-B3LYP/6-31G(d) level; black line is **ii → ig** (**ig'**) surface, blue dased line is **ii → gi** (**gi'**) surface, red line is **ig → gg** surface, and black dashed line is **gi → gg** surface. ΔE is the energy relative to the lowest energy conformer (φC8-O6-C1-O7 and φC9-O7-C1-O6 = 0°).

According to the computationally finding, the endo-isomer of σ-species, endo-**CP4a**, was calculated to be more stable in energy than the exo isomer, exo-**CP4a**, by 35.8 (37.9) kJ mol⁻¹ at the (R)B3LYP/6-31G(d) and

(R)CAM-B3LYP/6-31G(d) level of theory. The energetic preference of the endo-isomer is rationalized by the electron delocalization of lone-pair electrons (LP) on the nitrogen atoms to the C–C σ* (BD*) of the cyclopropane ring. Indeed, the N5–C2 bond in endo-**CP4a**, 1.48 (1.47) Å, was found to be shorter than that in exo-**CP4a**, 1.50 (1.48) Å (Scheme 21). Furthermore, the

Scheme 21. Two conformers of σ-bonded species; (a) endo-isomer and (b) exo-isomer.
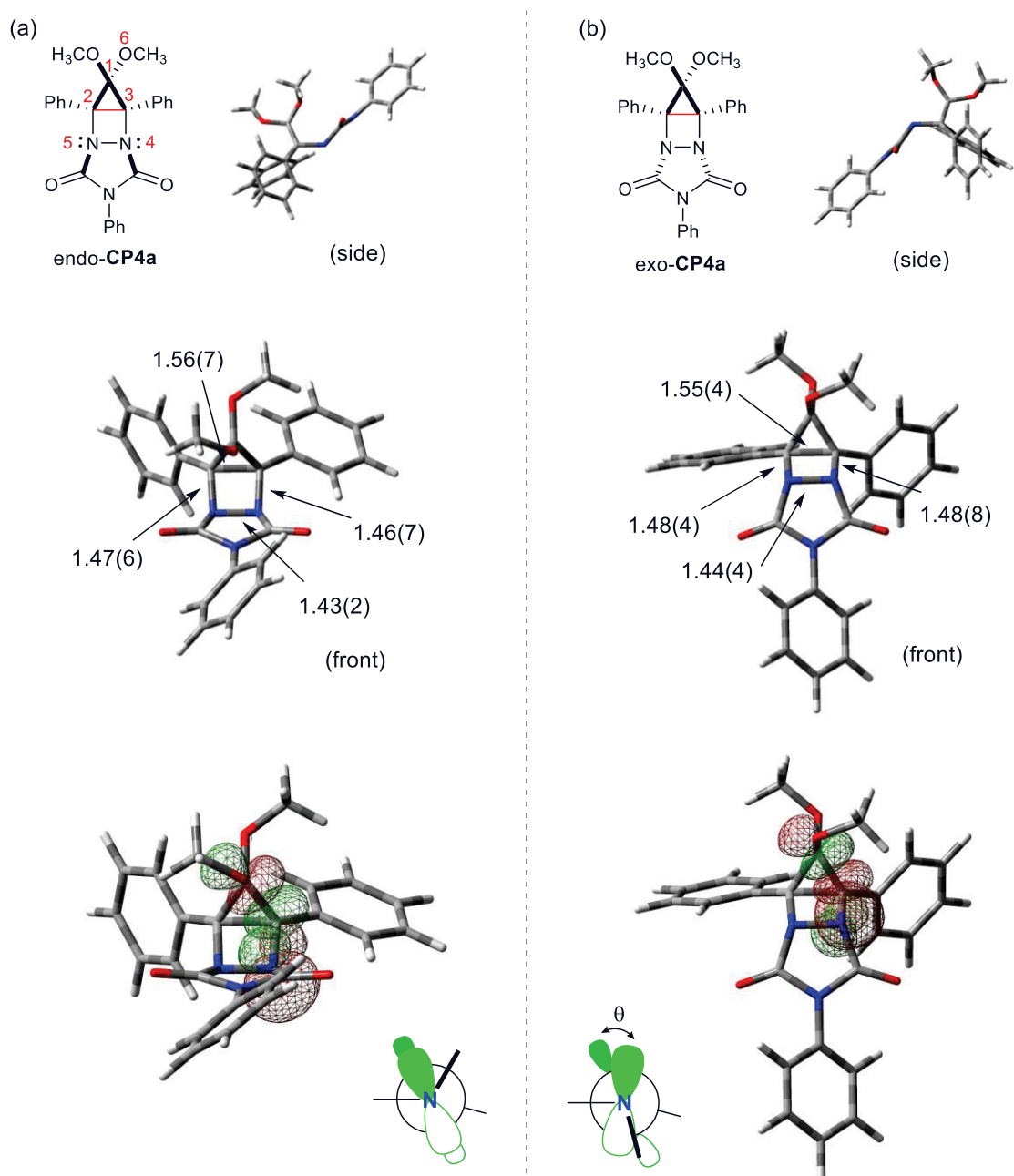
In gas phase at (R)CAM-B3LYP/6-31G(d) level of theory. Isovalue: 0.06 in NBO basis.

130

second-order perturbation theory energy analysis in the natural bond orbital (NBO) basis[5] at the (R)CAM-B3LYP/6-31G(d) level of theory illustrated that the $n_N \to \sigma_{CC}^*$ interaction between the nitrogen lone-pair and the cyclopropane ring C1–C2 (or C1–C3) of the endo-isomer were seen to give the strongest stabilization, ca. 33.0 kJ mol^{-1}, compared to that of the exo-isomer, ca. 11.7 kJ mol^{-1}. In addition, only endo-isomer was found to interact between the nitrogen lone-pairs and one of the acetal moieties, C1–O6, ca. 3.47 kJ mol^{-1} (Table 9, Figure 91). The N4–N5 bond distance in endo-**CP4a**, 1.44 (1.43) Å, was shorter than that in exo-**CP4a**, 1.45 (1.44) Å. The bond-distance of C2–C3 in endo-**CP4a**, 1.588 (1.567) Å, was found to be longer than that in exo-**CP4a**, 1.568 (1.554) Å.

Table 9. Hyperconjugative stabilization by donor (LP: nitrogen lone-pair)–acceptor (BD*: anti-bonding orbital of cyclopentane) interactions in NBO basis.

Ring-closure products	Donor NBO	Acceptor NBO	Stabilization Energy / kJ mol^{-1}
exo-isomer	**LP** (N4)	**BD*** (C1–C3)	11.42
	LP (N5)	**BD*** (C1–C2)	11.97
endo-isomer	**LP** (N4)	**BD*** (C1–C3)	35.98
	LP (N4)	**BD*** (C1–O6)	3.39
	LP (N5)	**BD*** (C1–C2)	29.96
	LP (N5)	**BD*** (C1–O6)	3.56

In gas phase at (R)CAM-B3LYP/6-31G(d) level of theory.
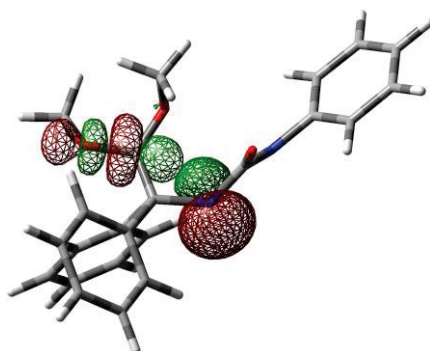
Figure 89. The $n_{N(4)\ \text{and}\ (5)} \to \sigma_{CO}^*$ interaction between nitrogen lone-pairs and anti-bonding orbital acetal moiety of endo-**CP4a**. Isovalue: 0.06 in NBO basis.

4.3   The electronic properties of 1,2-diazacyclopentane-3,5-diyls

In Chapter 2, the electronic properties of S-**DR4** were experimentally clarified by effects of substituent and solvent on the singlet diradicals. In this chapter, the electronic properties of the singlet state of 4,4-dimethoxy 1,2-diazacyclopentane-3,5-diyls were investigated in terms of computational study by means of the second-order perturbative estimates of donor–acceptor interactions in NBO basis at the (U)CAM-B3LYP/6-31G(d) level of theory (Table 10, Figure 92). The $n_{N(6)} \to n^*_{C(2)}$ and $n_{N(7)} \to \sigma^*_{CC(aromatic\ ring)}$ interaction between the nitrogen lone-pair (LP) and the vacant p orbital (LP* (C2)) expected to derive from zwitterionic resonance structure, **ZI2**, were observed from the α spin state. Subsequently, the $n_{C(3)} \to \sigma^*_{CO}$ interaction between the benzylic carbon (C3) and the anti-bonding orbital of acetal moiety, C1–O4 (or C1–O5), expected to derive from **ZI3** were also found. The respective interactions at β spin are described in Table 10. The electronic properties of the singlet diradicals, S-**DR4**, which were deduced from experiments certainly rationalized by these computational findings. Once described, there was also a slight interaction between the radical sites, C2 and C3, ca. 0.40 kcal mol^{-1} (Table 10).
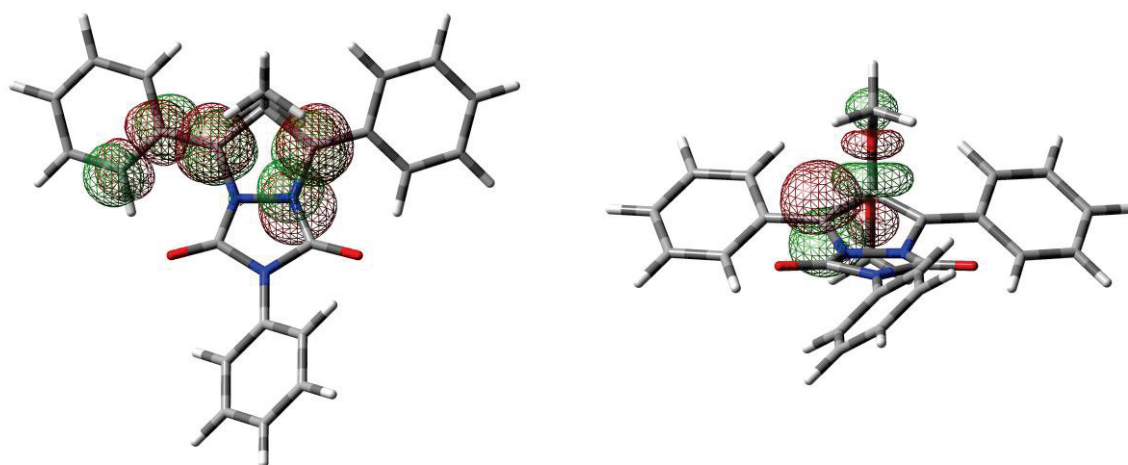
Figure 90. Natural bond orbital of S-**DR4a-ii** (α spin), left: $n_{N(6)} \to n^*_{C(2)}$ and $n_{N(7)} \to \sigma^*_{CC(aromatic\ ring)}$ interaction expected to derive from **ZI2**, right: $n_{C(3)} \to \sigma^*_{CO}$ interaction expected to derive from **ZI3**. Isovalue: 0.06 in NBO basis.

132

Table 10. Second-order perturbative estimates of donor–acceptor interactions in NBO basis.
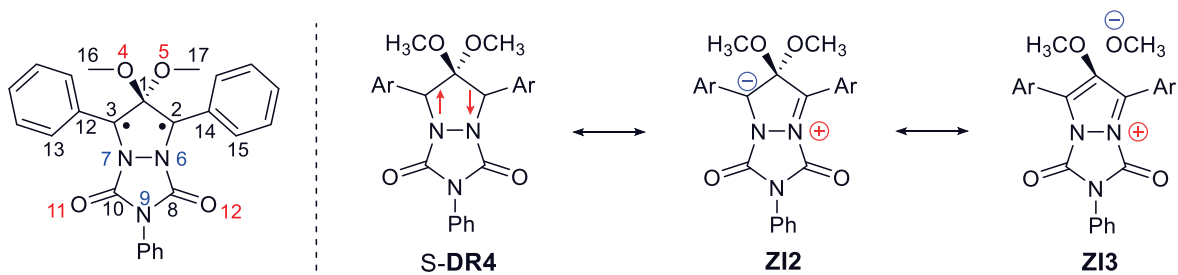
Spin	Donor NBO	Acceptor NBO	Stabilization Energy / kcal mol^{-1}	Contribution type
	LP (N6)	**LP*** (C2)	45.65	**ZI2**
	LP (N6)	**BD*** (C8–O12)	26.93	
	LP (N7)	**BD*** (C10–O11)	31.64	
	LP (N9)	**BD*** (C8–O12)	33.14	
	LP (N9)	**BD*** (C10–O11)	33.49	
α	**LP*** (C2)	**BD*** (C1–O4)	3.55	
	LP* (C2)	**BD*** (C1–O5)	2.50	
	LP (C3)	**LP*** (C2)	0.39	
	LP (C3)	**BD*** (C1–O4)	8.50	**ZI3**
	LP (C3)	**BD*** (C1–O5)	6.34	**ZI3**
	LP (C3)	**BD*** (C12–C13)	34.95	**ZI2**
	LP (N7)	**LP*** (C3)	45.18	**ZI2**
	LP (N7)	**BD*** (C10–O11)	27.09	
	LP (N6)	**BD*** (C8–O12)	30.46	
	LP (N9)	**BD*** (C8–O12)	31.71	
	LP (N9)	**BD*** (C10–O11)	33.42	
β	**LP** (C2)	**LP*** (C3)	0.40	
	LP (C2)	**BD*** (C1–O4)	8.50	**ZI3**
	LP (C2)	**BD*** (C1–O5)	6.34	**ZI3**
	LP (C2)	**BD*** (C14–C15)	34.28	**ZI2**
	LP* (C3)	**BD*** (C1–O4)	3.55	
	LP* (C3)	**BD*** (C1–O5)	2.51	

In gas phase at (BS)-(U)CAM-B3LYP/6-31G(d) level of theory.

4.4 Effects of substituent and solvent on the thermal equilibrium

To evaluate the effect of solvent on the thermal equilibrium for S-**DR4**, the computational study was conducted by using polarizable continuum model (PCM).[6] Although the energy difference between S-**DR4** and **CP4** were overestimated at the several types of density functional theory (DFT) level of theory, (BS)-(R,U)B3LYP[7], M06-2x[8], and ωB97XD[9]/6-31G(d)[10]; respective $\Delta E_{\text{S-DR-ii}-\text{endo-CP}} \approx -14.4 \sim -27.7$ kJ mol^{-1}, 28.1 kJ mol^{-1}, and 17.5 kJ mol^{-1}, the equilibrium constant K which were estimated computational results at the CAM-B3LYP/6-31G(d) level were good agreement with that of experiments, except for aryl-asymmetrically donor–accepter substituted S-**DR4** (X = MeO, Y = Cl or Br) (Table 11).

Table 11. Solvent polarity (PCM) and aryl-substituent dependency on the thermal equilibrium between the singlet diradicals S-**DR4** and its σ-bonded species **CP4**.

K = [endo-**CP4**] / [S-**DR4-ii**]

Substituents	gas phase		toluene (ε = 2.38)			acetonitrile (ε = 36.64)		
(X, Y)	$\Delta E_{\text{DR–CP}}$	$K_{\text{calc.}}$	$\Delta E_{\text{DR–CP}}$	$K_{\text{calc.}}$	$K_{\text{expt.}}$	$\Delta E_{\text{DR–CP}}$	$K_{\text{calc.}}$	$K_{\text{expt.}}$
(H, H)	+0.75	1.35	+1.40	1.76	1.74	−0.07	0.97	0.95
(MeO, MeO)	−1.75	0.49	−1.23	0.61	0.67	−2.12	0.43	0.49
(Cl, Cl)	−3.14	0.28	−2.08	0.43	0.49	−3.79	0.22	0.23
(CN, CN)	−9.30	0.02	−8.67	0.03	~0.00	−10.73	0.01	~0.00
(MeO, Cl)	−3.25	0.27	−2.46	0.37	N/R	−4.17	0.19	N/R
(MeO, Br)	−3.26	0.27	−3.08	0.29	0.50	−4.44	0.17	0.28

in kJ mol^{-1} for $\Delta E_{\text{DR–CP}}$.

Respective equilibrium constants $K_{\text{calu.}}$, and $K_{\text{expt.}}$ at 298.15 K.

at the CAM-B3LYP/6-31G(d) level of theory.

The experimental finding on the effects of substituent and solvent on the rate constant (k_{CP}) for the ring-closing reaction of S-**DR4** to **CP4** suggested that the positive charge at the benzylic position increases with the radical–radical coupling (Chapter 2). To clarify the electron movement involved in the ring-closing/-opening reactions between S-**DR4** and **CP4**, the nitrogen atoms and benzylic moiety (including aromatic ring) of the respective structures; S-**DR4a-ii**, **TS-gg**, and endo-**CP4a**, charges were caluculated by natural population analysis (NPA)[5b] and atomic polar tensor (APT)[11] at the (R,U)CAM-B3LYP/6-31G(d) level of theory, respectively (Scheme 22).

Scheme 22. Charge movement at the benzyl moiety and nitrogen atoms during ring-closing reaction S-**DR4a-ii** to endo-**CP4a** via **TS-gg**. Comparison of individual atom charges calculated by natural population analysis (NPA) and atomic polar tensor (APT, values in parenthesis) at the (BS)-(R,U)CAM-B3LYP/6-31G(d) level of theory.
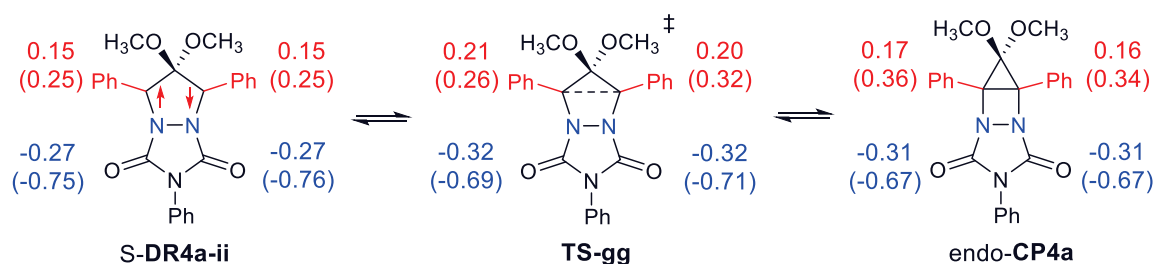
The NPA charge on the benzyl moiety and nitrogen atoms of S-**DR4a-ii** clearly suggested an important contribution to **ZI2**, which possesses anionic characteristics at the benzylic position and cationic characteristics at the nitrogen atoms, because the NPA charge on the benzyl moiety is small and that on the nitrogen atom is large as compared with **TS-gg**; 0.21 in **TS-gg** > 0.15 in S-**DR4a-ii** (benzil moiety), –0.27 in S-**DR4a-ii** > –0.32 in **TS-gg** (nitrogen atoms). Furthermore, the NPA charge on the benzyl moiety increased from 0.15 to 0.21 during the C–C bond formation. Thus, the predicted electron movement in terms of computationally study was consistent with the experimental observation of the effects of substituent and solvent.

4.5 Potential energy surface

4.5.1 Thermal equilibrium reaction between a localized singlet diradicals and its σ-bonded species

The ring-closing reaction of S-**DR4a-ii** to endo-**CP4a** was computed at the (BS)-(R,U)CAM-B3LYP/6-31G(d) level of theory to support experimentally information on the reactivity of S-**DR4a** (Scheme 23). According to the computational finding regarding rotation of the acetal moiety in Chapter 4.2, which conformer of S-**DR4,** i.e. **-ii**, **-ig**, **-gi** or **-gg**, is involved in radical–radical coupling plays a key role in the ring-closing reaction (Figure 90). The intrinsic reaction coordinate (IRC) analysis revealed that only gauche-gauche transition state, **TS-gg**, was connected with S-**DR4a-gg** and endo-**CP4a**, even though two endo-transition states, i.e. **TS-gg** (imaginary number: –509.85 cm^{-1}) and **TS-ig** (–62.63 cm^{-1}), that produce the en-

Scheme 23. Theoretically study as to thermal equilibrium between S-**DR4a** and **CP4a**.

136
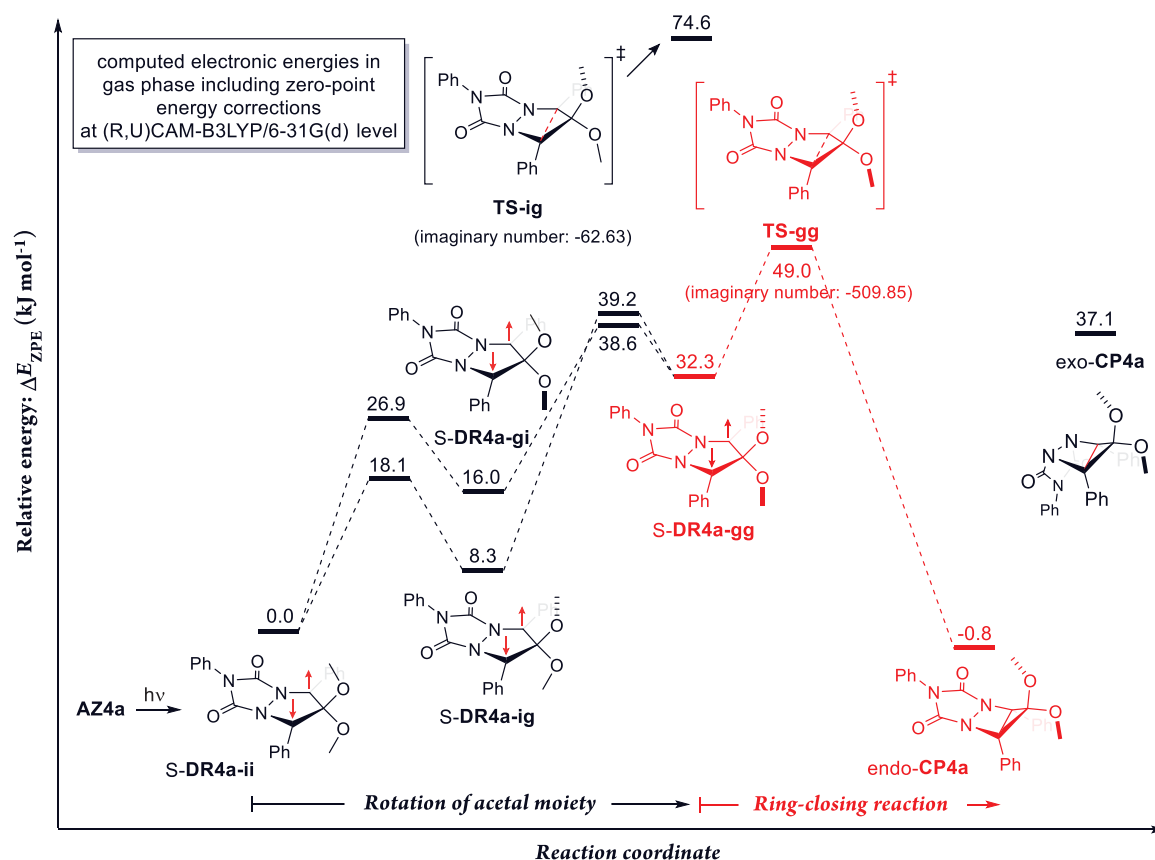
do-**CP4a** were found at this level of theory. Therefore, the C–C bond formation via **TS-gg** takes place after conformational change of S-**DR4a-ii** to S-**DR4a-gg**. Indeed, the energy barrier (E_{ZPE}) from S-**DR4a-ii** to endo-**CP4a** was calculated to be 49.0 kJ mol^{-1} in gas phase at this level of theory. Thus, the DFT computations reproduced the experimentally obtained energy barrier of the ring-closing reaction, E_a = 39.8 kJ mol^{-1} (Table 1 in Chapter 2).

4.5.2   Alkoxy-group migration reactions

The methoxy migration step was computed at the (U)B3LYP/6-31G(d) and (U)CAM-B3LYP/6-31G(d) level of theory. The activation energy of 75.4 (107.9) kJ mol^{-1} was computed for the formation of **MG$_C$4aa** (Scheme 24a). The endo-methoxy group for S-**DR4a** was found to preferably migrated to the benzyl carbon to afford **MG$_C$4aa**. The C–O bond scission in T-**DR4a** was also computed to estimate the energy barrier. The energy barrier was 62.0 (84.0) kJ mol^{-1}, which was smaller than the migration step in S-**DR4a** to afford **MG$_C$4aa** (Scheme 24b). The computed energy profile at B3LYP/6-31G(d) level of theory is qualitatively agreement with the experimental observation; $\Delta G^{\ddagger}_{(\text{S-DR4a} \to \text{MGc4aa})}$ = 68.9 kJ mol^{-1}, $\Delta G^{\ddagger}_{(\text{S-DR4a} \to \text{T-DR4a})}$ = 64.7 kJ mol^{-1} at 298 K in toluene.

Scheme 24. Theoretically study of the alkoxy-group migrated reaction. (a) concerted alkoxy-group 1,2-migrated reaction, and (b) stepwise alkoxy-group migrated reaction via intersystem crossing process.

(a)

		S-**DR4a**	**TS$_C$**	**MG$_C$4aa**
ΔE_{zpe} in kJ mol^{-1}		0.0 (0.0)	+75.4 (+107.9)	-110.3 (-104.4)

(b)

MG$_{CO}$4aa	**TS$_{CO}$**	**T-DR4a**	**S-DR4a**	
-189.0 (-184.2)	+87.9 (+106.0)	+25.9 (+22.0)	0.0 (0.0)	ΔE_{zpe} in kJ mol^{-1}
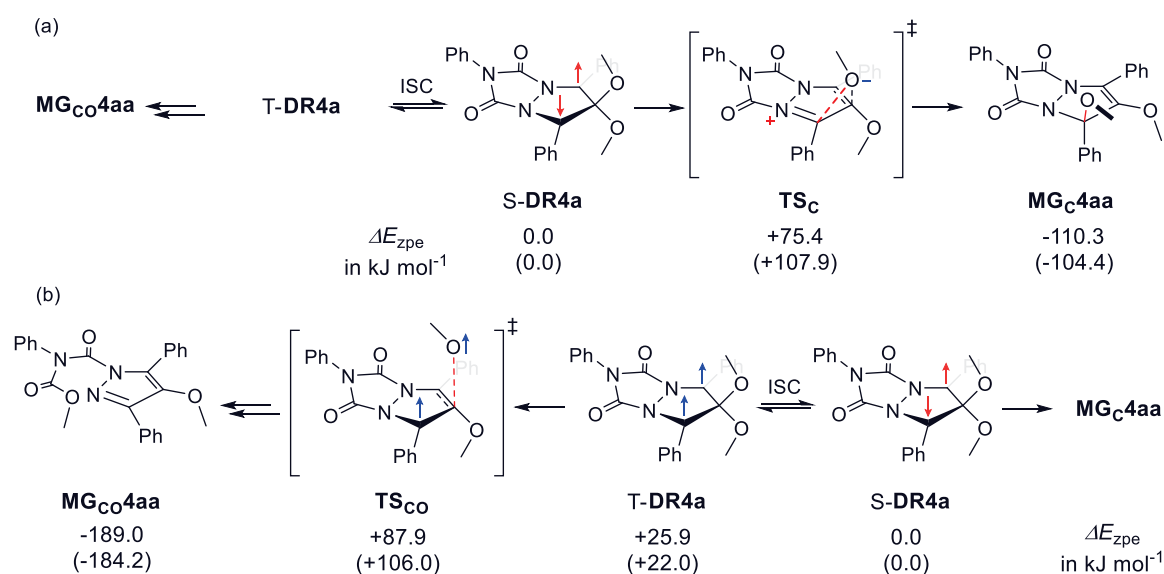
4.6   Chapter summary

In Chapter 4, the singlet 4,4-dimethoxy-1,2-diazacyclopentane-3,5-diyls, S-**DR4a**, and its reactivity were computationally investigated to make the experimental part more definite. Isodesmic reaction indicated that hyper-conjugative zwitterionic resonance structures, **ZI**, play an important role in the thermodynamically stabilization of S-**DR4**. The natural bond orbital (NBO) analysis also revealed I) important contribution to **ZI2,3**, and II) the electron movement involved in the ring-closing reaction S-**DR4** to **CP4**. These computational findings regarding thermal equilibrium reaction and alkoxy-group rearrangement processes made the experimental findings more rational (Scheme 25).

Scheme 25. Computational (in gas) and experimental (in toluene) potential energy surface.

138
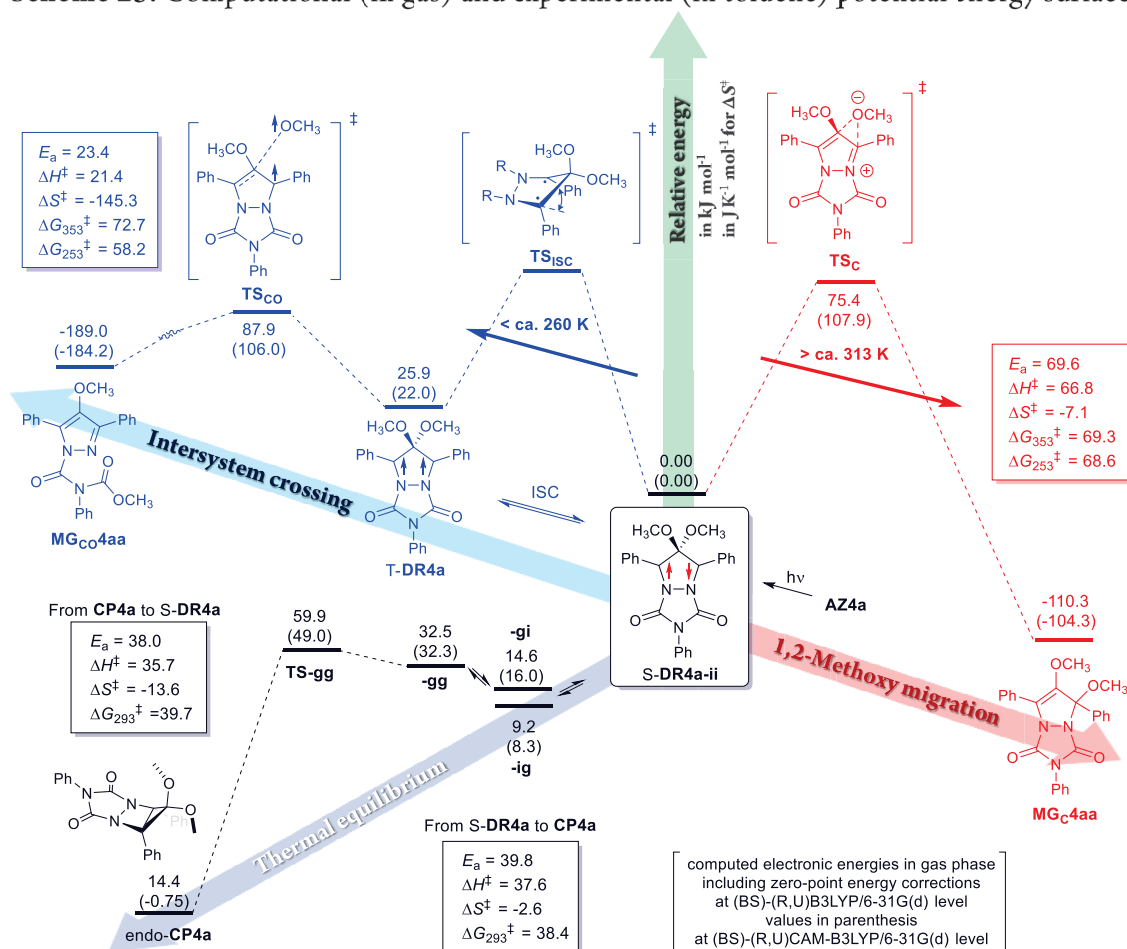
4.7   Supplementary material
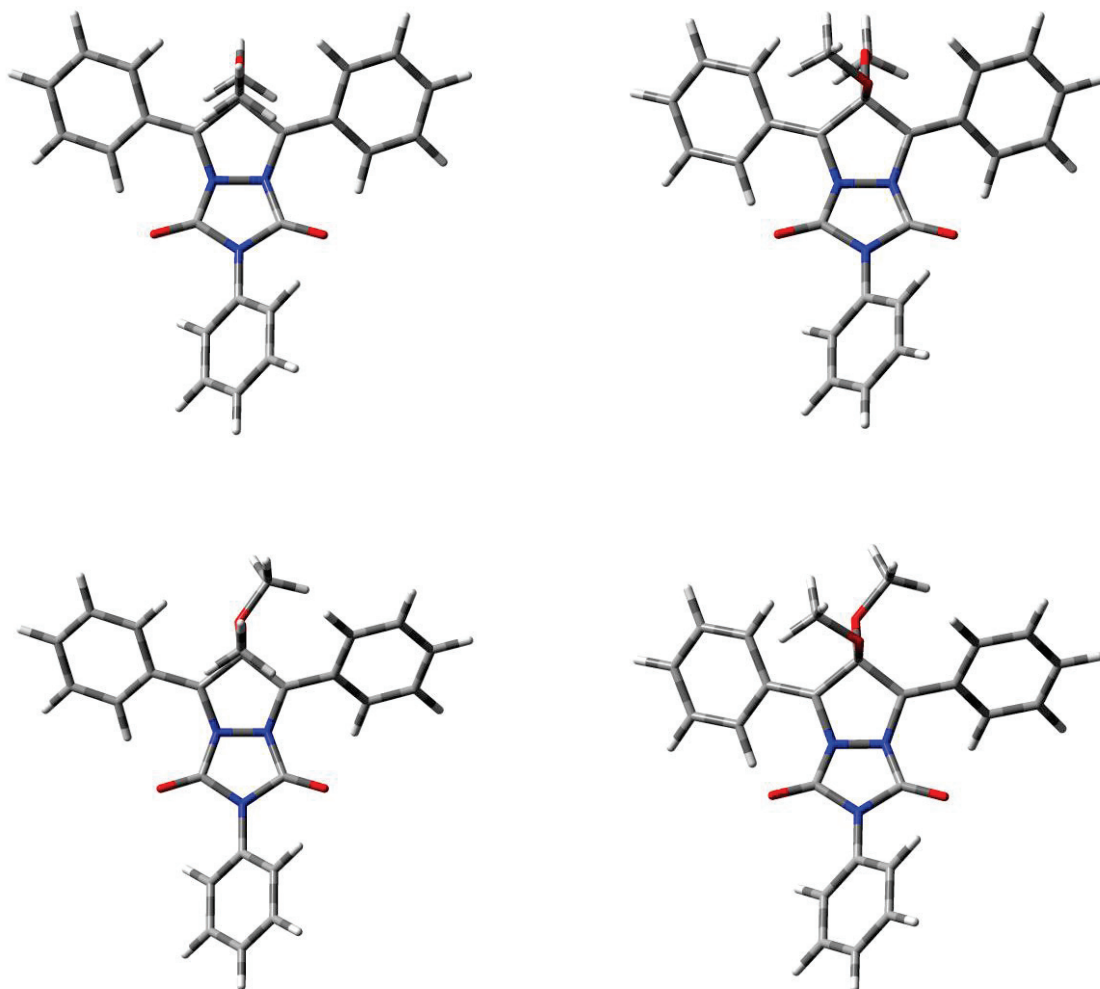
Figure 91. Four conformers of the open-shell singlet state of S-**DR4a**; (in, in): left top, (in, gauche): right top, (gauche, in): left down, and (gauche, gauche): right down.
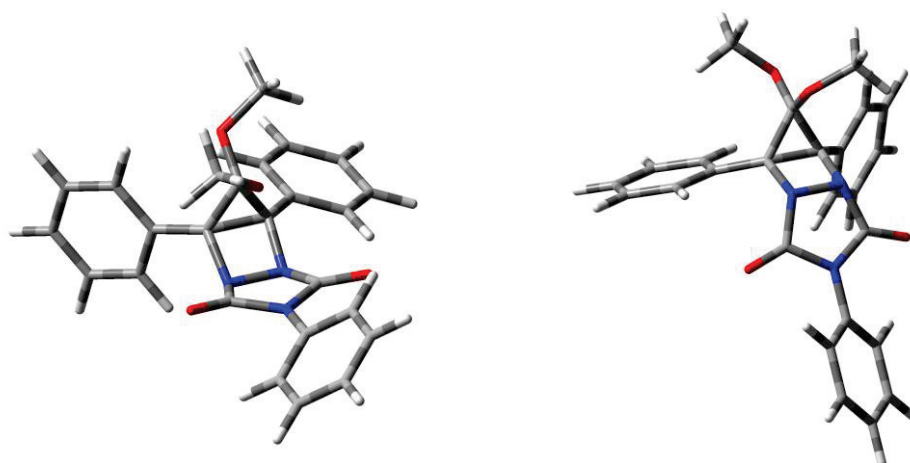
Figure 92. Two ring-closing compounds; endo-isomer (left) and exo-isomer (right).
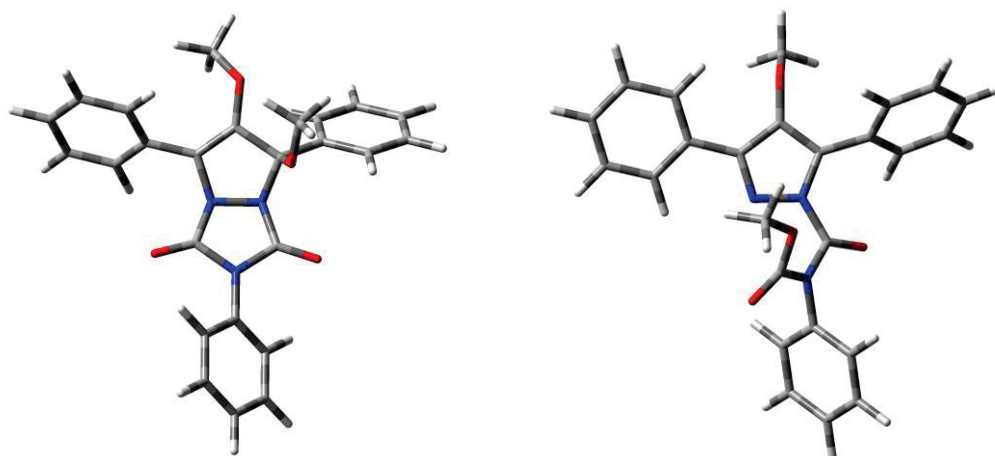
Figure 93. Alkoxy-group migrated products; **MG$_C$4aa** (left) and **MG$_{CO}$4aa** (right)
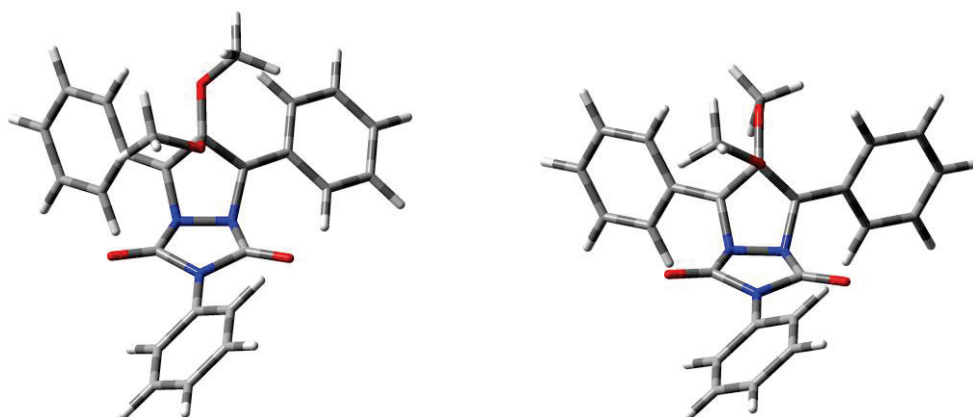
Figure 94. Transition state between S-**DR4a** and endo-**CP4a**. left: **TS-gg** (relative energy: 49.0 kJ mol^{-1}, imaginary number: −509.85 cm^{-1}) and right: **TS-ig** (74.6 kJ mol^{-1}, −62.63 cm^{-1})

S-**DR4a-ii**

at the (BS)-(U)B3LYP/6-31G(d)

Zero-point correction= 0.414779 (Hartree/Particle)

Thermal correction to Energy= 0.441940

Thermal correction to Enthalpy= 0.442884

Thermal correction to Gibbs Free Energy= 0.356676

Sum of electronic and zero-point Energies= -1429.957511

Sum of electronic and thermal Energies= -1429.930350

Sum of electronic and thermal Enthalpies= -1429.929406

Sum of electronic and thermal Free Energies= -1430.015615

at the (BS)-(U)M06-2x/6-31G(d)

Zero-point correction= 0.419743 (Hartree/Particle)

Thermal correction to Energy= 0.446703

Thermal correction to Enthalpy= 0.447647

Thermal correction to Gibbs Free Energy= 0.361551

Sum of electronic and zero-point Energies= -1429.383279

Sum of electronic and thermal Energies= -1429.356320

Sum of electronic and thermal Enthalpies= -1429.355375

Sum of electronic and thermal Free Energies= -1429.441471

at the (BS)-(U)ωB97XD/6-31G(d)

Zero-point correction= 0.420364 (Hartree/Particle)

Thermal correction to Energy= 0.447286

Thermal correction to Enthalpy= 0.448231

Thermal correction to Gibbs Free Energy= 0.362051

Sum of electronic and zero-point Energies= -1429.501266

Sum of electronic and thermal Energies= -1429.474343

Sum of electronic and thermal Enthalpies= -1429.473399

Sum of electronic and thermal Free Energies= -1429.559578

at the (BS)-(U)CAM-B3LYP/6-31G(d)

Zero-point correction= 0.419206 (Hartree/Particle)

Thermal correction to Energy= 0.446211

Thermal correction to Enthalpy= 0.447155

Thermal correction to Gibbs Free Energy= 0.360683

Sum of electronic and zero-point Energies= -1429.287399

Sum of electronic and thermal Energies= -1429.260394

Sum of electronic and thermal Enthalpies= -1429.259450

Sum of electronic and thermal Free Energies= -1429.345922

(toluene)

Zero-point correction= 0.420427 (Hartree/Particle)

Thermal correction to Energy= 0.447238

Thermal correction to Enthalpy= 0.448182

Thermal correction to Gibbs Free Energy= 0.362568

Sum of electronic and zero-point Energies= -1429.245355

Sum of electronic and thermal Energies= -1429.218544

Sum of electronic and thermal Enthalpies= -1429.217600

Sum of electronic and thermal Free Energies= -1429.303214

(acetonitrile)

Zero-point correction= 0.420100 (Hartree/Particle)

Thermal correction to Energy= 0.446987

Thermal correction to Enthalpy= 0.447931

Thermal correction to Gibbs Free Energy= 0.361907

Sum of electronic and zero-point Energies= -1429.253876

Sum of electronic and thermal Energies= -1429.226989

Sum of electronic and thermal Enthalpies= -1429.226045

Sum of electronic and thermal Free Energies= -1429.312069

at the (BS)-(U)CAM-B3LYP/6-31G+(d,p)

Zero-point correction= 0.418302 (Hartree/Particle)

Thermal correction to Energy= 0.445311

Thermal correction to Enthalpy= 0.446255

Thermal correction to Gibbs Free Energy= 0.359842

Sum of electronic and zero-point Energies= -1429.318704

Sum of electronic and thermal Energies= -1429.291695

Sum of electronic and thermal Enthalpies= -1429.290751

Sum of electronic and thermal Free Energies= -1429.377164

S-**DR4a-ig**

at the (BS)-(U)B3LYP/6-31G(d)

Zero-point correction= 0.414711 (Hartree/Particle)

Thermal correction to Energy= 0.441892

Thermal correction to Enthalpy= 0.442836

Thermal correction to Gibbs Free Energy= 0.356598

Sum of electronic and zero-point Energies= -1429.953977

Sum of electronic and thermal Energies= -1429.926796

Sum of electronic and thermal Enthalpies= -1429.925851

Sum of electronic and thermal Free Energies= -1430.012090

at the (BS)-(U)CAM-B3LYP/6-31G(d)

Zero-point correction= 0.420598 (Hartree/Particle)

Thermal correction to Energy= 0.447365

Thermal correction to Enthalpy= 0.448310

Thermal correction to Gibbs Free Energy= 0.362905

Sum of electronic and zero-point Energies= -1429.235996

Sum of electronic and thermal Energies= -1429.209229

Sum of electronic and thermal Enthalpies= -1429.208285

Sum of electronic and thermal Free Energies= -1429.293690

S-**DR4a-gi**

at the (BS)-(U)B3LYP/6-31G(d)

Zero-point correction= 0.414322 (Hartree/Particle)

Thermal correction to Energy= 0.441804

Thermal correction to Enthalpy= 0.442748

Thermal correction to Gibbs Free Energy= 0.353986

Sum of electronic and zero-point Energies= -1429.951878

Sum of electronic and thermal Energies= -1429.924396

Sum of electronic and thermal Enthalpies= -1429.923452

Sum of electronic and thermal Free Energies= -1430.012214

at the (BS)-(U)CAM-B3LYP/6-31G(d)

Zero-point correction= 0.420404 (Hartree/Particle)

Thermal correction to Energy= 0.447362

Thermal correction to Enthalpy= 0.448306

Thermal correction to Gibbs Free Energy= 0.361895

Sum of electronic and zero-point Energies= -1429.233064

Sum of electronic and thermal Energies= -1429.206105

Sum of electronic and thermal Enthalpies= -1429.205161

Sum of electronic and thermal Free Energies= -1429.291572

S-**DR4a-gg**

at the (BS)-(U)B3LYP/6-31G(d)

Zero-point correction= 0.414363 (Hartree/Particle)

Thermal correction to Energy= 0.441619

Thermal correction to Enthalpy= 0.442563

Thermal correction to Gibbs Free Energy= 0.355844

Sum of electronic and zero-point Energies= -1429.945127

Sum of electronic and thermal Energies= -1429.917872

Sum of electronic and thermal Enthalpies= -1429.916928

Sum of electronic and thermal Free Energies= -1430.003647

at the (BS)-(U)CAM-B3LYP/6-31G(d)

Zero-point correction= 0.420448 (Hartree/Particle)

Thermal correction to Energy= 0.447228

Thermal correction to Enthalpy= 0.448172

Thermal correction to Gibbs Free Energy= 0.362578

Sum of electronic and zero-point Energies= -1429.226829

Sum of electronic and thermal Energies= -1429.200049

Sum of electronic and thermal Enthalpies= -1429.199105

Sum of electronic and thermal Free Energies= -1429.284699

T-**DR4a**-ii

at the (U)B3LYP/6-31G(d)

Zero-point correction= 0.414577 (Hartree/Particle)

Thermal correction to Energy= 0.441818

Thermal correction to Enthalpy= 0.442762

Thermal correction to Gibbs Free Energy= 0.355367

Sum of electronic and zero-point Energies= -1429.951304

Sum of electronic and thermal Energies= -1429.924063

Sum of electronic and thermal Enthalpies= -1429.923119

Sum of electronic and thermal Free Energies= -1430.010514

at the (U)CAM-B3LYP/6-31G(d)

Zero-point correction= 0.420382 (Hartree/Particle)

Thermal correction to Energy= 0.447269

Thermal correction to Enthalpy= 0.448214

Thermal correction to Gibbs Free Energy= 0.361348

Sum of electronic and zero-point Energies= -1429.234569

Sum of electronic and thermal Energies= -1429.207682

Sum of electronic and thermal Enthalpies= -1429.206738

Sum of electronic and thermal Free Energies= -1429.293603

endo-**CP4a**

at the (R)B3LYP/6-31G(d)

Zero-point correction= 0.416348 (Hartree/Particle)

Thermal correction to Energy= 0.443277

Thermal correction to Enthalpy= 0.444221

Thermal correction to Gibbs Free Energy= 0.357805

Sum of electronic and zero-point Energies= -1429.952018

Sum of electronic and thermal Energies= -1429.925090

Sum of electronic and thermal Enthalpies= -1429.924145

Sum of electronic and thermal Free Energies= -1430.010562

at the (R)CAM-B3LYP/6-31G(d)

Zero-point correction= 0.422763 (Hartree/Particle)

Thermal correction to Energy= 0.449228

Thermal correction to Enthalpy= 0.450172

Thermal correction to Gibbs Free Energy= 0.364612

Sum of electronic and zero-point Energies= -1429.239428

Sum of electronic and thermal Energies= -1429.212963

Sum of electronic and thermal Enthalpies= -1429.212019

Sum of electronic and thermal Free Energies= -1429.297579

(toluene)

Zero-point correction= 0.422417 (Hartree/Particle)

Thermal correction to Energy= 0.448965

Thermal correction to Enthalpy= 0.449909

Thermal correction to Gibbs Free Energy= 0.363893

Sum of electronic and zero-point Energies= -1429.245888

Sum of electronic and thermal Energies= -1429.219340

Sum of electronic and thermal Enthalpies= -1429.218396

Sum of electronic and thermal Free Energies= -1429.304412

(acetonitrile)

Zero-point correction= 0.422085 (Hartree/Particle)

Thermal correction to Energy= 0.448716

Thermal correction to Enthalpy= 0.449661

Thermal correction to Gibbs Free Energy= 0.363020

Sum of electronic and zero-point Energies= -1429.253850

Sum of electronic and thermal Energies= -1429.227218

Sum of electronic and thermal Enthalpies= -1429.226274

Sum of electronic and thermal Free Energies= -1429.312915

exo-CP4a

at the (R)B3LYP/6-31G(d)

Zero-point correction= 0.415661 (Hartree/Particle)

Thermal correction to Energy= 0.442779

Thermal correction to Enthalpy= 0.443723

Thermal correction to Gibbs Free Energy= 0.356670

Sum of electronic and zero-point Energies= -1429.938390

Sum of electronic and thermal Energies= -1429.911272

Sum of electronic and thermal Enthalpies= -1429.910328

Sum of electronic and thermal Free Energies= -1429.997381

at the (R)CAM-B3LYP/6-31G(d)

Zero-point correction= 0.422122 (Hartree/Particle)

Thermal correction to Energy= 0.448766

Thermal correction to Enthalpy= 0.449710

Thermal correction to Gibbs Free Energy= 0.363751

Sum of electronic and zero-point Energies= -1429.225007

Sum of electronic and thermal Energies= -1429.198363

Sum of electronic and thermal Enthalpies= -1429.197419

Sum of electronic and thermal Free Energies= -1429.283377

TS-gg (S-**DR4a** ⇄ **CP4a**)

at the CAM-B3LYP/6-31G(d)

Zero-point correction= 0.420609 (Hartree/Particle)

Thermal correction to Energy= 0.446862

Thermal correction to Enthalpy= 0.447806

Thermal correction to Gibbs Free Energy= 0.363073

Sum of electronic and zero-point Energies= -1429.220469

Sum of electronic and thermal Energies= -1429.194215

Sum of electronic and thermal Enthalpies= -1429.193271

Sum of electronic and thermal Free Energies= -1429.278005

Imaginary frequency: -509.85 cm^{-1}

Transition state TS_C (S-DR4a-ii → MG_C4aa): C–O bond scission in S-DR4a

at the (BS)-(U)B3LYP/6-31G(d)

Zero-point correction= 0.412018 (Hartree/Particle)

Thermal correction to Energy= 0.439481

Thermal correction to Enthalpy= 0.440425

Thermal correction to Gibbs Free Energy= 0.352982

Sum of electronic and zero-point Energies= -1429.928781

Sum of electronic and thermal Energies= -1429.901319

Sum of electronic and thermal Enthalpies= -1429.900374

Sum of electronic and thermal Free Energies= -1429.987818

Imaginary frequency: -324.42 cm^{-1}

at the (BS)-(U)CAM-B3LYP/6-31G(d)

Zero-point correction= 0.417825 (Hartree/Particle)

Thermal correction to Energy= 0.444922

Thermal correction to Enthalpy= 0.445866

Thermal correction to Gibbs Free Energy= 0.359134

Sum of electronic and zero-point Energies= -1429.198056

Sum of electronic and thermal Energies= -1429.170958

Sum of electronic and thermal Enthalpies= -1429.170014

Sum of electronic and thermal Free Energies= -1429.256747

Imaginary frequency: -432.78 cm^{-1}

TS$_{CO}$ (T-DR4a-ii → MG$_{CO}$4aa): C-O bond scission in T-DR4a

at the (BS)-(U)B3LYP/6-31G(d)

Zero-point correction= 0.411235 (Hartree/Particle)

Thermal correction to Energy= 0.439106

Thermal correction to Enthalpy= 0.440050

Thermal correction to Gibbs Free Energy= 0.350015

Sum of electronic and zero-point Energies= -1429.924018

Sum of electronic and thermal Energies= -1429.896147

Sum of electronic and thermal Enthalpies= -1429.895203

Sum of electronic and thermal Free Energies= -1429.985238

Imaginary frequency: -290.33 cm^{-1}

at the (BS)-(U)CAM-B3LYP/6-31G(d)

Zero-point correction= 0.417029 (Hartree/Particle)

Thermal correction to Energy= 0.444546

Thermal correction to Enthalpy= 0.445491

Thermal correction to Gibbs Free Energy= 0.356063

Sum of electronic and zero-point Energies= -1429.198769

Sum of electronic and thermal Energies= -1429.171251

Sum of electronic and thermal Enthalpies= -1429.170307

Sum of electronic and thermal Free Energies= -1429.259735

Imaginary frequency: -301.42 cm^{-1}

Alkoxy-group migrated species **MG$_{CO}$4aa**

at the (R)B3LYP/6-31G(d)

Zero-point correction= 0.416081 (Hartree/Particle)

Thermal correction to Energy= 0.444149

Thermal correction to Enthalpy= 0.445093

Thermal correction to Gibbs Free Energy= 0.352562

Sum of electronic and zero-point Energies= -1430.029500

Sum of electronic and thermal Energies= -1430.001432

Sum of electronic and thermal Enthalpies= -1430.000488

Sum of electronic and thermal Free Energies= -1430.093019

at the (R)CAM-B3LYP/6-31G(d)

Zero-point correction= 0.422044 (Hartree/Particle)

Thermal correction to Energy= 0.449809

Thermal correction to Enthalpy= 0.450753

Thermal correction to Gibbs Free Energy= 0.358429

Sum of electronic and zero-point Energies= -1429.309305

Sum of electronic and thermal Energies= -1429.281540

Sum of electronic and thermal Enthalpies= -1429.280595

Sum of electronic and thermal Free Energies= -1429.372919

Alkoxy-group migrated species **MG$_C$4a**

at the (R)B3LYP/6-31G(d)

Zero-point correction= 0.416577 (Hartree/Particle)

Thermal correction to Energy= 0.443766

Thermal correction to Enthalpy= 0.444710

Thermal correction to Gibbs Free Energy= 0.357096

Sum of electronic and zero-point Energies= -1429.994475

Sum of electronic and thermal Energies= -1429.967286

Sum of electronic and thermal Enthalpies= -1429.966342

Sum of electronic and thermal Free Energies= -1430.053955

at the (R)CAM-B3LYP/6-31G(d)

Zero-point correction= 0.422858 (Hartree/Particle)

Thermal correction to Energy= 0.449596

Thermal correction to Enthalpy= 0.450540

Thermal correction to Gibbs Free Energy= 0.364086

Sum of electronic and zero-point Energies= -1429.278896

Sum of electronic and thermal Energies= -1429.252157

Sum of electronic and thermal Enthalpies= -1429.251213

Sum of electronic and thermal Free Energies= -1429.337667

C$_{H,H}$

at the (R)CAM-B3LYP/6-31G(d)

Zero-point correction= 0.440138 (Hartree/Particle)

Thermal correction to Energy= 0.460879

Thermal correction to Enthalpy= 0.461824

Thermal correction to Gibbs Free Energy= 0.391047

Sum of electronic and zero-point Energies= -1003.425212

Sum of electronic and thermal Energies= -1003.404471

Sum of electronic and thermal Enthalpies= -1003.403527

Sum of electronic and thermal Free Energies= -1003.474303

N$_{H,H}$

at the (R)CAM-B3LYP/6-31G(d)

Zero-point correction= 0.447693 (Hartree/Particle)

Thermal correction to Energy= 0.474210

Thermal correction to Enthalpy= 0.475154

Thermal correction to Gibbs Free Energy= 0.390069

Sum of electronic and zero-point Energies= -1430.471025

Sum of electronic and thermal Energies= -1430.444508

Sum of electronic and thermal Enthalpies= -1430.443563

Sum of electronic and thermal Free Energies= -1430.528649

Substituent and solvent effects

at the (BS)-$(U)CAM$-B3LYP/6-31G(d)

S-**DR4b-ii** $(X = MeO, Y = MeO)$

Zero-point correction= 0.486892 (Hartree/Particle)

Thermal correction to Energy= 0.518980

Thermal correction to Enthalpy= 0.519924

Thermal correction to Gibbs Free Energy= 0.422032

Sum of electronic and zero-point Energies= -1658.130163

Sum of electronic and thermal Energies= -1658.098075

Sum of electronic and thermal Enthalpies= -1658.097131

Sum of electronic and thermal Free Energies= -1658.195023

(toluene)

Zero-point correction= 0.486568 (Hartree/Particle)

Thermal correction to Energy= 0.518693

Thermal correction to Enthalpy= 0.519637

Thermal correction to Gibbs Free Energy= 0.421663

Sum of electronic and zero-point Energies= -1658.138046

Sum of electronic and thermal Energies= -1658.105921

Sum of electronic and thermal Enthalpies= -1658.104977

Sum of electronic and thermal Free Energies= -1658.202950

(acetonitrile)

Zero-point correction= 0.486178 (Hartree/Particle)

Thermal correction to Energy= 0.518381

Thermal correction to Enthalpy= 0.519325

Thermal correction to Gibbs Free Energy= 0.420992

Sum of electronic and zero-point Energies= -1658.148216

Sum of electronic and thermal Energies= -1658.116014

Sum of electronic and thermal Enthalpies= -1658.115070

Sum of electronic and thermal Free Energies= -1658.213403

S-DR4e-ii (X = Cl, Y = Cl)

Zero-point correction= 0.401184 (Hartree/Particle)

Thermal correction to Energy= 0.430517

Thermal correction to Enthalpy= 0.431461

Thermal correction to Gibbs Free Energy= 0.338999

Sum of electronic and zero-point Energies= -2348.457800

Sum of electronic and thermal Energies= -2348.428467

Sum of electronic and thermal Enthalpies= -2348.427523

Sum of electronic and thermal Free Energies= -2348.519985

(toluene)

Zero-point correction= 0.400975 (Hartree/Particle)

Thermal correction to Energy= 0.430313

Thermal correction to Enthalpy= 0.431257

Thermal correction to Gibbs Free Energy= 0.338856

Sum of electronic and zero-point Energies= -2348.464225

Sum of electronic and thermal Energies= -2348.434887

Sum of electronic and thermal Enthalpies= -2348.433943

Sum of electronic and thermal Free Energies= -2348.526344

(acetonitrile)

Zero-point correction= 0.400580 (Hartree/Particle)

Thermal correction to Energy= 0.430014

Thermal correction to Enthalpy= 0.430958

Thermal correction to Gibbs Free Energy= 0.338012

Sum of electronic and zero-point Energies= -2348.472698

Sum of electronic and thermal Energies= -2348.443264

Sum of electronic and thermal Enthalpies= -2348.442320

Sum of electronic and thermal Free Energies= -2348.535266

S-DR4g-ii $(X = CN, Y = CN)$

Zero-point correction= 0.417791 (Hartree/Particle)

Thermal correction to Energy= 0.448297

Thermal correction to Enthalpy= 0.449241

Thermal correction to Gibbs Free Energy= 0.354606

Sum of electronic and zero-point Energies= -1613.647234

Sum of electronic and thermal Energies= -1613.616728

Sum of electronic and thermal Enthalpies= -1613.615784

Sum of electronic and thermal Free Energies= -1613.710419

(toluene)

Zero-point correction= 0.417713 (Hartree/Particle)

Thermal correction to Energy= 0.448193

Thermal correction to Enthalpy= 0.449137

Thermal correction to Gibbs Free Energy= 0.354625

Sum of electronic and zero-point Energies= -1613.657902

Sum of electronic and thermal Energies= -1613.627423

Sum of electronic and thermal Enthalpies= -1613.626478

Sum of electronic and thermal Free Energies= -1613.720990

(acetonitrile)

Zero-point correction= 0.417409 (Hartree/Particle)

Thermal correction to Energy= 0.447977

Thermal correction to Enthalpy= 0.448921

Thermal correction to Gibbs Free Energy= 0.353746

Sum of electronic and zero-point Energies= -1613.670603

Sum of electronic and thermal Energies= -1613.640035

Sum of electronic and thermal Enthalpies= -1613.639091

Sum of electronic and thermal Free Energies= -1613.734266

S-DR4-ii (X = MeO, Y = Cl)

Zero-point correction= 0.444104 (Hartree/Particle)

Thermal correction to Energy= 0.474798

Thermal correction to Enthalpy= 0.475743

Thermal correction to Gibbs Free Energy= 0.380639

Sum of electronic and zero-point Energies= -2003.294218

Sum of electronic and thermal Energies= -2003.263524

Sum of electronic and thermal Enthalpies= -2003.262580

Sum of electronic and thermal Free Energies= -2003.357684

(toluene)

Zero-point correction= 0.443826 (Hartree/Particle)

Thermal correction to Energy= 0.474545

Thermal correction to Enthalpy= 0.475489

Thermal correction to Gibbs Free Energy= 0.380363

Sum of electronic and zero-point Energies= -2003.301332

Sum of electronic and thermal Energies= -2003.270614

Sum of electronic and thermal Enthalpies= -2003.269670

Sum of electronic and thermal Free Energies= -2003.364796

(acetonitrile)

Zero-point correction= 0.443424 (Hartree/Particle)

Thermal correction to Energy= 0.474224

Thermal correction to Enthalpy= 0.475168

Thermal correction to Gibbs Free Energy= 0.379632

Sum of electronic and zero-point Energies= -2003.310597

Sum of electronic and thermal Energies= -2003.279796

Sum of electronic and thermal Enthalpies= -2003.278852

Sum of electronic and thermal Free Energies= -2003.374389

S-DR4h-ii (X = MeO, Y = Br)

Zero-point correction= 0.443600 (Hartree/Particle)

Thermal correction to Energy= 0.474551

Thermal correction to Enthalpy= 0.475496

Thermal correction to Gibbs Free Energy= 0.379089

Sum of electronic and zero-point Energies= -4114.899599

Sum of electronic and thermal Energies= -4114.868648

Sum of electronic and thermal Enthalpies= -4114.867703

Sum of electronic and thermal Free Energies= -4114.964110

(toluene)

Zero-point correction= 0.443234 (Hartree/Particle)

Thermal correction to Energy= 0.474262

Thermal correction to Enthalpy= 0.475206

Thermal correction to Gibbs Free Energy= 0.378469

Sum of electronic and zero-point Energies= -4114.906795

Sum of electronic and thermal Energies= -4114.875766

Sum of electronic and thermal Enthalpies= -4114.874822

Sum of electronic and thermal Free Energies= -4114.971560

(acetonitrile)

Zero-point correction= 0.442993 (Hartree/Particle)

Thermal correction to Energy= 0.474032

Thermal correction to Enthalpy= 0.474976

Thermal correction to Gibbs Free Energy= 0.378218

Sum of electronic and zero-point Energies= -4114.915963

Sum of electronic and thermal Energies= -4114.884924

Sum of electronic and thermal Enthalpies= -4114.883980

Sum of electronic and thermal Free Energies= -4114.980738

endo-**CP4b** (X = MeO, Y = MeO)

Zero-point correction= 0.489085 (Hartree/Particle)

Thermal correction to Energy= 0.520751

Thermal correction to Enthalpy= 0.521695

Thermal correction to Gibbs Free Energy= 0.424037

Sum of electronic and zero-point Energies= -1658.129497

Sum of electronic and thermal Energies= -1658.097831

Sum of electronic and thermal Enthalpies= -1658.096887

Sum of electronic and thermal Free Energies= -1658.194545

(toluene)

Zero-point correction= 0.488761 (Hartree/Particle)

Thermal correction to Energy= 0.520465

Thermal correction to Enthalpy= 0.521409

Thermal correction to Gibbs Free Energy= 0.423707

Sum of electronic and zero-point Energies= -1658.137579

Sum of electronic and thermal Energies= -1658.105876

Sum of electronic and thermal Enthalpies= -1658.104932

Sum of electronic and thermal Free Energies= -1658.202634

(acetonitrile)

Zero-point correction= 0.488302 (Hartree/Particle)

Thermal correction to Energy= 0.520094

Thermal correction to Enthalpy= 0.521038

Thermal correction to Gibbs Free Energy= 0.422892

Sum of electronic and zero-point Energies= -1658.147410

Sum of electronic and thermal Energies= -1658.115618

Sum of electronic and thermal Enthalpies= -1658.114674

Sum of electronic and thermal Free Energies= -1658.212820

endo-**CP4e** (X = Cl, Y =Cl)

Zero-point correction= 0.403269 (Hartree/Particle)

Thermal correction to Energy= 0.432237

Thermal correction to Enthalpy= 0.433181

Thermal correction to Gibbs Free Energy= 0.340753

Sum of electronic and zero-point Energies= -2348.456605

Sum of electronic and thermal Energies= -2348.427637

Sum of electronic and thermal Enthalpies= -2348.426693

Sum of electronic and thermal Free Energies= -2348.519121

(toluene)

Zero-point correction= 0.402811 (Hartree/Particle)

Thermal correction to Energy= 0.431920

Thermal correction to Enthalpy= 0.432864

Thermal correction to Gibbs Free Energy= 0.339716

Sum of electronic and zero-point Energies= -2348.463431

Sum of electronic and thermal Energies= -2348.434322

Sum of electronic and thermal Enthalpies= -2348.433378

Sum of electronic and thermal Free Energies= -2348.526526

(acetonitrile)

Zero-point correction= 0.402581 (Hartree/Particle)

Thermal correction to Energy= 0.431691

Thermal correction to Enthalpy= 0.432635

Thermal correction to Gibbs Free Energy= 0.339476

Sum of electronic and zero-point Energies= -2348.471253

Sum of electronic and thermal Energies= -2348.442144

Sum of electronic and thermal Enthalpies= -2348.441199

Sum of electronic and thermal Free Energies= -2348.534358

endo-**CP4g** (X = CN, Y = CN)

Zero-point correction= 0.419879 (Hartree/Particle)

Thermal correction to Energy= 0.450046

Thermal correction to Enthalpy= 0.450990

Thermal correction to Gibbs Free Energy= 0.356370

Sum of electronic and zero-point Energies= -1613.643691

Sum of electronic and thermal Energies= -1613.613525

Sum of electronic and thermal Enthalpies= -1613.612581

Sum of electronic and thermal Free Energies= -1613.707201

(toluene)

Zero-point correction= 0.419520 (Hartree/Particle)

Thermal correction to Energy= 0.449804

Thermal correction to Enthalpy= 0.450748

Thermal correction to Gibbs Free Energy= 0.355443

Sum of electronic and zero-point Energies= -1613.654600

Sum of electronic and thermal Energies= -1613.624315

Sum of electronic and thermal Enthalpies= -1613.623371

Sum of electronic and thermal Free Energies= -1613.718677

(acetonitrile)

Zero-point correction= 0.419312 (Hartree/Particle)

Thermal correction to Energy= 0.449604

Thermal correction to Enthalpy= 0.450548

Thermal correction to Gibbs Free Energy= 0.355193

Sum of electronic and zero-point Energies= -1613.666517

Sum of electronic and thermal Energies= -1613.636225

Sum of electronic and thermal Enthalpies= -1613.635281

Sum of electronic and thermal Free Energies= -1613.730636

endo-**CP4** (X = MeO, Y = Cl)

Zero-point correction= 0.446202 (Hartree/Particle)

Thermal correction to Energy= 0.476517

Thermal correction to Enthalpy= 0.477461

Thermal correction to Gibbs Free Energy= 0.382389

Sum of electronic and zero-point Energies= -2003.292979

Sum of electronic and thermal Energies= -2003.262664

Sum of electronic and thermal Enthalpies= -2003.261720

Sum of electronic and thermal Free Energies= -2003.356792

(toluene)

Zero-point correction= 0.445739 (Hartree/Particle)

Thermal correction to Energy= 0.476181

Thermal correction to Enthalpy= 0.477125

Thermal correction to Gibbs Free Energy= 0.381420

Sum of electronic and zero-point Energies= -2003.300396

Sum of electronic and thermal Energies= -2003.269954

Sum of electronic and thermal Enthalpies= -2003.269010

Sum of electronic and thermal Free Energies= -2003.364715

(acetonitrile)

Zero-point correction= 0.445427 (Hartree/Particle)

Thermal correction to Energy= 0.475899

Thermal correction to Enthalpy= 0.476844

Thermal correction to Gibbs Free Energy= 0.380969

Sum of electronic and zero-point Energies= -2003.309010

Sum of electronic and thermal Energies= -2003.278538

Sum of electronic and thermal Enthalpies= -2003.277593

Sum of electronic and thermal Free Energies= -2003.373468

endo-**CP4h** $(X = MeO, Y = Br)$

Zero-point correction= 0.445744 (Hartree/Particle)

Thermal correction to Energy= 0.476318

Thermal correction to Enthalpy= 0.477262

Thermal correction to Gibbs Free Energy= 0.380821

Sum of electronic and zero-point Energies= -4114.898359

Sum of electronic and thermal Energies= -4114.867785

Sum of electronic and thermal Enthalpies= -4114.866841

Sum of electronic and thermal Free Energies= -4114.963282

(toluene)

Zero-point correction= 0.445456 (Hartree/Particle)

Thermal correction to Energy= 0.476066

Thermal correction to Enthalpy= 0.477010

Thermal correction to Gibbs Free Energy= 0.380583

Sum of electronic and zero-point Energies= -4114.905622

Sum of electronic and thermal Energies= -4114.875012

Sum of electronic and thermal Enthalpies= -4114.874067

Sum of electronic and thermal Free Energies= -4114.970495

(acetonitrile)

Zero-point correction= 0.445120 (Hartree/Particle)

Thermal correction to Energy= 0.475774

Thermal correction to Enthalpy= 0.476718

Thermal correction to Gibbs Free Energy= 0.379949

Sum of electronic and zero-point Energies= -4114.914271

Sum of electronic and thermal Energies= -4114.883617

Sum of electronic and thermal Enthalpies= -4114.882673

Sum of electronic and thermal Free Energies= -4114.979441

Table 12. Comparsion of individual atom charges of S-**DR4a-ii**, **TS-gg**, and endo-**CP4a** calculated by natural population analysis (NPA) and atomic polar tensor (APT) at the (BS)-(R,U)CAM-B3LYP/6-31G(d) level of theory. Pale yellow and pale green: benzylic carbon + aromatic ring moiety.

| Atom | Number | S-**DR4a-ii** | | **TS-gg** | | endo-**CP4a** | |
		Natural Charge	APT	Natural Charge	APT	Natural Charge	APT
C	1	0.52695	1.065703	0.53754	0.734924	0.59062	0.870031
C	2	0.14527	0.216102	0.18612	0.323575	0.14169	0.281498
C	3	0.14535	0.21527	0.16801	0.296786	0.12852	0.368533
O	4	-0.57801	-0.815908	-0.60536	-0.769265	-0.58989	-0.849157
O	5	-0.57097	-0.792156	-0.5903	-0.743362	-0.58391	-0.798374
N	6	-0.27098	-0.758556	-0.31652	-0.710199	-0.31109	-0.664663
N	7	-0.2711	-0.749577	-0.31479	-0.68591	-0.31044	-0.668898
C	8	0.85305	1.47921	0.86517	1.419569	0.85927	1.357199
N	9	-0.5113	-1.018277	-0.51334	-0.95301	-0.51261	-1.007219
C	10	0.85158	1.477798	0.85394	1.393008	0.84769	1.347484
O	11	-0.59611	-0.798036	-0.60317	-0.757391	-0.60448	-0.778713
O	12	-0.59817	-0.795626	-0.60479	-0.772339	-0.60889	-0.795165
C	13	0.13528	0.500941	0.13921	0.493759	0.14005	0.474603
C	14	-0.2331	-0.040026	-0.23679	-0.044737	-0.23777	-0.045452
C	15	-0.2312	-0.109798	-0.2343	-0.118282	-0.23678	-0.120367
C	16	-0.22981	-0.104214	-0.23175	-0.10815	-0.23051	-0.10033
C	17	-0.2281	0.000059	-0.22942	0.005207	-0.22983	0.00553
C	18	-0.22777	0.001155	-0.22904	0.005636	-0.22971	0.004615
H	19	0.26293	0.085874	0.26602	0.092657	0.26656	0.09428
H	20	0.25796	0.075679	0.25836	0.07616	0.25768	0.072785
H	21	0.24459	0.022323	0.2428	0.019661	0.24252	0.019411
H	22	0.24472	0.02259	0.24266	0.019649	0.24194	0.019125
H	23	0.24261	0.023271	0.24058	0.020637	0.24012	0.020236
C	24	-0.1173	0.018598	-0.10717	0.027186	-0.08885	0.054212
C	25	-0.22604	-0.052509	-0.22791	-0.064192	-0.23487	-0.032655
C	26	-0.20324	-0.04701	-0.21493	-0.060097	-0.21251	-0.08626
C	27	-0.20163	-0.057064	-0.19726	-0.071706	-0.22041	-0.064667

Continuation of **Table 12** (Atom No. 28–53).

Atom	Number	S-**DR4a-ii**		TS-**gg**		endo-**CP4a**	
		Natural Charge	APT	Natural Charge	APT	Natural Charge	APT
C	28	-0.2385	-0.030511	-0.2328	0.021137	-0.23219	-0.016745
C	29	-0.24036	-0.003355	-0.23546	-0.041597	-0.22958	0.005331
H	30	0.26091	0.087844	0.24949	0.066792	0.25975	0.087838
H	31	0.25208	0.069588	0.25701	0.074899	0.25271	0.057285
H	32	0.24141	0.015767	0.24331	0.016366	0.24101	0.017222
H	33	0.24096	0.014492	0.24057	0.013994	0.243	0.019543
H	34	0.23803	0.016324	-0.10955	-0.028724	0.24002	0.017572
C	35	-0.11693	0.016976	-0.22052	-0.050188	-0.09363	-0.015753
C	36	-0.22589	-0.052561	-0.18979	-0.04769	-0.22666	-0.013836
C	37	-0.2014	-0.056067	-0.1975	-0.038672	-0.19848	-0.052663
C	38	-0.20304	-0.047338	-0.23856	-0.031895	-0.2062	-0.062653
C	39	-0.2402	-0.002489	-0.23647	-0.01828	-0.23532	-0.017565
C	40	-0.23842	-0.031907	0.25308	0.053661	-0.23266	-0.024765
H	41	0.25082	0.068469	0.25758	0.073327	0.25317	0.059418
H	42	0.26102	0.088216	0.24083	0.013581	0.25451	0.068214
H	43	0.24103	0.014707	0.24287	0.016732	0.24113	0.016911
H	44	0.24111	0.016063	-0.33502	0.37905	0.24263	0.018641
H	45	0.23807	0.016518	0.23234	0.005804	0.24064	0.019235
C	46	-0.33035	0.415823	0.21908	0.016693	-0.32927	0.416064
H	47	0.23393	-0.002305	0.20294	-0.022987	0.23453	0.004262
H	48	0.20216	-0.023762	-0.32471	0.454353	0.2228	0.014902
H	49	0.20324	-0.023103	0.21775	-0.006288	0.2078	-0.018221
C	50	-0.32677	0.415442	0.21381	-0.022026	-0.32264	0.460952
H	51	0.20488	-0.021084	0.2264	-0.000607	0.21152	-0.02672
H	52	0.23209	-0.006508	0.23994	0.016366	0.22844	-0.002009
H	53	0.20467	-0.021058	0.23977	0.01642	0.21884	-0.010081
* Total		0	0	0	0	0	0

4.8 Reference

(1). Yamaguchi, K.; Jensen, F.; Dorigo, A.; Houk, K. N. A spin correction procedure for unrestricted Hartree-Fock and Moller-Plesset wavefunctions for singlet diradicals and polyradicals. *Chem. Phys. Lett.* **1988**, *149*, 537.

(2). Yanai, T.; Tew, D. P.; Handy, N. C. A new hybrid exchange–correlation functional using the Coulomb-attenuating method (CAM-B3LYP). *Chem. Phys. Lett,* **2004,** *393,* 51–57.

(3). Zhang, D. Y.; Hrovat, D. A.; Abe, M.; Borden, W. T. DFT Calculations on the Effects of Para Substituents on the Energy Differences between Singlet and Triplet States of 2,2-Difluoro-1,3-diphenylcyclopentane-1,3-diyls. *J. Am. Chem. Soc.* **2003**, *125*, 12823.

(4). Yoshidomi, S.; Mishima, M.; Seyama, S.; Abe, M.; Fujiwara, Y.; Ishibashi, T. Direct Detection of a Chemical Equilibrium between a Localized Singlet Diradical and Its σ-Bonded Species by Time-Resolved UV/Vis and IR Spectroscopy. *Angew. Chem., Int. Ed.* **2017,** *56,* 2984–2988.

(5). (a) Reed, A. E.; Curtiss, L. A.; Weinhold, F. Intermolecular interactions from a natural bond orbital, donor-acceptor viewpoint. *Chem. Rev.,* **1988,** *6,* 899–926. (b) Reed, A. E.; Weinstock, R. B.; Weinhold, F. Natural population analysis. *J. Chem. Phys.* **1985,** *83,* 735–746.

(6). (a) Miertuš, S.; Scrocco, E.; Tomasi, J. Electrostatic interaction of a solute with a continuum. A direct utilizaion of AB initio molecular potentials for the prevision of solvent effects. *Chem, Phys.* **1981,** *55,* 117–129. (b) Tomasi, J.; Mennucci, B.; Cammi, Roberto. Quantum Mechanical Continuum Solvation Models. *Chem. Rev.,* **2005,** *105,* 2999–3094.

(7). (a) Becke, A.D. Densityfunctional thermochemistry. III. The role of exact exchange. *J. Chem. Phys.* **1993,** *98,* 5648–5652. (b) Lee, C.; Yang, W. ; Parr, R. Development of the Colle-Salvetti correlationenergy formula into a functional of the electron density. G. *Phys. Rev. B* **1988,** *37,* 785–789.

(8). Zhao, Y.; Truhlar, D. The M06 suite of density functionals for main group thermochemistry, thermochemical kinetics, noncovalent interactions, excited states, and transition elements: two new functionals and systematic testing of four M06-class functionals and 12 other functionals. *Theor. Chem. Acc.* **2008,** *120,* 215–241.

(9). Chai, J.-D.; Head-Gordon, M. Systematic optimization of long-range corrected hybrid density functionals. *J. Chem. Phys.* **2008,** *128,* 084106.

(10). Ditchfield, R.; Hehre, W. J.; Pople, J. A. Self-Consistent Molecular-Orbital Methods. IX. An Extended Gaussian-Type Basis for Molecular-Orbital Studies of Organic Molecules. *J. Chem. Phys.* **1971,** *54,* 724–728.

(11). Stephens, P. J.; Jalkanen, K. J.; Kawiecki, R. W. Theory of Vibrational Rotational Strengths: Comparison of a Priori Theory and Approximate Models. *J. Am. Chem. Soc.* **1990,** *112,* 6518–6529.

Chapter 5

Conclusions

Localized singlet diradicals are key intermediates involved in the bond-homolytic process. A thorough research study of the molecular structure, electronic structure and reactivity of localized singlet diradicals is essential to understand the mechanism of homolytic bond-cleavage and bond-formation reactions. These fundamental findings promise attractive applications to many fields of chemistry, such as material chemistries, organic synthesis, and biological chemistry.

In the present study, the chemistry of homolytic bond-cleavage and bond-formation was carefully investigated using notable nitrogen atom effect on a localized singlet diradicals, viz. 4,4-dialkoxy-1,2-diazacyclopentane-3,5-diyls, S-**DR4**. There are especially three important findings in this research; (1) The thermal equilibrium between S-**DR4**, and its σ-bonded species, **CP4**, was directly detected for the first time by time-resolved UV/Vis and IR spectroscopy. (2) The characteristics and reactivity of S-**DR4** were thoroughly investigated by transient absorption spectroscopic analysis in the photochemical denitrogenation of the aryl-/alkoxy-groups symmetrically and asymmetrically substituted azoalkanes, **AZ4**, by applying laser flush photolysis (LFP) experiments. In the transient absorption spectroscopic analysis, dual-decay processes, i.e. fast and slow processes, were found for all the electron-donating and electron-withdrawing groups substituted with S-**DR4**, except S-**DR4g** (X = Y = CN). The characteristics of S-**DR4** were revealed by the effects of solvent and substituent on the equilibration constant K with their corresponding σ-bonded species **CP4**, $K = k_{CP}/k_{DR}$. In other words, the zwitterionic resonance structures, **ZI2**, in which the anionic characteristic exists in benzylic carbon, and **ZI3** were revealed to make a significant contribution to S-**DR4**. The ring-closing process (k_{CP}) of S-**DR4** and ring-opening process (k_{DR}) of **CP4** were also investigated in detail using their Hammett-type plots of σ_p^+ and $\sigma_C^{\cdot}$. These experimental findings, as well as computational findings, revealed that S-**DR4** possess both characteristics of diradicals and zwitterion, which play an important role in determining the reactivity of the localized singlet diradicals. (3) The slow process was found to be the alkoxy-group migration reaction to afford two types alkoxy-group migrated species, **MG$_{CO}$4** and **MG$_C$4**. The crossover, spin-trapping, and LFP experiments for the slow decay process demonstrated the reaction mechanism of the formation of alkoxy-group migration species, **MG$_{CO}$4** and **MG$_C$4**, which are the slow decay process of S-**DR4**. The unique effect of the temperature on the product selectively also

clarified the individual reaction mechanism for the formation of $\mathbf{MG_{CO}4}$ and $\mathbf{MG_C4}$, that is, the rate-determining step is changeable by reaction temperature. The intersystem crossing (ISC) process was found to be a key step in the formation of $\mathbf{MG_{CO}4}$. The intramolecular migration process for the formation of the alkoxy-group 1,2-migrated species $\mathbf{MG_C4}$ was found to be accelerated by a polar solvent. This unique nitrogen atom effect on the singlet 1,3-diradicals makes it possible to open up a new series of localized singlet diradicals which are key intermediates in bond-homolytic process.

Acknowledgements

Finally, I am so grateful to have met this brilliant and exciting study, *Notable Nitrogen Atom Effect on Reactivity of the Localized Singlet 1,3-Diradicals.*

I was satisfied more than enough.

February, 2019
Shohei Yoshidomi

List of Publications

Article

(1) Direct Detection of a Chemical Equilibrium between a Localized Singlet Diradical and Its σ-Bonded Species by Time-Resolved UV/Vis and IR Spectroscopy.
Yoshidomi, S.; Mishima, M.; Seyama, S.; Abe, M.; Fujiwara, Y.; Ishibashi, T.
Angew. Chem. Int. Ed. **2017,** *56,* 2984–2988.
DOI: 10.1002/anie.201612329

(2) 1,2-Diazacyclopentane-3,5-diyl Diradicals: Electronic Structure and Reactivity.
Yoshidomi, S.; Abe, M.
J. Am. Chem. Soc. **2019,** *141,* 3920–3933.
DOI: 10.1021/jacs.8b12254